

REPORT DOCUMENTATION PAGE			Form Approved OMB No. 0704-0188	
Public reporting burden for this collection of information is estimated to average 1 hour per response, including the time for reviewing instructions, searching existing data sources, gathering and maintaining the data needed, and completing and reviewing the collection of information. Send comments regarding this burden estimate or any other aspect of this collection of information, including suggestions for reducing this burden, to Washington Headquarters Services, Directorate for Information Operations and Reports, 1215 Jefferson Davis Highway, Suite 1204, Arlington, VA 22202-4302, and to the Office of Management and Budget, Paperwork Reduction Project (0704-0188), Washington, DC 20503.				
1. AGENCY USE ONLY (Leave blank)		2. REPORT DATE 30.Jul.03		3. REPORT TYPE AND DATES COVERED DISSERTATION
4. TITLE AND SUBTITLE "THERMAL CONDUCTIVITY EVALUATION OF INITIAL STAGE PHENOMENA"				5. FUNDING NUMBERS
6. AUTHOR(S) MAJ SCHLAEFER CONSTANCE E				
7. PERFORMING ORGANIZATION NAME(S) AND ADDRESS(ES) PENNSYLVANIA STATE UNIVERSITY				8. PERFORMING ORGANIZATION REPORT NUMBER  CI02-1015
9. SPONSORING/MONITORING AGENCY NAME(S) AND ADDRESS(ES) THE DEPARTMENT OF THE AIR FORCE AFIT/CIA, BLDG 125 2950 P STREET WPAFB OH 45433				10. SPONSORING/MONITORING AGENCY REPORT NUMBER
11. SUPPLEMENTARY NOTES				
12a. DISTRIBUTION AVAILABILITY STATEMENT Unlimited distribution In Accordance With AFI 35-205/AFIT Sup 1				12b. DISTRIBUTION CODE
13. ABSTRACT (Maximum 200 words)				
<div style="display: flex; justify-content: space-between; align-items: center;"> <div style="text-align: center;"> <b>DISTRIBUTION STATEMENT A</b>            Approved for Public Release            Distribution Unlimited         </div> <div style="border: 1px solid black; padding: 10px; font-size: 2em; font-weight: bold;">           20030822 177         </div> </div>				
14. SUBJECT TERMS				15. NUMBER OF PAGES 235
				16. PRICE CODE
17. SECURITY CLASSIFICATION OF REPORT		18. SECURITY CLASSIFICATION OF THIS PAGE		19. SECURITY CLASSIFICATION OF ABSTRACT
20. LIMITATION OF ABSTRACT				

The Pennsylvania State University

The Graduate School

Department of Engineering Science and Mechanics

**THERMAL CONDUCTIVITY EVALUATION  
OF INITIAL STAGE SINTERING PHENOMENA**

A Thesis in

Engineering Science and Mechanics

by

Constance E. Schlaefer

© 2003 Constance E. Schlaefer

Submitted in Partial Fulfillment  
of the Requirements  
for the Degree of

Doctor of Philosophy

August 2003

The thesis of Constance E. Schlaefer has been reviewed and approved\* by the following:

Randall M. German  
Brush Chair Professor in Materials  
Thesis Advisor  
Chair of Committee

Bernhard R. Tittmann  
Schell Professor of Engineering Science and Mechanics

John R. Hellmann, Jr  
Professor of Materials Science and Engineering

Renata S. Engel  
Professor of Engineering Science and Mechanics

Ivica Smid  
Associate Professor of Engineering Science and Mechanics

Judith A. Todd  
P. B. Breneman Department Head Chair

\* Signatures are on file at the Graduate School.

## ABSTRACT

The onset of sinter bonding and concomitant handling strength is a critical period in the processing of powder metallurgy materials. Mechanical characterization of this evolution during predensification sintering is difficult, due to the fragile nature of the materials. Thermal properties such as thermal diffusivity and thermal conductivity also evolve during the onset of sinter bonding. This research investigates the potential for assessing mechanical strength through thermal conductivity evaluation, using the non-contact technique of laser flash analysis.

Thermal conductivity and transverse rupture strength were evaluated for a nickel powder system in three different formats: injection-molded, low-density die-compacted, and high-density die-compacted. Measurements focused on post-sintering strength and thermal conductivity evolution from 20 to 700°C for the first two formats. *In situ* strength was evaluated for the high-density die-compacted material.

Thermal conductivity was demonstrated to be a linear function of neck diameter, versus a function of the neck area as anticipated. Strength evaluation confirmed previous research that strength is a function of the neck area. Based on both properties' dependence on neck size, an integrated relationship was constructed, allowing mechanical strength to be directly predicted from thermal conductivity measurement for the given system.



## TABLE OF CONTENTS

LIST OF FIGURES.....	vii
LIST OF TABLES .....	xv
ACKNOWLEDGMENTS .....	xvii
LIST OF SYMBOLS .....	xviii
Chapter 1 Introduction .....	1
Chapter 2 Background .....	3
2.1 Key Powder Metallurgy Concepts .....	3
2.1.1 Shaping .....	3
2.1.2 Sintering .....	4
2.2 Sintering Monitors.....	13
2.3 Conductivity of Powder Metallurgy Materials .....	14
2.3.1 Theory and Models .....	14
2.3.2 Measurement .....	27
2.4 Strength of Powder Metallurgy Materials.....	38
2.4.1 Theory and Models .....	38
2.4.2 Measurement .....	42
2.5 Statement of Thesis.....	44
2.6 Potential Impact of Research .....	45
Chapter 3 Experimental Procedures.....	46
3.1 Outline of Activities .....	46
3.2 Powder Characterization.....	46
3.2.1 Particle Size Distribution.....	47
3.2.2 Pycnometer Density.....	49
3.2.3 Tap Density.....	50
3.2.4 Apparent Density .....	51
3.2.5 Scanning Electron Microscope Observation .....	51
3.3 Dilatometric Analysis .....	51
3.4 Sample Preparation .....	54
3.4.1 Die-compacted Samples .....	54
3.4.2 Quasi-Powder-Injection-Molded Samples.....	56
3.4.3 Injection-molded Samples .....	60

3.5 Transverse Rupture Strength .....	62
3.6 Thermal Conductivity .....	67
3.7 Ultrasonic Evaluation .....	73
3.8 Resonant Frequency Evaluation .....	75
3.9 Electrical Conductivity .....	80
3.10 Metallography and Microstructural Analysis .....	82
Chapter 4 Experimental Results.....	85
4.1 Initial Characterization .....	85
4.1.1 Powder Characterization.....	85
4.1.2 Dilatometric Analysis .....	88
4.2 Primary Results.....	89
4.2.1 Thermal Conductivity.....	89
4.2.2 Transverse Rupture Strength Testing .....	107
4.2.3 Relationship between Thermal and Mechanical Results.....	111
4.3 Secondary Results.....	113
4.3.1 Archimedes Density.....	114
4.3.2 Ultrasonic Evaluation .....	115
4.3.3 Resonant Frequency Evaluation .....	116
4.3.4 Electrical Conductivity Testing .....	119
4.3.5 Microstructural Observations .....	121
Chapter 5 Modeling .....	129
5.1 Physical Description of Circuit Model .....	129
5.2 Computer Simulation of Neck Growth.....	138
5.3 Modeled Thermal Conductivity Evolution .....	143
Chapter 6 Discussion .....	145
6.1 Relationship between Strength and Thermal Conductivity .....	145
6.1.1 Experimental Observations .....	146
6.2 Modeling Thermal Conductivity and Strength .....	169
6.2.1 Thermal Conductivity Models.....	169
6.2.2 Transverse Rupture Strength Model.....	177
6.2.3 Relating Strength to Thermal Conductivity.....	183
6.3 Modeling Capability .....	184
6.4 Impact of Secondary Results .....	185
Chapter 7 Conclusions .....	192
References .....	195
Appendix A Transverse Rupture Strength Raw Data .....	205

Appendix B Raw Thermal Diffusivity Data .....	208
Appendix C Room Temperature Ultrasonic Evaluation Raw Data .....	211
Appendix D Room Temperature Resonant Frequency Evaluation Raw Data .....	212
Appendix E Room Temperature Electrical Conductivity Raw Data .....	213
Appendix F Thermal Properties for Nickel.....	214
Appendix G Fortran Code for Computer Simulation Program, SintWin 2.3 .....	218

## LIST OF FIGURES

Figure 2.1: Two-sphere model for initial stage sintering.....	6
Figure 2.2: Examples of particle packing models.....	20
Figure 2.3: Cylindrical resistance elements modeling particles in simple cubic stacking. Shaded area represents an interfacial resistance element. ....	21
Figure 2.4: Ideal normalized time-temperature profile on rear face of laser flash disk.....	36
Figure 3.1: Schematic of Horiba LA-920 laser particle size analyzer .....	48
Figure 3.2: Schematic of Anter Unitherm 1161 vertical pushrod dilatometer.....	53
Figure 3.3: Schematic of CM vertical quench furnace .....	58
Figure 3.4: Time-temperature profile for PIM samples, thermally debound and quenched in air. Heating rate is 2°C/min, with a 2 hour hold at 425°C. Samples were heated in flowing hydrogen, held at temperature for 15 minutes while hydrogen was purged, then removed from the furnace and air-cooled. Each point represents a separate run. ....	63
Figure 3.5: Schematic of elevated temperature three-point bend system, also known as the FTT. ....	65
Figure 3.6: Schematic of the Anter Flashline® 5000 laser flash thermal diffusivity system. ....	67
Figure 3.7: Two disks rest in the sample holder, ready to be loaded into the test chamber.....	68
Figure 3.8: Technique for sanding thickness of disks while keeping faces parallel. ...	72
Figure 3.9: Schematic of time-of-flight ultrasonic evaluation of the quasi-PIM TRBs. ....	75
Figure 3.10: Schematic for resonant frequency test configuration .....	77

Figure 3.11: Bar excited in fundamental a) flexural and b) torsional resonance modes.....	78
Figure 3.12: Schematic for electrical conductivity test set-up.....	81
Figure 4.1: Scanning electron microscope image of the as-received Novamet 4SP-10 powder, showing spherical shape and relatively low surface roughness.....	87
Figure 4.2: Scanning electron microscope image showing layered microstructure of etched carbonyl powder.....	87
Figure 4.3: Linear percent shrinkage and shrinkage rate of loose powder, heated at 10°C/min to 1100°C in H <sub>2</sub> . ....	88
Figure 4.4: <i>In situ</i> thermal diffusivity evolution of quasi-PIM samples during heating-cooling cycle under hydrogen, nitrogen, and low vacuum atmospheres. Wrought properties are derived from the Thermophysical Properties Research Center (TPRC) database. <sup>21</sup> .....	90
Figure 4.5: Normalized <i>in situ</i> thermal diffusivity of quasi-PIM samples during heating-cooling cycle in hydrogen, nitrogen, and low vacuum atmospheres .....	91
Figure 4.6: SEM images of the a) top and b) bottom faces of quasi-PIM nickel disk after 24 laser flash measurements. ....	93
Figure 4.7: Cross-section at a) top and b) bottom face of quasi-PIM disk after <i>in situ</i> laser flash analysis up to 800°C. No significant differences or damage due to laser flash were noted.....	94
Figure 4.8: Percent shrinkage versus temperature for quasi-PIM Ni during heating-cooling cycle approximating laser flash heating-cooling cycle, flowing hydrogen atmosphere.....	96
Figure 4.9: Effective thermal conductivity of quasi-PIM nickel versus temperature, as developed during heating-cooling cycle in flowing hydrogen. ...	99
Figure 4.10: Normalized effective thermal conductivity of quasi-PIM nickel versus temperature, as developed during heating-cooling cycle in flowing hydrogen. ....	100
Figure 4.11: Normalized <i>in situ</i> thermal diffusivity of PIM disks during heating-cooling cycle, flowing nitrogen atmosphere. The error bars represent a 95% confidence level. ....	101
Figure 4.12: Normalized thermal conductivity of air-quenched PIM disks versus peak sintering temperature. Disks were removed from furnace at indicated	

peak temperature, cooled in air, and measured at 100°C. Sintering conducted in flowing hydrogen at 2°C/min to 425°C, 2 hour hold, 2°C/min to 700°C.....	102
Figure 4.13: PIM sample with layer of ash after laser flash measurement. Samples had been thermally debound in flowing hydrogen at 2°C/min to 200°C, removed from the furnace and air-cooled. Laser flash measurement was made at 100°C.....	103
Figure 4.14: Normalized <i>in situ</i> data for raw nickel powder. Sintering conducted in flowing nitrogen with a heating rate of 2°C/min to 425°C, 2 hour hold, 2°C/min to 500°C.....	104
Figure 4.15: Normalized thermal diffusivity versus sintering temperature of PIM and raw powder. Powder measured <i>in situ</i> in flowing nitrogen. PIM samples sintered in flowing hydrogen, air cooled, and measured at 100°C.....	105
Figure 4.16: Normalized thermal conductivity versus peak sintering temperature of air-quenched die-compacted disks. Measurements made in nitrogen at 200°C. The 200°C samples were also measured at room temperature, giving the same result. ....	106
Figure 4.17: <i>In situ</i> transverse rupture strength of die compacted samples as a function of temperature. Samples heated in flowing hydrogen at 3°C/min to test temperature with a 15-minute hold. Initial specimen fractional density was 0.75. ....	108
Figure 4.18: Room temperature transverse rupture strength of quasi-PIM samples as a function of sintering temperature. Samples were heated in flowing hydrogen at 10°C/min to peak temperature and quenched in water. Specimen initial fractional density was 0.55. ....	109
Figure 4.19: Room temperature transverse rupture strength and fractional density of PIM samples versus peak sintering temperature. Samples were heated at 2°C/min in flowing hydrogen to 425°C, held for 2 hours, and heated at 2°C/min to 700°C. Individual samples were removed at indicated peak temperature and air-cooled. Specimen initial fractional density was 0.58. Fractional density does not include binder mass. ....	110
Figure 4.20: Normalized transverse rupture strength versus normalized thermal conductivity for PIM air-quenched samples. Error bars represent 95% confidence level. ....	111
Figure 4.21: Normalized <i>in situ</i> transverse rupture strength versus thermal conductivity for die-compacted samples. Both properties are normalized by values of the wrought material at the test temperature. Error bars represent 95% confidence level.....	112

Figure 4.22: Normalized room temperature strength versus thermal conductivity for quasi-PIM samples. Samples were heated in flowing hydrogen at 10°C/min and quenched at 400°C, 500°C, 600°C, 700°C and 800°C. Original specimen fractional density was 0.55. Error bars represent 95% confidence level. ....	113
Figure 4.23: Fractional density versus sintering temperature for quasi-PIM material. Measurements made using Archimedes water immersion technique. Samples were sintered at 10°C/min in flowing hydrogen. ....	115
Figure 4.24: Room temperature longitudinal modulus versus sintering temperature for quasi-PIM material measured via ultrasonic evaluation .....	116
Figure 4.25: Young's modulus as a function of sintering temperature in quasi-PIM material as measured by resonant frequency inspection. ....	117
Figure 4.26: Shear modulus versus sintering temperature for quasi-PIM material, as measured by resonant frequency inspection. ....	118
Figure 4.27: Comparison of room temperature Young's modulus data versus peak sintering temperature for quasi-PIM material. Measurements made via ultrasonic and resonant frequency evaluations. ....	119
Figure 4.28: Room temperature electrical conductivity as a function of sintering temperature for quasi-PIM nickel samples. ....	120
Figure 4.29: Room temperature electrical conductivity for quasi-PIM samples, measured versus calculated via the Wiedemann-Franz ratio .....	121
Figure 4.30: SEM images of as-received powder and fracture surfaces for quasi-PIM material at increasing sintering temperatures. ....	122
Figure 4.31: SEM images of as-received powder and fracture surfaces for PIM material at increasing sintering temperatures. ....	124
Figure 4.32: Neck size ratio versus sintering temperature for quasi-PIM and PIM materials. Measurements of neck size were made via SEM, and normalized against a median particle size with respect to a population distribution. ....	125
Figure 4.33: Microscopy of PIM air-quenched TRBs at increasing sintering temperatures. Samples were etched with Fry's reagent. ....	126
Figure 4.34: Microscopy of quasi-PIM water-quenched TRBs at 400°C through 700°C. Samples were etched with Fry's reagent. ....	127
Figure 4.35. Microscopy of quasi-PIM water-quenched TRBs at 800°C through 1100°C. Samples etched with Fry's reagent. ....	128

Figure 5.1: Resistance element model cell for one-dimensional heat flow in simple-cubic packed structure .....	131
Figure 5.2: Computer simulated linear shrinkage iteration, loose nickel powder heated at 10°C in flowing hydrogen .....	141
Figure 5.3: Computer simulation of neck size evolution versus temperature for quasi-PIM material. Initial neck size ratio of 0.11 was used. ....	143
Figure 5.4: Computer simulation of thermal conductivity versus temperature for quasi-PIM material. Thermal conductivity is normalized with respect to wrought thermal conductivity at measurement temperature. ....	144
Figure 6.1: Room temperature transverse rupture strength versus thermal conductivity for quasi-PIM nickel. Samples heated at 10°C/min in hydrogen to the indicated peak temperature, water quenched. Linear trend line indicates a 0.99 correlation, with 99% confidence in statistical significance. ....	147
Figure 6.2: Room temperature transverse rupture strength versus thermal conductivity for injection molded nickel bars, heated at 3°C/min, with 2-hour hold at 425°C. Samples heated in hydrogen, removed from the furnace at the indicated temperatures, and cooled in air. Linear trend line shows a 0.93 correlation, with less than 95% confidence in statistical significance. ....	148
Figure 6.3: Room temperature transverse rupture strength versus thermal conductivity for quasi-PIM nickel. Samples heated at 10°C/min in hydrogen to the indicated peak temperature, water quenched. Second order polynomial trend line indicates 0.99 correlation, with 99% confidence in statistical significance. ....	149
Figure 6.4: Room temperature transverse rupture strength versus thermal conductivity for injection molded nickel bars, heated at 3°C/min, with 2-hour hold at 425°C. Samples heated in hydrogen, removed from the furnace at the indicated temperatures, and cooled in air. 2nd order polynomial trend line shows a 0.99 correlation, with 99% confidence in statistical significance. ....	150
Figure 6.5: Logarithm of normalized room temperature TRS versus logarithm of normalized thermal conductivity for quasi-PIM and PIM nickel. Temperatures indicate lowest and highest peak temperatures for each set of samples. ....	151
Figure 6.6: Logarithm of normalized strength versus logarithm of neck size ratio for quasi-PIM material. Neck size measurements made via SEM observation of ruptured bonds on fracture faces. ....	153



Figure 6.7: Room temperature transverse rupture strength versus neck size for PIM material. Trend line extended to determine a neck size that would match measured transverse rupture strength for 425°C sample. ....	154
Figure 6.8: Logarithm of normalized thermal conductivity versus logarithm of neck size ratio for quasi-PIM material.....	155
Figure 6.9: Thermal conductivity versus neck size for PIM material. Trend line extended to determine a neck size that would match measured thermal conductivity for 425°C sample. ....	156
Figure 6.10: SEM image of fracture surface of PIM sample. Light spots on the particle surface indicate interparticle bonds that ruptured during fracture. Sample was heated to 425°C in flowing hydrogen, and cooled in air to room temperature for transverse rupture testing. Arrows indicate necks that were counted in the measurement. ....	159
Figure 6.11: SEM image of fracture surface of PIM sample. Light spots on the particle surface indicate interparticle bonds that ruptured during fracture. Sample was heated to 500°C in flowing hydrogen, and cooled in air to room temperature for transverse rupture testing. Arrows indicate necks that were counted in the measurement. ....	160
Figure 6.12: Thermal conductivity versus neck size ratio for PIM material, using revised neck size of 0.034 for 425°C sample .....	162
Figure 6.13: Logarithm of thermal conductivity divided by transverse rupture strength versus logarithm of the neck size for both quasi-PIM and PIM specimens. The slope shows the difference between the two properties' relation with neck size. ....	164
Figure 6.14: Fractional density versus neck size ratio for various green fractional densities. Both calculated and experimental values are shown, along with the limit of the model, and the experimentally observed limit of neck size ratio at full density. <sup>80,112</sup> .....	166
Figure 6.15: <i>In situ</i> transverse rupture strength versus thermal conductivity for die-compacted nickel, heated at 3°C/min. Samples heated in hydrogen, removed from the furnace at the indicated temperatures, and cooled in air. ....	167
Figure 6.16: SEM image of flattened contact points on a fracture face of the die-compacted material. Samples were compacted to a fractional density of 0.75. This sample has been heated to 150°C to allow the paraffin wax binder to melt and flow to interparticle contact points. Sample was fractured at room temperature. ....	168

Figure 6.17: Experimental versus calculated thermal conductivity versus temperature for PIM material. Models use values of X/D as measured in SEM analysis. ....	170
Figure 6.18: Experimental versus calculated thermal conductivity versus temperature for quasi-PIM material. Models use values of X/D as measured in SEM analysis. ....	172
Figure 6.19: Calculated and experimental thermal conductivity versus peak sintering temperature. Conductivity values are normalized by conductivity for the wrought material at test temperature. Neck size ratio values experimentally determined from SEM images. ....	174
Figure 6.20: Measured thermal conductivity versus peak temperature for PIM material and raw powder. PIM material measured at 100°C, powder measured <i>in situ</i> . Both sets of measurements are normalized by wrought values at the measurement temperature. ....	175
Figure 6.21: Experimental and modeled thermal conductivity versus peak temperature for PIM material and raw powder. ....	177
Figure 6.22: Experimental versus calculated transverse rupture strength for PIM material. Heating profile was 3°C/min, with 2-hour hold at 425°C. Samples heated in hydrogen, removed from the furnace and cooled in air. ....	178
Figure 6.23: Experimental and calculated transverse rupture strength versus peak sintering temperature for PIM material. Samples were tested at room temperature. Error bars reflect a 90% confidence level. ....	181
Figure 6.24: Experimental and calculated transverse rupture strength using multiple models for quasi-PIM material. Heating profile was 10°C/min to peak temperature, no hold. Samples heated in hydrogen, water quenched. ....	182
Figure 6.25: Elastic modulus versus neck size ratio for quasi-PIM material. Slope of linear regression indicates exponent of neck size in Young's modulus model. Confidence in statistical significance is 99% for both sets of data. ....	186
Figure 6.26: Calculated and measured bulk modulus of quasi-PIM material versus peak sintering temperature. Bulk modulus calculated from Young's modulus and Poisson's ratio values measured via resonant frequency evaluation. ....	187
Figure 6.27: Calculated and experimental room temperature electrical conductivity versus peak sintering temperature for quasi-PIM material. Heating profile was 10°C/min to peak temperature, no hold. Samples were heated in hydrogen and water quenched. ....	189

Figure 6.28: Electrical conductivity versus neck size for quasi-PIM material. Slope of linear regression indicates exponent of neck size in electrical conductivity model. ....	190
Figure F.1: Thermal diffusivity of nickel as a function of temperature, based on TPRC data <sup>21</sup> .....	214
Figure F.2: Thermal conductivity of solid nickel as a function of temperature, based on TPRC data <sup>107</sup> .....	215
Figure F.3: Specific heat of solid nickel as a function of temperature, based on TPRC data <sup>105</sup> .....	216

## LIST OF TABLES

Table 2.1: Summary of variables for sintering mechanisms in initial stage sintering equation.....	11
Table 2.2: Examples of models for electrical conductivity ( $\lambda$ ) and thermal conductivity ( $\kappa$ ) in porous materials .....	24
Table 2.3: Examples of strength models for powder metallurgy materials .....	40
Table 3.1: Molding parameters for nickel/polymer-wax TRBs .....	61
Table 3.2: Polishing method for porous nickel samples, epoxy mounts.....	84
Table 4.1: Summary of Novamet 4SP-10 powder characterization data .....	86
Table 5.1: Sintering parameters for 4SP-10 nickel powder system .....	139
Table A.1: Room temperature transverse rupture strength raw data, quasi-PIM material. Samples sintered in vertical furnace at 10°C/min in hydrogen, no hold, water quenched. ....	205
Table A.2: Room temperature transverse rupture strength raw data, PIM material. Samples sintered in retort furnace at 2°C/min in hydrogen, 15 minute hold, air quenched. ....	206
Table A.3: <i>In situ</i> transverse rupture strength raw data, die-compacted material. Samples sintered at 3°C/min in hydrogen, no hold, fractured at indicated sinter temperature. ....	207
Table B.1: Post-sinter thermal diffusivity measurements, quasi-PIM material. Samples sintered in vertical furnace at 10°C/min in hydrogen, no hold, water quenched. Measurements were made at room temperature. ....	208
Table B.2: Post-sinter thermal diffusivity measurements, PIM material. Samples sintered in retort furnace at 2°C/min in hydrogen, with a 2-hour hold at 425°C, air cooled. Measurements made at 100°C. ....	209

Table B.3: Post-sinter thermal diffusivity measurements, die-compacted material. Samples sintered in Flaming Tensile Tester at 3°C/min in hydrogen, air-cooled. Measurements made at 200°C.....	210
Table C.1: Room temperature ultrasonic evaluation raw data for quasi-PIM material. Young's modulus calculated from time-of-flight data. Samples sintered in vertical furnace at 10°C/min in hydrogen, water-quenched at indicated sintering temperature.....	211
Table D.1: Room temperature resonant frequency raw data for quasi-PIM material. Samples sintered in vertical furnace at 10°C/min in hydrogen, water-quenched at indicated sintering temperature. ....	212
Table E.1: Room temperature electrical conductivity raw data for quasi-PIM materials. Samples sintered in vertical furnace at 10°C/min in hydrogen, water-quenched at indicated sintering temperature. ....	213
Table F.1: Thermal properties of nickel as a function of temperature, based on TPRC data <sup>21, 107, 105</sup> .....	217

## ACKNOWLEDGMENTS

My first acknowledgement must go to the United States Air Force. I am deeply grateful for the opportunity to pursue a doctorate as a member of the armed services, a rare and cherished privilege. I also thank Colonel Cary Fisher, who selected me for this opportunity, and Lt Col Greg Shoales, whose advice pointed me to Penn State.

I must next express deep gratitude to my advisor, Professor Randall German, who allowed me free rein in his world-class research facility. It has been an amazing experience to work with one of the top experts in the field of materials, sintering, and powder metallurgy. His advice and support have been invaluable. I also gratefully acknowledge the support of the Harvey Brush Chair for my research expenses.

My thanks also to the members of Anter Corporation, who provided the laser flash equipment that was a key component of this research. Their continued support and advice has been extremely helpful.

My friends and coworkers here in the P/M lab have been a great part of this experience. Debby, Suri, and Ravi have been with me through thick and thin. Sundar, Lou, Tracy, Tim, Julian and Kristina helped me pull it all together. Thanks to all of you.

Most of all, thanks to my family, and especially my husband, who is my sounding board, confidante, and best friend. His support and love carried me through this effort.

## LIST OF SYMBOLS

$A$	Cross-sectional area ( $\text{m}^2$ )
$A_i$	Cross-sectional area of the interface element ( $\text{m}^2$ )
$A_n$	Cross-sectional area of the neck element ( $\text{m}^2$ )
$A_p$	Cross-sectional area of the pore element ( $\text{m}^2$ )
$A_s$	Cross-sectional area of the shoulder element ( $\text{m}^2$ )
$a$	Shape parameter describing the winding shape of the metal around the pore
$B, B_0$	Kinetic terms in sintering; Effective and wrought bulk modulus
$b$	Burgers vector (m)
$C$	Concentration of atoms or vacancies (atoms or vacancies/ $\text{m}^3$ )
$C'$	Empirical constant representing phonon contributions to thermal conductivity
$C_{ab}$	Absorption coefficient for the solid
$C_o$	Equilibrium concentration of vacancies (vacancies/ $\text{m}^3$ )
$C_p$	Heat of the material per unit mass, assuming constant pressure ( $\text{J/g}\cdot\text{K}$ )
$C_s$	Shape factor for resonant frequency calculation
$C_{sc}$	Scattering coefficient for the solid
$D$	Particle diameter (m)
$D_b$	Grain boundary diffusivity ( $\text{m}^2/\text{s}$ )
$D_p$	Pore diameter (m)
$D_s$	Surface diffusivity ( $\text{m}^2/\text{s}$ )
$D_v$	Volume diffusivity ( $\text{m}^2/\text{s}$ )
$d_o, d_i$	Outer and inner diameters of a cylinder (m)
$E$	Young's modulus (Pa)
$E_{gen}$	Energy generated in a unit volume (J)
$E_{in}$	Energy input in a unit volume (J)
$E_{out}$	Energy output from a unit volume (J)
$\Delta E$	Net change in energy of a unit volume (J)
$F$	Pore shape parameter
$f$	Pore shape factor
$f_f$	fundamental flexural frequency ( $\text{s}^{-1}$ )
$f_t$	fundamental torsional frequency ( $\text{s}^{-1}$ )
$G$	Shear modulus (Pa)
$g$	Empirical processing and geometry exponent; depth of heat penetration from laser flash (m)
$H$	Slab thickness (m)
$H_{init}$	Initial slab thickness (m)
$H_{corr}$	Corrected slab thickness (m)
$h$	heat transfer coefficient ( $\text{W}/(\text{m}^2\cdot\text{K})$ )

I	Applied current (A)
J	Net atomic flux (atoms/(m <sup>2</sup> ·s))
K	Stress concentration factor
k	Boltzmann's constant (1.381 × 10 <sup>-23</sup> J/K)
L	Lorentz function (W·Ω/K <sup>2</sup> )
L'	Empirical constant representing Lorentz function (W·Ω/K <sup>2</sup> )
L <sub>b</sub>	Length of bar (m)
L <sub>CYL</sub>	Length of cylinder resistance element (m)
L <sub>i</sub>	Length of interface resistance element (m)
L <sub>n</sub>	Length of neck resistance element (m)
L <sub>p</sub>	Distance between contact probes (m)
L <sub>s</sub>	Length of shoulder resistance element (m)
L <sub>sup</sub>	Span between supports (m)
M	Molecular weight (g/mol)
M <sub>p</sub>	Dimensionless parameter describing pore shape
m	Sintering exponent; Neck size exponent for thermal conductivity
m <sub>b</sub>	Mass of the bar (g)
m <sub>dry</sub>	Mass of the dry sample (g)
m <sub>imm</sub>	Mass of the oil-impregnated sample immersed in water (g)
m <sub>oil</sub>	Mass of the sample impregnated with oil (g)
N <sub>c</sub>	Coordination number
n	Sintering exponent; Neck size exponent for transverse rupture strength
n <sub>R</sub>	Refractive index of the solid
P	Load at rupture (N)
P <sub>v</sub>	Vapor pressure (Pa)
t <sub>w</sub>	Cylinder wall thickness (m)
p	Filet radius (m)
Q	Activation energy (kJ/mol); Quantity of heat input (J/m <sup>2</sup> )
q	Flow rate of heat energy (W)
q''	Heat flux (W/m <sup>2</sup> )
q'''	Rate of heat generation for a unit volume (W/m <sup>3</sup> )
R	Electrical or thermal resistance (Ω or (W/K) <sup>-1</sup> )
R <sub>A</sub>	Resistance circuit representing interparticle contact (W/K) <sup>-1</sup>
R <sub>B</sub>	Resistance circuit representing half of particle bulk (W/K) <sup>-1</sup>
R <sub>cyl</sub>	Electrical or thermal resistance through a cylinder (Ω or (W/K) <sup>-1</sup> )
R <sub>s</sub>	Shape factor in resonant frequency relation; Resistance of shoulder element (W/K) <sup>-1</sup>
R <sub>p</sub>	Resistance of the pore element (W/K) <sup>-1</sup>
R <sub>sph</sub>	Electrical or thermal resistance (Ω or W/K) <sup>-1</sup> ) through a sphere
R <sub>1</sub> , R <sub>2</sub>	Radii of curvature (m)
S	Empirical processing and geometry factor
T	Absolute temperature (K)
$\mathcal{T}$	Normalized temperature
t	Time (s)



$t_b$	Thickness of the bar (m)
$t_{1/2}$	Half rise time (s)
$V$	Volume ( $m^3$ ); Voltage (V)
$V_s$	Fractional density
$v_L$	Longitudinal velocity (m/s)
$w_b$	Width of bar (m)
$X$	Interparticle neck diameter (m)
$\alpha$	Thermal diffusivity ( $m^2/s$ )
$\alpha_{eff}$	Effective thermal diffusivity ( $m^2/s$ )
$\alpha_{meas}$	Measured thermal diffusivity ( $m^2/s$ )
$\chi$	Thermal conductivity parameter
$\delta$	Grain boundary width (m)
$\epsilon$	Porosity
$\epsilon_{eng}$	Percent elongation at failure
$\gamma$	Surface energy ( $J/m^2$ ); Thermal conductivity parameter
$\eta$	Viscosity (Pa·s)
$\phi$	Emmissivity of the pore walls
$\kappa$	Thermal conductivity (W/m·K)
$\kappa_{conv}$	Convective contribution to effective thermal conductivity (W/m·K)
$\kappa_{eff}$	Effective thermal conductivity (W/m·K)
$\kappa_g$	Thermal conductivity of gas (W/m·K)
$\kappa_i$	Thermal conductivity of interface material (W/m·K)
$\kappa_n$	Thermal conductivity neck material (W/m·K)
$\kappa_o$	Thermal conductivity of a fully dense material (W/m·K)
$\kappa_{rad}$	Radiative contribution to effective thermal conductivity (W/m·K)
$\kappa_s$	Thermal conductivity of shoulder material (W/m·K)
$\lambda_{eff}$	Effective electrical conductivity ( $\Omega \cdot m$ ) <sup>-1</sup>
$\lambda_g$	Conductivity of the gas in the pore ( $\Omega \cdot m$ ) <sup>-1</sup>
$\lambda_o$	Electrical conductivity of a fully dense material ( $\Omega \cdot m$ ) <sup>-1</sup>
$\nu$	Poisson's ratio
$\theta$	Pore orientation parameter
$\rho_{H_2O}$	Density of water ( $kg/m^3$ )
$\rho_m$	Material resistivity ( $\Omega \cdot m$ )
$\rho_o$	Theoretical density ( $kg/m^3$ )
$\rho_s$	Dry sintered density ( $kg/m^3$ )
$\rho_t$	Tap density ( $kg/m^3$ )
$\sigma_B$	Stefan-Boltzmann constant (approximately $5.7 \times 10^{-8} W/(m^2 \cdot K)$ )
$\sigma_{eng}$	Engineering strength (Pa)
$\sigma_o$	Wrought strength (Pa)
$\sigma_s$	Sintered strength (Pa)
$\sigma_{surf}$	Surface stress (Pa)
$\sigma_{true}$	True strength (Pa)

$\sigma_{\text{ult}}$	Ultimate tensile strength (Pa)
$\sigma_{\text{RAD}}$	Radial crush strength (Pa)
$\sigma_{\text{TRS}}$	Transverse rupture strength (Pa)
$\Omega$	Atomic volume ( $\text{m}^3$ )
$\omega$	Normalized time

## **Chapter 1**

### **Introduction**

Powder metallurgy is a manufacturing technique used to produce “net-shape” (i.e. in final dimensions) or “near-net-shape” components in an economic, high-volume manner. The key steps of this technique are the shaping of the powdered metal into desired form, and sintering, which is the bonding of the powder through thermally activated mechanisms. It is the beginning of this second step, the onset of bonding between the powders, which will be the focus of this research.

The onset of sintering represents a transition from individual particles to a cohesive network of solid material. This transition is reflected in the physical and mechanical properties of the material, so the measurement of these properties may be used to infer the degree of sintering. Much work has been done in the study of properties at higher density, resulting in many physical and mechanical models based on porosity. However, the measurement of properties of a powder as it is beginning to bond is difficult, which has limited the experimental investigation of this critical point in the sintering process. This difficulty, due to the very fragile nature of the material at the onset of sintering, defines the motivation and the proposed methods of this research.

The characterization of mechanical strength in the material as it is sintering is key to predicting and controlling damage mechanisms. In powder metallurgy materials, density gradients, thermal gradients, and even dimensional gradients can generate stresses

during the sintering process. If these stresses are larger than the *in situ* strength of the material, distortion or cracking can result. A solid understanding of the *in situ* strength evolution is essential to predict both when the material is most vulnerable to these damage mechanisms, and when significant handling strength emerges. However, the very low mechanical strength of the material makes the measurement of this property difficult, which leads to the examination of non-contact means of characterizing this evolution. Laser flash analysis, which is a non-contact technique for measuring thermal diffusivity in a material, presents such a means for measuring the *in situ* evolution of thermal properties.

This work pulls together several existing capabilities to create a new methodology for determining *in situ* thermal and mechanical properties. Laser flash analysis is used to assess thermal property evolution in pre-densification sintering. Strength evolution is also investigated and characterized using standard and specially configured three-point bend test equipment. A semi-empirical model integrates the relationship between these two properties. The impact of this model and methodology is the ability to evaluate and predict the development of thermal and mechanical properties of a powder metallurgy system via laser flash analysis.

## **Chapter 2**

### **Background**

This chapter provides a description of the key concepts involved in the creation of the hypothesis for this research. It presents fundamental background in the areas of powder metallurgy and particularly sintering that provide the basis for the modeling process used in this work. A review of past work and models for both thermal conductivity and strength of powder metallurgy products is presented, leading up to the statement of hypothesis, and its potential impact on the field of powder metallurgy.

#### **2.1 Key Powder Metallurgy Concepts**

Powder metallurgy offers the intriguing capability of creating net-shaped components while tailoring materials and microstructure to obtain desirable properties. Within the manufacturing process, two key steps define the creation of an engineering component from a powdered metal: shaping and sintering.

##### **2.1.1 Shaping**

Die compaction and injection molding are the two primary methods used to form metal powders into a desired component shape. Die compaction relies on the application of compressive force to powders, plastically deforming the particles to create an inter-

locking network. It is this network that provides the room temperature handling strength, or green strength, of the part. Metal powder is poured into a die of the desired shape, and is compressed into the die by the movement of a punch. Powdered wax or stearate may be blended with the powder to act as a lubricant, easing die wear.<sup>1</sup> Die compaction allows simply shaped parts to be formed at a relatively low cost, producing parts with a high degree of dimensional precision, although typically some residual porosity remains. Alternatively, metal injection molding allows more shape complexity with a homogeneous, but less dense, green structure. In this process, metal powder is blended with a binder material or combination of materials, typically organic with a melting temperature below 200°C. Upon heating the mixture, the binder material acts as a liquid carrier for the powder, creating a paste that can be injected into a mold in the shape of the desired part. Once the binder material cools and hardens, the part is ejected. In this case, it is the hardened binder material that provides the room temperature handling strength, or green strength, for the component. This material is removed prior to sintering, often by chemical or thermal decomposition, or a combination of the two.

### **2.1.2 Sintering**

The sintering of solid powders is the bonding of individual particles through the thermally activated movement of atoms. Reduction of surface energy is the driving force for this process. Since a free surface has a higher energy than material in the bulk, the high surface-to-volume ratio of powders drives a reduction of energy through the reduction of surface area. As a result, two particles in contact will tend to form a metallurgical

bond, or neck, transitioning from two free solid surfaces to a grain boundary at the contact point. The establishment of this bond, and its subsequent growth to approximately one third of the length of the particle diameter is generally termed initial stage sintering.<sup>2</sup> Intermediate stage sintering is characterized by the elimination of the interconnected pore network and a related densification of the material as the particles draw together. This discussion will focus on initial stage sintering.

The initiation and growth of the interparticle neck depends on mass flow to the contact point between the two particles. Mass transport occurs both at the surface of the particles, and through the bulk of the solid. Surface transport mechanisms such as surface diffusion and evaporation/condensation result in growth of the neck, but cause no change in the relative distance between particles.<sup>2</sup> Bulk mechanisms such as volume diffusion, grain boundary diffusion, plastic flow, and viscous flow transport atoms to the neck from the interior of the particle. This redistribution of mass results in both neck growth and movement of the particle centers closer together – densification.<sup>2</sup> The relative contributions of each of these sintering mechanisms are a function of the bulk material properties, particle size, time, and temperature.

A general model for initial stage sintering<sup>3</sup> is based on the analysis of two spheres in contact described by Kuczynski,<sup>4</sup> Coble,<sup>5</sup> and Kingery and Berg<sup>6</sup> in the late 1940s and 1950s. These models assume monosized spheres joined at a circular neck. The spheres are of diameter  $D$ , with a neck of diameter  $X$  at the contact point, as shown in Figure 2.1. Once this neck is established, the difference in curvature between the neck region and the rest of the sphere surface creates a driving force for mass flow. This gradient is illus-

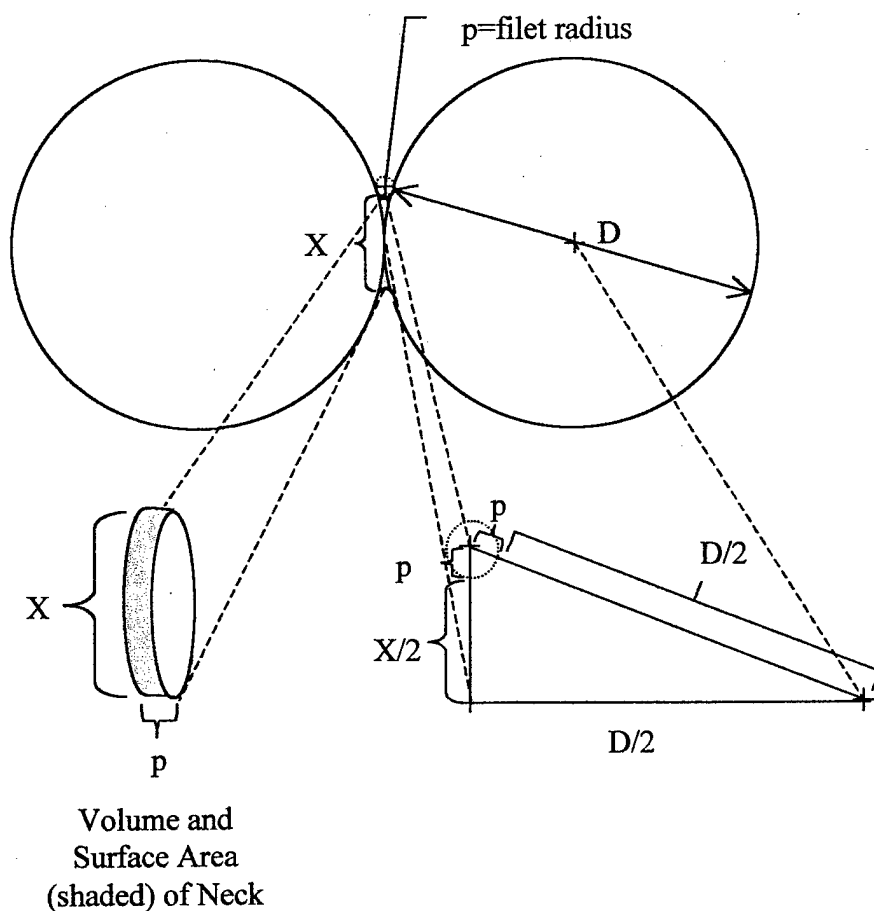


Figure 2.1: Two-sphere model for initial stage sintering

trated by comparing the surface stress of the particles in the region of the neck to surface stresses elsewhere on the sphere. Surface stress is described by the Laplace equation, shown as Equation 2.1:



$$\sigma_{Surf} = \gamma \left( \frac{1}{R_1} + \frac{1}{R_2} \right) \quad ( 2.1 )$$

where  $\gamma$  is the surface energy of the material ( $\text{J/m}^2$ ), and  $R_1$  and  $R_2$  are radii of curvature (m), perpendicular with respect to each other, describing curvature of the surface. For the particle surface away from the neck,  $R_1$  and  $R_2$  are both equal to half the particle diameter, therefore surface stress is shown in Equation 2.2 as:

$$\sigma_{Surf} = \frac{4\gamma}{D} \quad ( 2.2 )$$

At the particle neck,  $R_1$  is centered in the circular cross-section of the neck, with dimension  $X/2$ , and  $R_2$  is the radius  $p$ , which is centered outside the solid, and is therefore by convention shown as negative. Using the geometry of the right triangle shown in Figure 2.1,  $p$  is approximately equal to  $X^2/4D$ . Surface stress at the neck is shown in Equation 2.3:

$$\sigma_{Surf} = \gamma \left( \frac{2}{X} - \frac{4D}{X^2} \right) \quad ( 2.3 )$$

When  $X$  is small, the stress given by Equation 2.3 is much larger than that given in Equation 2.2. The stress gradient due to this difference is initially large when the neck is small, but decreases as the neck grows.

A model for the kinetics of initial stage sintering is based on atomic diffusion.<sup>2</sup>

The change in volume of the neck over time ( $dV/dt$ ) is described by Equation 2.4:

$$\frac{dV}{dt} = JA\Omega \quad ( 2.4 )$$

where  $J$  is the net atomic flux (atoms/( $m^2 \cdot s$ )),  $A$  is the cross-sectional area through which the atoms flow ( $m^2$ ), and  $\Omega$  is the volume of the atom ( $m^3$ ).  $J$  is described by Fick's First Law, which is a function of atomic diffusion. Using the case of volume diffusion, this relation is shown in Equation 2.5:

$$J = -D_v \frac{dC}{dx} \quad ( 2.5 )$$

where  $D_v$  is the diffusivity of an atom through the volume of a given material ( $m^2/s$ ),  $dC$  is the concentration gradient of atoms or vacancies (atoms or vacancies/ $m^3$ ) over distance  $dx$  (m). The concentration of vacancies ( $C$ ) is a function of temperature and of curvature, and is described by Equation 2.6:

$$C = C_o \left[ 1 - \frac{\gamma \Omega}{kT} \left( \frac{1}{R_1} + \frac{1}{R_2} \right) \right] \quad ( 2.6 )$$

where  $C_0$  is the equilibrium concentration of vacancies (vacancies/m<sup>3</sup>),  $k$  is Boltzmann's constant ( $1.381 \times 10^{-23}$  J/K), and  $T$  is absolute temperature (K). The distance over which this comparison is made is the width of the neck, which is approximated as  $p$ . The area through which the flux occurs is the surface area of the neck as shown in Figure 2.1, which is given in Equation 2.7:

$$A = 2 \pi \frac{X}{2} \left[ \frac{X^2}{4D} \right] = \frac{\pi X^3}{4D} \quad ( 2.7 )$$

The volume of the neck is described by Equation 2.8 as:

$$V = \pi \left[ \frac{X}{2} \right]^2 \left[ \frac{X^2}{4D} \right] = \frac{\pi X^4}{16D} \quad ( 2.8 )$$

Equation 2.4 may be restated in terms of Equation 2.8, as shown in Equation 2.9:

$$\frac{dV}{dt} = \frac{\pi X^3}{4D} \left( \frac{dX}{dt} \right) \quad ( 2.9 )$$

Substituting Equations 2.5, 2.6, and 2.7 in Equation 2.4, then setting Equation 2.4 equal to Equation 2.9 provides a relationship between neck size, particle size, time, temperature, and material properties, which can be simplified in the form of Equation 2.10:

$$\left(\frac{X}{D}\right)^n = \frac{Bt}{D^m} \quad (2.10)$$

where  $B$  represents the material and temperature parameters in an Arrhenius relation, shown in Equation 2.11:

$$B = B_0 \exp\left(\frac{-Q}{kT}\right) \quad (2.11)$$

In this case,  $B_0$  contains material constants, and  $Q$  is an activation energy (kJ/mol).

The initial stage sintering relation shown in Equation 2.10 provides the framework for many models representing the various sintering mechanisms operating under isothermal conditions. These models reflect the effect of temperature, and material and geometric parameters in the variables  $m$ ,  $n$ , and  $B$ . German summarizes these variables for different sintering mechanisms as shown in Table 2.1.<sup>2</sup>

Table 2.1: Summary of variables for sintering mechanisms in initial stage sintering equation

Mechanism	m	n	B
Viscous Flow	1	2	$3\gamma/\eta$
Plastic Flow	1	2	$9\pi\gamma b D_v/kT$
Evaporation-Condensation	2	3	$(3P_v\gamma/\rho_o 2)(\pi/2)^{1/2}(M/kT)^{3/2}$
Volume Diffusion	3	4	$80D_v\gamma\Omega/kT$
Grain Boundary Diffusion	4	6	$20\delta D_b\gamma\Omega/kT$
Surface Diffusion	4	7	$56D_s\gamma\Omega^{4/3}/kT$
$\gamma$ = surface energy (J/m <sup>2</sup> ) $\eta$ = viscosity (Pa·s) $\rho_o$ = theoretical density (g/m <sup>3</sup> ) $\delta$ = grain boundary width (m) $\Omega$ = atomic volume (m <sup>3</sup> ) $b$ = Burgers vector (m) $D_v$ = Volume diffusivity (cm <sup>2</sup> /s) $D_b$ = Grain boundary diffusivity (cm <sup>2</sup> /s) $D_s$ = Surface diffusivity (cm <sup>2</sup> /s) $P_v$ = Vapor pressure (Pa) $M$ = Molecular weight (g/mol) $k$ = Boltzmann's constant ( $1.381 \times 10^{-23}$ J/K) $T$ = Absolute temperature (K)			

The initial stage sintering equation provides a model for both computer simulations and experimental laboratory exploration of sintering kinetics. Computer simulations based on Equation 2.10 can predict both neck growth and densification by calculating contributions of surface mass transport mechanisms and bulk transport

mechanisms separately.<sup>7</sup> Ashby's *HIP 6.0*<sup>8,9</sup> is an example of such a program, which allows the input of sintering parameters, and predicts the dominant sintering mechanism and resultant shrinkage for a given time-temperature combination. Since the dominant mechanism depends on material, geometric, and temperature considerations, a "map" can be constructed with borders indicating transfer from one dominant mechanism to another.<sup>10</sup> Although Equation 2.10 assumes isothermal conditions, it can be used for heating rate calculations by using a time-step approach, calculating neck growth at increasing temperatures in a series of time increments. Hwang, German, and Lenel describe this approach<sup>11</sup> by rearranging Equation 2.4 as shown in Equation 2.12:

$$\dot{X} = \frac{J A}{dV/dX} \quad ( 2.12 )$$

where  $\dot{X}$  is the growth rate of the neck (m/s). Note that definitions for flux and area vary with each sintering mechanism, and the atomic volume,  $\Omega$ , in this case is imbedded in the definition of flux. Hwang, German and Lenel's approach is the basis for the computer simulation program, SintWin 2.3,<sup>12</sup> discussed in Chapter 5.

Laboratory experiments can assess sintering kinetics via the initial stage sintering equation by measuring properties such as neck size, neck growth, and densification. The rate of sintering as measured from these properties can then provide an activation energy, from which the experimenter may infer the sintering mechanisms.<sup>13</sup> Different types of sintering monitors are described in Section 2.2.

## 2.2 Sintering Monitors

A wide variety of techniques have been proposed and explored as avenues to monitor the sintering process. One approach to describing the types of proposed monitors is to categorize them as direct versus indirect techniques.<sup>14</sup> Direct techniques such as quantitative microscopy, SEM hot stage, and video imaging provide visual data to quantify neck growth and densification. Physical measurements of surface area via gas adsorption evaluation, and densification via dilatometry also are considered direct techniques, offering physical insight into separate sintering mechanisms—for example neck growth caused by surface diffusion with no contribution to densification.<sup>15</sup> Indirect methods, on the other hand, study the initiation and growth of interparticle bonds by assessing other properties of the material, and inferring an interparticle neck size or density. For example, the electrical and thermal conductivities of a compact increase during the early stages of sintering, so measuring conductivity could show the relative change in interparticle contact area. The elastic properties, such as bulk modulus, also change, which allow ultrasonic evaluation of the sintering process. Mechanical evaluations, such as hardness and strength testing, also indicate the extent of interparticle bonding. *In situ* transverse rupture testing has been the basis of key work on strength evolution,<sup>16</sup> but this type of test provides only one piece of data per test run, and the more fragile injection-molded compacts are difficult to evaluate with accuracy.<sup>17</sup> In considering various techniques for investigation of pre-densification sintering phenomena, especially in the case of injection-molded materials, the fragility of the material prompts the examination of minimally invasive or non-contact means of monitoring interparticle bonding *in situ*. To

this end, the focus of background research was on the use of field properties, specifically electrical and thermal conductivity, to monitor sintering phenomena and extend previous observations on *in situ* strength evolution.

## 2.3 Conductivity of Powder Metallurgy Materials

### 2.3.1 Theory and Models

The models for electrical and thermal conductivity of powder metallurgy components are closely related, and for many purposes, identical. The similarity lies in the nature of the energy carriers in a metal. Electrical conductivity in a metal is a function of the number of charge carriers (electrons) and their mobility. Thermal conductivity in a metal is a function of two mechanisms: electron motion, again a function of number of carriers and mobility, and lattice wave (phonon) motion.<sup>18</sup> Of these two contributors, electron motion is the dominant means of transferring thermal energy.<sup>19</sup> Since the valence electron acts as both a charge carrier and energized particle, the electrical conductivity is directly related to the electron contribution to thermal conductivity. This relationship is known as the Wiedemann-Franz ratio, which is shown in Equation 2.13:

$$\frac{\kappa}{\lambda T} = L \quad ( 2.13 )$$



where  $\kappa$  is the thermal conductivity (W/m·K),  $\lambda$  is electrical conductivity ( $\Omega^{-1}$ ), and  $L$  is known as the Lorenz function, typically equal to  $2.45 \times 10^{-8} \text{ W}\cdot\Omega/\text{K}^2$ . An adaptation of this equation that incorporates the phonon component is shown in Equation 2.14:

$$\kappa = L'\lambda T + C' \quad ( 2.14 )$$

where  $L'$  and  $C'$  are empirical constants, with  $L'$  representing the Lorentz function corresponding to electron contributions to thermal conduction, and  $C'$  representing phonon contributions.<sup>20,21</sup> It is the close relationship between thermal and electrical conductivity that makes the experimental methods and model development of electrical conductivity relevant to later discussion on thermal conductivity, particularly since electrical conductivity has been the more thoroughly explored avenue of monitoring sintering.

Electrical conductivity has been cited since the 1950's as an experimental method to investigate compact density and look for defects in powdered metal parts, and has continued to be a topic of active investigation through the years.<sup>22,23,24,25,26,27</sup> Changes in the electrical conductivity are particularly informative in the early stages of sintering, indicating sintering activity at lower temperatures than other techniques may reveal.<sup>22</sup> Comparisons of electrical conductivity evolution versus dilatometry indicate enhanced conductivity before the onset of densification.<sup>28</sup> There is general agreement in the literature that for metal powders, interparticle contacts dominate conductivity behavior at low temperatures.<sup>24,29</sup> The nature of the particle surface in terms of contaminants, lubricants, oxides and roughness all increase resistance at the interparticle contact.<sup>27</sup> As a compact

is heated, particularly in a reducing atmosphere, dewaxing, and reduction of oxides contribute to increasing conductivity. For a die-compacted powder, annealing acts to relieve residual stresses caused by compaction, further increasing the conductivity of the compact.<sup>26</sup> In a ceramic, or an injection-molded metal powder, no plastic deformation is assumed at the interparticle contacts, so the very small contact area constricts the flow of current. The area of interparticle contact, or contiguity, is directly related to the electrical conductivity of the compact.<sup>30</sup> Consequently, if surface phenomena and annealing can be distinguished from contiguity, electrical conductivity may be used to evaluate neck growth in initial stage sintering, even in the absence of densification.

Models describing conductivity, either electrical or thermal, of a two-phase material usually assume a continuous network of one of the phases. In the most basic sense, a rule of mixtures model may be applied, using effective load bearing area<sup>26</sup> or minimum solid area<sup>31</sup> to represent the average cross-section of interconnected solid in a porous material. This approach is shown in Equation 2.15 for the case of electrical conductivity:

$$\lambda_{eff} = \lambda_o(1 - \varepsilon) \quad ( 2.15 )$$

where  $\lambda_{eff}$  is the electrical conductivity of the sintered material ( $\Omega^{-1}$ ),  $\lambda_o$  is the conductivity of the fully dense material, and  $\varepsilon$  is the porosity ( $0 < \varepsilon < 1.0$ ), which is dimensionless.<sup>32</sup> This representation assumes zero conductivity in the pores and solid conductivity equivalent to that of a wrought bar the same size as the effective load bearing area. This simple model can provide an upper limit for conductivity, but particularly at higher porosities

and early stages of sintering, pore shape, pore size distribution, and interparticle contacts limit conductivity to much lower values. A step toward incorporating pore shape can be made by incorporating an additional variable as shown in Equation 2.16:

$$\lambda_{eff} = a\lambda_o(1 - \varepsilon) \quad ( 2.16 )$$

where  $a$  describes the winding shape of the metal around the pore.<sup>33</sup> Since the pore shape is normally related to the porosity, i.e. as porosity decreases, pore shape becomes less convoluted; the parameter  $a$  is shown in Equation 2.17 as:

$$a = M_p(1 - \varepsilon) \quad ( 2.17 )$$

A solution for conductivity of the porous material is shown by Equation 2.18:

$$\lambda_{eff} = M_p\lambda_o(1 - \varepsilon)^2 \quad ( 2.18 )$$

with  $M_p$  as a dimensionless parameter describing pore shape. During later stages of sintering, as porosity approaches zero and  $M_p$  approaches 1 (spherical pore shape), the limit of this equation shows that for low porosities (less than or equal to 20%), conductivity may be modeled as Equation 2.19:

$$\lambda_{eff} = \lambda_o(1 - 2\varepsilon) \quad ( 2.19 )$$

An upper and lower bound system of equations incorporating pore shape and orientation is shown in Equation 2.20 as:<sup>34</sup>

$$\lambda_{eff} = \lambda_o (1 - \varepsilon)^{\frac{\cos^2 \theta (3F-1) - 2F}{2F(F-1)}} \quad ( 2.20 )$$

where  $\cos^2 \theta$  describes pore orientation and F describes pore shape, ranging from lenticular to spherical. These equations reduce to Equation 2.21 for an upper bound:

$$\lambda_{eff} = \lambda_o (1 - \varepsilon)^{\frac{3}{2}} \quad ( 2.21 )$$

and Equation 2.22 as a lower bound for isotropic porous materials:

$$\lambda_{eff} = \lambda_o (1 - \varepsilon)^3 \quad ( 2.22 )$$

However, these equations still do not account for the more complex pore shapes encountered in initial stage sintering. In order to establish a valid lower bound for thermal conductivity evolution, analysis must start with a bed of granular material.

The most basic model for conduction in a bed of loose powder assumes a simple cubic stacking of mono-sized spherical particles,<sup>35</sup> with effective conductivity a function of the number of contact points on a single particle, also known as the coordination num-

ber, and the quality of the contacts.<sup>36, 37</sup> Models for more densely packed structures, as well as random packing, may be extrapolated by increasing the coordination number. Examples of particle packing models are shown in Figure 2.2. As a lower bound, the particles may be considered in point contact, although this is not strictly possible in the mathematical sense. Batchelor and O'Brien's analysis<sup>38</sup> of this problem is widely referenced for this application. For a random packed granular bed, conductivity may be described by Equation 2.23:

$$\lambda_{eff} = \lambda_g \left[ 4 \ln \left( \frac{\lambda_o}{\lambda_g} \right) - 11 \right] \quad ( 2.23 )$$

where  $\lambda_g$  is conductivity of the gas in the pore and  $\lambda_o$  is conductivity of the solid.

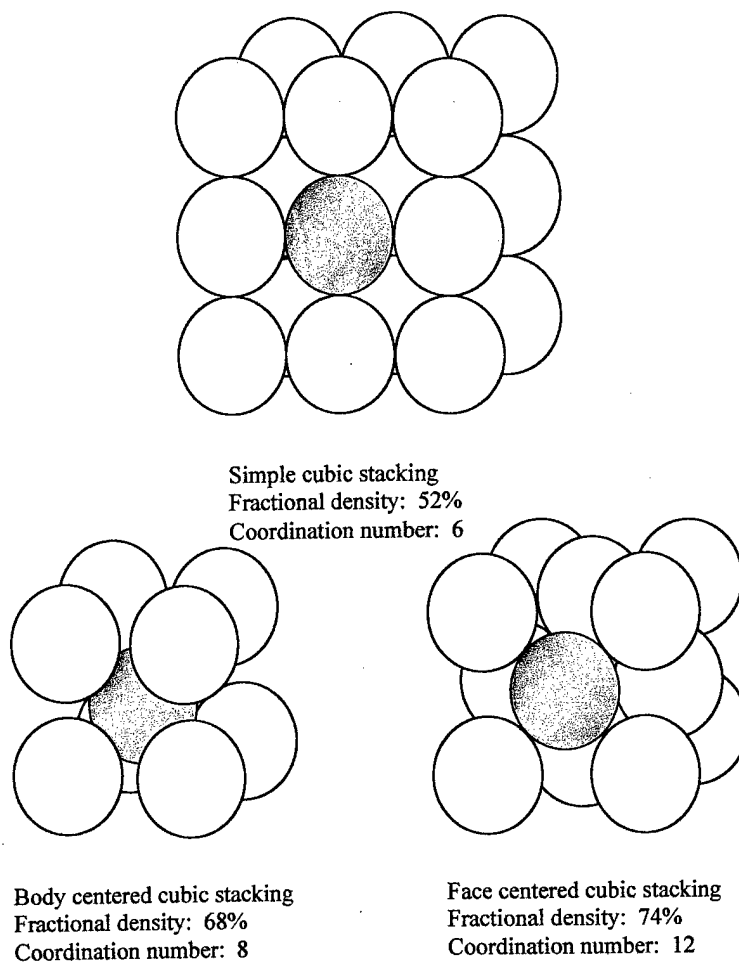


Figure 2.2: Examples of particle packing models.

Once particle contact is considered to have dimensions of area, a basic unit cell is usually modeled with particle contacts described as cylinders in end-to-end contact, as shown in Figure 2.3. Contact resistance and other interface issues can be modeled as an additional interfacial resistance element.

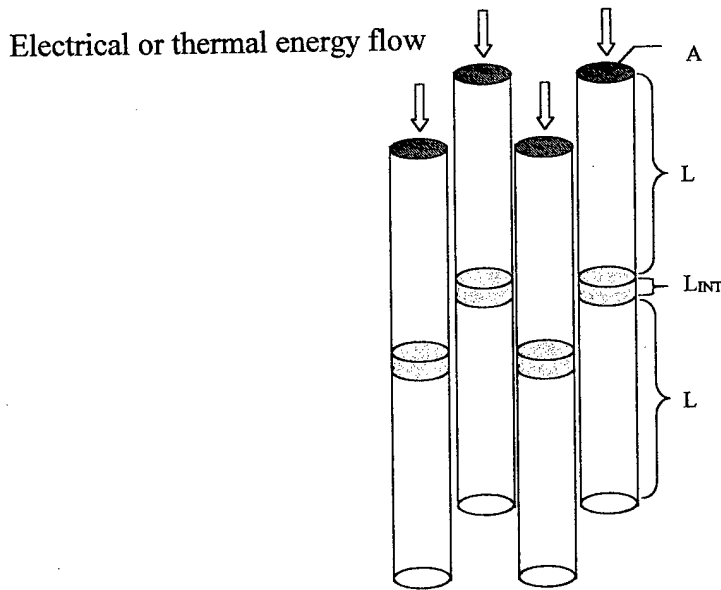


Figure 2.3: Cylindrical resistance elements modeling particles in simple cubic stacking. Shaded area represents an interfacial resistance element.

Such a configuration can be described as an electrical or thermal resistance element.

Equation 2.24 shows the relation using electrical conductivity:

$$R = \frac{L_{CYL}}{\lambda A} \quad ( 2.24 )$$

where  $R$  is the resistance ( $\Omega$ ),  $L_{CYL}$  is the cylinder height (m),  $\lambda$  is the electrical conductivity ( $\Omega \cdot m$ )<sup>-1</sup>, and  $A$  is the cross-sectional area (m<sup>2</sup>). Haviar, Panek and Sajgalik used such an approach, modeling the cross-sectional geometry in terms of neck radius ( $X/2$ ).<sup>39</sup>

The area of the neck grows during sintering, and accommodates the conservation of volume. The solution is approximated as shown in Equation 2.25:

$$\frac{\lambda}{\lambda_o} = \frac{1}{K \left( Y + Z \ln \left( \frac{X}{D} \right) \right)} \quad ( 2.25 )$$

where K is a constant representing particle packing (2 for simple cubic). Y and Z are constants associated with the numerical approximation of the geometry, and are 0.4244 and -0.6904 respectively.

The more complex modeling of spheres in contact may be approximated by heat flow from a finite circular area to a semi-infinite half space, which Carslaw and Jaeger<sup>40</sup> have solved as Equation 2.26:

$$\frac{R_{Sph}}{R_{Cyl}} = \frac{\pi}{4} \left( \frac{X}{D} \right)^{-1} \quad ( 2.26 )$$

where  $R_{Sph}$  is resistance ( $\Omega$  or  $m \cdot K/W$ ) experienced by a sphere normalized by  $R_{Cyl}$ , the resistance of a cylinder of equivalent contact area. This relation shows constriction effects as heat flows through a reduced cross-sectional area. Efforts to transition from spheres with small contacts to larger deformed faces have been demonstrated using both thermal resistance elements and more elaborate finite element modeling techniques.<sup>41</sup>



An alternate technique for modeling multi-phase systems is "volume averaging", which integrates a field variable such as temperature over a sample volume. Hadley<sup>42</sup> used this approach to develop a semi-empirical formulation for two-phase and three-phase systems. Properties of solid phases are combined to determine an "effective conductivity", which is then combined with a model for porosity. Upper and lower limits of porosity can be defined using Maxwell's models,<sup>43</sup> i.e. isolated solid spheres suspended in liquid and isolated liquid spheres suspended in contiguous solid. This multiphase model may be used to represent metal powder covered by a layer of oxide (two solid phases) in a gas or fluid matrix, as well as other combinations of solid powders.

Recent work on thermal conductivity evolution during sintering, focused on initial stage sintering of ceramics, models thermal conductivity as a function of neck growth using finite element methods.<sup>44,45</sup> The two-sphere model is used to represent an average particle contact, with neck growth occurring via surface diffusion as described by Coble.<sup>5</sup> Calculations of the effective thermal conductivity of a powder compact using a 3-d numerical model show a linear relationship between thermal conductivity ( $\kappa$ ) and neck size ratio ( $X/D$ ). This model accounts for the change in bulk thermal conductivity with temperature, and change in neck size and particle size with temperature and time via the initial stage sintering equation. The model assumes the presence of a pre-existing neck, and that surface diffusion is the only active sintering mechanism.

All of the models described up to this point have been essentially interchangeable between electrical and thermal conductivity. A sampling of electrical and thermal models is shown in Table 2.2. However, there are some distinctions between the two proper

Table 2.2: Examples of models for electrical conductivity ( $\lambda$ ) and thermal conductivity ( $\kappa$ ) in porous materials

Model	Author, Reference	Comments
$\lambda_{eff} = \lambda_o(1 - \varepsilon)$	Hirschhorn, 32	Rule of mixtures; $\lambda_o$ is the wrought conductivity
$\lambda_{eff} = \lambda_o(1 - 2\varepsilon)$	Boccinni, 33	Porosity less than 20%
$\lambda_{eff} = \lambda_o(1 - \varepsilon)^{\frac{3}{2}}$ $\lambda_{eff} = \lambda_o(1 - \varepsilon)^3$	Ondracek, 34	Upper and lower bounds for porous, isotropic material
$\lambda_{eff} = \lambda_o \frac{1 - \varepsilon}{1 + \chi \varepsilon^2}$	Koh and Fortini, 46	$\chi$ represents pore distribution and shape—typically about 11
$\lambda_{eff} = \lambda_o \left[ N_c - \frac{N_c - 1}{(1 - \varepsilon)^{1/3}} \right]$	Jernot, 30	Incorporates different packing schemes by changing coordination number.
$\lambda_{eff} = \lambda_g \left[ 4 \ln \left( \frac{\lambda_o}{\lambda_g} \right) - 11 \right]$	Batchelor and O'Brien, 38	Loose powder in point contact
$\frac{\lambda}{\lambda_o} = \frac{1}{K \left( Y + Z \ln \left( \frac{X}{D} \right) \right)}$	Haviar, Panek, and Sajgalik, 39	K represents particle packing, 2 for simple cubic. Y and Z are system constants 0.4244 and -0.6904 respectively.
$\kappa_{eff} = \kappa_g \left[ \varepsilon + \frac{\beta(1 - \varepsilon)}{\phi + \zeta(\kappa_g / \kappa_o)} \right]$	Kunii and Smith, 48	Heat transfer in loose powder; $\beta$ and $\gamma$ usually 1 and 2 respectively; $\phi$ represents heat transfer mechanism
$\kappa_{eff} = 376 \left[ \frac{14.2(X/D) + 0.15}{T} \right]$	Birnboim <i>et al.</i> , 44	Heat transfer. Incorporates neck growth and temperature; ZnO using laser flash

ties that bear further discussion. Although the assumption of zero effective conductivity through the pores is valid for electrical conductivity, such an assumption is not entirely true for thermal conductivity. In addition to thermal conduction in the network of solid material, conduction through the gas in the pores, convection in the pores, and radiation across the pores must also be considered, although the values may be so small that they are ultimately negligible.

Conductivity through the gas in the pores, while quite limited, becomes relevant to calculations particularly at lower densities (higher porosity), when conductivity at the interparticle contact is low. Howard and Kozack<sup>47</sup> used Maxwell's isolated pore model<sup>43</sup> as an upper limit and the Kunii-Smith loose powder model<sup>48</sup> as a lower limit to explore density and pore conductivity effects. In addition to demonstrating the intuitive conclusion that effective conductivity increases with fractional density, their calculations indicated that the process gas has a surprisingly significant impact on effective conductivity. A particle bed infiltrated with a hydrogen process gas resulted in an effective conductivity five times larger than a particle bed infiltrated with nitrogen process gas.<sup>47</sup>

Convection within a porous material is the transfer of heat from one wall of a pore to the opposite wall through the movement of gas in the pore. Assuming free, versus forced, flow of the gas through the porous network, the flow is dependent on a characteristic dimensioning of the distance between the walls – in this case the pore diameter. Luikov<sup>49</sup> describes the contribution of convection in a porous material as the product of the heat transfer coefficient,  $h$ , and the distance between solid faces, which is the pore diameter,  $D_p$ , as shown in Equation 2.27:

$$\kappa_{\text{conv}} = hD_p \quad ( 2.27 )$$

where  $h$  has the dimensions of  $W/(m^2 \cdot K)$ . Since the circulation of the gas is dependent on the pore diameter, if the dimension is very small, i.e. less than 5 mm, circulation within the pore becomes negligible, and any transfer of heat through the gas is considered as conduction across the pore.

Radiation in a porous material is often considered negligible at lower temperatures,<sup>50</sup> but rapidly increases in magnitude as a function of temperature. In general, radiation within a pore is proposed to have a  $T^3$  dependence,<sup>51</sup> which is described by Equation 2.28:

$$\kappa_{\text{rad}} = F_{\text{rad}} T^3 \quad ( 2.28 )$$

where  $F_{\text{rad}}$  is a material-related constant and  $T$  is the absolute temperature (K). This relationship agrees with experimental observations on low-density porous materials.<sup>52</sup> A more detailed representation is used by Murashov and White<sup>50</sup> as shown in Equation 2.29:

$$\kappa_{\text{rad}} = \frac{16n_R^2 \sigma_B T^3}{3(C_{ab} + C_{sc})} \quad ( 2.29 )$$

where  $n_R$  is the refractive index of the solid,  $\sigma_B$  is the Stefan-Boltzmann constant (approximately  $5.7 \times 10^{-8} \text{ W}/(\text{m}^2 \cdot \text{K})$ ), and  $C_{ab}$  and  $C_{sc}$  are the absorption and scattering coefficients for the solid. A second form that accounts for pore shape and size as well as material emissivity is shown in Equation 2.30:

$$\kappa_{rad} = 4 f \phi \sigma_B T^3 D_p \quad ( 2.30 )$$

where  $f$  is a dimensionless pore shape factor usually less than or equal to 1,<sup>53</sup>  $\phi$  is the dimensionless emissivity of the pore walls, and  $D_p$  is the diameter of the pore.<sup>54</sup>

### 2.3.2 Measurement

Electrical conductivity for powder metallurgy materials is measured via direct current resistivity testing as described by ASTM standard test method,<sup>55</sup> using a 4-point contact system. In the 4-point configuration, current flows between two outer contacts, and the voltage drop is measured between two inner contacts. Ohm's Law, shown in Equation 2.31, is used to calculate the resistivity of the sample:

$$V = IR \quad ( 2.31 )$$

where  $I$  is the applied current (A),  $R$  is the resistivity of the sample ( $\Omega$ ), and  $V$  is the measured voltage (V). Results of this type of characterization may also be described in

terms of electrical conductivity,  $\lambda$ , which is the reciprocal of resistivity. In practice, results are very sensitive to probe contact, and probe pressure may cause surface damage, particularly in green materials.<sup>56</sup> Several examples of non-standard experimental probe configurations designed to circumvent these problems include contact arrays<sup>57</sup> and plate contacts in a two-point piston configuration,<sup>58</sup> offering larger contact area to increase measurement reliability.

A number of different methods are available to measure thermal conductivity. Speyer gives a review of basic techniques including radial heat flow, calorimeter method, hot wire method, and guarded hot plate method.<sup>59</sup> These are all contact methods, where thermal energy is input and measured through physical contacts on the sample material, and are subject to losses through contact resistance. Additionally, surface heat losses occur over time while achieving and maintaining thermal equilibrium, which is necessary for a direct thermal conductivity measurement. An alternative to these methods is the laser flash method, a non-contact means of measuring thermal diffusivity within the span of a few seconds. While thermal (and electrical) conductivity are steady state properties, thermal diffusivity is a dynamic property, from which thermal conductivity may be inferred. A brief background description of thermal diffusivity and its relation to thermal conductivity will be presented, followed by a description of the laser flash technique for measurement of thermal diffusivity and thermal conductivity.

From the first law of thermodynamics (the conservation of energy), the energy,  $E$ , of a volume element can be described by Equation 2.32:<sup>60</sup>

$$E_{in} + E_{gen} - E_{out} = \Delta E \quad ( 2.32 )$$

where  $E_{in}$  and  $E_{out}$  are heat flowing in and out of the unit volume,  $E_{gen}$  is heat generated in the volume, and  $\Delta E$  is the net change in energy of the volume. The energy added to an element ( $E_{in}$ ) can be described by the heat flux,  $q''$ . Consider a single direction,  $x$ , in a cubic volume element. For a steady-state flow of heat, i.e. one that does not change with time, the flow rate of heat energy  $q_x$ , through a cross-sectional area,  $A$ , is represented by the Fourier equation, Equation 2.33:

$$\frac{q_x}{A} = q_x'' = -\kappa \left[ \frac{\partial T}{\partial x} \right] \quad ( 2.33 )$$

where  $q_x''$  is the heat flux ( $W/m^2$ ),  $\kappa$  is a constant of proportionality called thermal conductivity ( $W/m \cdot K$ ), and  $\delta T/\delta x$  represents a thermal differential across a given distance in direction  $x$  ( $K/m$ ). The same relation may be established for directions  $y$  and  $z$ . Considering this flux coming into a unit volume from all three directions, as in Equation 2.34, over a given time increment,  $dt$ :

$$E_{in} = q_x'' dy dz dt + q_y'' dx dz dt + q_z'' dx dy dt \quad ( 2.34 )$$

Energy generated within the volume may be described as the rate of heat generation for a unit volume,  $q'''$ , times the unit volume and the increment of time, shown in Equation 2.35:

$$E_{gen} = q''' dx dy dz dt \quad ( 2.35 )$$

Energy leaving the volume element is represented as the flux equation, Equation 2.34, over an increment in time, as shown in Equation 2.36:

$$E_{out} = \left( q_x'' + \frac{\partial q_x''}{\partial x} dx \right) dy dz dt + \left( q_y'' + \frac{\partial q_y''}{\partial y} dy \right) dx dz dt + \left( q_z'' + \frac{\partial q_z''}{\partial z} dz \right) dx dy dt \quad ( 2.36 )$$

The initial internal energy of the material,  $E_{int}$ , is shown in Equation 2.37:

$$E_{int} = C_p T \rho_o dx dy dz \quad ( 2.37 )$$

where  $C_p$  is the heat of the material per unit mass, assuming constant pressure (J/g·K),  $T$  is the absolute temperature (K), and  $\rho_o$  is the theoretical density of the material (g/m<sup>3</sup>). The change in internal energy over a time increment for a unit volume is then shown in Equation 2.38:



$$\Delta E = C_p \frac{\partial T}{\partial t} \rho_o dx dy dz dt \quad ( 2.38 )$$

Revisiting the original energy relation described in Equation 2.32 and incorporating the respective definitions yields Equation 2.39:

$$-\frac{\partial q_x''}{\partial x} - \frac{\partial q_y''}{\partial y} - \frac{\partial q_z''}{\partial z} + q''' = \rho_o C_p \frac{\partial T}{\partial t} \quad ( 2.39 )$$

The definition of heat flux as described in Equation 2.32 may be used to bring temperature more directly into the result, as shown in Equation 2.40:

$$-\frac{\partial}{\partial x} \left[ \kappa \frac{\partial T}{\partial x} \right] - \frac{\partial}{\partial y} \left[ \kappa \frac{\partial T}{\partial y} \right] - \frac{\partial}{\partial z} \left[ \kappa \frac{\partial T}{\partial z} \right] + q''' = \rho_o C_p \frac{\partial T}{\partial t} \quad ( 2.40 )$$

By considering  $\kappa$  as a constant through the material, a new material constant may be used combining the material properties  $\kappa$ ,  $\rho_o$ , and  $C_p$ , shown in Equation 2.41:

$$\alpha \left[ \frac{\partial^2 T}{\partial x^2} + \frac{\partial^2 T}{\partial y^2} + \frac{\partial^2 T}{\partial z^2} \right] + q''' \frac{\alpha}{\kappa} = \frac{\partial T}{\partial t} \quad ( 2.41 )$$

where  $\alpha$  is the thermal diffusivity of the material in  $\text{m}^2/\text{s}$ . If no heat is generated within the unit volume, Equation 2.41 can be restated in the following manner (Equation 2.42):

$$\frac{\partial T}{\partial t} = \alpha \left[ \frac{\partial^2 T}{\partial x^2} + \frac{\partial^2 T}{\partial y^2} + \frac{\partial^2 T}{\partial z^2} \right] \quad ( 2.42 )$$

In this format, it is easier to see a similarity to Fick's second law, a key principle in the study of materials science describing atomic diffusivity under non-steady state conditions. Thermal diffusivity is analogous to atomic diffusivity — the former a function of temperature gradient, and the latter a function of atomic concentration gradient. The solution to this differential equation depends on the boundary conditions. For the application of laser flash testing, Carslaw and Jaeger<sup>40</sup> presented a solution detailed later in this section.

The laser flash method for measuring thermal diffusivity was first proposed by Parker, Jenkins, Butler, and Abbott<sup>61</sup> in the early 1960's, under sponsorship from the United States Air Force, and has developed into an ASTM standardized technique for assessing thermal diffusivity of a material.<sup>62</sup> This technique overcomes the difficulties of surface heat losses and contact resistance at heat sources and sinks, as well as the sometimes complex or large sample size requirements encountered in other thermal conductivity techniques. The flash method uses a small disk of sample material (12 mm in diameter, 1 to 3 mm thick). One face of the disk is irradiated with an "instantaneous" burst of energy from a xenon flash, laser, or electron beam, and the resulting temperature rise on the far face of the disk is measured using an infrared sensor. The short time frame minimizes heat loss, and the non-contact energy input and measurement minimizes thermal contact problems. In combination with specific heat and density data, thermal con-

ductivity of a material may be calculated according to the relationship drawn from Equations 2.40 and 2.41, shown here as Equation 2.43:

$$\kappa = \alpha C_p \rho_s \quad ( 2.43 )$$

where  $\kappa$  is thermal conductivity (W/m·K),  $\alpha$  is thermal diffusivity ( $\text{m}^2/\text{s}$ ),  $C_p$  is the specific heat of the sample material at constant pressure (J/kg·K), and  $\rho_s$  is the sintered density ( $\text{g}/\text{m}^3$ ). A comparative method may also be used to extract thermal conductivity from the laser flash technique. By comparing diffusivity measurements of both a sample and reference material whose specific heat and density data are known, conductivity may be calculated without a separate specific heat measurement.<sup>63</sup>

The theory behind the laser flash technique begins with the solution to the heat conduction equation, Equation 2.42, which provides a temperature profile description for one-dimensional heat flow through a slab of thickness  $H$ . This solution, as presented by Carslaw and Jaeger<sup>40</sup>, is shown in Equation 2.44:

$$T(x,t) = \frac{1}{H} \int_0^H T(x,0) dx + \frac{2}{H} \sum_{n=1}^{\infty} \exp\left(\frac{-n^2 \pi^2 \alpha t}{H^2}\right) \cos \frac{n \pi x}{H} \int_0^H T(x,0) \cos \frac{n \pi x}{H} dx \quad ( 2.44 )$$

where  $x$  is distance into the slab in meters and  $t$  is time in seconds. Initially, a very thin layer on the front face, to a depth 'g', is heated by the laser flash to a constant tempera-

ture, which leads to boundary conditions shown in Equations 2.45 and 2.46. Referencing the equilibrium starting temperature,  $T$ , at  $t=0$ :

$$T(x,0) = \frac{Q}{\rho_o C_p g} \text{ for } 0 < x < g \quad (2.45)$$

$$T(x,0) = 0 \text{ for } g < x < H \quad (2.46)$$

where  $Q$  is the quantity of heat input on the front face ( $J/m^2$ ),  $C_p$  is the specific heat ( $J/g \cdot K$ ), and  $\rho_o$  is the theoretical density of the material ( $g/m^3$ ). At the rear face, where  $x=H$ , the temperature varies with time as shown in Equation 2.47:

$$T(H,t) = \frac{Q}{\rho_o C_p H} \left[ 1 + 2 \sum_{n=1}^{\infty} (-1)^n \exp\left(\frac{-n^2 \pi^2 \alpha t}{H^2}\right) \right] \quad (2.47)$$

Grouping terms under the variables  $\omega$  and  $\mathcal{T}$  as shown in Equation 2.48:

$$\omega = \frac{\pi^2 \alpha t}{H^2} \text{ and } \mathcal{T} = \frac{T}{T_{\max}} \quad (2.48)$$

the normalized rear face temperature can be expressed as Equation 2.49:

$$\mathcal{T} = 1 + 2 \sum_{n=1}^{\infty} (-1)^n \exp(-n^2 \omega) \quad (2.49)$$

If the temperature and time data are measured on the back face, the time corresponding to 50% of the maximum temperature rise, also called the half-rise time ( $t_{1/2}$ ), is the reference time, and the diffusivity is determined from the definition for  $\omega$  when  $\omega$  at  $\mathcal{F}=0.5$  is 1.38, given in Equation 2.50.

$$\alpha = \frac{1.38H^2}{\pi^2 t_{1/2}} \quad ( 2.50 )$$

The profile of the normalized temperature-time curve is shown in Figure 2.4.

This derivation is based on several assumptions regarding boundary conditions: energy input is instantaneous and there are no surface heat losses. Several corrections to the original solution have been proposed to account for departures from these conditions. Cowan<sup>64</sup> proposed a correction for heat losses from the faces based on the cooling portion of the time-temperature curve. Cape and Lehman<sup>65</sup> expanded upon this analysis by also considering two-dimensional conduction and incorporating surface losses from the sides of the disk. Cape and Lehman, followed by Taylor and Cape,<sup>66</sup> also proposed adjustments to account for a finite (versus instantaneous) pulse width on the front face of the sample. Experimentally, surface losses increase with thicker samples and longer rise times, but finite pulse effects decrease, so a balance must be struck between these two departures from ideal boundary conditions when determining optimal sample thickness. Clark and Taylor presented a new approach to address surface losses through radiation

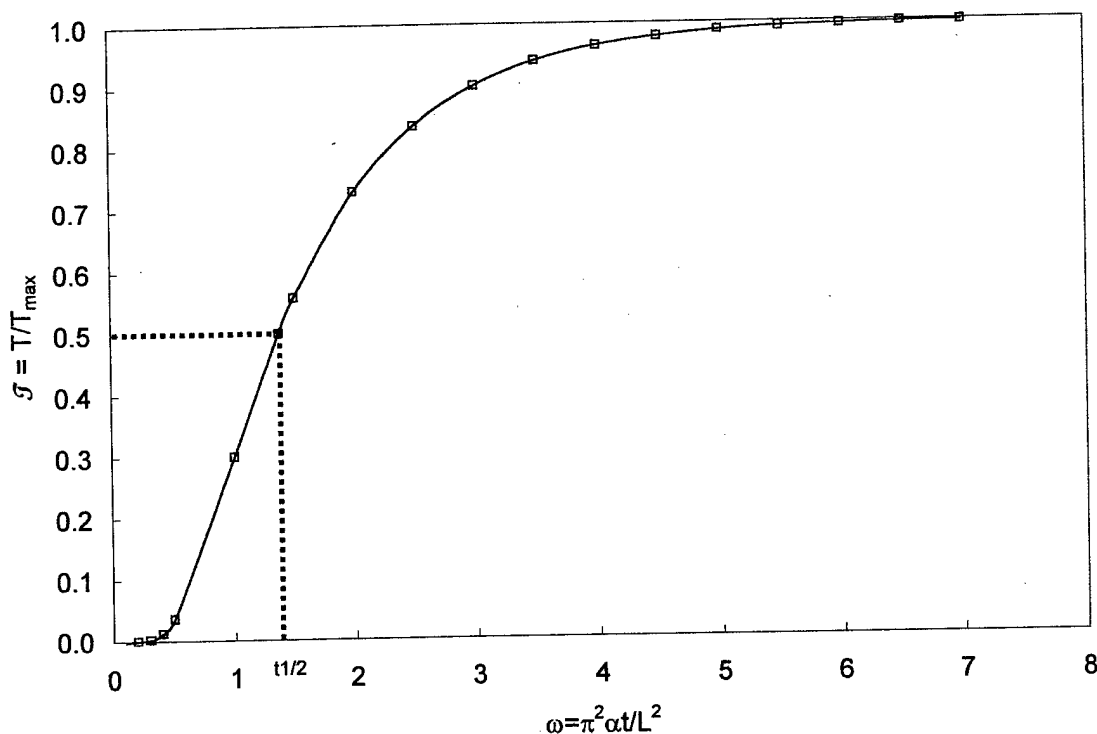


Figure 2.4: Ideal normalized time-temperature profile on rear face of laser flash disk

and convection.<sup>67</sup> They used the heating portion of the time-temperature curve, comparing ratios of points on the normalized experimental curve, which should meet prescribed values matching those of the ideal curve. Koski<sup>68</sup> expanded upon the surface loss algorithms presented by Cowan, and Clark and Taylor, presenting numerical approximations of different surface loss and finite pulse conditions, which are matched to the experimental data. Factors for the closest approximation are implemented to correct results to true diffusivity values. The Clark and Taylor and Koski corrections are the standard correc-

tions used in laser flash software today,<sup>69</sup> although efforts to refine and correct these measurements continue.<sup>70,71</sup>

Thermal diffusivity measurement via laser flash is an attractive technique for *in situ* observations of powder metallurgy materials for several reasons:

- It is non-contact, therefore alleviating some of the problems associated with electrical conductivity and direct thermal conductivity measurements;
- It allows multiple measurements to be made in a single sintering cycle;
- Existing commercial equipment allows measurements to be made *in situ*, in desired sintering temperature and process gas environments.

Although researchers have attributed increases in observed thermal diffusivity of porous materials to sintering,<sup>72</sup> and more recently investigated its use as a sintering monitor,<sup>44,45,73</sup> these investigations have been on ceramics, or die-compacted powdered metal materials only. This work will be the first to address powder-injection-molded materials, and the first to extend those observations to other properties, such as mechanical strength. This technique is quite promising for the examination of neck growth, but it is not without its own degree of experimental uncertainty. Some of the potential sources of error anticipated prior to this work were:

- The porous nature of the material creates a complex combination of heat transfer mechanisms that must be considered in any results;
- Shrinkage in a sintering sample will change the thickness and density of the sample material during measurement

Added to these concerns are the possibilities of damage or localized sintering due to the high-energy input from the laser flash. Each of these issues will be addressed in the discussion of research, Chapter 6.

## 2.4 Strength of Powder Metallurgy Materials

### 2.4.1 Theory and Models

Strength models for powder metallurgy materials traditionally focus on the higher density, lower porosity condition, since this is the most common in application. The higher density, porosity-based models have the general form, originally described by Bal'shin,<sup>74</sup> of Equation 2.51:

$$\sigma_s = \sigma_o S(\rho_s / \rho_o)^g \quad ( 2.51 )$$

where  $\sigma_s$  is the sintered strength (MPa),  $\sigma_o$  is the wrought strength (MPa),  $\rho_s$  and  $\rho_o$  are sintered and theoretical densities ( $\text{g}/\text{m}^3$ ).  $S$  and  $g$  are dimensionless factors dependent on processing and geometry, which entail experiments and curve-fitting for a given system.<sup>1</sup> As porosity decreases below 20%, strength becomes a complex function of porosity, pore shape, pore distribution, and prior particle interfaces, and these parameters are empirically determined for a given system. At lower densities, which better represent the early sintering of an injection-molded material, the size of the interparticle bonds dominates



the strength of a sintered material.<sup>31,75,76</sup> Studies on ceramics are particularly relevant here, since a ceramic will not undergo plastic deformation during the shaping step, and therefore develops mechanical strength based on initial stage sintering mechanisms. Building on the classic Coble model, more recent work continues to demonstrate the initial bond development as a result of surface diffusion, demonstrating a corresponding increase in strength and elastic properties.<sup>77,78</sup> Biaxial and 4-point transverse rupture tests on high porosity alumina show a substantial increase in mechanical strength prior to significant densification. In addition, Young's modulus has been shown to be even more sensitive to porosity than strength.<sup>79</sup>

Xu<sup>17</sup> and German<sup>80</sup> proposed a strength model incorporating dependence on neck size as shown in Equation 2.52:

$$\sigma_s = \frac{\sigma_o V_s N_c}{K\pi} \left[ \frac{X}{D} \right]^2 \quad ( 2.52 )$$

where  $K$  is a stress concentration factor related to neck curvature,  $V_s$  is the fractional density (measured density normalized with respect to theoretical density),  $N_c$  is the coordination number, and  $\sigma_o$  is the wrought strength (MPa) as a function of temperature. In considering this relation,  $K$  may be described in terms of neck size ratio, as shown in Equation 2.53:

$$K = \frac{1}{2} \left[ \frac{X}{D} \right]^{-2} \quad (2.53)$$

This strength equation is appropriate for both room temperature and high temperature application, and demonstrates an increase in strength due to neck growth until thermal softening decreases the bulk material strength at high temperatures. This model, along with several other examples of strength models, are summarized in Table 2.3.

Table 2.3: Examples of strength models for powder metallurgy materials

Model	Author, Reference	Comments
$\sigma = \sigma_o S(\rho_s / \rho_o)^g$	Bal'shin, 74	S and g are geometry/processing constants
$\sigma = \sigma_o \frac{-\ln(0.6\varepsilon)(1-\varepsilon)}{5000}$	Coble and Kingery, 81	Empirical fit to alumina and die-compacted iron data
$\sigma = \sigma_o \exp(-b\varepsilon)$	Rice, 82	b is system constant; approximately 4 for random packing
$\sigma_s = \frac{\sigma_o V_s N_c}{K\pi} \left[ \frac{X}{D} \right]^2$	Xu, 17	K is stress concentration factor
$\sigma = \sigma_o \left[ \frac{D}{2} \right]^{1/2} \left[ \frac{E}{E_o} \right] g(b)^{-1/2}$	Arato <i>et al.</i> , 83	For brittle materials; g is geometry factor from Griffith calculation; b is defect size
$\sigma_{SE} = \sigma_G (1 - R_f \beta) + f_T \sigma_s$	Shoales, 84	$R_f \beta$ represents strength lost in recovery; $f_T$ is empirical thermal softening

The strength predicted by Equation 2.52 may be demonstrated using mechanical testing, both at room temperature and at elevated temperatures. Shoales conducted transverse rupture tests on die-compacted bronze at elevated temperatures,<sup>85</sup> and his experimental data compares favorably with this model. However, fractional density, coordination number, and neck size ratio remain essentially constant for the die-compacted samples, so this work empirically captures the bonding of particles already mechanically interlocked, with no true initial stage sintering. Although this research lends excellent insight into strength evolution, particularly the impact of thermal softening on strength development, it is system dependent. Xu extended these observations to true initial-stage sintering by conducting transverse rupture strength tests on slurry-cast bronze both *in situ* and at room temperature.<sup>17,86,87</sup> In this set of experiments, the bronze bars were pre-sintered at 600 °C for 2 hours to provide initial handling strength. The resulting data, while very valuable for modeling the case of a pre-existing neck, does not include the strength evolution information at the transition between binder-based strength and strength due to sinter bonds. This observation is supported by the fact that there was no significant decrease in reported *in situ* strength from room temperature through the onset of strengthening at 600°C; however, the magnitude of these measured strengths is very small (approximately 1 MPa). Aside from this observation, both room temperature and elevated temperature bend tests were in excellent agreement with the predictions of Equation 2.52. These data are of great importance in showing the full impact of the strength predictions as fractional density, coordination number, and neck size ratios evolve. Since all three of these parameters can be related via neck size, an initial stage sintering model

can generate neck size ratios for a given time-temperature profile. Fractional density, coordination number and stress concentration factor can be developed from the neck size ratio, and these parameters, combined with bulk strength as a function of temperature, may be used to predict *in situ* strength.

#### 2.4.2 Measurement

Techniques for measuring strength of powder metallurgy materials are outlined in the Metal Powder Industries Federation Standard Test Methods.<sup>88</sup> Tensile testing, described in Standard 10, is the most common form of mechanical test,<sup>89</sup> with the strength a simple calculation of the load at failure,  $P$  (N), distributed over the cross-sectional area of the gauge length,  $A$  ( $m^2$ ). Tests may be conducted using a flat bar, modified flat bar (dog bone), or conventional threaded round bar configuration. This test is conducted on sintered or heat-treated materials, strong enough to withstand the stresses associated with gripping the material and loading to failure along the gauge length. An adaptation of tensile test specimen configuration is delineated for injection-molded debound and sintered materials in Standard 50. The load for these samples is applied via a link-pin threaded through holes at each end of the specimen.

Radial crush strength, as outlined in Standard 55,<sup>88</sup> is intended to assess strength in sintered or heat-treated materials that have negligible ductility. A ring shaped specimen is placed on its side and is loaded under compression between two flat, parallel plates. Strength,  $\sigma_{RAD}$  (MPa) is calculated according to Equation 2.54:

$$\sigma_{RAD} = \frac{P \left[ \frac{d_o + d_i}{2} \right]}{L_{cyl} \left[ \frac{d_o - d_i}{2} \right]^2} = \frac{P(d_o - t_w)}{L_{cyl} t_w^2} \quad ( 2.54 )$$

where  $P$  is the compressive force at rupture (N),  $d_o$  and  $d_i$  are the outer and inner diameters of the cylinder (m),  $L_{cyl}$  is the cylinder height (m), and  $t_w$  is the wall thickness (m).

The strength of green, die-compacted samples is evaluated through transverse rupture testing as described in Standard 15, with Standard 41 describing the same test for sintered samples.<sup>88</sup> The specimen configuration is a rectangular bar, 31.7 mm long x 12.7 mm wide x 6.35 mm thick. The sample is simply supported, resting perpendicular with respect to the two parallel supporting rods. A transverse load is applied midway between the two supports. Strength is calculated assuming flexure of an elastic beam, with maximum stress and failure occurring in the outer fibers, according to Equation 2.55:

$$\sigma_{TRS} = \frac{3PL_{sup}}{2w_b t_b^2} \quad ( 2.55 )$$

where  $\sigma_{TRS}$  is the transverse rupture strength (MPa),  $P$  is the transverse load at rupture (N),  $L_{sup}$  is the span between supports (m),  $w_b$  is the width of the bar (m), and  $t_b$  is the thickness of the bar (m). This test configuration avoids the issue of gripping the fragile samples, and has been used with success for *in situ* testing.<sup>16,17</sup> However, this type of test is sensitive to edge failures, which is reflected as reduced strength, creating a variability

in results. Since stress in the cross section varies from zero at the neutral axis to a maximum at the outer fiber, only the outer fibers are exposed to the maximum value of stress. As a result, rupture strength as calculated by Equation 2.55 is typically higher than the axial tensile strength, often 1.6 to 2 times the magnitude of the ultimate tensile strength.<sup>80</sup> However, because elastic behavior is the basis of the strength measurement, once significant plastic deformation takes place Equation 2.55 is no longer strictly valid and the test becomes a qualitative evaluation of strength evolution.

## 2.5 Statement of Thesis

Both theory and practice point to the importance of the evolution of the interparticle bond in the development of mechanical and physical properties in the early stages of sintering. Past work indicates that thermal conductivity and mechanical strength are both functions of the interparticle bond. Current experimental capabilities provide a non-contact means of measuring thermal properties *in situ*. The culmination of these facts leads to the following hypothesis:

If early stage strength evolution is a function of microstructure, characterized by size, number, and quality of interparticle contacts, and thermal conductivity evolution is also a function of these parameters, then early stage strength evolution (prior to significant densification) can be profiled in a nondestructive manner by measuring the evolution of thermal conductivity of a sintering compact.

Successful demonstration of this hypothesis will provide a new means of assessing strength and thermal diffusivity of a material during sintering. The potential impact is the capability to manipulate strength and avoid damage mechanisms.

## **2.6 Potential Impact of Research**

The application of laser flash analysis to directly assess thermal diffusivity and indirectly assess strength evolution during sintering has a two-fold benefit. First, the evolution of thermal diffusivity and conductivity affect the flow of heat to the interior of a sintering component. Thermal gradients are particularly important in large parts, and may be a major source of stress during sintering. Depending on the strength of the material at the time, these gradients may cause cracking or warping of a component. Thermal conductivity values may be directly incorporated in constitutive modeling to better predict and control final shapes and properties of a sintered component. A second effect is the capability to assess strength during a sintering material's most vulnerable window – the transition from powder to a continuous solid network. The indirect assessment of sinter bonding, and corresponding strength evolution, will provide insight into areas of a sinter cycle that may be more vulnerable to damage. This work has potential application as a non-destructive evaluation technique, embedded as part of a closed loop control system.

## Chapter 3

### Experimental Procedures

#### 3.1 Outline of Activities

The general approach for this research was to correlate previous mechanical models with new thermal models for *in situ* behavior during sintering of both die-compacted and injection-molded materials. Higher density die-compacted samples were profiled for strength evolution and thermal conductivity evolution during initial stage sintering. The same powder was evaluated as both a lower density die-compacted and injection-molded system, profiling strength evolution (at room temperature) and thermal conductivity evolution after increments in initial stage sintering. Strength evolution observations were enhanced with other measures of mechanical properties and microstructural evolution. This chapter will report on each type of test performed in terms of equipment description, operating principles, calibration and test procedures.

#### 3.2 Powder Characterization

Nickel was chosen as a baseline solid-state sintering system due to its stable nature — no solid-state phase changes, and resistance to persistent oxidation. The powder (type: 4SP-10; supplier: Novamet Specialty Products Corporation, Wyckoff, NJ), is a



carbonyl nickel powder with relatively low surface roughness (versus the spiky surface normally associated with carbonyl nickel) and spherical shape. The powder is air-classified by the manufacturer for a narrow particle-size distribution, with a median particle size of 6.9 micrometers. The chemical composition as provided by the manufacturer is: Ni (99.9%), oxygen (500 ppm), carbon (500 ppm), iron (<20 ppm), and sulfur (2 ppm).

### 3.2.1 Particle Size Distribution

Measurement of the particle size distribution was conducted using a laser scattering particle size distribution analyzer (model: LA-920, supplier: Horiba Instruments Incorporated, Irvine, CA). This equipment illuminates a stream of particles in a fluid suspension using two light sources: a He-Ne laser (632.8 nm wavelength) and a tungsten lamp (filtered to 405 nm wavelength). According to Mie theory,<sup>90</sup> light is scattered at an angle inversely proportional to the particle size. Larger particles ( $> 3 \mu\text{m}$ ) scatter light forward, in the direction of the light's original travel. This forward-scattered light is focused through a condenser lens, resulting in a pattern of concentric rings often described as Fraunhofer dispersion. A ring-shaped array of silicon photo diodes measures the forward-scattered light. Smaller particles scatter light to the sides, and back toward the light source. A series of photo diodes to the sides and rear of the stream of particles sense light dispersed at these higher angles. A schematic of the equipment components is shown in Figure 3.1.

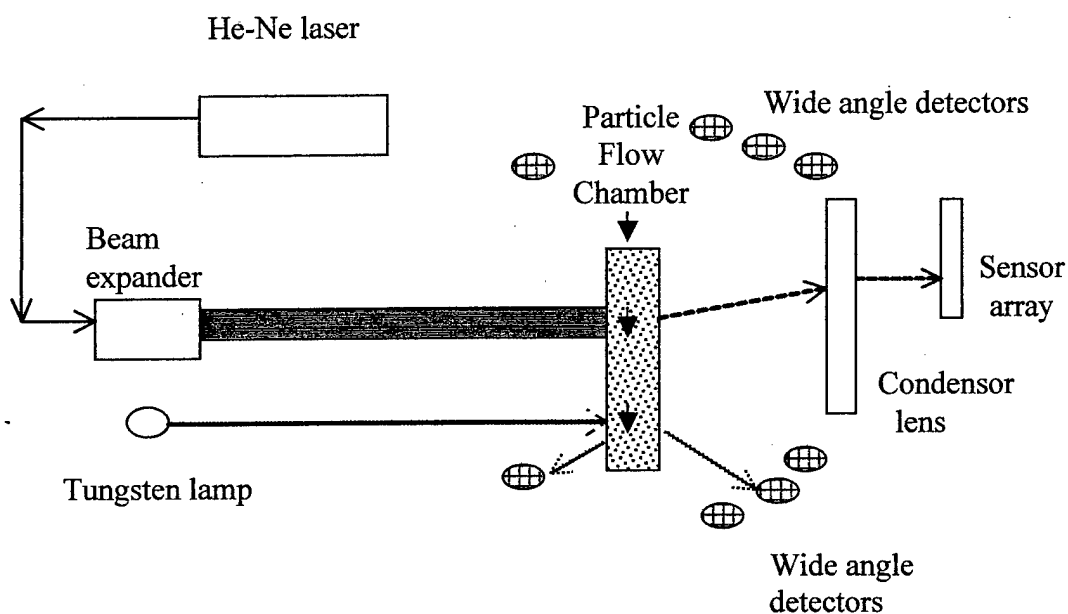


Figure 3.1: Schematic of Horiba LA-920 laser particle size analyzer

This equipment is checked monthly for drift in results by measuring two reference sets of powders: an iron carbonyl powder with a median diameter of 4  $\mu\text{m}$  and a larger stainless steel powder, median diameter of 97  $\mu\text{m}$ . These periodic readings must be within 2% of the baseline values to verify calibration.

For this testing, approximately one gram of nickel powder was mixed with 3 ml distilled water and one drop of liquid soap to create a suspension fluid. Several drops of the fluid were then added to approximately 200 ml of distilled water circulating through

the system. Three measurements were taken, with an in-system ultrasonic horn used to reduce agglomeration prior to each measurement.

### 3.2.2 Pycnometer Density

An evaluation of internal porosity was conducted using a pycnometer (model: Accupyc 1330; supplier: Micrometrics, Norcross, GA). This equipment has two adjoining chambers of known volume: a reference (empty) chamber ( $V_e$ ), and a chamber containing the sample powder ( $V_s$ ). Initially, a valve between the two chambers is sealed. The sample chamber is pressurized to  $P_1$  with helium, and the reference chamber is evacuated. The valve between the two chambers is then opened, and a second pressure ( $P_2$ ) is measured. Given the two pressures, constant temperature, and the known volumes, the only unknown is the volume of the powder ( $V_p$ ), which may be derived using the ideal gas law as shown in Equation 3.1:

$$P_1(V_s - V_p) = P_2(V_s - V_p + V_e) \quad ( 3.1 )$$

The mass of the powder divided by the volume yields the pycnometer density. This volume is then compared with the theoretical density of the material (8.90 g/cm<sup>3</sup> for nickel).

Calibration of the pycnometer is verified monthly using reference spheres. The spheres are of a known volume, and measured values must fall within  $\pm 0.05\%$  to validate the system calibration.

For this test, the mass of the powder was measured using a balance (model: AE 200; supplier: Mettler-Toledo, Inc., Columbus, OH) with a measurement precision of  $10^{-4}$  g. Ten volume measurements of the powder were made.

### 3.2.3 Tap Density

Tap density of the powder was determined via an auto-tapping device (model: Dual AutoTap; supplier: QuantaChrome Corporation, Fairfield, NJ) using procedures outlined in Metal Powder Industries Federation (MPIF) Standard 46<sup>91</sup>. This technique places 100 g of powder, again measured using the Mettler AE 200 balance, in a 25 cm<sup>3</sup> graduated cylinder, which is then tapped (raised and dropped a distance of 3 to 3.2 mm) until no settling is observed. The final volume is determined via a visual inspection of the lines on the side of the graduated cylinder. The tap density ( $\rho_t$ ) is the measured mass divided by the observed volume. The precision of the test is limited by the resolution of the volume measurement. The smallest increment on the cylinder is 0.2 cm<sup>3</sup>, which limits the accuracy of the volume measurement to  $\pm 0.1$  cm<sup>3</sup>. For a 20 cm<sup>3</sup> sample, this results in an accuracy of  $\pm 0.5\%$  or  $\pm 0.025$  g/cm<sup>3</sup>.

For this test, two measurements were made, with each sample tapped 3,000 times at a rate of 260 taps per minute.

### 3.2.4 Apparent Density

Apparent density, which is a description of how closely the powder will pack without additional vibration, was measured using an Arnold meter, as described in MPIF Standard 48<sup>91</sup>. This simple test apparatus consists of a hardened steel block with a hole through the center. The hole is machined to a volume of 20 cm<sup>3</sup>. A bushing is placed on top of the block, and filled with powder. The bushing is slid over the hole in two passes, first rotating, then straight, leaving the hole full and leveled with powder. The block is lifted away from the powder, and the remaining powder is then weighed. The apparent density ( $\rho_A$ ) is the mass of the powder divided by the volume of the hole (20 cm<sup>3</sup>). Three separate measurements were made on the powder, with a variation of  $\pm 0.4\%$ .

### 3.2.5 Scanning Electron Microscope Observation

Qualitative observations of particle size, size distribution, and shape were made using a scanning electron microscope (model: ABT-32; supplier: Topcon Industrial Products, Paramus, NJ). Inspections were made in secondary electron mode, and images were recorded using Printerface for Windows 2.10 electronic image capturing system software.

### 3.3 Dilatometric Analysis

All thermal expansion/shrinkage tests were conducted on a vertical pushrod dilatometer (model: 1161 Unitherm; supplier: Anter Corporation, Pittsburgh, PA). Dimensional changes are monitored via an alumina pushrod, which contacts the sample. The

force due to the weight of the pushrod is offset by a dead-weight counterbalance, leaving a small positive force (1.25 N) to ensure the pushrod follows the sample as it shrinks. Movement of the pushrod is measured by a digital displacement transducer with a resolution of  $\pm 63.5^{-6}$  cm. Sample temperature is monitored by an S-type thermocouple encased in an alumina sheath, located next to the sample. The sample and the pushrod are enclosed in an alumina muffle tube, located inside a Super Kanthal<sup>®</sup> radiant furnace. A schematic of the dilatometer is shown in Figure 3.2.

Displacement measurements were calibrated using a reference sample of single crystal sapphire. Measured values were compared to National Institute of Standards and Technology (NIST) values, and were accurate within 1.5% on average, with a maximum difference of 3.71% from handbook values. Temperature measurements were calibrated using the solid-state phase change in iron. A pure iron reference sample was heated, and the volume change associated with the characteristic transformation at 910 °C from body-centered cubic to face-centered cubic crystal structure was monitored. The measured values during heating and cooling were within 1.0% of handbook values. Sintering events were initially profiled with a dilatometry test on loose nickel powder with no binder present. The powder was poured into an alumina crucible, then tapped until no further settling was observed. An alumina disk was placed on top of the powder to provide a firm point of contact for the pushrod and to distribute the load across the surface of the powder. The disk was approximately 10% smaller than the inner diameter of the crucible, to allow the disk to float freely as the powder expanded and contracted. The initial

test was conducted with a constant heating rate of  $10^{\circ}\text{C}/\text{min}$  to  $1100^{\circ}\text{C}$ , followed by a 1-hour hold, in hydrogen with an inlet dewpoint of  $-51^{\circ}\text{C}$ .

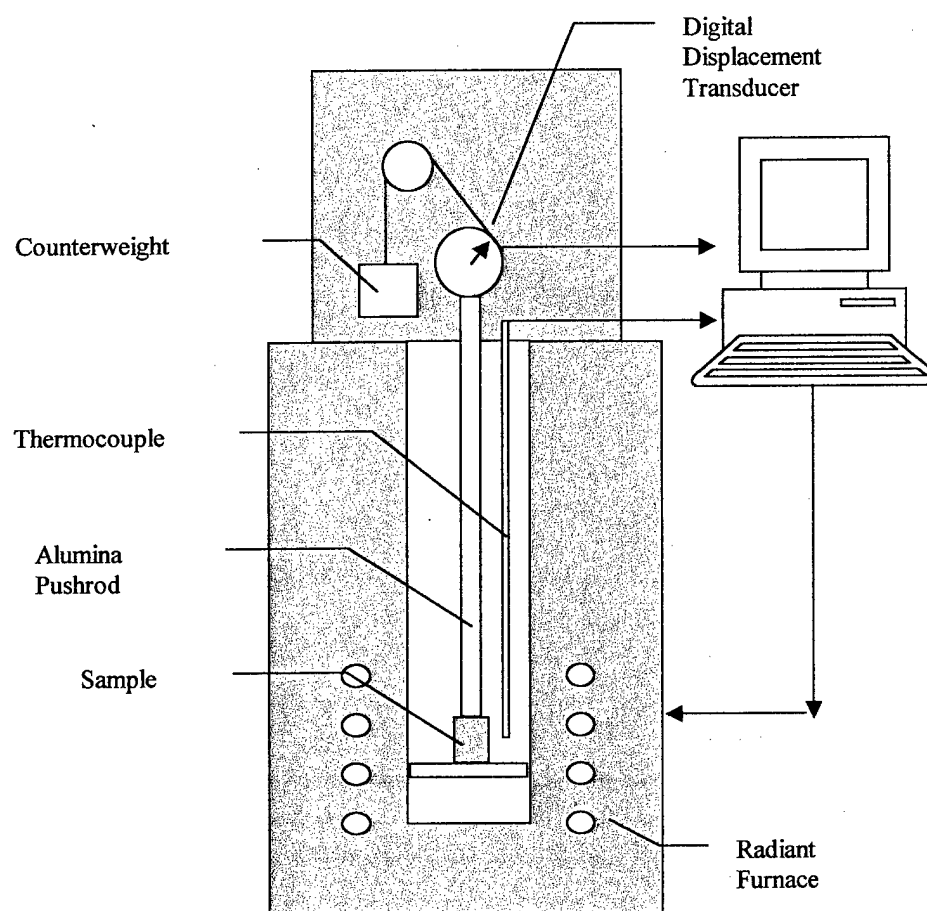


Figure 3.2: Schematic of Anter Unitherm 1161 vertical pushrod dilatometer

A second set of loose powder tests were conducted to characterize the behavior of the powder during a thermal debind cycle without the presence of the binder. Three runs were conducted in flowing hydrogen, consisting of a 1.2 °C/min ramp to 425°C, a 120 minute hold, then a 1.2°C/min ramp to 500°C, followed by a 30 minute hold, and a furnace cool.

### **3.4 Sample Preparation**

Initial plans for sample preparation included preparing a set of higher density die-compacted samples and a set of lower density die-compacted samples simulating powder-injection-molded (PIM) material (referred to as quasi-PIM). This initial plan was later expanded to incorporate an injection-molded system.

#### **3.4.1 Die-compacted Samples**

Die-compacted samples were pressed into 31.7 mm x 12.7 mm x 6 to 7 mm transverse rupture bars (TRBs) and 12.7 mm diameter, 3 mm thick disks on a 60-ton hydraulic press (model: N/A; supplier: Gasbarre Press Division, Dubois, PA). To overcome the difficulty of pressing a relatively small, spherical powder, the 4SP-10 nickel powder was blended with 2 wt% granulated paraffin wax (melting point 45°C) to increase cohesion in the powder. The powder-wax mixture was heated to 70°C to melt the wax, and then mixed by hand to distribute the wax through the powder. After the wax had cooled and hardened, clumps of powder were sifted, crushed and rebled to redistribute the poly-



mer-heavy portions throughout the powder. TRBs and disks were compacted with 550 MPa uniaxial pressure to a fractional density of  $75\% \pm 0.5\%$ . Each sample was double-pressed, which increased parallelism of the top and bottom faces, and uniformity of density from part to part. To combat delamination of the TRBs during ejection from the die, a hold-down pressure of 1 MPa was used. All die-compacted samples were heated in retort ovens to 150°C to melt the paraffin wax, and allow the molten wax to flow within the interconnected pore structure. Initially, the plan was to place test samples in beds of fine alumina powder to provide a wicking action for the molten wax. However, a comparison of a free-standing sample to a sample packed in alumina showed no additional mass loss in the alumina-packed sample, so all test samples were treated free-standing at 150°C. The effect of this treatment was to draw the molten wax via capillary action to the contact points between particles, creating pendular bonds. This effectively opens the pore structure, allowing for later outgassing during thermal decomposition at higher temperatures. These heat treatments for the die-compacted samples, as well as pre-sintering activities for quasi-PIM and PIM materials were conducted in a single retort furnace (furnace model: CF56822C; supplier: Lindberg/Blue, Asheville NC; controller model: 2404, supplier: Eurotherm, Leesburg, VA). This furnace was thermally characterized using a K-type thermocouple encased in an Inconel sheath, located near the sample in the hot zone of the furnace. All presintering temperatures described in this work incorporate the offsets as determined by the thermal characterization.

### 3.4.2 Quasi-Powder-Injection-Molded Samples

A quasi-powder-injection-molded (quasi-PIM) concept was initially pursued to approximate an injection-molded system because injection molding is resource- and material-intensive. A small-volume alternative was sought, which would allow the manufacture of small batches of parts with different shapes. A single-phase binder was considered desirable to allow the capture of data from room temperature through the entire sintering cycle, while minimizing sources of damage and error. Several water-soluble binders provided excellent green strength, but interior voids and bubbles persisted through vibration, vacuum and pressure conditions. As an alternative method, the nickel powder was mixed and lightly pressed with 2% by weight ethylene bisstearamide powder (EBS, trade name Acrawax® C). Samples were compacted at a pressure of 20 MPa, with a goal of gaining enough green strength to form a cohesive part by flowing the polymer binder without plastically deforming the powder. Inspections of fractured bars in the scanning electron microscope revealed no observable flattened faces. Samples were pressed on a manual press (model: 3853; supplier: Carver, Wabash, IN) in 31.7 mm x 12.7 mm x 5-7 mm TRBs and 12.7 mm diameter disks. The bars and disks were presintered in hydrogen at 2°C/min to 400°C with a 2-hour hold. This removed the binder material, and established a minimal interparticle bond.

The transverse rupture bars were then sintered and quenched in a specially configured vertical tube furnace (model: 1625VT; supplier: CM Furnaces Inc., Bloomfield, NJ). The vertical furnace is equipped with two electro-magnetic switches. One switch controls a magnetic cap at the top of the tube, from which a wire basket is suspended, and

the second switch controls a trap door at the bottom of the tube. At the desired quench temperature, a high volume of nitrogen is flowed through the furnace to purge the hydrogen process gas, the bottom switch releases the trap door, which swings open. The magnetic cap at the top of the tube releases the wire basket, which drops through the bottom of the tube into a bucket of water. The furnace configuration is shown in Figure 3.3.

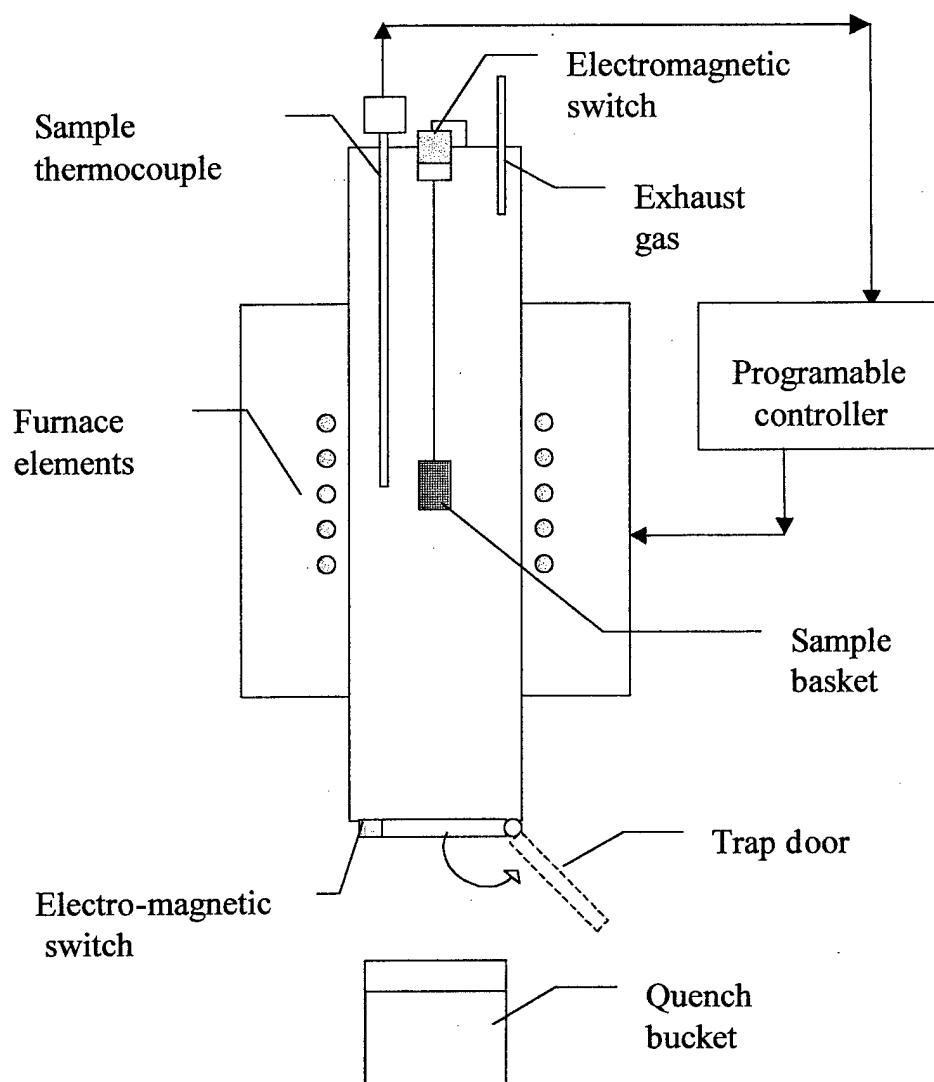


Figure 3.3: Schematic of CM vertical quench furnace

This furnace was calibrated for temperature offsets by heating reference materials to their melting temperature. Gold (99.999% pure,  $T_m=1064.4^\circ\text{C}$ ) and aluminum (99.99% pure,  $T_m=660.4^\circ\text{C}$ ) were used as calibration materials to encompass the range of

temperatures used during quench tests. During each calibration test, a piece of reference material was placed in the wire basket, which was suspended from the electromagnetic switch at the top of the tube furnace. Temperature was measured with a B-type thermocouple encased in an alumina sheath, suspended next to the wire basket. The reference material was heated in 100% hydrogen process gas at a rate of 10°C/minute to the setpoint, with a hold for 30 minutes at the setpoint, and a furnace cool. The reference material was then inspected for visible indications of melting. Using this technique, furnace offsets were verified within  $\pm 2.5^{\circ}\text{C}$ .

After calibration of the quench furnace, the quasi-PIM TRBs were sintered in hydrogen in groups of three along a constant heating rate profile of 10°C/min. Samples were heated to peak temperatures of 500 to 1100°C, then quenched in non-agitated water. Based on surface temperatures of the quenched samples, cooling to room temperature occurred within 20 seconds, for a cooling rate of at least 40°C/second for an 800°C sample.

The final density of each set of samples (i.e. each quench temperature) was calculated using the water immersion method (commonly referred to as the "Archimedes density"), which is described in MPIF Standard 42.<sup>91</sup> This technique determines the volume of a porous part by determining the volume of water it displaces while immersed in water. This volume, combined with the measured mass, is used to calculate the density of the porous material. One sample from each set was evaluated. Each sample was weighed dry, then placed in light mineral oil under vacuum to impregnate the open pore network. Each sample was then lightly wiped to remove excess oil from the surface, and

then weighed again. Finally, each sample was weighed while immersed in water.

Density was calculated using Equation 3.2:

$$\rho_s = \frac{m_{dry} \rho_{H2O}}{m_{oil} - m_{imm}} \quad ( 3.2 )$$

where  $m_{dry}$  is the mass of the dry sample,  $m_{oil}$  is the mass of the sample impregnated with oil, and  $m_{imm}$  is the mass of the impregnated sample immersed in water (tared to eliminate the mass of the weighing apparatus). The dry density is  $\rho_s$ , and  $\rho_{H2O}$  is the density of water at the test temperature (0.9982 g/cm<sup>3</sup> at 20°C). The denominator in this case represents the mass of the water displaced by the sample (solid plus the oil-filled pores). Using the density of the water at the test temperature, the volume of the displaced water is calculated. With the dry mass of the solid in the numerator, and the displaced volume in the denominator, the calculation yields the dry density of the porous material.

### 3.4.3 Injection-molded Samples

A third set of samples was fabricated using a traditional PIM polymer-wax system. The nickel powder was combined in a 58 volume% mixture with the binder powders. The binder mixture consisted of 50 weight% paraffin wax (BP 7355 Paraffin Wax), 40 weight% polypropylene (PolyVisions ProFlow 3000), and 10 weight% linear low density polyethylene (DuPont Fusabond MB-2260D). Transverse rupture bars (32 mm x 12.79 mm x 3.25 mm) were molded on a 30-ton reciprocating screw injection-molding

machine (model: 270V; supplier: ARBURG, Inc., Newington, CT). Detailed molding parameters are shown in Table 3.1. Disks were cut from the bars using a heated circular stamp, 12.79 mm in diameter. The PIM samples were solvent- debound in a warm

Table 3.1: Molding parameters for nickel/polymer-wax TRBs

Temperature, °C:		Parameters:	
Nozzle	155	Shot Size	10 cm <sup>3</sup>
Barrel Zone 2	150	Back Pressure	0.5 MPa
Barrel Zone 3	145	Cooling Time	14 s
Barrel Zone 4	145		
Barrel Zone 5	140		
Injection Profile:	Step 1	Step 2	Step 3
Speed (cm <sup>3</sup> /s)	40	20	12
Pressure (MPa)	111	1.1	111
Cutoff (cm <sup>3</sup> )	7	5	2.2
Packing Profile:	Step 1	Step 2	Step 3
Pressure (MPa)	86	63	53
Time (s)	4	4	3

heptane bath (60°C for 120 minutes) to remove the paraffin wax, thereby opening interconnected porosity to allow for outgassing of thermal decomposition products. Thermogravimetric analysis was conducted on the solvent-debound material to determine the decomposition temperatures of the backbone polymers, and design the thermal debind cycle. Based on this analysis, the thermal debind profile was established as 2°C/min to 425°C, 2 hour hold, then cooling at 2°C/min to room temperature.

One batch of samples was prepared to assess the evolution of thermal conductivity and bend strength at increments along the thermal debind cycle. Each sample set was composed of two disks and three TRBs. Sets were thermally debound to increments along the thermal profile shown in Figure 3.4. Each mark on the graph indicates a set of samples which were debound to that point in the cycle, held at constant temperature for 15 minutes while the furnace was purged of hydrogen, then removed from the sintering furnace and air-cooled.

### 3.5 Transverse Rupture Strength

Room temperature transverse rupture tests were performed on a electromechanical load frame (model: Sintech 20/D; supplier: MTS Systems Corporation, Eden Prairie, MN) with a 4450 N (1000 lb) load cell (model: 3187-104, supplier: same). Test supports were arranged in the standard 3-point bend configuration, with the sample resting on parallel supports, and a transverse load applied to the sample midway between the supports. Test execution was conducted as described in MPIF Standard 41<sup>92</sup> and data management was controlled using Testworks software. Crosshead movement was displacement-



controlled at a constant rate of 3 mm/minute. Data acquisition was accomplished using a digital controller at a frequency of 1000 Hz, recording load and crosshead displacement. Transverse rupture strength ( $\sigma_{TRS}$ ) of the bar was calculated using Equation 2.54:

$$\sigma_{TRS} = \frac{3PL_{sup}}{2w_b t_b^2} \quad ( 3.3 )$$

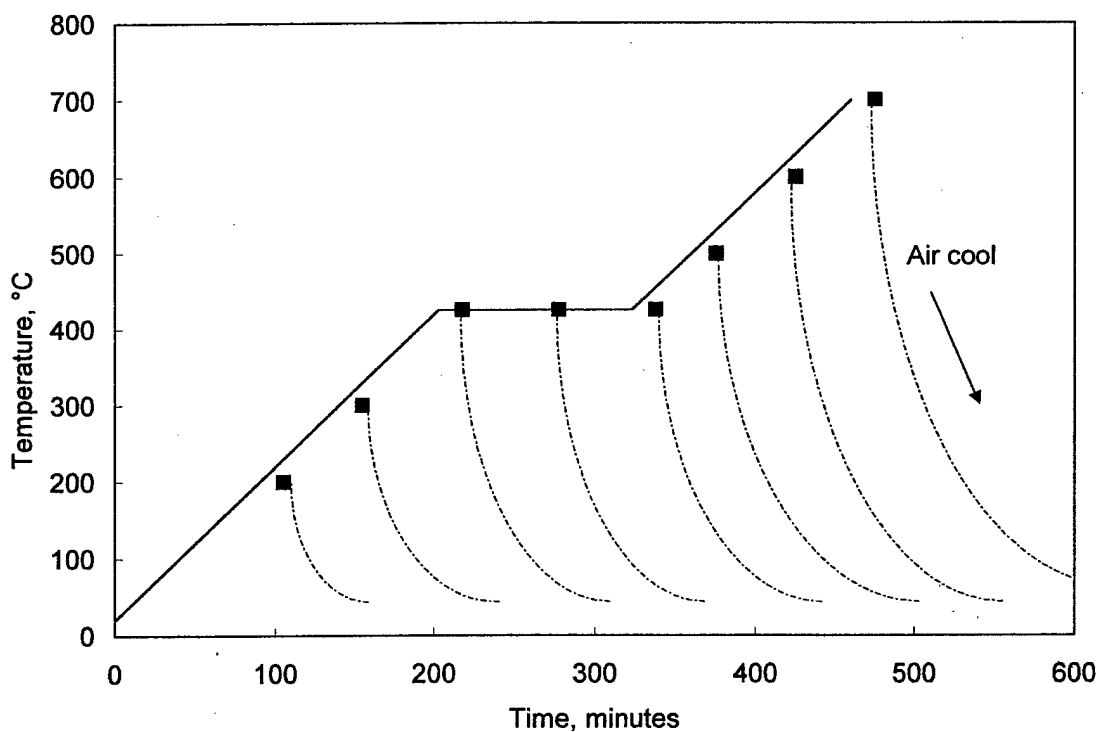


Figure 3.4: Time-temperature profile for PIM samples, thermally debound and quenched in air. Heating rate is 2°C/min, with a 2 hour hold at 425°C. Samples were heated in flowing hydrogen, held at temperature for 15 minutes while hydrogen was purged, then removed from the furnace and air-cooled. Each point represents a separate run.

where  $\sigma_{\text{TRS}}$  is the transverse rupture strength (MPa),  $P$  is the transverse load at rupture (N),  $L_{\text{sup}}$  is the span between supports (m),  $w_b$  is the width of the bar (m), and  $t_b$  is the thickness of the bar (m)

*In situ* transverse rupture testing was conducted on an in-house system known as the Flaming Tensile Tester (FTT). Despite the name, the test equipment is actually a three-point bend test stand enclosed in a retort furnace. A full account of construction details is included in other works.<sup>16</sup> The test stand with parallel supports is encased in an Inconel retort. An opening at the top of the retort allows clearance for the vertical motion of the ram, which applies the transverse load to the sample. Figure 3.5 shows a schematic of the test assembly. As in the room temperature tests, the sample rested across two parallel supports, and a displacement-controlled load was applied to the sample midway between them. Applied force was measured via a piezoelectric force link (model: 9332A; supplier: Kistler Instrument Corporation, Amherst, NY) located as part of the load train below the retort, just above the rigid support structure. The electric signal generated by the applied load was input into a control monitor (model: 58855A; supplier: same), which translated the signal to Newtons ( $4.04 \text{ pC} = 1 \text{ N}$ ). Vertical travel of the ram was measured using a linear variable displacement transducer (model: GPD-121-500, supplier: Schaevitz, Hampton, VA) and signal conditioner. The transducer converted displacement of  $\pm 12.7 \text{ mm}$  to a signal of  $\pm 20.0 \text{ V}$ . Both force and displacement data were acquired at a frequency of 1000 Hz using LabView software. To accommodate elevated temperature testing, the retort was encased in insulating material lined with semi-cylindrical resistance ribbon for radiant heating. Thermal profiles were program-

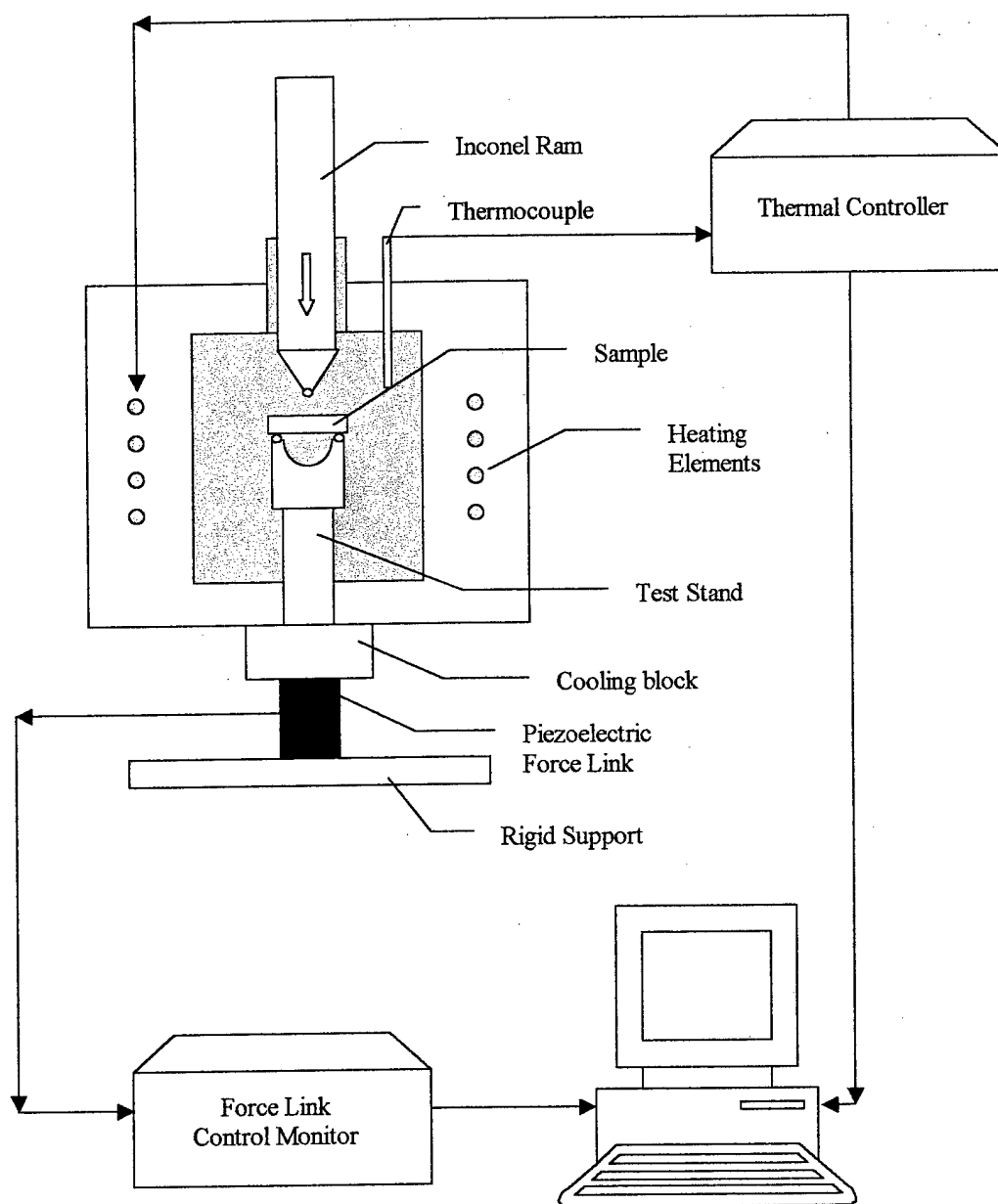


Figure 3.5: Schematic of elevated temperature three-point bend system, also known as the FTT.

med and regulated using a micro-processor based thermal controller (model: 981; supplier: Watlow, St Louis, MO). The furnace temperature was monitored using a K-type thermocouple located inside the retort, approximately 2 cm away from the sample.

Load measurements were calibrated using reference masses from 200 g (2 N) through 7413 g (72.73 N). The weights were placed on the test supports, and a static force measurement was made. Within the resolution of the force link ( $\pm 1$  N), all tests were within 0.5%, which is the NIST-documented bias uncertainty for the transducer. Temperature control was evaluated through a series of tests using the melting point of a reference material, zinc (99.99% purity), as a primary indicator of the true temperature inside the retort. In addition, during these calibration tests, temperature was monitored via a second K-type thermocouple in contact with a sample TRB, which gave an indication of the actual sample temperature as it approached equilibrium. Using these two measures, thermal control was verified within a  $\pm 2.5^\circ\text{C}$  range.

Die-compacted TRBs were tested at increments along the constant heating rate profile of  $3^\circ\text{C}/\text{min}$ , followed by a 15-minute hold at the setpoint. Samples were heated in a 100% hydrogen environment, which was then purged by flowing nitrogen during the 15-minute hold. Three separate tests were run at each temperature, with ram movement at a rate of 6 mm/min. To make a comparison between die-compacted transverse rupture strength and thermal diffusivity, 12.7 mm disks were included in the retort to experience the same heat treatment conditions as the TRBs. During one test at each temperature, two laser flash disks were placed alongside the TRB on a low-density alumina setting plate. These disks were later tested for thermal diffusivity as described in Section 3.6.

### 3.6 Thermal Conductivity

Thermal diffusivity measurements were made using a laser flash thermal analysis system (model: Flashline<sup>®</sup> 5000; supplier: Anter Corporation, Pittsburgh, PA). The equipment consists of a 35 J Nd/glass laser, a Kanthal<sup>®</sup> radiant sintering furnace, and an In/Sb infrared sensor. A general schematic of the system is shown in Figure 3.6. To take

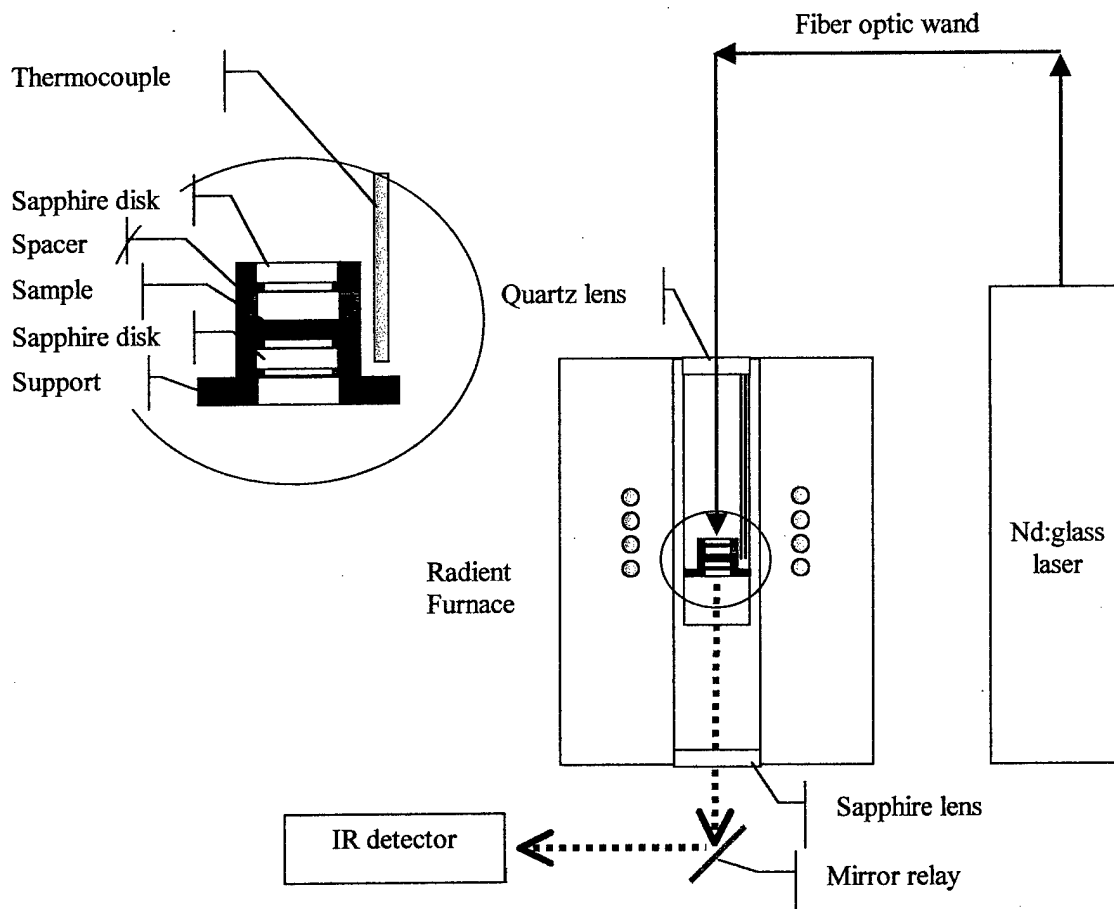


Figure 3.6: Schematic of the Anter Flashline<sup>®</sup> 5000 laser flash thermal diffusivity system.

a measurement, the laser generates a thermal pulse 200 to 300  $\mu$ s in duration. The energy is directed to the top of the sintering furnace via a proprietary fiber optic wand. The pulse travels through a quartz window at the top of the furnace muffle tube, and illuminates the top surface of the sample. An alumina holder located in the center of the hot zone supports two sample disks (12.7 mm in diameter, 2 to 4 mm thick), as shown in Figure 3.7. The IR detector views the bottom face through a sapphire window and mirror

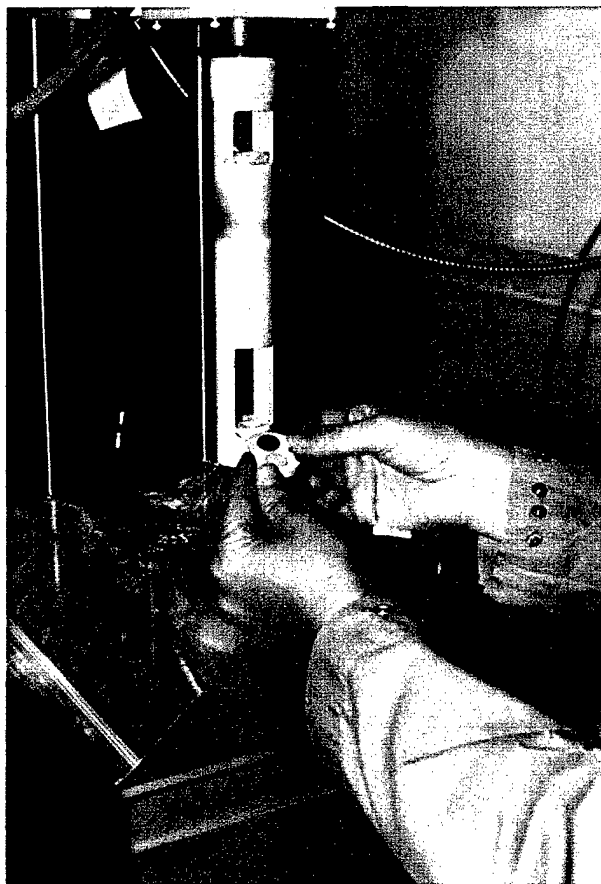


Figure 3.7: Two disks rest in the sample holder, ready to be loaded into the test chamber

relay, recording the equilibrium temperature, and the subsequent temperature rise at a frequency of 15 kHz. The general relation used to translate the time-temperature measurement into a value for thermal diffusivity is shown in Equation 3.4 as:

$$\alpha = \frac{1.38H^2}{t_{1/2}} \quad ( 3.4 )$$

where  $\alpha$  is the thermal diffusivity ( $\text{cm}^2/\text{s}$ ),  $H$  is the sample thickness (cm), and  $t_{1/2}$  is the half-rise time (seconds), i.e. the time corresponding with half the temperature rise ( $\Delta T/2$ ). As described in Section 2.3.2, literature-based algorithms are used to correct for surface heat losses and finite pulse effects.

The expected temperature rise of the sample ( $\Delta T$ ) was estimated using the relationship described in Equation 3.5:<sup>61</sup>

$$\Delta T_p = \frac{Q}{H\rho C_p} \quad ( 3.5 )$$

$Q$  represents the heat absorbed by the sample. A typical laser charging voltage of 1400V generates 10 J of energy, with approximately 20% of this energy attenuated in transmission through the fiber optic wand.<sup>92</sup> Assuming an absorptivity equal to the emissivity of oxidized nickel, 0.47,<sup>93</sup> the energy absorbed is 47% that of the energy irradiating the top face. Since the laser energy irradiates the entire face, the area of the disk (with a diameter of 0.0127 m) was included in the calculation. The typical thickness of the sample

disk,  $H$ , was approximately 3 mm, or 0.003 m. The density of the porous material,  $\rho$ , was 58% of the density of solid nickel (8900 kg/m<sup>3</sup>). The specific heat capacity,  $C_p$ , for the bulk material at a test temperature of 100°C was 470 J/(kg·K). Applying these values to Equation 3.5 yields Equation 3.6:

$$\Delta T = \frac{(10 \text{ J})(0.8)(0.47) / \left( \frac{\pi}{4} \right) (0.0127 \text{ m})^2}{(0.003 \text{ m})(8900 \text{ kg/m}^3)(0.58)(470 \text{ J/kg} \cdot \text{K})} = 4.1 \text{ K} \quad (3.6)$$

Therefore, assuming zero heat loss to the surroundings, the maximum temperature rise of the sample with each “shot” was estimated at about 4°C. Typically, temperature increases of 2 to 4°C are described in the literature.<sup>62,67</sup> Using this same approach, the theoretical increase in temperature for a layer 1/100<sup>th</sup> of the sample thickness is 410°C. If the layer is 1/1000<sup>th</sup> of the sample thickness (3 µm – approximately the size of the nickel powder), the theoretical temperature of the layer is 4,100°C. As a consequence, destructive effects on the material were a concern, and the samples were examined for signs of degradation or altered appearance.

Accuracy of the test set-up and method was assessed by measuring several reference materials representing a range of behavior. NIST-traceable graphite, double vacuum melted electrolytic iron, and Pyroceram 9606 were all characterized on the Flashline® 5000. The reference samples represented a range of behaviors, from relatively high thermal diffusivity for the graphite and iron, to relatively low thermal diffu-



sivity for the pyroceram ( $\alpha$  of 0.437, 0.191, and 0.0607 cm<sup>2</sup>/s respectively at 100°C).

Since the expected  $\alpha$  of the nickel experimental materials was less or equal to that of the pyroceram, protocols yielding the highest accuracy with the pyroceram were followed. For example, in the case of smooth, solid materials, it is common practice to spray-coat the top and bottom surfaces to increase sample surface emissiveness. The spray-coat increases both the ability to absorb energy from the laser flash and emit radiation to the infrared detector, thereby increasing the strength and accuracy of the signal received. Reference testing of the commonly used graphite (emissivity of 0.99)<sup>94</sup> and boron nitride (emissivity of 0.7)<sup>94</sup> sprays demonstrated the use of boron nitride spray coating as the most effective technique for low diffusivity materials. This step was only necessary for the die-compacted samples, since the other two systems had more porous, low-reflectivity surfaces. In addition, the Koski algorithm<sup>68</sup> for thermogram correction yielded the most accurate results for low diffusivity materials, and was chosen as the standard used for the reference tests and all results presented here. Using these protocols, the measured thermal diffusivity matched handbook values within 3% in the temperature range of 20 to 1000°C.

Initial measurements were made on quasi-PIM samples, presintered at 400°C, to qualitatively assess the ability to observe neck growth via an increase in thermal diffusivity. Tests were conducted in hydrogen, nitrogen, argon, and low vacuum (95 torr or 13 kPa) environments. A programmed heating rate of 10°C/minute was used, although the requirement for a stable temperature when the measurements are taken necessitated a much lower rate (1°C/min) as the furnace approached each target temperature. A stepped

hysteresis cycle was used, with measurements taken both during heating and cooling. The typical sequence was testing at 100°C, 400°C, 500°C, 600°C, 500°C, 400°C, and 100°C. Three measurements were taken on each sample at each temperature. The same test cycle was then used for thermally debound PIM samples, using multiple samples to establish a confidence level for the measurements.

PIM air-quenched samples were tested at 100°C. The slightly elevated temperature was chosen to enhance the signal strength for the IR detector. Samples were sanded to a thickness of approximately 2 mm to decrease the time needed for the thermal wave to reach the back surface, which in turn decreased surface heat losses. To maintain parallel faces during sanding, the disks were placed in a cylindrical sleeve with a sliding rod insert, as shown in Figure 3.8.

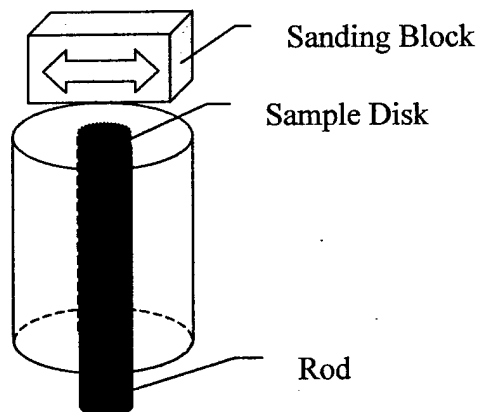


Figure 3.8: Technique for sanding thickness of disks while keeping faces parallel.

Loose powder was tested to examine the transition from powder to sinter-bonded particles. These measurements were made *in situ* in a nitrogen atmosphere, using a cycle mimicking the thermal debind profile used for the PIM samples: 2°C/min to 425°C, with a 120 minute hold at 425°C, and a continued ramp to 500°C. The powder was sandwiched between sapphire disks, which are transparent to incoming and exiting radiation. Since it is critical to know the thickness of the laser flash sample, dilatometry was run as described in Section 3.3 to characterize the linear expansion and shrinkage during the given time-temperature profile. The heating rate used for the dilatometer test was decreased from 2°C/min to 1.2°C/min to average the ramp plus the hold time spent at each measurement temperature.

Die-compacted disks which had been sintered in the FTT as described in Section 3.5 were tested via laser flash in a nitrogen atmosphere at 100 and 200°C. Since the surfaces of the disks were smooth and reflective, each sample was sprayed with a thin coating of boron nitride to increase emissiveness.

### 3.7 Ultrasonic Evaluation

To obtain a profile of elastic modulus evolution of the quenched quasi-PIM samples, room temperature measurements of longitudinal time-of-flight were made using the through transmission technique, as described in ASTM Standard E494<sup>95</sup>. This method is suggested for highly attenuating materials, such as powdered metal materials with micro-porosity.<sup>96</sup> A schematic of the test configuration is shown in Figure 3.9. Ultrasonic

pulses were generated and recorded by the Matech pulser/receiver toneburst generator model #EXP 2. Two 1.0 MHz KB-Aerotech Gamma D11042 transducers were used on either side of the thickness dimension (5 to 6 mm) of each sintered sample. Since the samples were porous, a layer of 1 mm thick polysorbane rubber was placed between the sample and transducer to act as a dry couplant. A thin layer of water-based Sonotech couplant was used between the transducer and the rubber. Longitudinal wave velocity was calculated using the thickness of each sample divided by the time-of-flight measurement. Time-of-flight through the dry layers was subtracted from the total time prior to calculating velocity. Young's modulus is related to wave velocity by Equation 3.7:<sup>95</sup>

$$E = \rho_s v_L^2 \quad ( 3.7 )$$

where  $\rho_s$  is the density of the material ( $\text{kg/m}^3$ ) and  $v_L$  is the wave velocity (m/s). Density values, obtained by the water immersion method as described in Section 3.4.2, were used in the calculation.

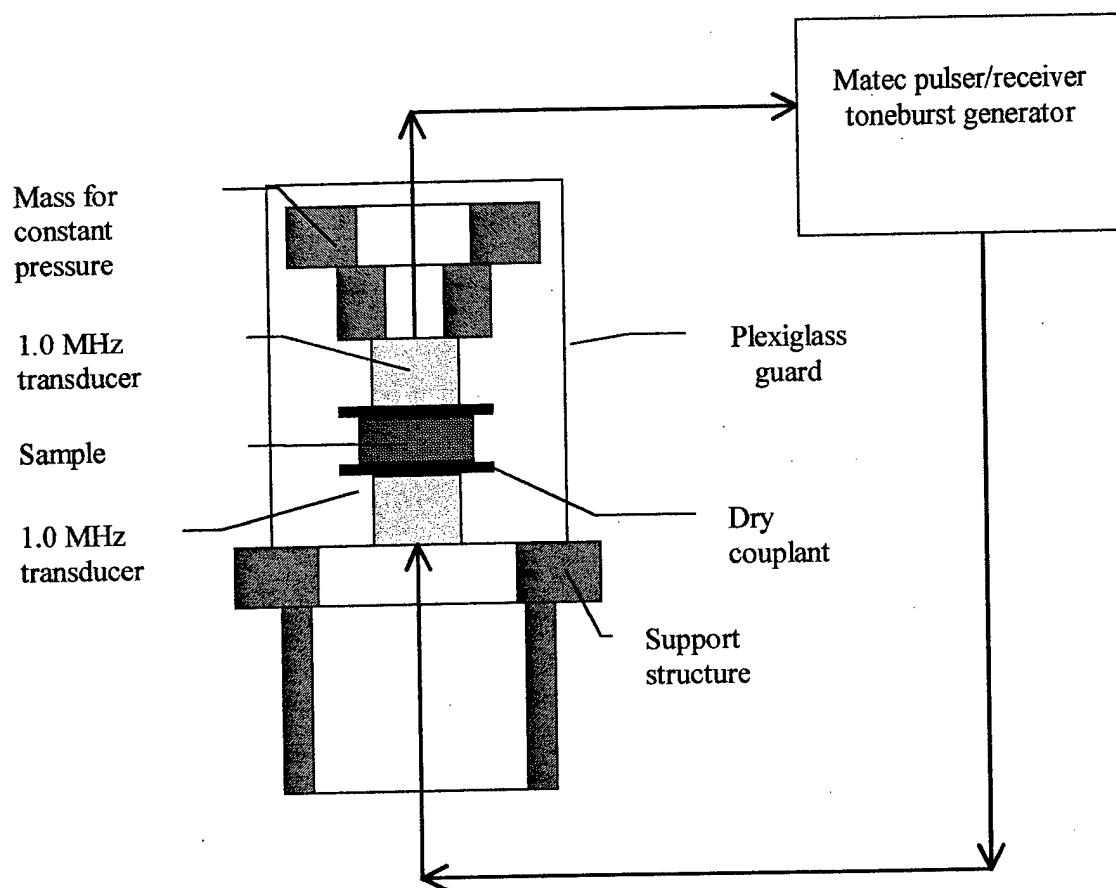


Figure 3.9: Schematic of time-of-flight ultrasonic evaluation of the quasi-PIM TRBs.

### 3.8 Resonant Frequency Evaluation

Dynamic elastic properties of the quenched quasi-PIM samples were determined using sonic resonance, as described in ASTM Standard Test Method E 1875-00<sup>97</sup>. In this test method, a variable frequency sinusoidal electrical signal was generated via SysID software package and soundboard, transmitted through an audio amplifier (Hafler

DH120 pre-amp and amp) to a piezo-electric transducer (a phonograph cartridge). The sample was suspended between two such transducers, with contact points in the center of each end. The test configuration is shown in Figure 3.10<sup>98,99</sup>. Although the test standard allows for support wires, none were needed for these samples—they were solidly suspended between the two contact points. The driving transducer generated a mechanical force on one end of the sample, exciting the bar in the flexural mode, shown in Figure 3.11a. A second transducer on the opposite end of the bar received the mechanical signal and transmitted an electrical signal back to the data acquisition computer. A fast Fourier transform performed on the returned signal yielded a voltage-frequency curve. A peak in the returned signal marked the fundamental resonant frequency. The equipment was capable of measuring a range of fundamental frequencies from zero to 25 kHz. Frequency, sample dimensions and mass were combined to derive the elastic modulus (E) using Equation 3.8, which is provided in the ASTM standard:

$$E = 0.94645 \left[ \frac{m_b f_f^2}{w_b} \right] \left[ \frac{L_b^3}{t_b^3} \right] C_s \quad ( 3.8 )$$

where  $C_s$  is calculated using Equation 3.9:

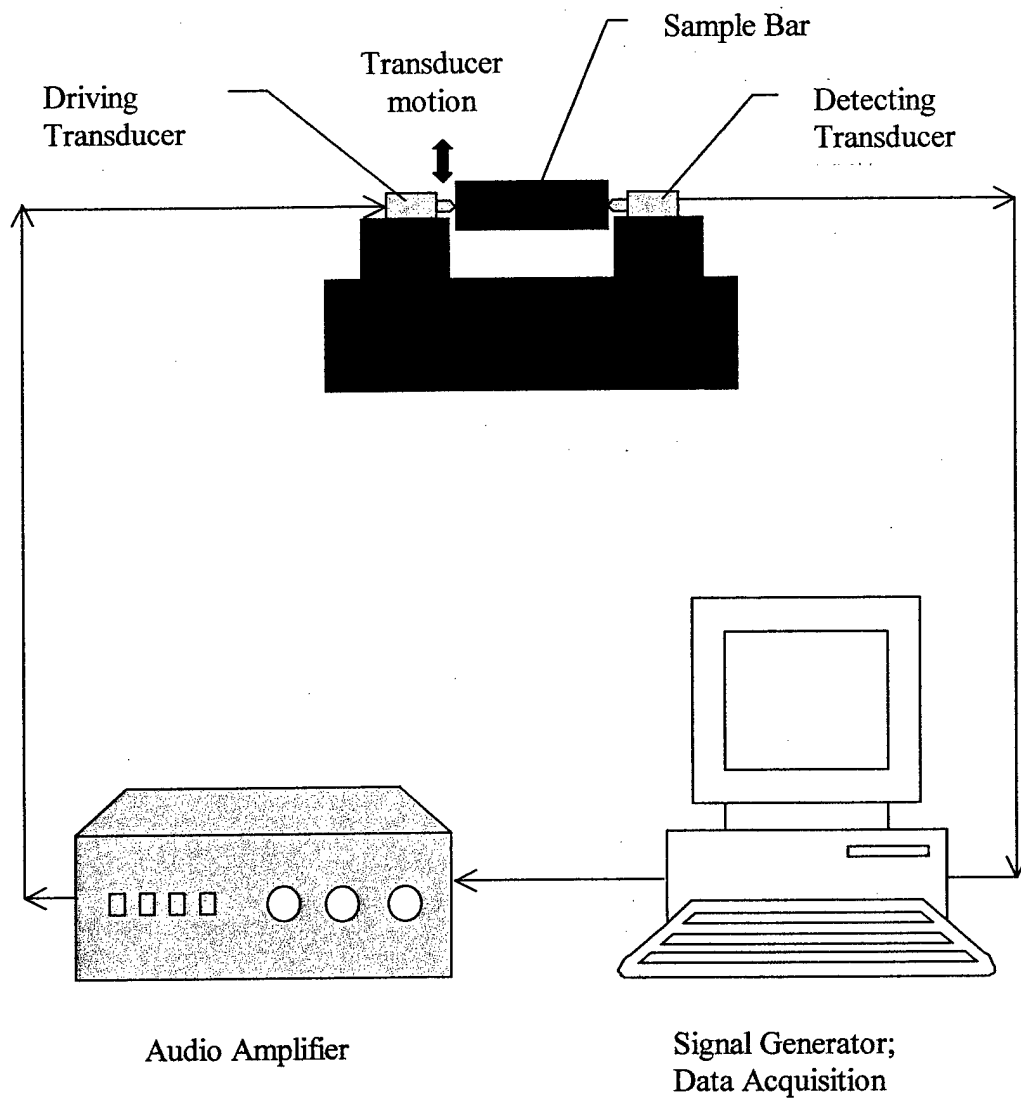


Figure 3.10: Schematic for resonant frequency test configuration

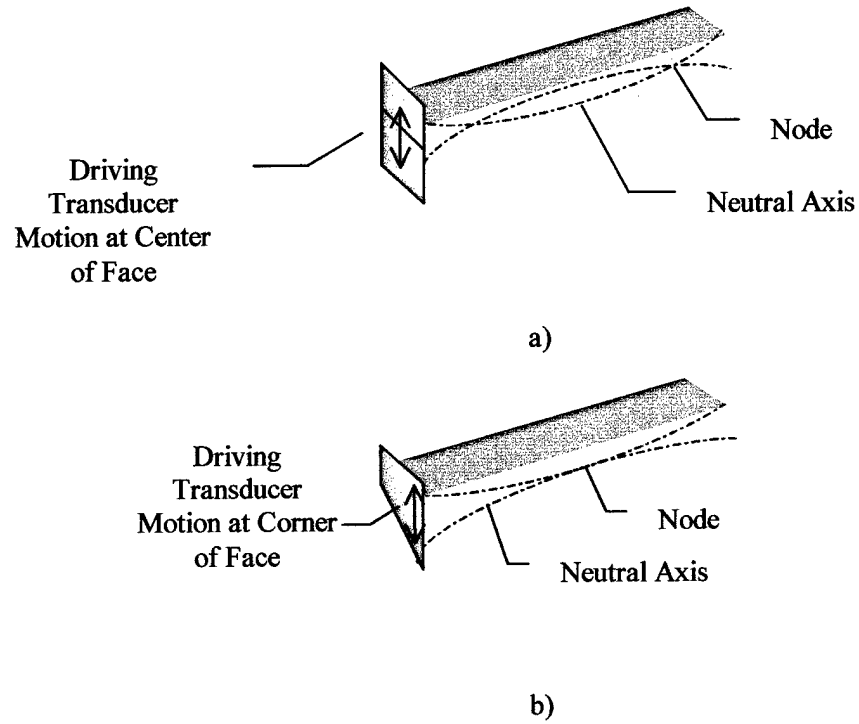


Figure 3.11: Bar excited in fundamental a) flexural and b) torsional resonance modes

$$C_s = 1 + 6.5850 \left( 1 + 0.0752\nu + 0.8109\nu^2 \right) \left( \frac{t_b}{L_b} \right)^2 - 0.86806 \left( \frac{t_b}{L_b} \right)^4$$

$$- \left[ \frac{8.340 \left( 1 + 0.2023\nu + 2.173\nu^2 \right) \left( \frac{t_b}{L_b} \right)^4}{1.000 + 6.338 \left( 1 + 0.1408\nu + 1.536\nu + 1.536\nu^2 \right) \left( \frac{t_b}{L_b} \right)^2} \right] \quad ( 3.9 )$$



In this calculation,  $L_b$  is the sample length,  $w_b$  is sample width,  $t_b$  is sample thickness,  $m_b$  is mass,  $f_f$  is the fundamental flexural frequency, and  $\nu$  is Poisson's ratio. To calculate  $E$ , an approximate value is used for Poisson's ratio, and Equation 3.9 is iterated until the value for  $E$  stabilizes. By modifying contact points between the sample and the transducers, the same process is used to find torsional stiffness. Contact points for torsional measurements were on opposite corners of the end faces, and the mechanical input excites a twisting mode of vibration, as shown in Figure 3.11b. The shear modulus ( $G$ ) is calculated using Equation 3.10:

$$G = \frac{4m_b L_b f_t^2}{w_b t_b} R_s \quad ( 3.10 )$$

where  $f_t$  is the fundamental torsional frequency (Hz), and  $R_s$  is a shape factor given by Equation 3.11:

$$R_s = \frac{w_b / t_b + t_b / w_b}{4(t_b / w_b) - 2.52(t_b / w_b)^2 + 0.21(t_b / w_b)^6} \quad ( 3.11 )$$

To verify equipment set-up and methods, two reference materials, 6061-T351 aluminum and Teflon, representing high and low ends of the expected sample material moduli, were evaluated. Measured values were within 4% and 1% of handbook values respectively.

The quasi-PIM samples were tested from higher moduli to lower moduli to maximize efficiency in detecting the frequency responses, with several samples randomly tested a second time to determine the repeatability of the measurements.

### 3.9 Electrical Conductivity

The evolution of electrical conductivity was profiled using the four-point method as described in ASTM B 63-90<sup>100</sup> adapted for application to the transverse rupture bars. The bar was held in a rubber-lined base block, with copper plates held against each end of the bar to maximize contact and evenly distribute current flow across the cross-section. Copper wire connected the two end contacts to an Epsco D-612T Filtered DC supply, which generated a constant current. Voltage was read using two contacts on the top of the bar, which were connected via copper wire to a Hewlett Packard 34401A Multimeter. Initial voltage measurements made with probe contacts indicated a large variation in readings, and a lack of repeatability. As noted in previous discussion, probe contact is also a potential source of damage to the fragile surface of the barely sintered parts. As a means of increasing surface contact in a non-damaging way, a contact pad was manufactured for placement across the top face of the bar. Flexible copper wire was secured to a soft rubber pad at a fixed spacing (11 mm). The pad was laid across the top of the bar and weighted to apply a constant pressure. This configuration, shown in Figure 3.12, provided a stable contact along the porous surface of the bar without the damage of a probe. No action was taken to remove surface oxides, to avoid damage to the very fragile bars. The output of the current supply was crosschecked using the multimeter. All

measurements were made using a current of 2.25 amps (2.0 amps gauge reading).

Voltage readings and applied current values were combined using Ohms Law, Equation 3.12, to determine the resistance ( $R$ ) of the sample bar:

$$R=V/I$$

( 3.12 )

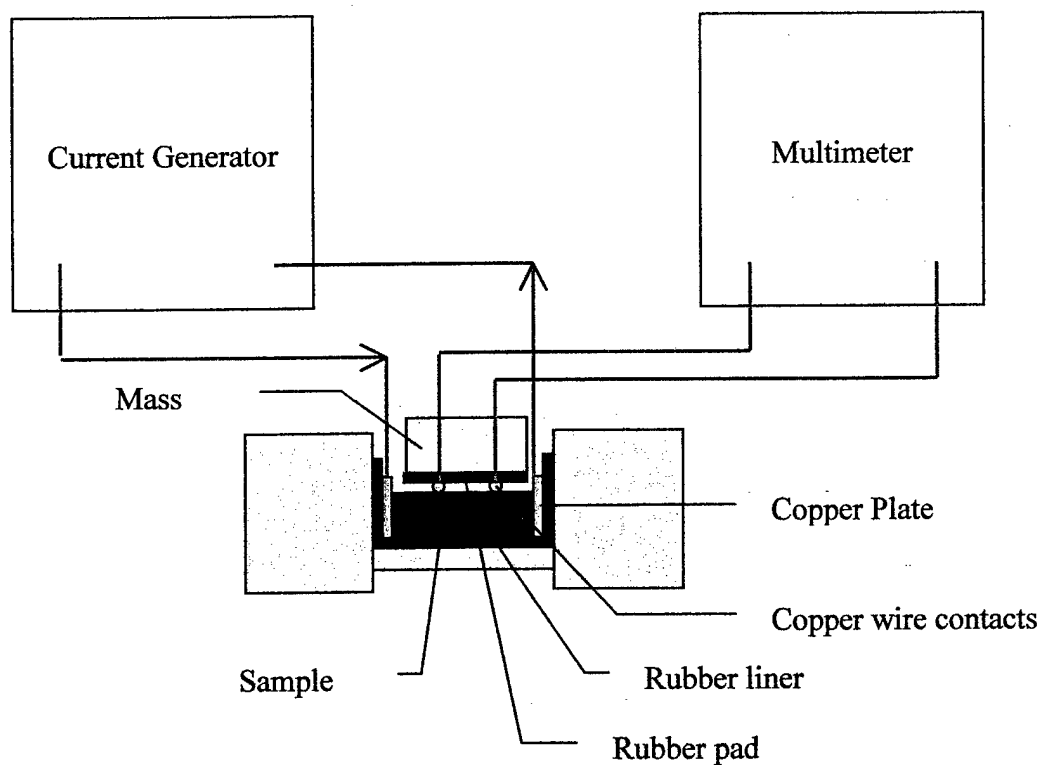


Figure 3.12: Schematic for electrical conductivity test set-up

where  $V$  is the measured voltage and  $I$  is the current as measured by the current generator. The resistance measurement was converted to a material resistivity,  $\rho_m$ , using the dimensions of the test piece, as shown in Equation 3.13:

$$\rho_m = RA/L_p \quad ( 3.13 )$$

where  $A$  is the cross-sectional area, and  $L_p$  is the length between the two voltage probes (11 mm).

A reference sample of 316 stainless steel ( $\rho = 74 \mu\Omega\text{-cm}$ )<sup>101</sup> was used to verify the overall accuracy of the equipment set-up. Measurements corresponded to handbook values within 0.5%.

Each quasi-PIM sample was measured once, with several samples measured a second time in random order to evaluate repeatability. A test was attempted on loose powder tapped into a rubber mold with the two copper contacts on either end. No current was able to pass through the powder bed, so conductivity was essentially zero.

### 3.10 Metallography and Microstructural Analysis

After fracture, one quasi-PIM sample from each test temperature was prepared for microstructural analysis. Samples were sectioned on an abrasive cut-off saw (model: Accutom-5; supplier: Struers, Westlake, OH) using a 357CA wheel, water-cooled at 3,000 RPM with a feed rate of 0.030 mm/s. Sectioned parts were dried in an air oven at 150°C

for 1 hour. The porous part was then infiltrated with epoxy to provide structural support during polishing. Struers EPOES Epofix resin HQ was mixed with Struers EPOES Epofix hardener HQ at an 89:11 ratio by weight. The porous nickel material was positioned sectioned-face-down in a small plastic cup, covered with the epoxy mixture and placed under low vacuum to draw the liquid into the pores. The samples were then allowed to cure at room temperature for 12 hours. Once the epoxy had hardened, the sample was ejected from the cup, and the bottom face was sanded with 600 grit SiC paper until the sectioned metal face was exposed and plane. Sample polishing was carried out on a Struers Rotapol-22/Rotoforce-4 autopolisher, and consisted of the three steps detailed in Table 3.2.<sup>102</sup> Samples were etched by swabbing with Fry's reagent (4 g cupric chloride dissolved in 20 ml concentrated hydrochloric acid and 20 ml water) for 60-90 seconds to bring out grain boundaries.

Table 3.2: Polishing method for porous nickel samples, epoxy mounts.

Step	Diamond Polish 1	Diamond Polish 2	Oxide Polish 3
Surface	MD-Dac	MD-Dac	OP-Chem
Abrasive	diamond suspension	diamond suspension	colloidal silica (OP-S)
Grain Size	9 $\mu\text{m}$	3 $\mu\text{m}$	0.04 $\mu\text{m}$
Lubricant	red	red	water
Wheel Speed (RPM)	150	150	150
Rotation direction	CW	CW	CCW
Force (N)	25	25	20
Time (min)	4	2	2:20

A qualitative assessment of the fracture surfaces for the quasi-PIM materials was made using the scanning electron microscope described in section 3.2. One sample from each temperature increment was examined. The fracture surface was examined for marks indicating ruptured bonds perpendicular to the viewing axis (e.g. in the plane of the viewing screen). For the quasi-PIM material, twenty-five rupture points were measured per bar. A more exhaustive count was done on the PIM samples, with at least 75 points measured per bar.

## **Chapter 4**

### **Experimental Results**

This chapter addresses results for all testing described in Chapter 3. The chapter is organized in the following manner: initial system characterization, primary results, and secondary results. Initial system characterization details the physical parameters of the sintering system, in this case a solid-state nickel powder system. This description includes powder characterization, and sintering characterization via dilatometry. Primary results are those directly referenced in the hypothesis -- thermal conductivity and mechanical strength data. Secondary results are those that support and further characterize the system evolution -- ultrasonic evaluation, resonant frequency evaluation, and electrical conductivity evaluation, as well as microstructural observations.

#### **4.1 Initial Characterization**

##### **4.1.1 Powder Characterization**

The Novamet 4SP-10 powder was characterized as a spherical powder with a narrow particle size distribution. The median particle size was approximately 7  $\mu\text{m}$ . Particle size distribution and density characterization data are summarized in Table 4.1:

Table 4.1: Summary of Novamet 4SP-10 powder characterization data

Particle Size:		
D <sub>10</sub> (μm):	4.0 ± 2.2%	
D <sub>50</sub> (μm):	6.9 ± 0.8%	
D <sub>90</sub> (μm):	10.9 ± 0.4%	
Method:	Wet laser scattering	
Densities:	g/cm <sup>3</sup>	% Pycnometer
Apparent:	3.8 ± 0.4%	42.9
Tap:	5.1 ± 0.1%	57.6
Pycnometer:	8.9 ± 0.1%	-

Scanning electron microscope (SEM) images confirmed a spherical powder shape, as shown in Figure 4.1. The spherical shape is characteristic of carbonyl nickel powder, but the relatively smooth surface is unusual -- achieved through a proprietary combination of pressure and temperature during the powder manufacturing.<sup>103</sup> Examination of the nickel powder mounted in epoxy, cross-sectioned, polished and etched revealed a layered microstructure, also characteristic of the carbonyl deposition process.<sup>104</sup> An SEM image of this microstructure is shown in Figure 4.2.



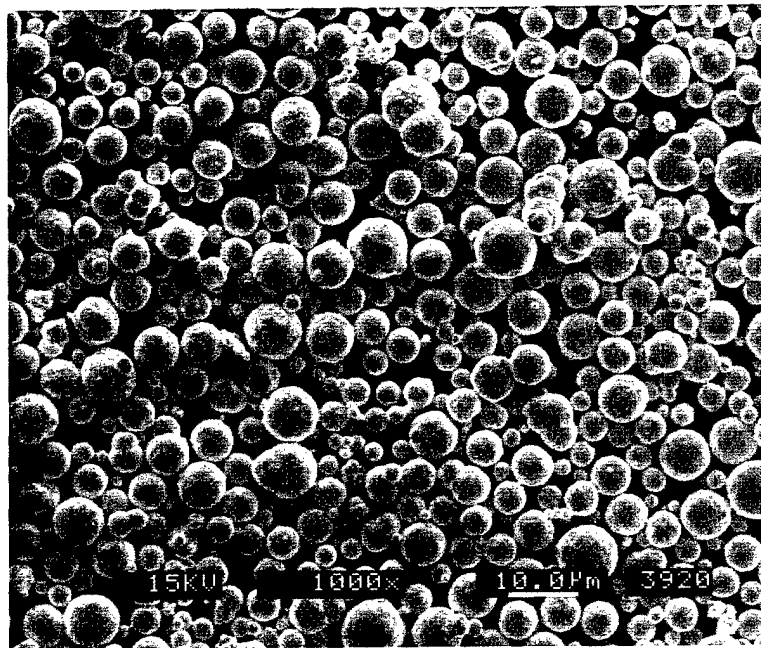


Figure 4.1: Scanning electron microscope image of the as-received Novamet 4SP-10 powder, showing spherical shape and relatively low surface roughness

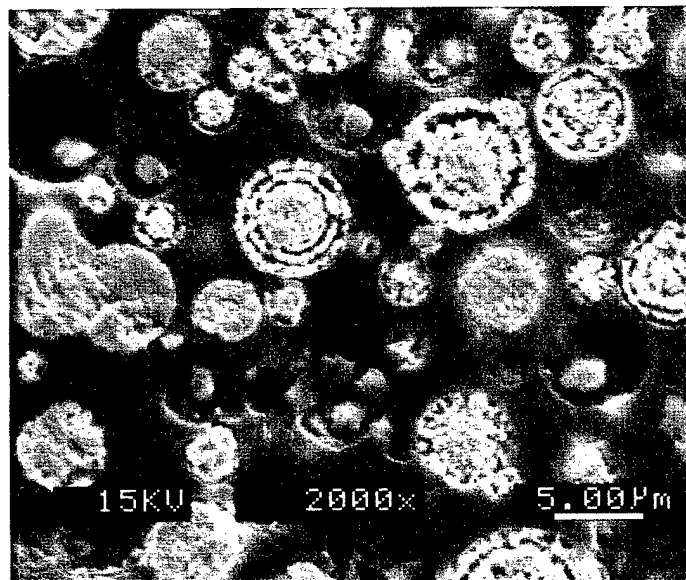


Figure 4.2: Scanning electron microscope image showing layered microstructure of etched carbonyl powder

#### 4.1.2 Dilatometric Analysis

The initial dilatometry profile characterized loose powder tapped in a crucible, sintered in a hydrogen atmosphere at  $10^{\circ}\text{C}/\text{min}$ . Percent shrinkage and shrinkage rate results are shown in Figure 4.3. Thermal expansion occurs during initial heating, but is overcome by densification, resulting in net zero shrinkage by  $400^{\circ}\text{C}$ . Densification rate steadily increases with temperature, reaching a maximum that extends from  $875$  to  $950^{\circ}\text{C}$ . The heating rate significantly drops as the furnace approaches the setpoint of

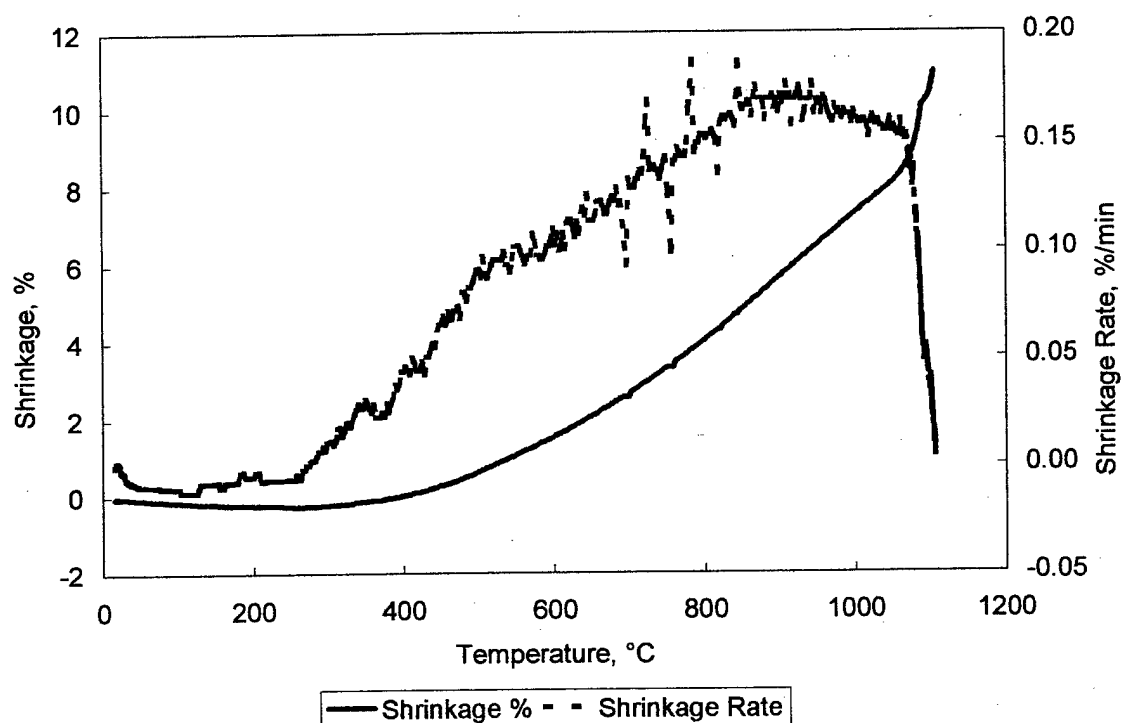


Figure 4.3: Linear percent shrinkage and shrinkage rate of loose powder, heated at  $10^{\circ}\text{C}/\text{min}$  to  $1100^{\circ}\text{C}$  in  $\text{H}_2$ .

1100°C. This appears as an increase in shrinkage on the percent shrinkage curve, but the shrinkage rate actually drops steeply at this point as the heating rate slows. Archimedes density evaluation of the sintered sample revealed a final density 93.5% that of theoretical. Based on this initial result, 400°C was designated as the presintering hold temperature for preparation of the quasi-PIM specimens.

## 4.2 Primary Results

Primary results are those that support (or disprove) the hypothesis. In this case, the premise of the hypothesis is that both thermal conductivity and mechanical strength are functions of the interparticle bond during pre-densification sintering. Built upon this premise, the hypothesis proposes that mechanical strength can be inferred from thermal conductivity measurements. The initial thrust of the primary results for both thermal conductivity and transverse rupture strength are to characterize the respective properties during initial stage sintering. The second thrust is to compare the two properties and capture the relationship between them.

### 4.2.1 Thermal Conductivity

Initial testing was performed on quasi-PIM disks to determine the feasibility of monitoring sintering in powder metallurgy materials by observing changes in thermal diffusivity. *In situ* measurements were made during a heating-cooling cycle in argon, hydrogen, and low vacuum (13 kPa) atmospheres. These results are shown in Figure 4.4,

which shows measured values along with the behavior of solid nickel as a function of temperature.<sup>21</sup> Nickel experiences a sharp dip in thermal and electrical conductivity around the Curie temperature of 358°C.

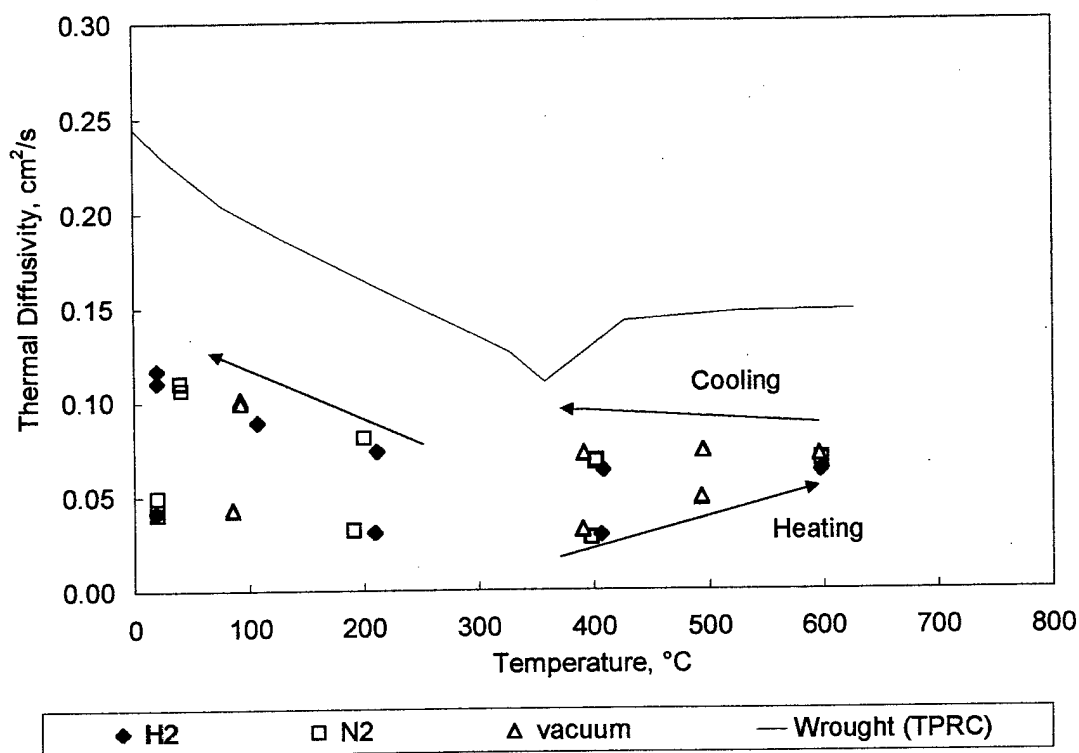


Figure 4.4: *In situ* thermal diffusivity evolution of quasi-PIM samples during heating-cooling cycle under hydrogen, nitrogen, and low vacuum atmospheres. Wrought properties are derived from the Thermophysical Properties Research Center (TPRC) database.<sup>21</sup>

These results indicate a net increase in the thermal diffusivity as temperature increases above 400°C (the pre-sintering hold temperature), clearly visible when compared with measurements made during the cooling cycle. This observation becomes more evident when the measurements are normalized by the behavior of solid nickel at tempera-

ture, as shown in Figure 4.5. Each *in situ* measurement is divided by the wrought properties at that temperature. These property values are given in Appendix F.

The results in Figure 4.5 show a constant behavior up to the presintering temperature of 400°C, an increase in diffusivity from 400 to 600°C, and relatively constant behavior during cooling from 600°C. It is interesting to note in these initial results that there was not a significant difference in measured values between the three atmospheres.

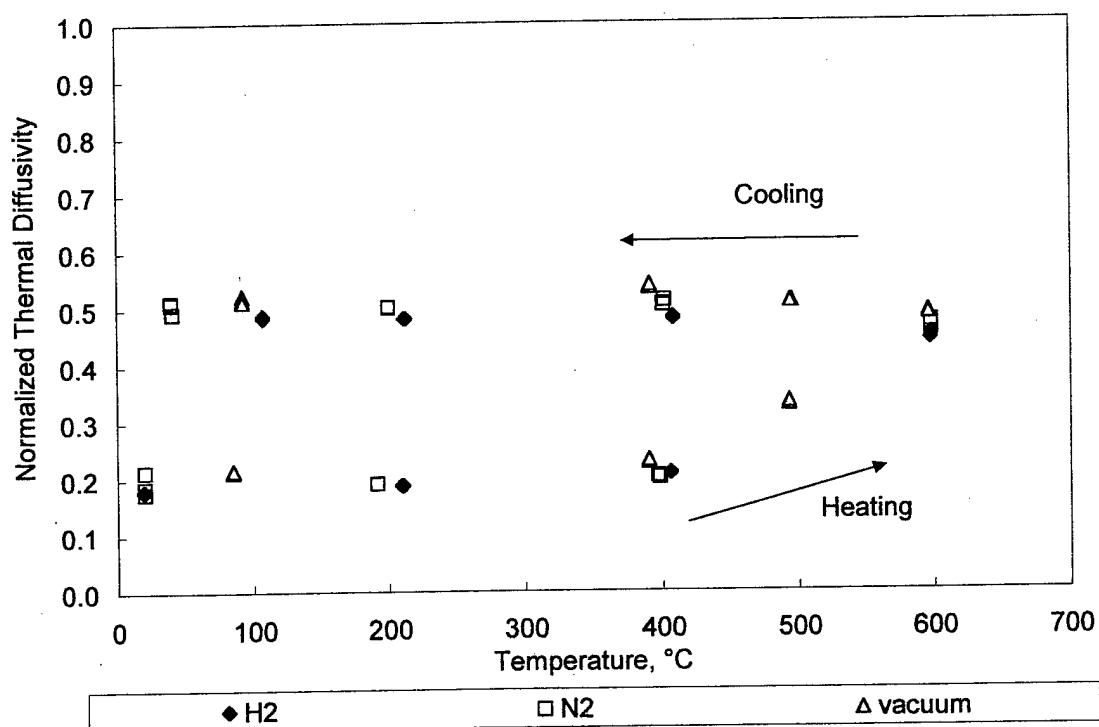
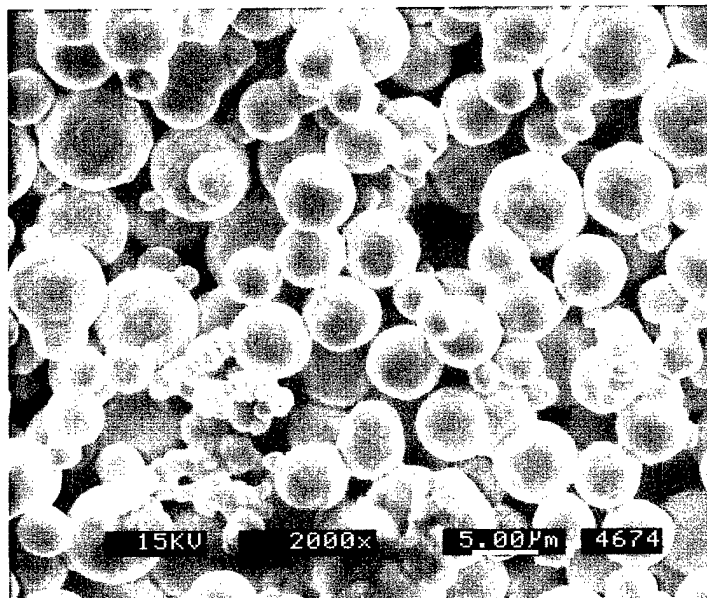
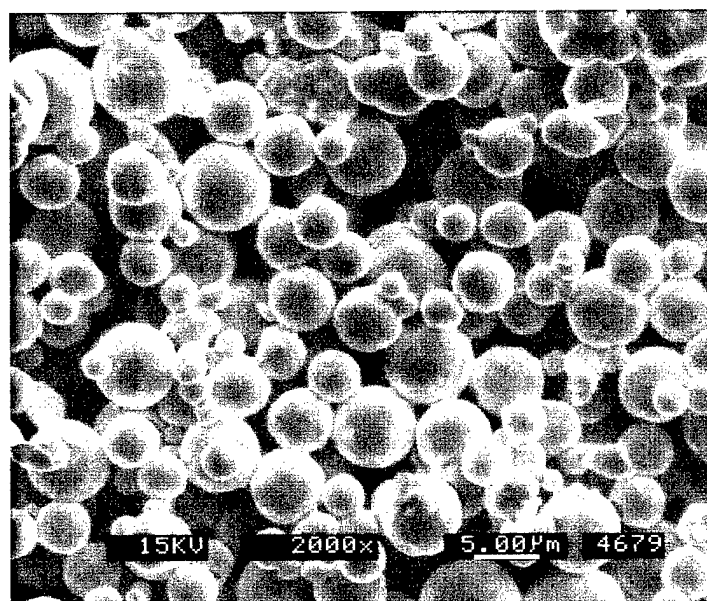


Figure 4.5: Normalized *in situ* thermal diffusivity of quasi-PIM samples during heating-cooling cycle in hydrogen, nitrogen, and low vacuum atmospheres

After initial confirmation that an increase in thermal diffusivity under sintering conditions could be observed, the samples were examined for destructive effects from the laser flash. Significant discoloration was present on the surfaces of the samples tested in nitrogen (cinnamon, violet, green and black with increasing temperatures) and vacuum (black). Particularly in the nitrogen samples, discoloration was noticeably heavier on the top face, which received the laser flash. However, the specimen tested in hydrogen showed no discoloration, which implied that the discoloration was a result of oxidation that did not persist in a reducing atmosphere. To isolate the effect of the laser flash, the top and bottom faces of the hydrogen sample were examined via scanning electron microscope (SEM). Images of the top and bottom faces are shown in Figure 4.6. The surfaces were examined for melting, charring, or any other signs of surface anomaly. Although some foreign particles on the surface of the disk did cause localized charring, no difference was observed between particle appearance on the top and bottom faces. A second sample was cross-sectioned and examined for differences between top and bottom faces. Micrographs of these faces are shown in Figure 4.7. No significant differences were observed, however an internal crack consistent with delamination difficulties encountered when pressing spherical powder was noted. These cracks often appear as layers perpendicular to the pressing direction, and are caused by the difference in constraint during ejection from the tool die.<sup>1</sup> Discoloration on the nitrogen samples was traced to impurities in the nitrogen process gas, which flows through the test chamber from top to bottom, causing the heavier discoloration on the top face. A higher purity nitrogen gas



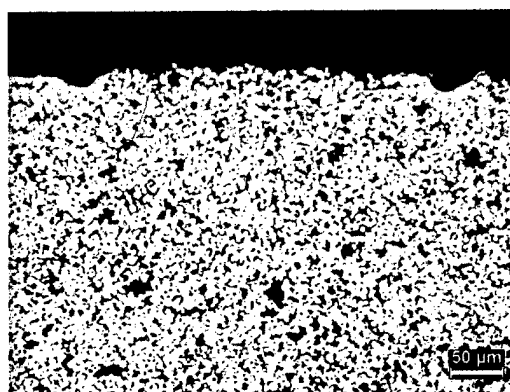
a)



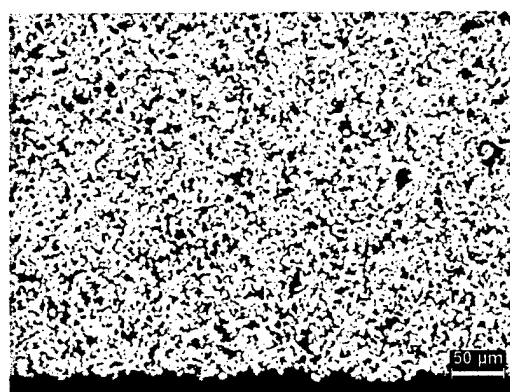
b)

Figure 4.6: SEM images of the a) top and b) bottom faces of quasi-PIM nickel disk after 24 laser flash measurements.

was used for subsequent tests, with a marked reduction in surface discoloration. Data from the oxidized samples were not included in data analysis or plots.



a)



b)

Figure 4.7: Cross-section at a) top and b) bottom face of quasi-PIM disk after *in situ* laser flash analysis up to 800°C. No significant differences or damage due to laser flash were noted.



Because the basic calculation for thermal diffusivity is dependent on the thickness of the disk squared, per Equation 2.49, it is critical to know the thickness,  $H$ , of the disk during the *in situ* measurements. As a reminder, the relationship is shown below, with  $t_{1/2}$  as the half rise time.

$$\alpha = \frac{1.38H^2}{\pi^2 t_{1/2}} \quad (2.49)$$

Dilatometry was used to examine the shrinkage of the same material for the time-temperature profile approximating that of the laser flash heating-cooling cycle. Initial attempts to match the ramp and hold behavior of the laser flash equipment proved to be extremely cumbersome. The time-temperature profile for the measurement was therefore approximated with a constant heating rate of 10°C/min to 400°C, slowing to a heating rate of 1.5°C/min from 400°C to 600°C. The linear shrinkage versus temperature is shown in Figure 4.8. The results show a linear thermal expansion to 400°C (the presintering hold temperature), with shrinkage occurring at a constant rate from 400°C to 600°C. The material shows a linear thermal contraction upon cooling. Total linear shrinkage was extrapolated to just over 3%, which was confirmed by physical measurement at room temperature.

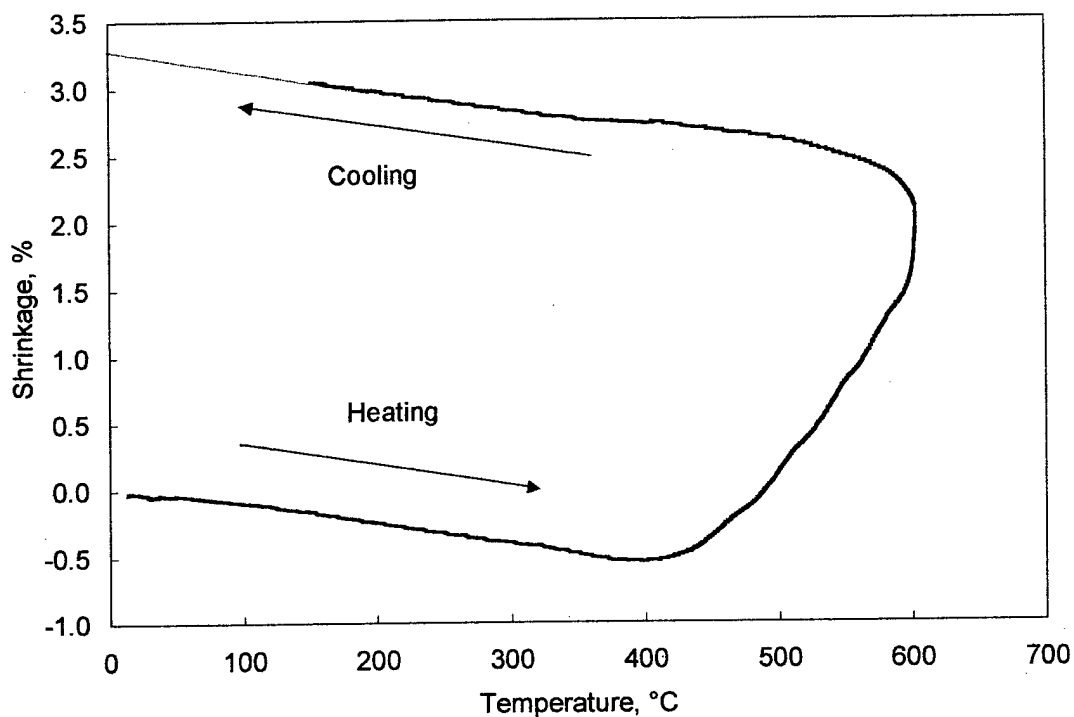


Figure 4.8: Percent shrinkage versus temperature for quasi-PIM Ni during heating-cooling cycle approximating laser flash heating-cooling cycle, flowing hydrogen atmosphere.

Measured thermal diffusivity values were then corrected using Equation 4.1:

$$\alpha_{eff} = \alpha_{meas} \left( \frac{H_{init}}{H_{corr}} \right)^2 = \alpha_{meas} \left( \frac{H_{init}}{H_{init} \left( 1 + \frac{\Delta H}{H_{init}} \right)} \right)^2 \quad ( 4.1 )$$

where  $\alpha_{\text{eff}}$  and  $\alpha_{\text{meas}}$  are effective and measured thermal diffusivities ( $\text{cm}^2/\text{s}$ ), and  $H_{\text{init}}$  and  $H_{\text{corr}}$  are the initial and corrected disk thicknesses (cm).  $\Delta H/H_{\text{init}}$  is the linear shrinkage, shown as positive for expansion and negative for shrinkage in this case.

Thermal diffusivity results can be converted to thermal conductivity values through the application of Equation 2.42, as described previously:

$$\kappa_{\text{eff}} = \alpha_{\text{corr}} C_p \rho_s \quad 2.42$$

where  $C_p$  is the specific heat of the bulk material at temperature, and  $\rho_s$  is the sintered density at temperature. Specific heat values may be obtained through differential scanning calorimetry, or handbook values may be used.<sup>105</sup> Density and specific heat of the gas in the pores are neglected for this calculation. Conductivity normalized by the wrought values,<sup>21</sup> designated with an "o" subscript, may then be shown by Equation 4.2:

$$\frac{\kappa_{\text{eff}}}{\kappa_o} = \frac{\alpha_{\text{corr}} C_p \rho_s}{\alpha_o C_p \rho_o} \quad (4.2)$$

Since  $C_p$  remains the same for the solid material at a given temperature, this relation simplifies to Equation 4.3:

$$\frac{\kappa_{\text{eff}}}{\kappa_o} = \frac{\alpha_{\text{corr}}}{\alpha_o} f_s \quad (4.3)$$

where  $f_s$  is the fractional (normalized) density and  $\alpha_o$  is the thermal diffusivity of solid nickel at the test temperature. The linear shrinkage may be used to approximate the sintered density using Equation 4.4:<sup>1</sup>

$$\rho_s = \frac{\rho_g}{\left(1 + \frac{\Delta H}{H_{init}}\right)^3} \quad (4.4)$$

Thermal conductivity and normalized thermal conductivity values for the quasi-PIM material as a function of temperature are shown in Figure 4.9 and Figure 4.10. Each point represents the mean value of three shots for one sample. A study of variability of the measurement was then conducted using PIM samples.

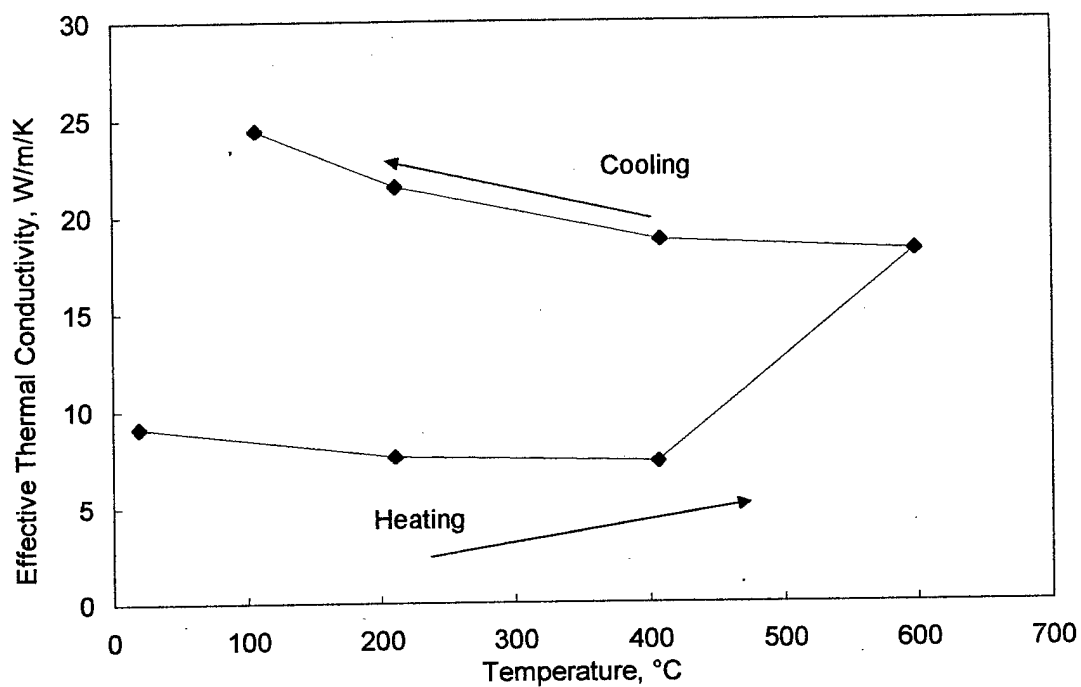


Figure 4.9: Effective thermal conductivity of quasi-PIM nickel versus temperature, as developed during heating-cooling cycle in flowing hydrogen.

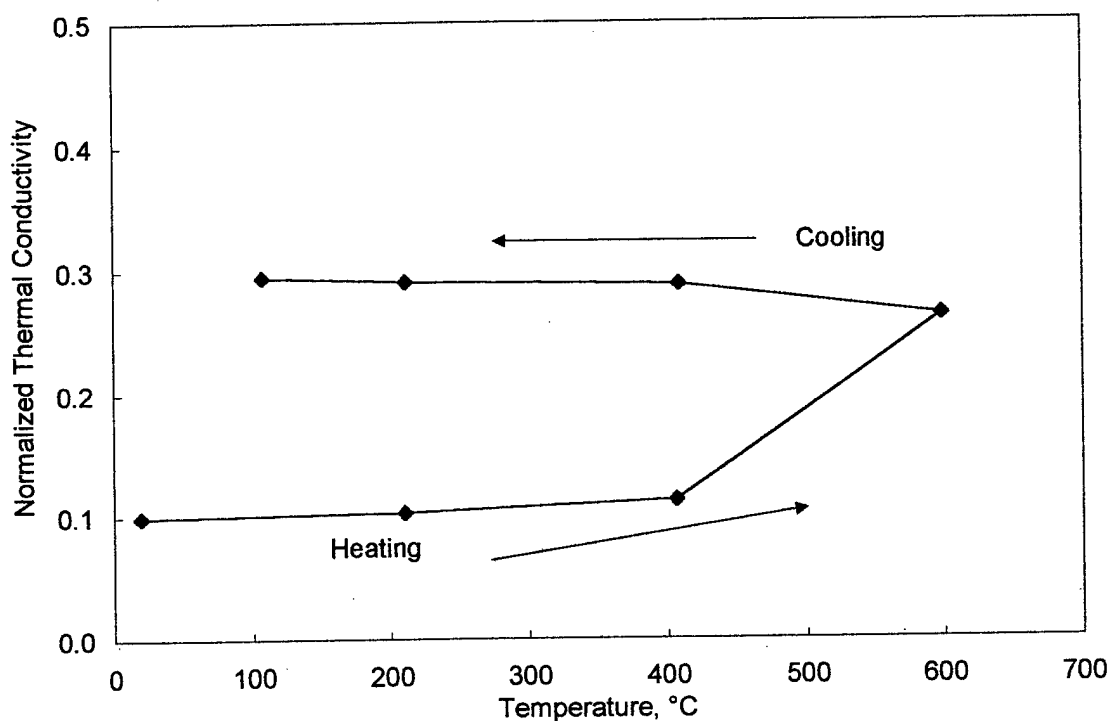


Figure 4.10: Normalized effective thermal conductivity of quasi-PIM nickel versus temperature, as developed during heating-cooling cycle in flowing hydrogen.

A set of heating-cooling cycles was performed on PIM samples to determine repeatability of the laser flash measurements from sample to sample. The results of these tests are shown in Figure 4.11. The error bars represent the normalized value at a 95% confidence level. Ten samples were measured at each temperature increment during the heating cycle, with three shots made per sample per measurement temperature. During the cooling cycle, fewer samples (2 to 4 samples) were measured at each temperature due to temperature-related equipment difficulties.

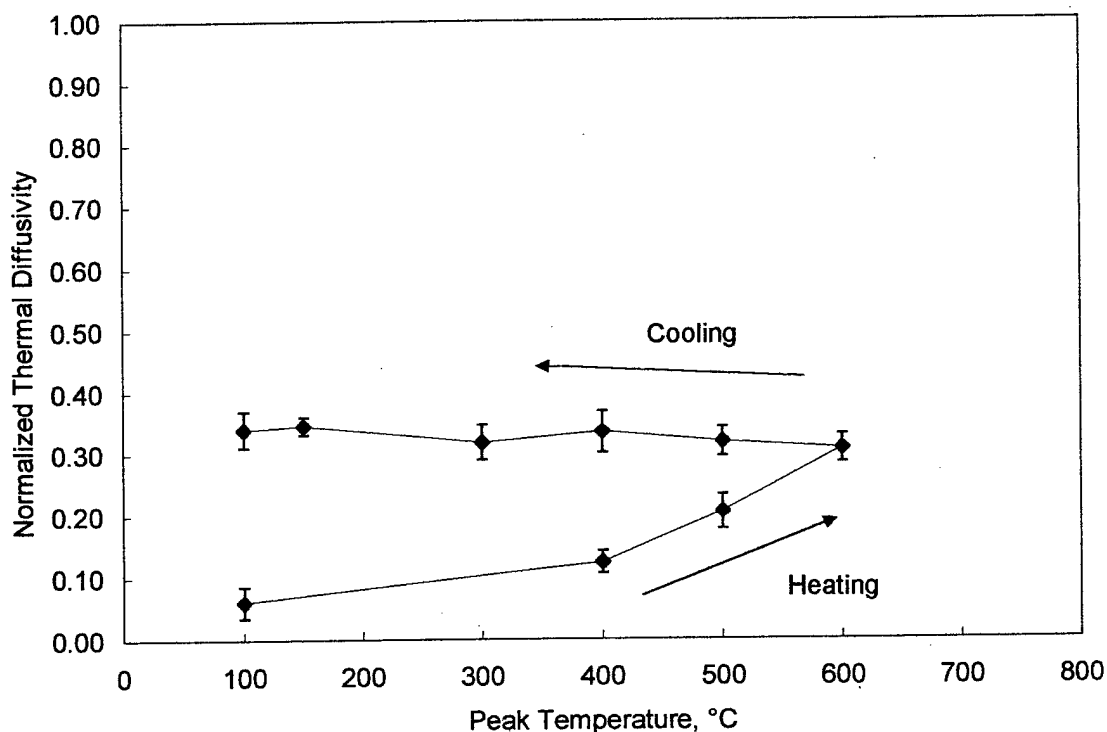


Figure 4.11: Normalized *in situ* thermal diffusivity of PIM disks during heating-cooling cycle, flowing nitrogen atmosphere. The error bars represent a 95% confidence level.

PIM disks were then evaluated to correspond directly with transverse rupture data during a typical thermal debinding and pre-sintering cycle. Disks and transverse rupture bars were thermally debound in a retort furnace, removed at increments along the thermal treatment cycle, and air-quenched. These disks were then measured in the laser flash at 100°C. The slightly elevated temperature was chosen to increase the strength of the infrared signal to the detector. These results are shown in Figure 4.12. The thermal conductivity remained essentially constant at 3 to 4% that of solid nickel, up to the hold

temperature of 425°C. Only after two hours at the hold temperature did the thermal conductivity increase to 7%. Following the hold, a linearly increasing trend of thermal conductivity with temperature was observed. Conductivity of the solid polymer backbone is approximately 0.3 W/m·K.<sup>104</sup>

The PIM samples contained residual polymer binder at temperatures below 425°C. Thermogravimetric analysis indicated onset of binder burnout at 423°C in a ni-

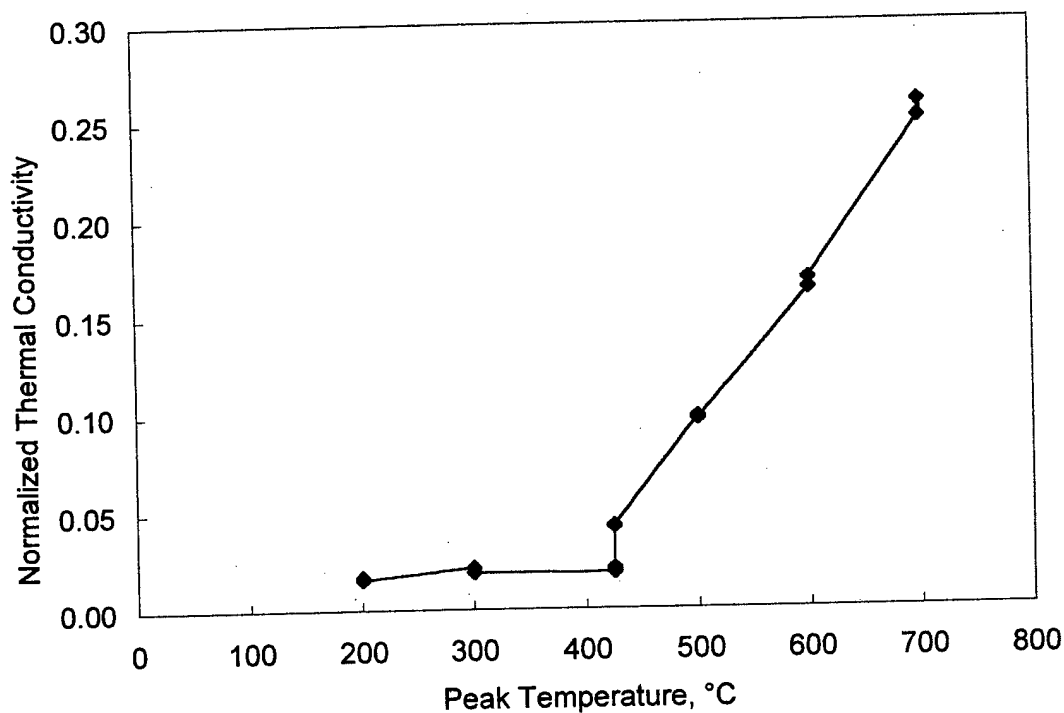


Figure 4.12: Normalized thermal conductivity of air-quenched PIM disks versus peak sintering temperature. Disks were removed from furnace at indicated peak temperature, cooled in air, and measured at 100°C. Sintering conducted in flowing hydrogen at 2°C/min to 425°C, 2 hour hold, 2°C/min to 700°C.



trogen atmosphere. Laser flash tests on the 200°C, 300°C, and 425°C (no hold) samples resulted in a layer of ash on the top surface of the disk. This layer formed during the first measurement, and subsequent measurements at the same temperature increment did not differ from the initial measurement. A post-measurement photograph is shown in Figure 4.13. In the photo, the sample on the right has been flashed, and the sample on the left has not. The ash has been wiped from the right side of the sample to show the clean surface underneath. No ash was observed on samples held at 425°C for one and two hours, or the higher temperature samples.

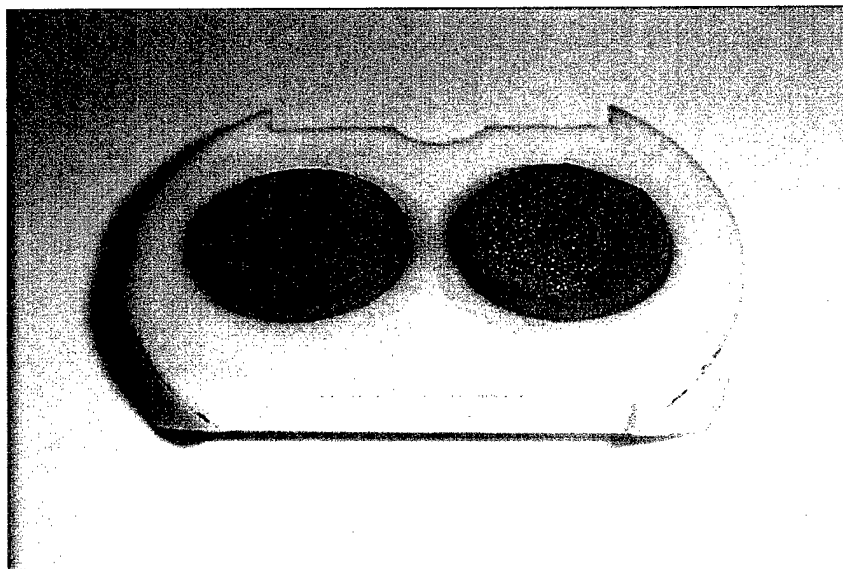


Figure 4.13: PIM sample with layer of ash after laser flash measurement. Samples had been thermally debound in flowing hydrogen at 2°C/min to 200°C, removed from the furnace and air-cooled. Laser flash measurement was made at 100°C.

Raw nickel powder was evaluated using the same time-temperature profile used for the PIM samples, although because the measurements were made *in situ* prior to an

operating hydrogen capability, a nitrogen atmosphere was used. Normalized data are shown in Figure 4.14.

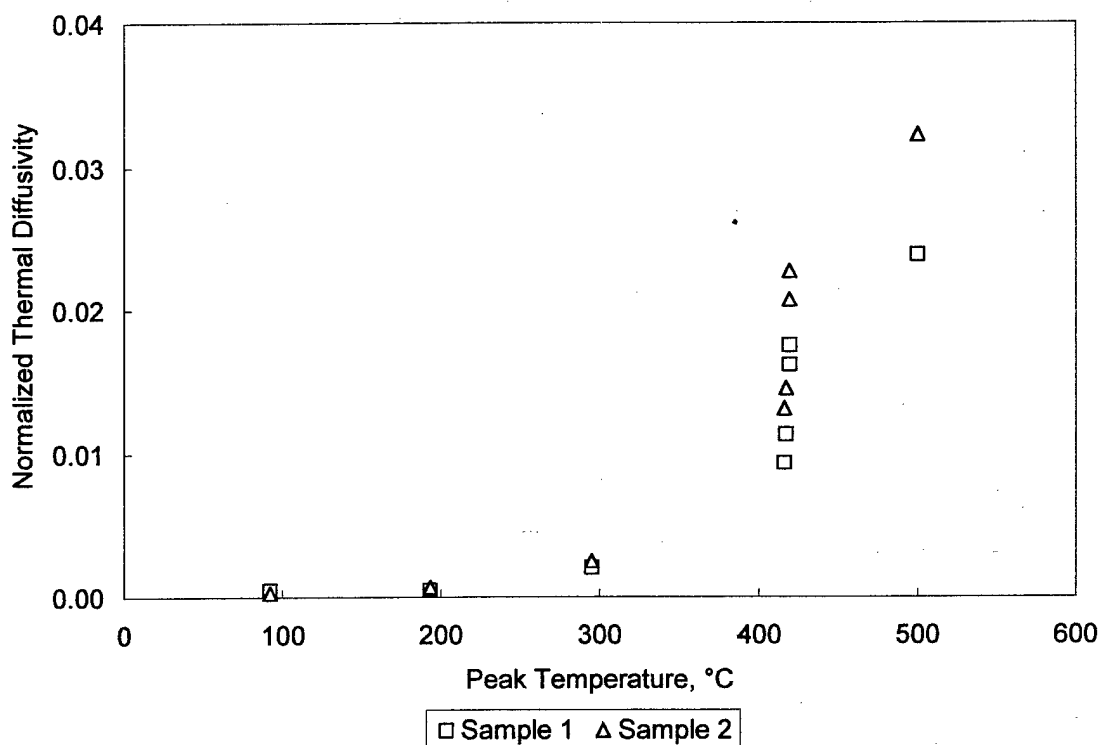


Figure 4.14: Normalized *in situ* data for raw nickel powder. Sintering conducted in flowing nitrogen with a heating rate of 2°C/min to 425°C, 2 hour hold, 2°C/min to 500°C.

The powder data initially show less than 0.2% normalized thermal diffusivity, increasing to approximately 2% at 300°C. Values are consistent between samples. However, during the hold at 425°C, a large amount of scatter developed between samples, continuing into higher temperatures. Raw powder data were compared to the air-

quenched PIM data, with both sets of data normalized against solid nickel thermal diffusivity at test temperature. This comparison is shown in Figure 4.15.

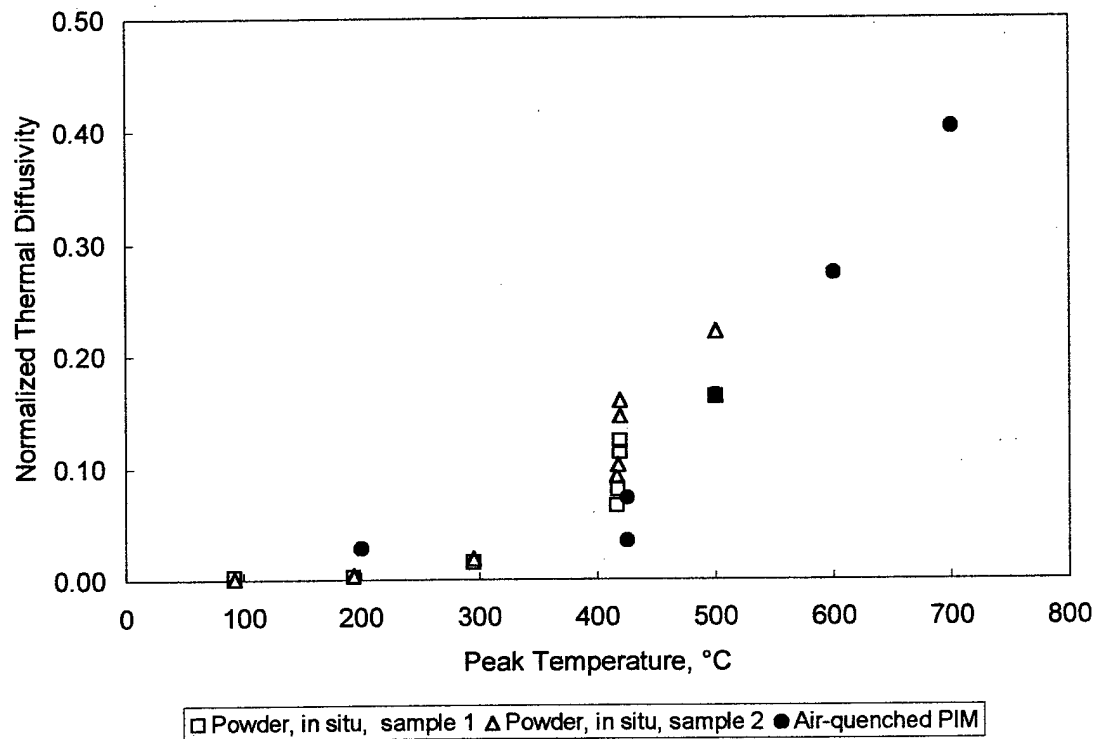


Figure 4.15: Normalized thermal diffusivity versus sintering temperature of PIM and raw powder. Powder measured *in situ* in flowing nitrogen. PIM samples sintered in flowing hydrogen, air cooled, and measured at 100°C.

Initially, the PIM samples show a higher thermal diffusivity than the powder samples. During the hold, the powder developed a higher effective diffusivity than the PIM material; with an average value twice that of the PIM material after a similar time frame.

Die-compacted specimens were evaluated to correspond directly with transverse rupture data. Disks were heated in the FTT along with transverse rupture bars. After the bars were fractured at the peak temperature, the furnace was opened, the disks were removed and air-cooled. These disks were then tested for thermal diffusivity at 200°C (sensor difficulties precluded measurements at 100°C). These results are shown in Figure 4.16.

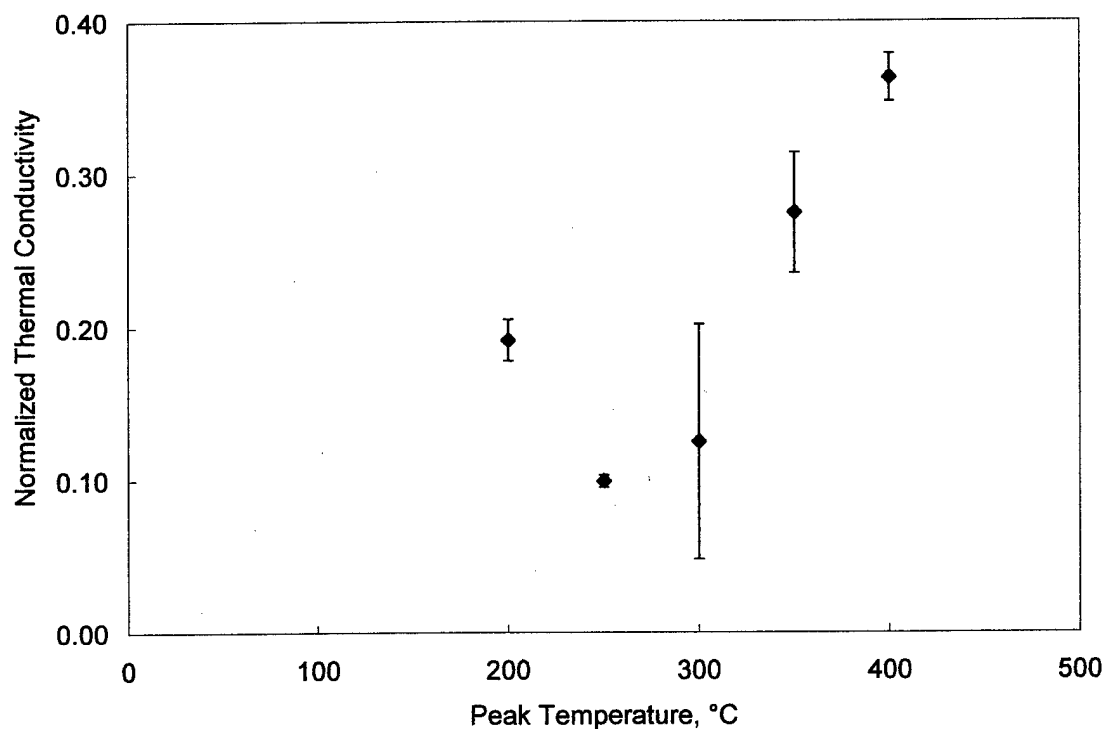


Figure 4.16: Normalized thermal conductivity versus peak sintering temperature of air-quenched die-compacted disks. Measurements made in nitrogen at 200°C. The 200°C samples were also measured at room temperature, giving the same result.

A general linear trend of effective thermal conductivity is shown with increasing temperature, with the exception of the datum at 200 °C. The 200°C samples were re-tested at room temperature to eliminate effects of binder melting, which had created instabilities noticeable in the raw data at 200°C. Room temperature measurements confirmed the higher normalized effective thermal conductivity for the 200°C samples.

#### **4.2.2 Transverse Rupture Strength Testing**

*In situ* transverse rupture strength for die-compacted samples is shown as a function of temperature in Figure 4.17. The average green strength at room temperature was 1.3 MPa, decreasing to 0.4 MPa at 200°C. Increasing temperatures yielded increases in strength to 500°C, peaking at approximately 10 MPa, before beginning a downward trend. Since the region of interest was the onset and initial development of strength, only one datum was taken at 500°C and 600°C.

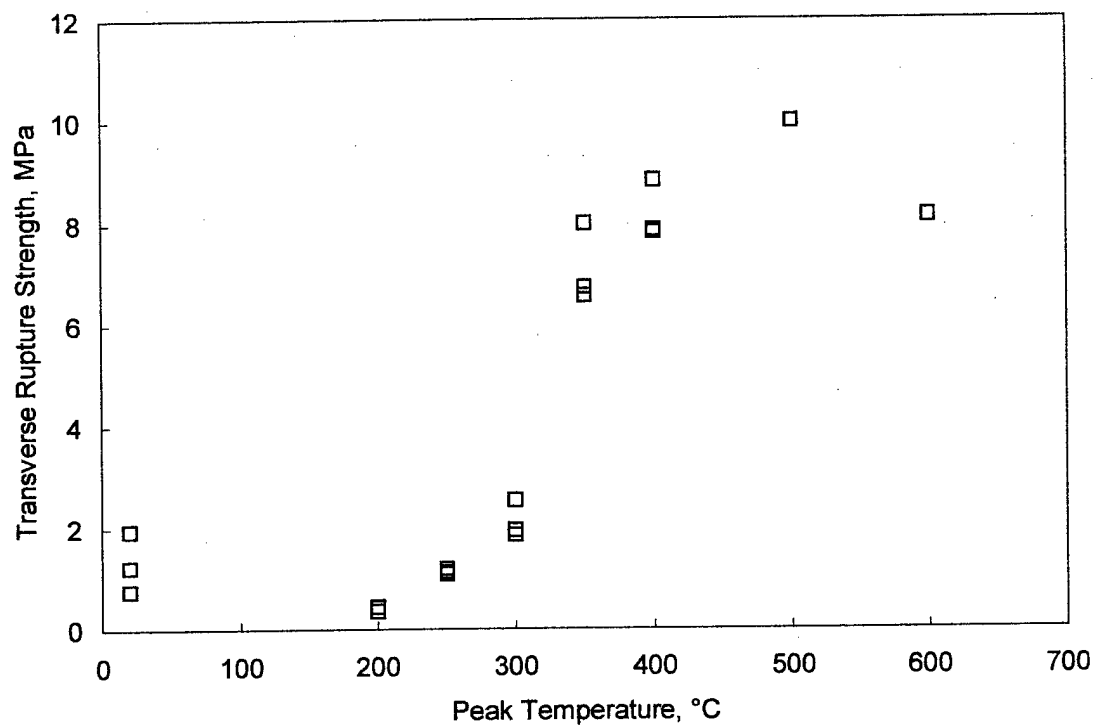


Figure 4.17: *In situ* transverse rupture strength of die compacted samples as a function of temperature. Samples heated in flowing hydrogen at 3°C/min to test temperature with a 15-minute hold. Initial specimen fractional density was 0.75.

Room temperature transverse rupture strength for quasi-PIM samples is shown in Figure 4.18. Initial strength of the presintered material (400°C datum) was 1.3 MPa. Strength increased to 3.4 MPa at 500°C, and subsequently showed a linear trend with increasing temperatures.

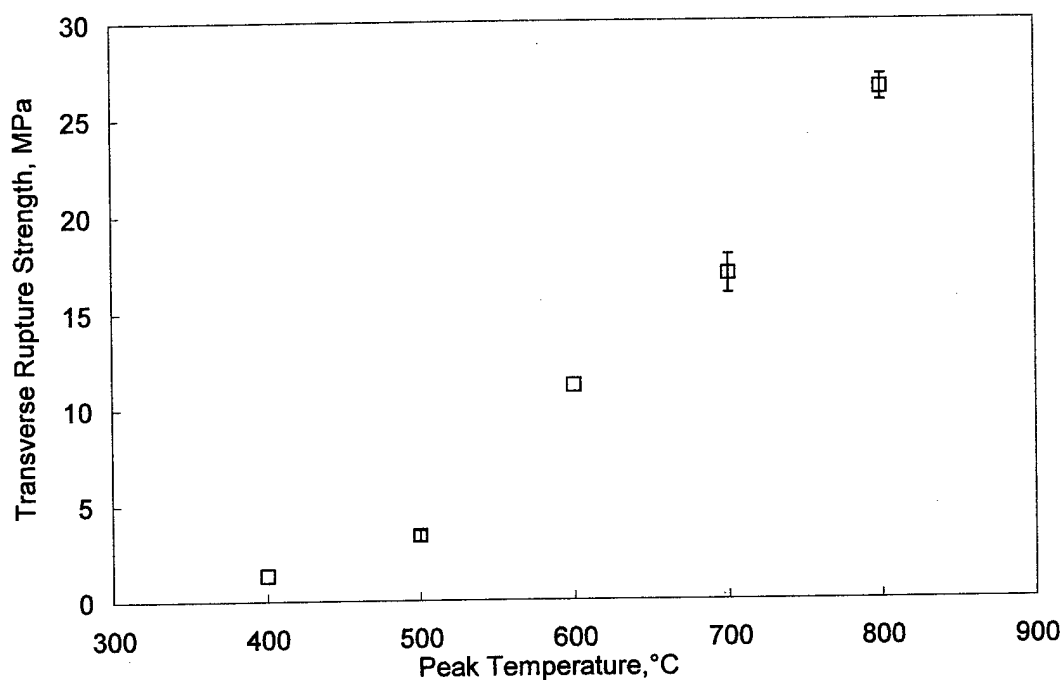


Figure 4.18: Room temperature transverse rupture strength of quasi-PIM samples as a function of sintering temperature. Samples were heated in flowing hydrogen at 10°C/min to peak temperature and quenched in water. Specimen initial fractional density was 0.55.

Room temperature transverse rupture strength results for injection molded bars are shown in Figure 4.19. The bars had been solvent debound and thermally debound to 100°C increments in the thermal debinding cycle. The green strength for the solvent-debound PIM material was 5.3 MPa, rising to 23 MPa at 200°C, and then dropping to 0.5 MPa at 425°C. Only after two hours at 425°C is there an increase in strength from 0.5 to 1.0 MPa. At higher temperatures, strength increases dramatically, reaching 98 MPa at 700°C. Shown with the strength measurements are the corresponding fractional densities

(measured dimensionally) with increasing peak sintering temperature. An increase in fractional density from 58 to 59% occurs between room temperature and 200°C, corresponding with the increase in transverse rupture strength.

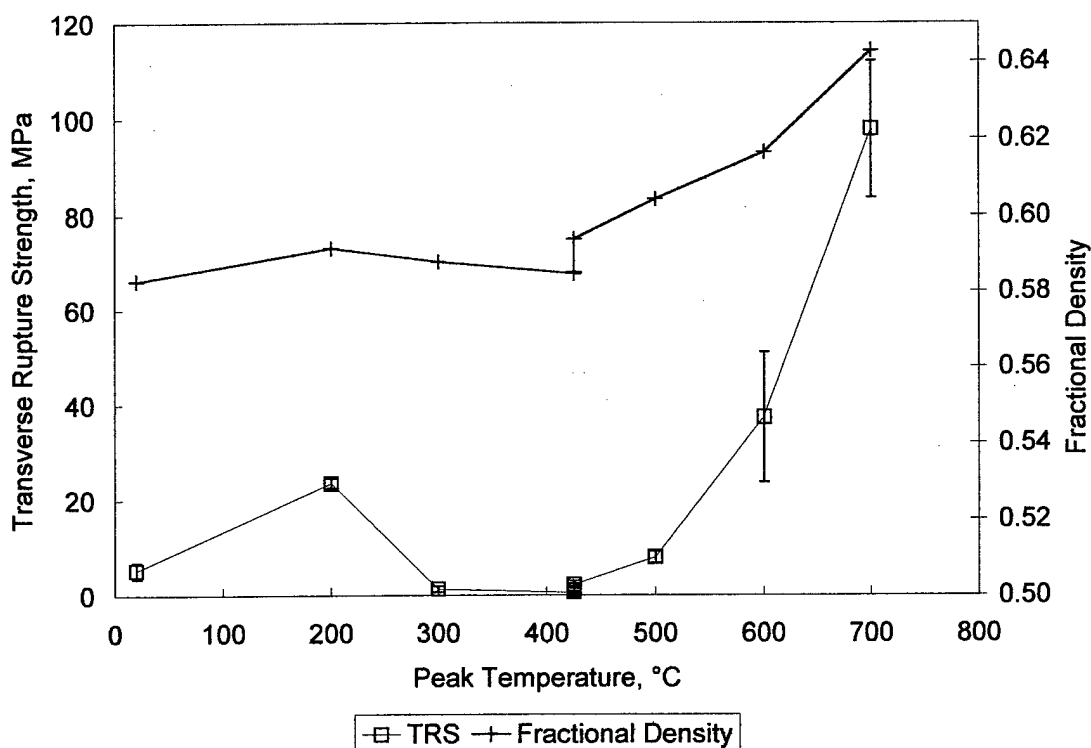


Figure 4.19: Room temperature transverse rupture strength and fractional density of PIM samples versus peak sintering temperature. Samples were heated at 2°C/min in flowing hydrogen to 425°C, held for 2 hours, and heated at 2°C/min to 700°C. Individual samples were removed at indicated peak temperature and air-cooled. Specimen initial fractional density was 0.58. Fractional density does not include binder mass.



### 4.2.3 Relationship between Thermal and Mechanical Results

A direct comparison of normalized thermal conductivity versus normalized transverse rupture results yields an indication of the relationship between the two properties. This comparison is shown for PIM air-quenched samples in Figure 4.20. Raw data for strength may be found in Appendix A, and thermal conductivity data are located in Appendix B. In Figure 4.20, room temperature transverse rupture strength data, normalized by wrought ultimate tensile strength of 360 MPa, are shown on a magnified scale, since the normalized values are on the order of  $10^{-3}$ . The data indicate an initial decrease in strength from 200 to 425°C, with a constant thermal conductivity. Stagnation in both

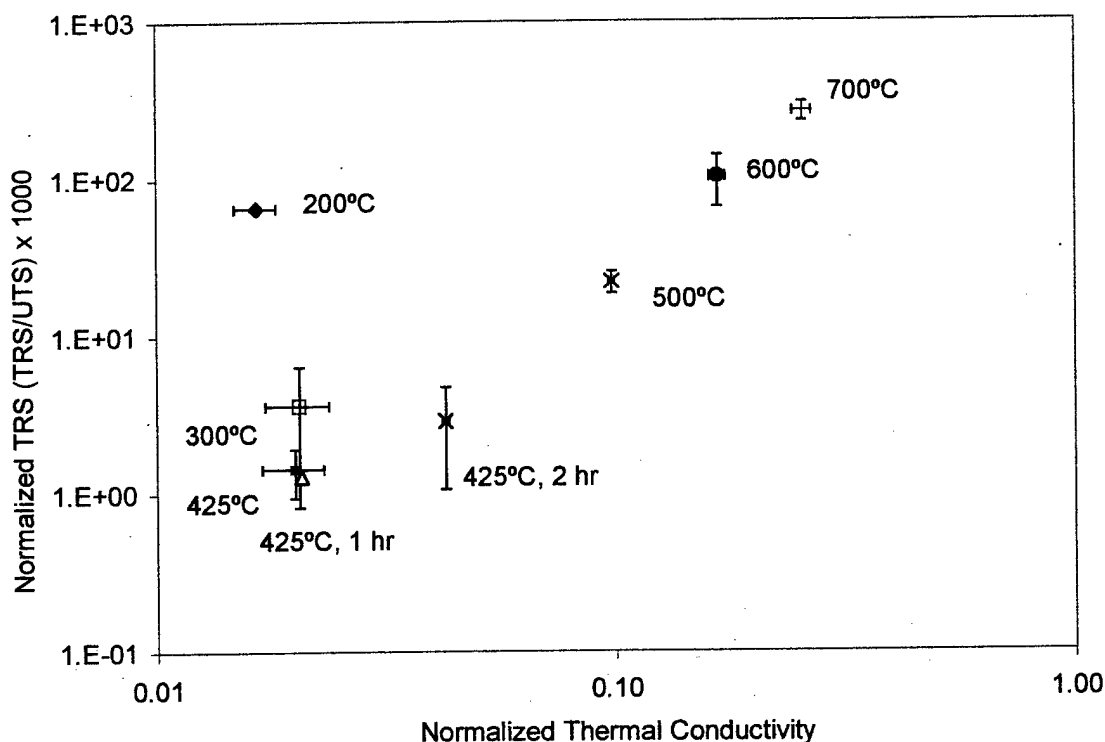


Figure 4.20: Normalized transverse rupture strength versus normalized thermal conductivity for PIM air-quenched samples. Error bars represent 95% confidence level.

strength and thermal conductivity development occurs through the first hour of the hold. After 2 hours at 425°C, thermal conductivity increases more rapidly than strength through 500°C, when both properties begin a significant increasing trend.

Similar data were compared for die-compacted samples, as shown in Figure 4.21. Although the relationship was not as clear between these two sets of data, a general trend of increasing values in both transverse rupture strength and thermal conductivity is apparent, with the exception of the 200°C samples.

The strength versus thermal conductivity data are also shown for the quasi-PIM

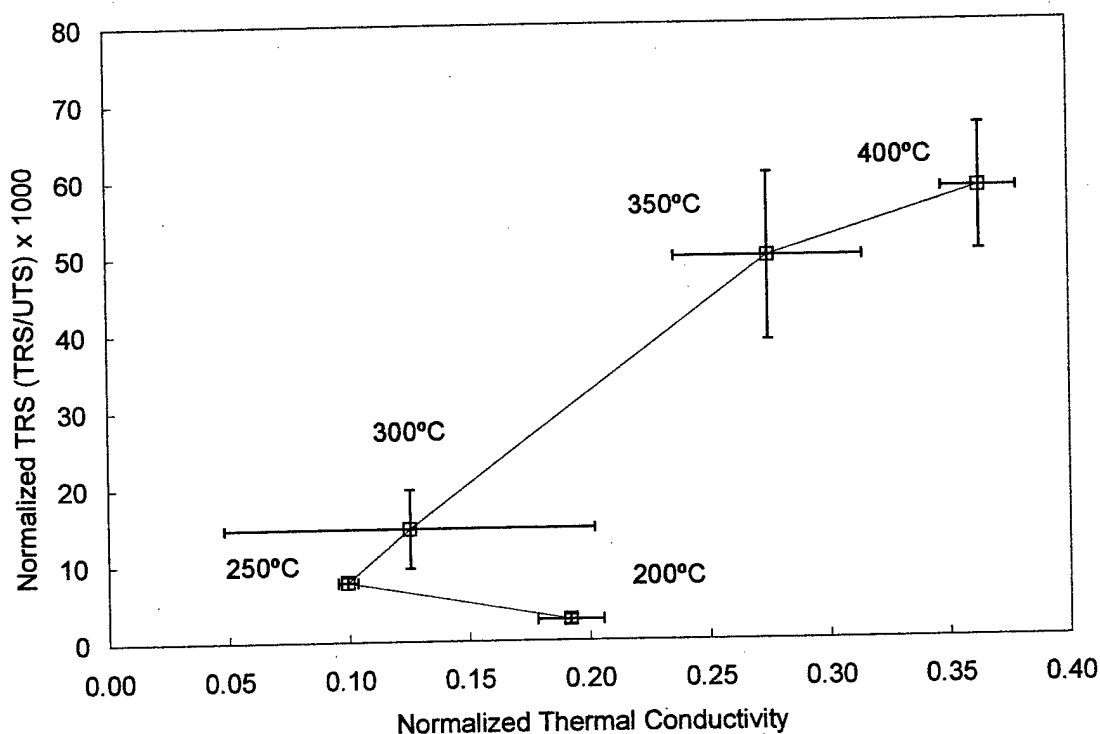


Figure 4.21: Normalized *in situ* transverse rupture strength versus thermal conductivity for die-compacted samples. Both properties are normalized by values of the wrought material at the test temperature. Error bars represent 95% confidence level.

material in Figure 4.22. These data are quite similar to the PIM data, although the initial values for both strength and thermal conductivity are higher.

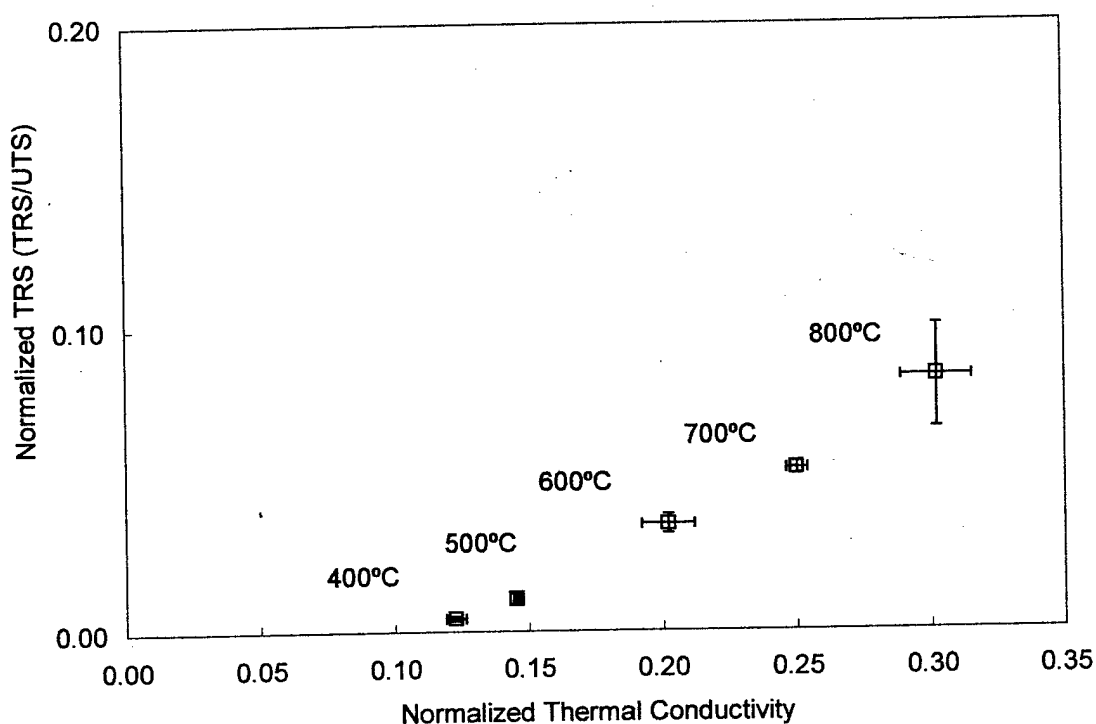


Figure 4.22: Normalized room temperature strength versus thermal conductivity for quasi-PIM samples. Samples were heated in flowing hydrogen at 10°C/min and quenched at 400°C, 500°C, 600°C, 700°C and 800°C. Original specimen fractional density was 0.55. Error bars represent 95% confidence level.

### 4.3 Secondary Results

A series of measurements were performed on the quasi-PIM transverse rupture bars prior to fracturing them in the three-point bend test. The goal was to explore meth-

ods complementing the strength and thermal conductivity evaluations. The quasi-PIM samples were the first samples manufactured in this research. As a result, they were sintered over a broader range of temperatures (400°C to 1100°C) than later tests with PIM and die-compacted materials, as the scope of research became more focused on initial stage sintering.

#### **4.3.1 Archimedes Density**

Densification with increasing sintering temperature is shown in Figure 4.23. Fractional density of the pre-sintered quasi-PIM material was 0.55, increasing to 0.64 by 700°C. The mean fractional density after sintering to 1100°C was 0.78.

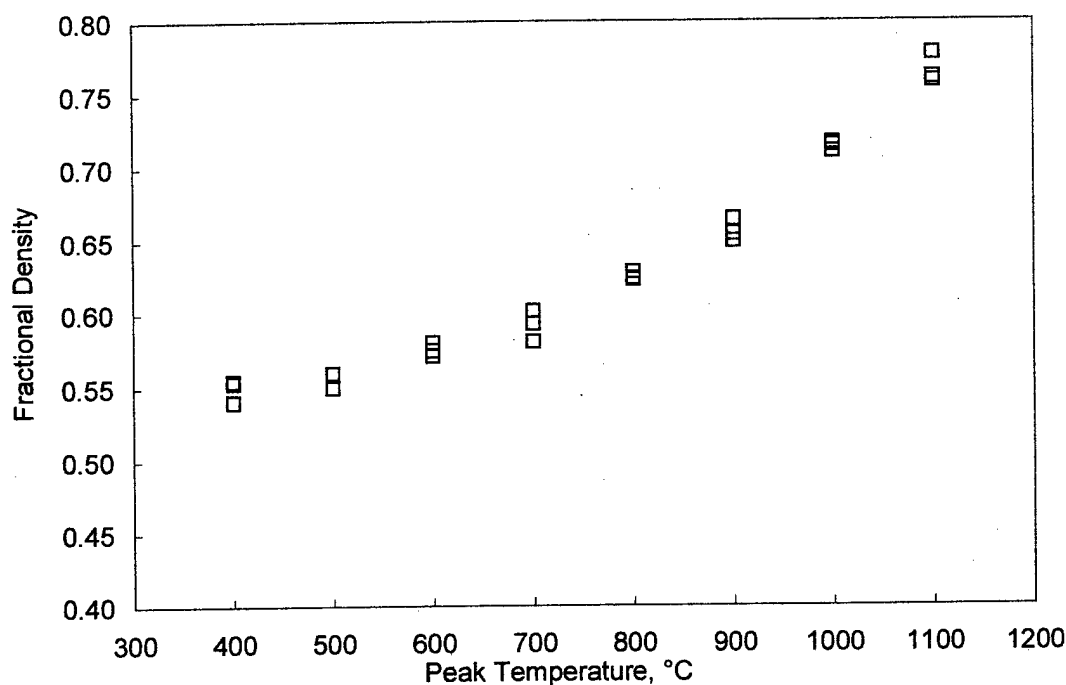


Figure 4.23: Fractional density versus sintering temperature for quasi-PIM material. Measurements made using Archimedes water immersion technique. Samples were sintered at 10°C/min in flowing hydrogen.

#### 4.3.2 Ultrasonic Evaluation

The quasi-PIM material was evaluated as described in Chapter 3.7 for time-of-flight values, from which sound velocity and Young's modulus were calculated. The evolution of room temperature Young's modulus versus sintering temperature is shown in Figure 4.24. The data were normalized by the room temperature value for Young's modulus, 214 GPa.<sup>101</sup> Raw data are located in Appendix C. The modulus shows a rela-

tively linear evolution with increasing sintering temperature, similar to that observed in strength and thermal conductivity evaluations.

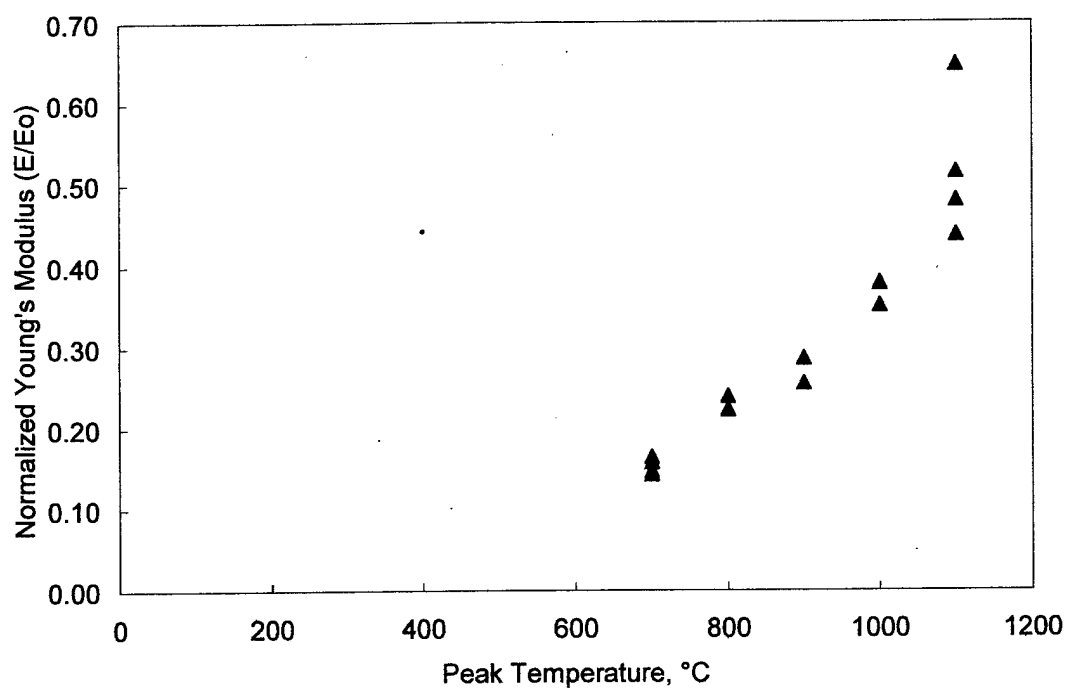


Figure 4.24: Room temperature longitudinal modulus versus sintering temperature for quasi-PIM material measured via ultrasonic evaluation

### 4.3.3 Resonant Frequency Evaluation

Elastic properties evaluated by resonant frequency evaluation as described in Section 3.8 yield results similar to those shown by ultrasonic evaluation. Young's modulus is shown in Figure 4.25 versus peak sintering temperature. Raw data are located in Appendix D.

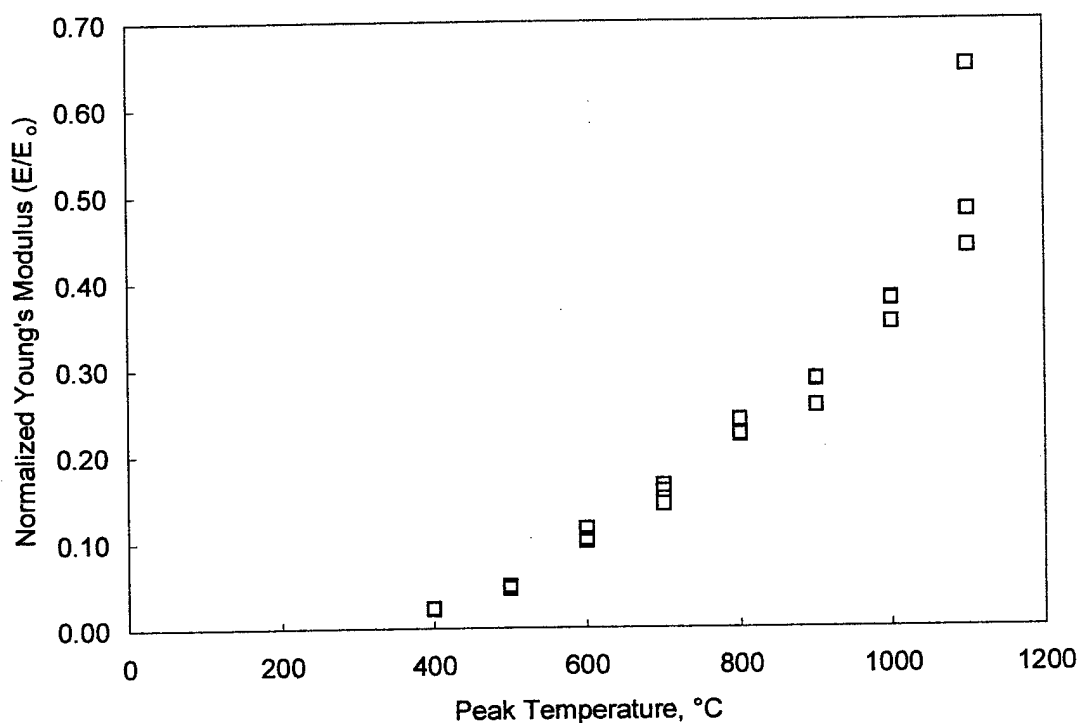


Figure 4.25: Young's modulus as a function of sintering temperature in quasi-PIM material as measured by resonant frequency inspection.

Shear modulus results are shown in Figure 4.26. Torsional resonant frequency measurements were limited by the configuration and density of the specimens. Samples sintered to temperatures above 800°C had expected fundamental resonant frequencies above the upper limit for the test equipment. This was confirmed by measurement of the three 900°C samples, with no torsional resonant frequency observed in the working range of zero to 25 kHz. A linear trend is shown with increasing sintering temperature, with a slightly larger increase with increasing temperature compared to Young's modulus (24% vs. 21% that of solid nickel for the 800°C samples).

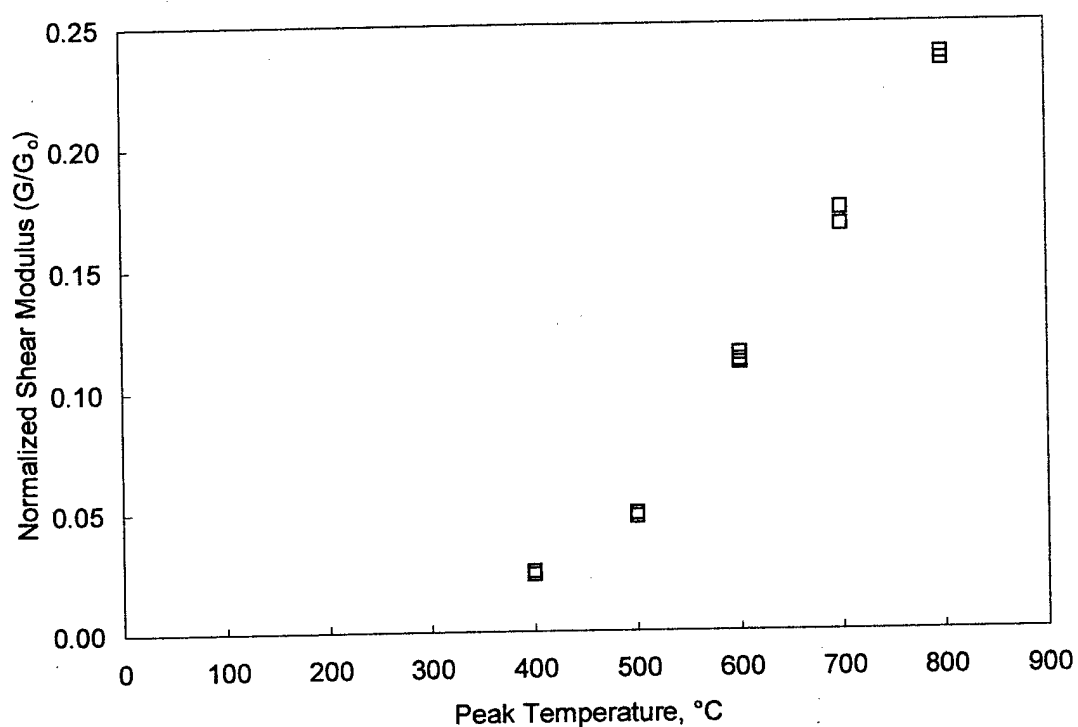


Figure 4.26: Shear modulus versus sintering temperature for quasi-PIM material, as measured by resonant frequency inspection.

A comparison of Young's modulus as measured by ultrasonic evaluation and resonant frequency evaluation is shown in Figure 4.27. Measured values from both evaluations are quite similar.



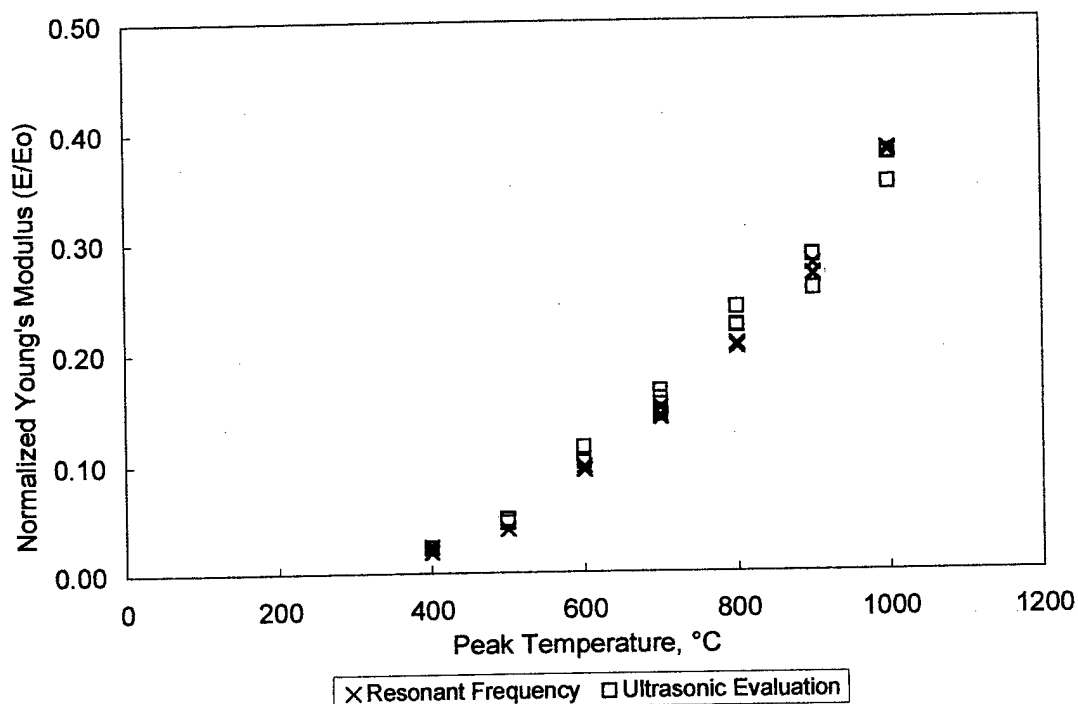


Figure 4.27: Comparison of room temperature Young's modulus data versus peak sintering temperature for quasi-PIM material. Measurements made via ultrasonic and resonant frequency evaluations.

#### 4.3.4 Electrical Conductivity Testing

Electrical conductivity as a function of sintering temperature was evaluated for the quasi-PIM materials. Raw data are located in Appendix E. Room temperature tests revealed a linear trend with increasing sintering temperature, as shown in Figure 4.28.

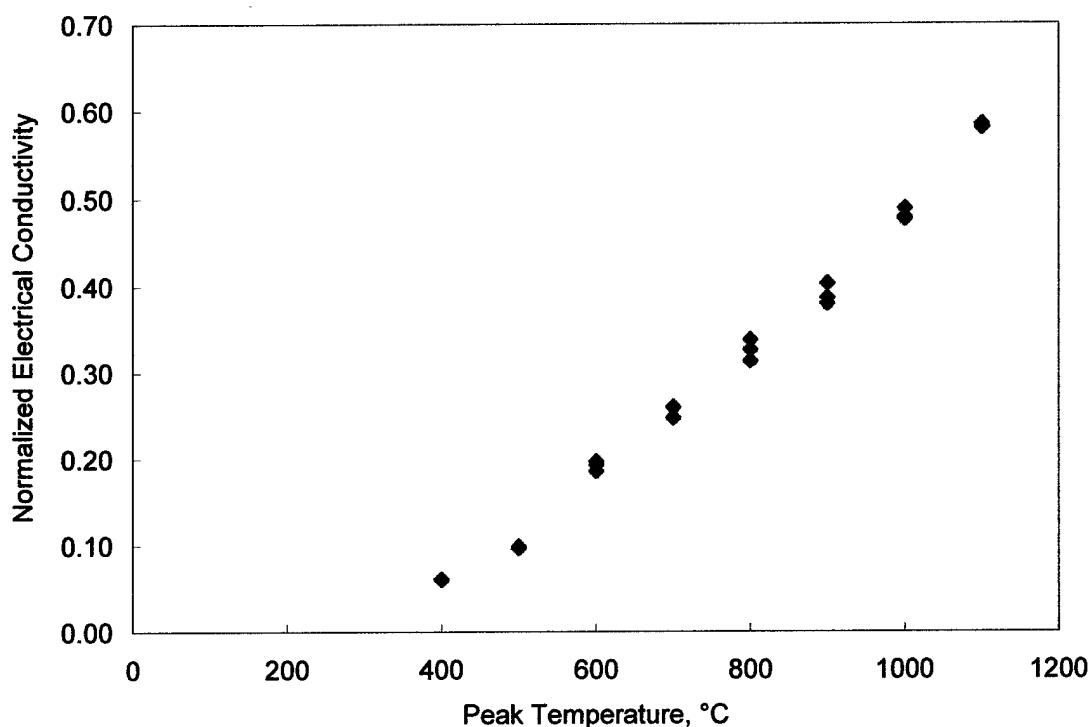


Figure 4.28: Room temperature electrical conductivity as a function of sintering temperature for quasi-PIM nickel samples.

Electrical conductivity as calculated by the Wiedemann-Franz relationship, Equation 2.13, is compared to the measured electrical conductivity values in Figure 4.29. Although both measured and calculated values show linear trends, the measured values show a greater increase in relative electrical conductivity with increased sintering temperature than the values calculated from measured thermal conductivity. Calculated values extend up to 800°C, the maximum temperature at which thermal conductivity was measured for quasi-PIM materials.

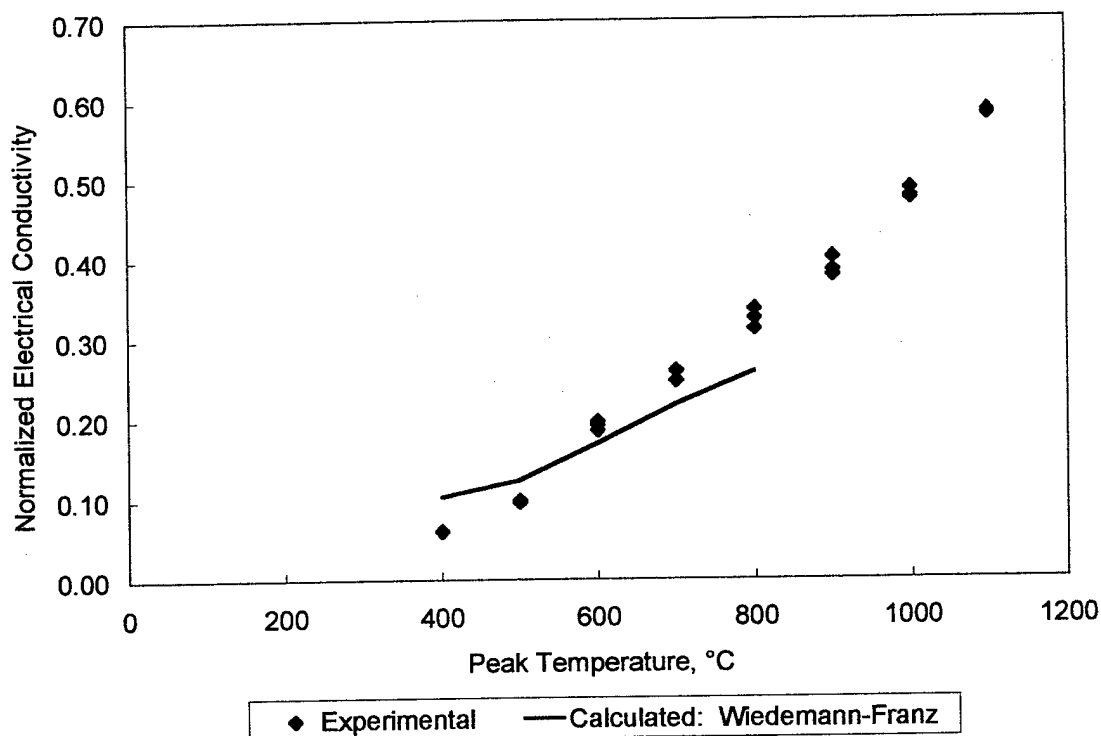
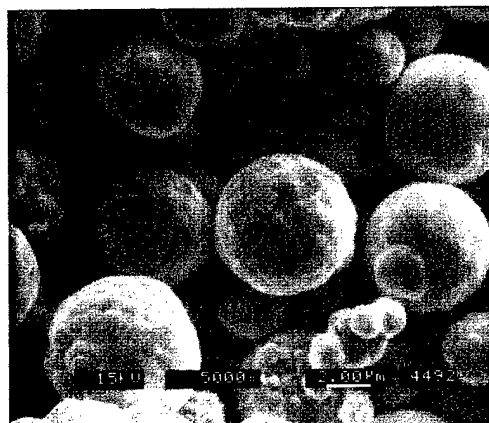


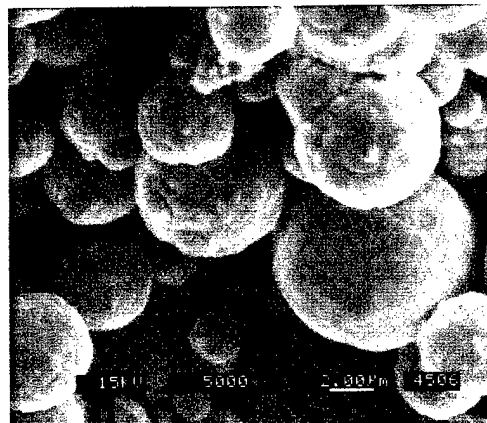
Figure 4.29: Room temperature electrical conductivity for quasi-PIM samples, measured versus calculated via the Wiedemann-Franz ratio

#### 4.3.5 Microstructural Observations

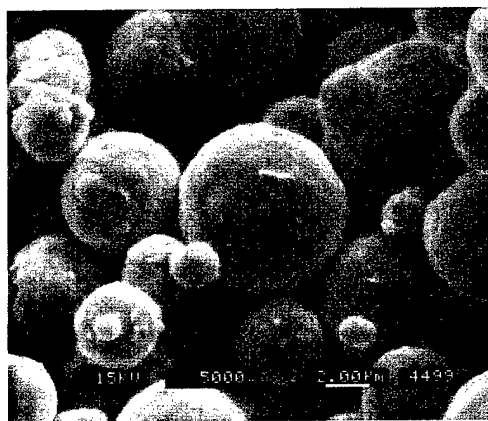
Scanning electron microscope images were used to qualitatively assess interparticle bonds at fracture surfaces. Ruptured bonds are visible as light spots on particle faces. A series of SEM images of the quasi-PIM material fracture surfaces at increasing temperatures is shown in Figure 4.30. An image of the as-received powder is included for comparison of surface appearance.



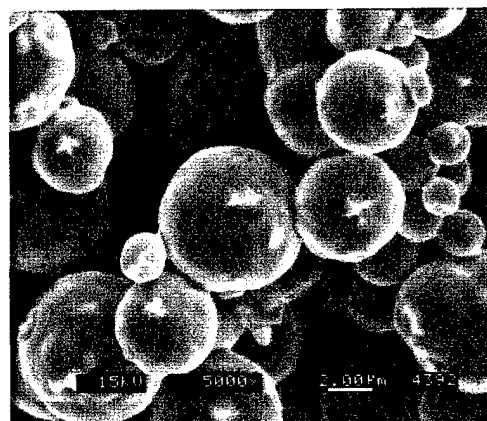
As-received powder



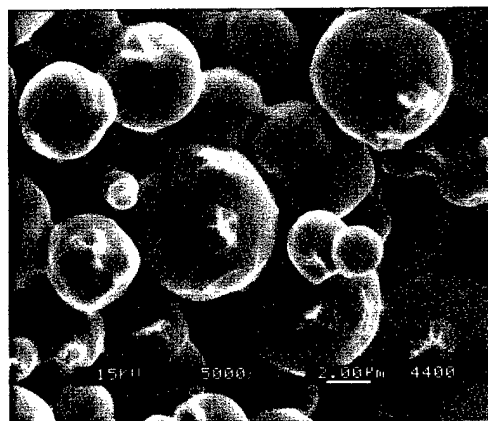
400 °C



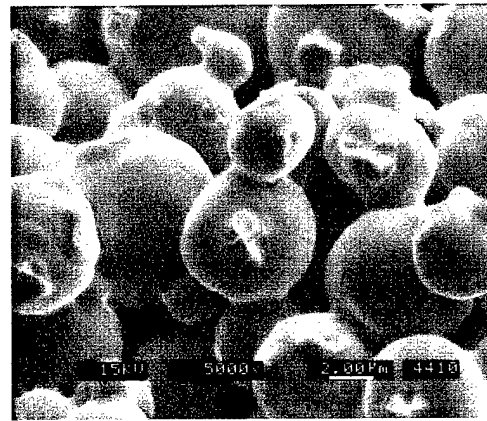
500 °C



600 °C



700 °C



800 °C

Figure 4.30: SEM images of as-received powder and fracture surfaces for quasi-PIM material at increasing sintering temperatures.

Particle surface texture remains constant until 600°C, where smoothing of the surface is evident. This smoothing continues at higher temperatures.

SEM images of the PIM material fracture surface are shown in Figure 4.31. Polymer at the interparticle contacts was visible in the 200°C sample, but was no longer visible after a hold at 425°C for one hour. No ruptured bonds were visible until after 2 hours at 425°C. These bonds became larger and more plentiful at increasing temperatures, although development lagged behind that observed in the quasi-PIM fracture surfaces.

A qualitative assessment of neck size ratio was made through SEM observation. The fracture surface of each sample was observed and the diameters of ruptured bonds were measured along the longest dimension (X). These neck size measurements were normalized by the median particle size. Since light scattering analysis results are based on a volume, or weight, distribution, the median particle size typically reported is with respect to this distribution, which is more heavily influenced by the coarser particles in the powder.<sup>1</sup> To correct this bias, particle size analysis results were converted to a population distribution, and the median value from this distribution was used. The median value for a population-based distribution was 4.22  $\mu\text{m}$ . Measured neck size for both quasi-PIM and PIM materials are shown in Figure 4.32. The measured neck size ratio for the quasi-PIM material in the presintered condition was 0.13.

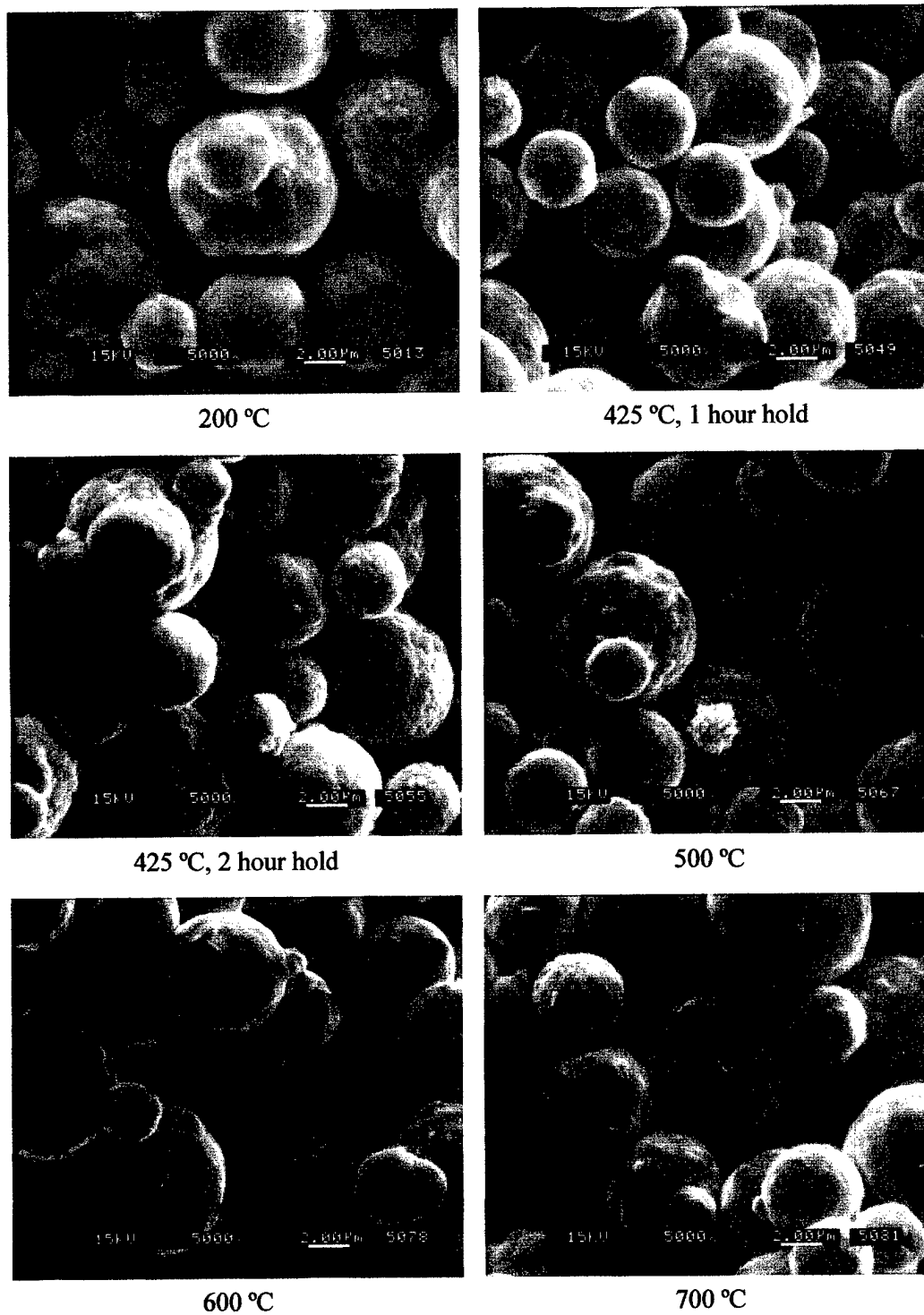


Figure 4.31: SEM images of as-received powder and fracture surfaces for PIM material at increasing sintering temperatures.

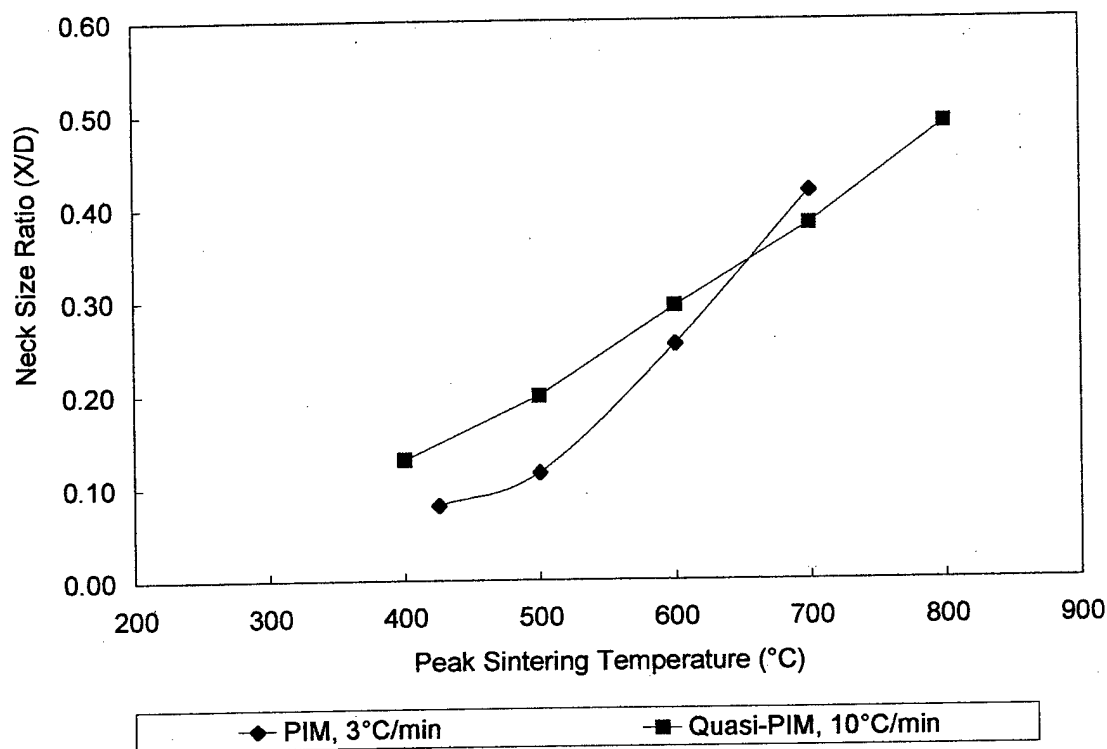


Figure 4.32: Neck size ratio versus sintering temperature for quasi-PIM and PIM materials. Measurements of neck size were made via SEM, and normalized against a median particle size with respect to a population distribution.

The microstructural evolution of the PIM material with sintering temperature is illustrated in Figure 4.33. The samples are mounted in epoxy, polished and etched with Fry's reagent. At lower temperatures, 425°C and 500°C, many of the spherical particles have pulled out of the epoxy during polishing, leaving visible holes. The large amount of pullout limited the analysis of connectivity between the particles using image analysis techniques, particularly at the lower temperatures. At higher temperatures, more interparticle contact is apparent, with fewer pullouts.

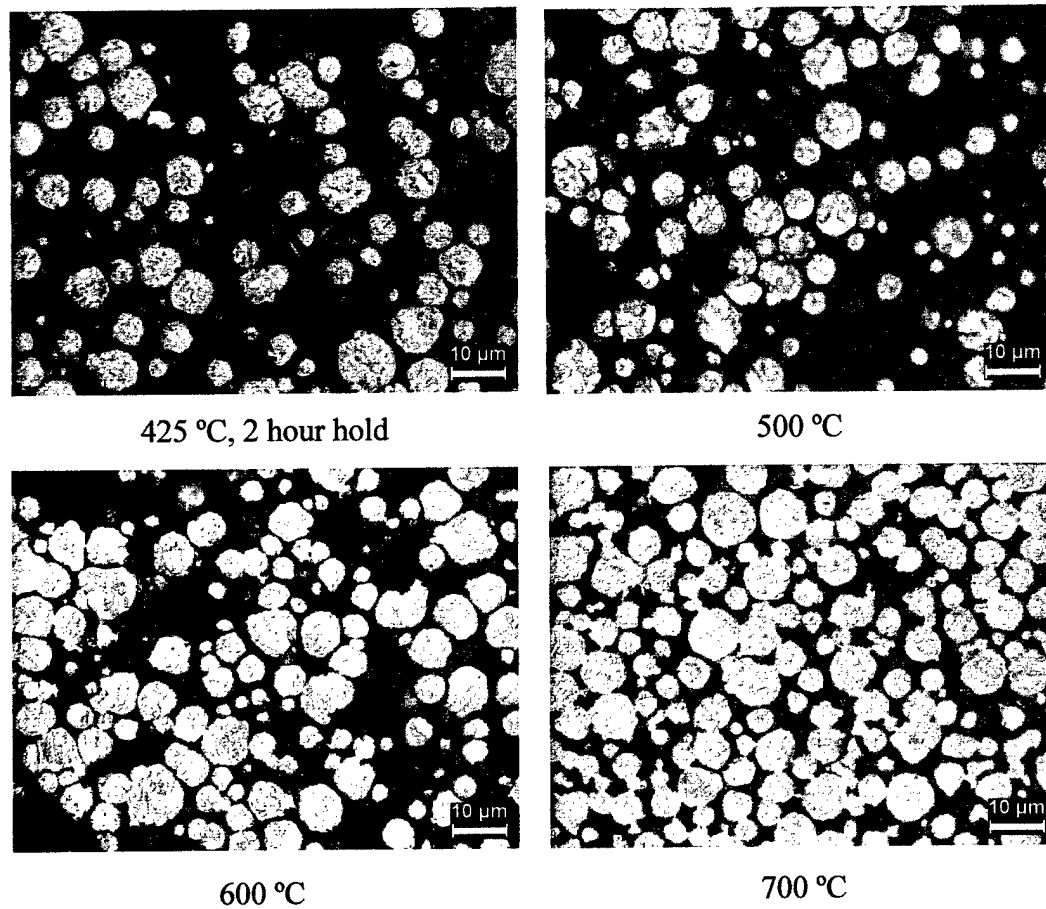


Figure 4.33: Microscopy of PIM air-quenched TRBs at increasing sintering temperatures. Samples were etched with Fry's reagent.

Microscopy images of the quasi-PIM materials from 400°C to 800°C are shown in Figure 4.34. These samples are also etched to qualitatively show the development of the grain structure with increasing temperature.



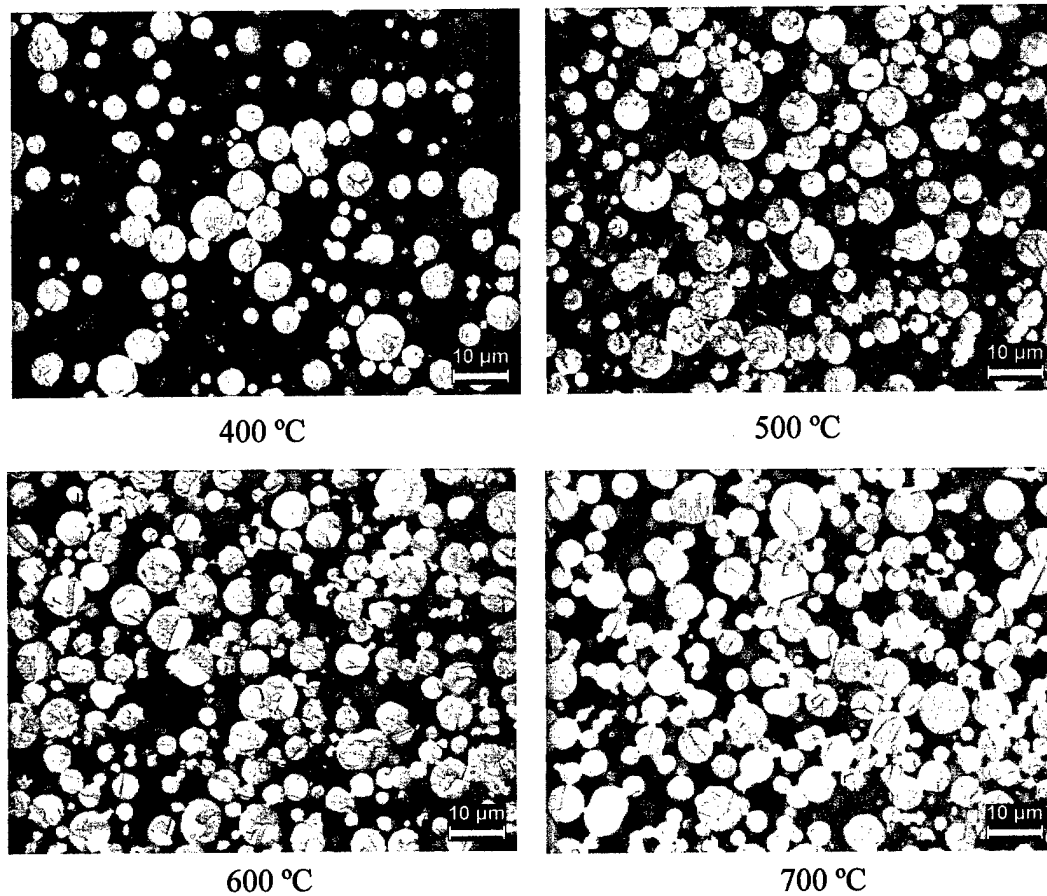


Figure 4.34: Microscopy of quasi-PIM water-quenched TRBs at 400°C through 700°C. Samples were etched with Fry's reagent.

Higher temperature samples, 900°C to 1100°C, are shown in Figure 4.35. With increasing temperatures, twin boundaries, shown as parallel lines within a particle, become more evident.

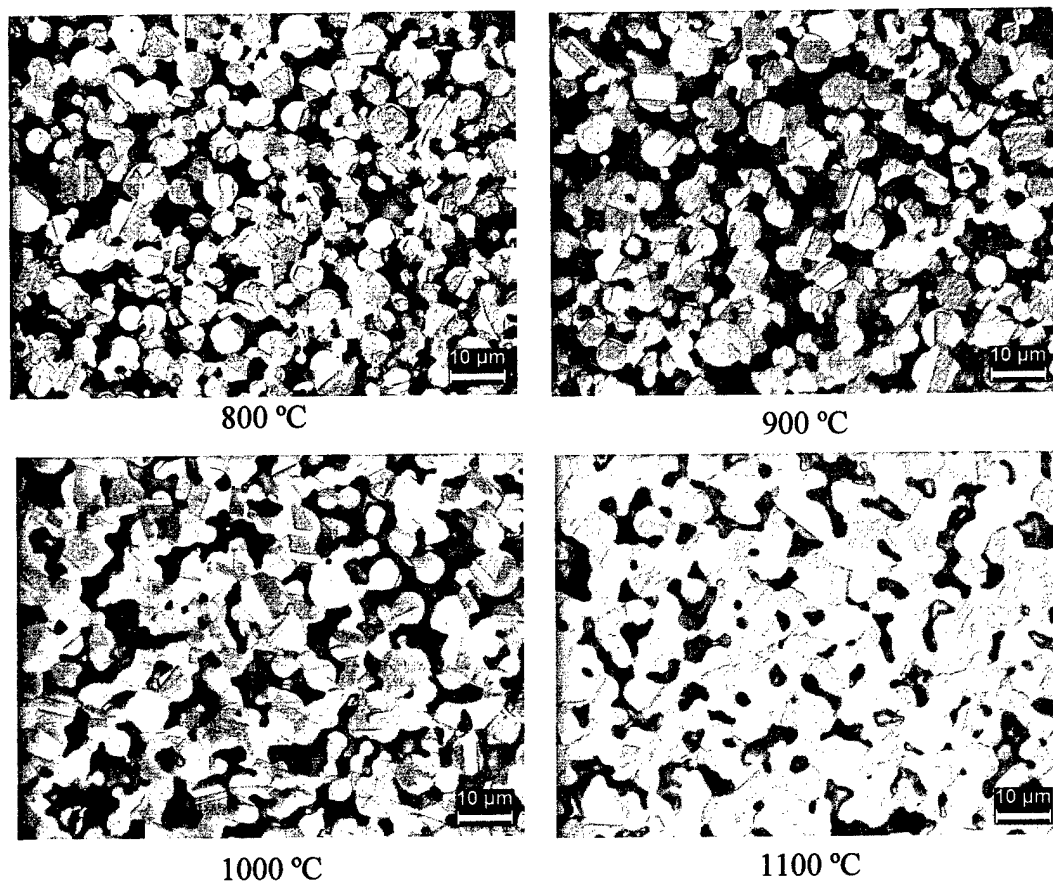


Figure 4.35. Microscopy of quasi-PIM water-quenched TRBs at 800°C through 1100°C. Samples etched with Fry's reagent.

## **Chapter 5**

### **Modeling**

This chapter describes the development of a model that can be used to predict thermal conductivity and mechanical strength of a sample system under a variety of time-temperature profiles. The chapter begins with a description of the physical model of a powder system undergoing initial stage sintering. The physical model is updated via computer simulation of neck growth, which is described in the second section. The integration of the physical model with the computer simulation, and the predicted evolution of thermal conductivity are described in the third section.

#### **5.1 Physical Description of Circuit Model**

The resistance element model described in Chapter 2 is the basis for the physical model used in this work. The model assumes that the thermal behavior of the system is dominated by the interparticle contact, which has a much smaller cross-sectional diameter than the particle diameter. The material is therefore represented with a series of resistance elements, one modeling the bulk of the particle and one modeling the interface. One-dimensional heat flow through the material is assumed. A simple cubic unit cell structure was chosen as a starting point, based on its ease for modeling one-dimensional heat flow, and its packing density of 52%, which was fairly close to the quasi-PIM mate-

rial's fractional density of 55%, and the injection molded material's fractional density of 58%. Interparticle contacts were modeled as cylinders stacked end-to-end, with neck size (cylinder diameter) increasing as sintering occurred. The bulk of the spherical particle of diameter 'D' away from the cylindrical neck was modeled as a square layer of D x D cross-section and 0.25D thickness. A sketch of this configuration is shown in Figure 5.1.

The overall effective thermal conductivity of the material was calculated by examining heat transfer within the model cell. Three mechanisms of heat transfer were considered: convection, radiation, and conduction.

Previous studies have demonstrated that convection may be ignored for porous media with pore sizes smaller than 5 mm.<sup>49,106</sup> A pore size on the same order of magnitude as the particle size was assumed, supported by a qualitative inspection of microscopy. With a particle size three orders of magnitude smaller than the 5 mm threshold, convection was assumed negligible.

Conduction was considered through the solid and through the gas in the pores. As shown in Figure 5.1, the model cell is comprised of two solid cylindrical "necks" in contact, with a solid interfacial layer between the two. The remainder of the particle bulk is modeled as two "shoulders" per particle. Shoulders of adjacent particles are separated by pore space, filled with gas. Each segment of the model was described as circuit of thermal resistors, analogous to an electrical circuit. The resistance of each segment was described by Equation 2.29:

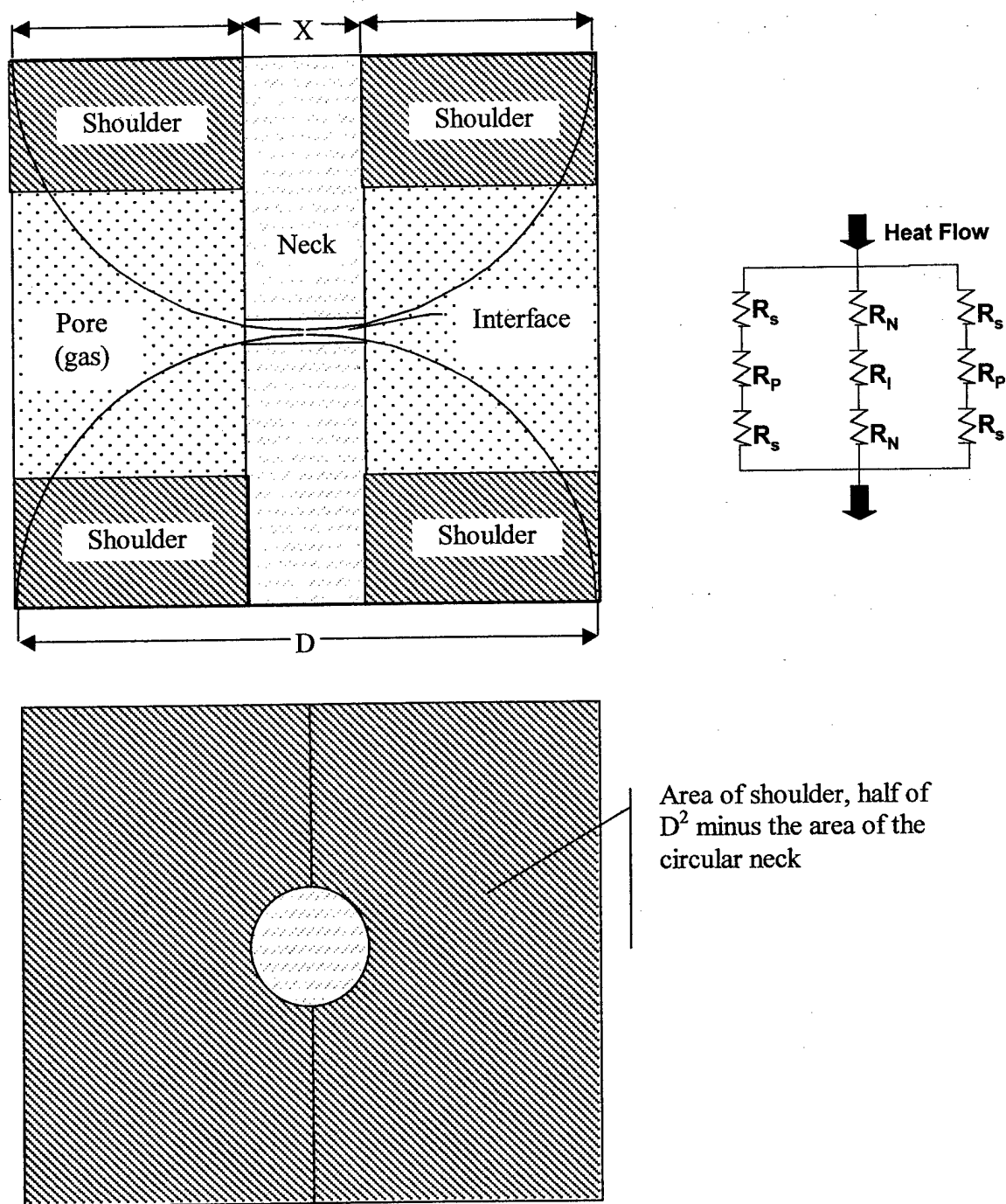


Figure 5.1: Resistance element model cell for one-dimensional heat flow in simple-cubic packed structure

$$R = \frac{L}{\kappa A} \quad 2.29$$

where  $L$  is the length of the segment,  $A$  is the cross-sectional area, and  $\kappa$  is the thermal conductivity of the solid or gas.

The neck-interface-neck portion of the model,  $R_A$ , was a series of resistors, which were added together as shown in Equation 5.1:

$$R_A = R_n + R_i + R_n \quad ( 5.1 )$$

where  $R_n$  is the resistance in one neck element, and  $R_i$  is the resistance in the interface element. The remainder of the unit cell is divided into halves represented as the shoulder-pore-shoulder structure, modeled as two identical series circuits,  $R_B$ , shown in Equation 5.2:

$$R_B = R_s + R_p + R_s \quad ( 5.2 )$$

where  $R_s$  and  $R_p$  are the resistances of the shoulder and pore, respectively. The effective thermal resistance of the unit cell ( $R_{eff}$ ) is described by three summed resistors in parallel, shown in Equation 5.3:

$$\frac{1}{R_{eff}} = \frac{1}{R_A} + \frac{1}{R_B} + \frac{1}{R_B} \quad ( 5.3 )$$

Since the effective conductivity is the reciprocal of the effective resistivity, Equation 5.3 represents the effective conductivity of the material, and can be shown as Equation 5.4:

$$\kappa_{eff} = \frac{1}{R_A} + \frac{1}{R_B} + \frac{1}{R_B} \quad ( 5.4 )$$

Revisiting Equation 5.1, which defines  $R_A$ , the reciprocal form is shown as Equation 5.5:

$$\frac{1}{R_A} = \frac{1}{2R_n + R_i} \quad ( 5.5 )$$

where  $R_n$  is the resistance of the cylindrical neck element, shown in Equation 5.6:

$$R_n = \frac{L_n}{\kappa_n A_n} = \frac{\left[ \frac{D - L_i}{2} \right]}{\kappa_s \left( \frac{\pi}{4} \right) X^2} \quad ( 5.6 )$$

where  $\kappa_s$  is the conductivity of the solid metal at temperature and  $L_i$  is the thickness of the interface. Similarly, the resistance of the interface layer,  $R_i$ , is shown by Equation 5.7:

$$R_i = \frac{L_i}{\kappa_i A_i} = \frac{\left[ \frac{L_i}{2} \right]}{\kappa_i \left( \frac{\pi}{4} \right) X^2} \quad ( 5.7 )$$

Substituting Equations 5.6 and 5.7 into Equation 5.5 yields Equation 5.8:

$$\frac{1}{R_A} = \frac{\kappa_i \kappa_s \pi X^2}{4\kappa_i (D - L_i) + 2\kappa_s L_i} \quad ( 5.8 )$$

Thermal conductivity of the solid metal is a function of atomic make-up, micro-structure, and temperature. Handbook values of thermal conductivity for wrought nickel as a function of temperature were used in the basic model, and are included in Appendix F.<sup>107</sup> The interface resistance element was included to capture contact resistance due to surface oxides, binder products, contaminants, and surface roughness. The interface was modeled as a 0.01D thick layer of NiO ( $\kappa=14$  W/(m·K) at 100°C)<sup>108</sup> at the beginning of the modeling cycle, shrinking to the width of a grain boundary at higher temperatures.

The resistance element  $R_B$ , comprised of the shoulders and pore, can be shown in the same form as Equation 5.5, incorporating resistance of two shoulder elements, and the resistance of the pore. The resistance of the shoulder element is described by Equation 5.9:



$$R_s = \frac{L_s}{\kappa_s A_s} = \frac{\frac{D}{4}}{\frac{\kappa_s}{2} \left[ D^2 - \frac{\pi}{4} X^2 \right]} \quad ( 5.9 )$$

The resistance element modeling the pore incorporates conductivity in the gas phase, as well as radiation across the pore. Preliminary calculations of conductivity across the pore considering effective conductivity contributions from conduction and radiation were made to determine if contributions from these two mechanisms were significant, or negligible. Thermal conductivity of gas is a function of atomic size, pressure, and temperature. Pressure was assumed constant at 101 kPa (atmospheric) for all process gasses, therefore conductivity for a given process gas is solely a function of temperature. Effective conductivity of the neck element, given an initial neck size ratio of 0.01, was compared to the effective conductivity of the pore due to gas conductance and radiation. Equation 5.8 was used to calculate effective conductivity of the neck circuit, with thermal property values for 100°C ( $\kappa_{ni}=82.9$  W/(m·K),  $\kappa_i=14$  W/(m·K)). The modeled effective conductivity of the neck circuit is  $8.14 \times 10^{-3}$  W/m/K. Conductivity across the gas, using the conductivity of nitrogen (the test atmosphere) at 100°C ( $\kappa_g=0.032$  W/m/K) is essentially equal to the gas alone, since the neck area is so small if  $X/D=0.01$ . This implies that the conductivity of the gas is not negligible at very small neck sizes, but likely becomes so with increasing neck size.

Effective conductivity due to radiation across the gas in the pore was described by Equation 2.29 as:

$$\kappa_{rad} = 4f\phi\sigma_B T^3 D_p \quad 2.29$$

where  $f$  is a dimensionless pore shape factor,  $\phi$  is the dimensionless emissivity of the pore walls, and  $D_p$  is the diameter of the pore<sup>109</sup>. For these calculations,  $f$  was taken as 1, and  $\phi$  was equal to the value for oxidized nickel, 0.47.<sup>93</sup>  $D_p$  was taken as the distance from one shoulder across the pore to the facing shoulder, a distance of  $0.5D$ , or  $3.5 \mu\text{m}$ . At  $100^\circ\text{C}$ , the effective conductivity contribution is  $1.01 \times 10^{-5} \text{ W}/(\text{m}\cdot\text{K})$ , two orders of magnitude smaller than the contribution of the neck circuit at its lowest neck size values. At  $600^\circ\text{C}$ , the effective conductivity contribution is  $2.72 \times 10^{-4} \text{ W}/(\text{m}\cdot\text{K})$ , versus a predicted contribution from the neck of  $3.62 \text{ W}/(\text{m}\cdot\text{K})$ . Based on this assessment, radiation contributions were regarded as negligible.

Equation 2.24 is again substituted for the resistance elements, yielding Equation 5.10:

$$R_p = \frac{L_p}{A_p \kappa_g} \quad (5.10)$$

In this case,  $L_p$  is the distance between the pore walls,  $0.5D$ , and  $A_p$  is identical to the shoulder area from Equation 5.9. Combining Equations 5.9 and 5.10 results in the relation shown in Equation 5.11:

$$R_p = \frac{\frac{D}{2}}{\frac{1}{2}\kappa_g \left[ D^2 - \left( \frac{\pi}{4} \right) X^2 \right]} \quad (5.11)$$

Following the example of Equation 5.5, the combination of Equations 5.9 and 5.11 creates a description of  $1/R_B$  shown in Equation 5.12:

$$\frac{1}{R_B} = \frac{1}{\frac{D}{\kappa_s \left[ D^2 - \frac{\pi}{4} X^2 \right]} + \frac{D}{\kappa_g \left[ D^2 - \frac{\pi}{4} X^2 \right]}} = \frac{\kappa_s \kappa_g \left( D^2 - \frac{\pi}{4} X^2 \right)}{D (\kappa_s + \kappa_g)} \quad (5.12)$$

Equations 5.8 and 5.12 are then substituted in Equation 5.4 to represent effective thermal conductivity for the model, shown in Equation 5.13

$$\kappa_{eff} = \frac{\kappa_i \kappa_n \pi X^2}{4\kappa_i (D - L_i) + 2\kappa_n L_i} + \frac{\kappa_s \kappa_g \left[ D^2 - \frac{\pi}{4} X^2 \right]}{D (\kappa_s + \kappa_g)} \quad (5.13)$$

Neck diameter can be normalized by the particle diameter,  $D$ , to create a common term between strength and conductivity, giving Equation 5.14

$$\kappa_{eff} = \frac{\kappa_i \kappa_n \pi \left( \frac{X}{D} \right)^2 D^2}{4\kappa_i (D - L_i) + 2\kappa_n L_i} + \frac{\kappa_s \kappa_g \left[ D^2 - \frac{\pi}{4} \left( \frac{X}{D} \right)^2 D^2 \right]}{D (\kappa_s + \kappa_g)} \quad (5.14)$$

Since the model is based on a unit cell, which in turn represents the particle diameter,  $D$  is set to unity. Using handbook values for solid and gas conductivities leaves two unknowns on the right hand side of Equation 5.14, the thickness of the interface,  $L_i$ , and neck diameter,  $X$ .  $L_i$  is modeled as a linear function with temperature, and  $X/D$  will be generated via computer simulation of initial stage sintering.

## 5.2 Computer Simulation of Neck Growth

A computer simulation based on the approach described by Hwang<sup>11</sup> and Dubois<sup>12</sup> was used to generate neck size for various sintering profiles. The program, SintWin 2.3, is written in Fortran code and is included as Appendix G. SintWin is an atomistic model based on two spheres in contact, with a circular contact area. The initial stage sintering equation as described in Chapter 2 is used to model each of the sintering mechanisms. Values for the sintering parameters described in Table 2.1 are input in the simulation. The output of the simulation is divided into densification and non-densification mechanisms. Specifically, the results are shown as surface area reduction, linear shrinkage, and the neck size ratio. Literature-based input values<sup>2</sup> and powder characteristics for the nickel system are shown in Table 5.1.

Table 5.1: Sintering parameters for 4SP-10 nickel powder system

Sintering Parameter	Value
Theoretical Density ( $\text{kg/m}^3$ )	8,900
Atomic Volume ( $\text{m}^3$ )	$7.99 \times 10^{-30}$
Melting Temperature (K)	1726
Volume Diffusion Frequency Factor ( $\text{m}^2/\text{s}$ )	0.00014
Activation Energy for Volume Diffusion (kJ/mol)	276
Surface Diffusion Frequency Factor ( $\text{m}^3/\text{s}$ )	$5.0 \times 10^{-12}$
Activation Energy for Surface Diffusion (kJ/mol)	164
Grain Boundary Diffusion Frequency Factor ( $\text{m}^3/\text{s}$ )	$4 \times 10^{-16}$
Activation Energy for Grain Boundary Diffusion (kJ/mol)	108
Vapor Pressure (MPa)	$3.10 \times 10^{-13}$
Activation Energy for Evaporation (kJ/mol)	376
Surface Energy ( $\text{J/m}^2$ )	1.80
Particle Diameter ( $\mu\text{m}$ )	7
Green Density ( $\text{kg/m}^3$ )	5164

SintWin does not account for thermal expansion, so thermal expansion was calculated separately, and added to shrinkage results. An effective coefficient of thermal expansion for the porous material is based on Equation 5.15:<sup>1</sup>

$$C_s = C_o \left( \frac{\rho_s}{\rho_o} \right)^{1/3} \quad ( 5.15 )$$

where  $C_s$  and  $C_o$  are the dimensionless coefficient of thermal expansion for the porous and wrought material, respectively. Density was calculated using the shrinkage generated by the computer simulation (assuming constant mass), as shown in Equation 5.16:<sup>1</sup>

$$\rho_s = \frac{\rho_g}{\left( 1 + \frac{\Delta H}{H} \right)^3} \quad ( 5.16 )$$

where  $\rho_s$  and  $\rho_g$  are the sintered and porous densities (or fractional densities), and  $\Delta H/H$  is the linear shrinkage (a negative value for shrinkage, as described in Chapter 4).

The computer-simulated shrinkage and neck size were compared to experimental observations, and sintering parameters were adjusted until a match with observed behavior was achieved. The initial comparison was made to the experimental shrinkage observed in the dilatometry of loose powder, tapped in a crucible, sintered at 10°C/min to 1100°C in flowing hydrogen. Density was assumed to be equivalent to the measured tap

density for the powder, a fractional density of 0.58, or  $5164 \text{ kg/m}^3$ . An example of this iterative process, using the lower temperature data, is shown in Figure 5.2.

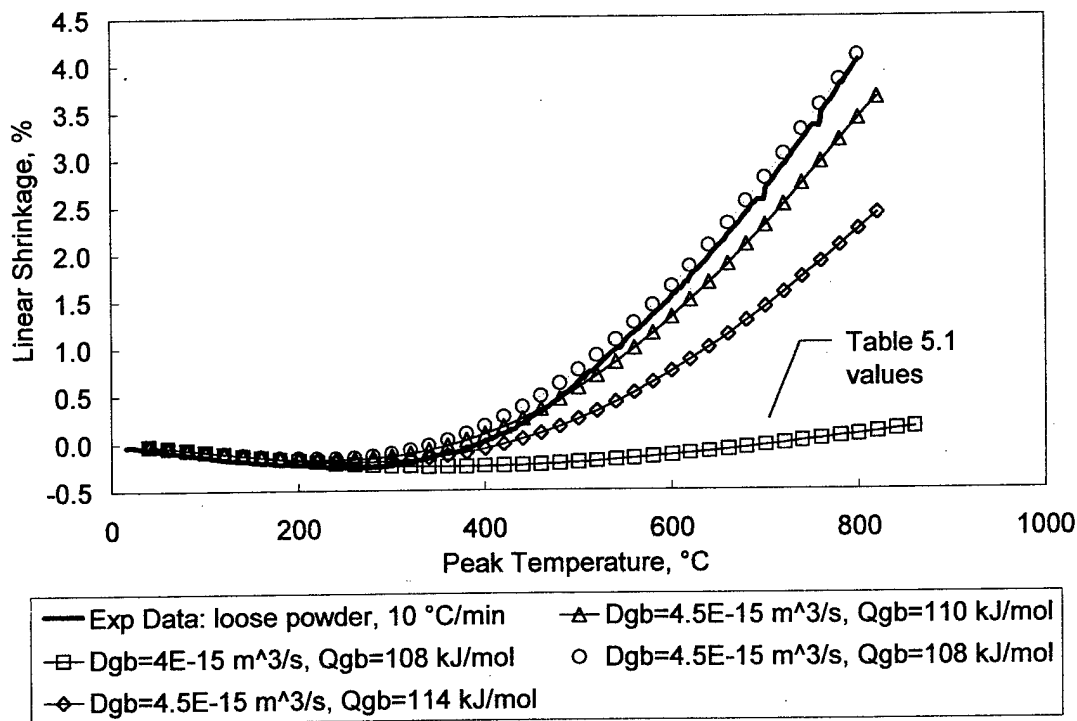


Figure 5.2: Computer simulated linear shrinkage iteration, loose nickel powder heated at  $10^\circ\text{C/min}$  in flowing hydrogen

Previous studies of nickel sintering mechanisms indicate that surface diffusion and grain boundary diffusion dominate initial stage sintering.<sup>106</sup> Sintwin results also indicated surface and grain boundary diffusion as the primary sources of neck growth. Therefore, values for surface diffusion activation energy and frequency factor, as well as grain boundary activation energy and frequency factor were considered for changes during the iterative process. Although surface diffusion does not directly contribute to

shrinkage, alterations to surface diffusion parameters impact shrinkage. As surface diffusion becomes more active, sintering potential (driven by curvature difference in initial stage sintering) is "used up" by neck growth without densification, resulting in lower shrinkage rates for the system.<sup>2</sup> The best-fitting curve resulted from altering the frequency factor for grain boundary diffusion from  $4 \times 10^{-16}$  to  $4.5 \times 10^{-15} \text{ m}^3/\text{s}$ .

Using these sintering parameters, neck size evolution was predicted for the quasi-PIM material for both the *in situ* heating-cooling cycle to 600°C, modeled as 1.5°C/min heating rate, and the 10°C/min constant heating rate cycle. Neck size versus temperature results are shown in Figure 5.3.



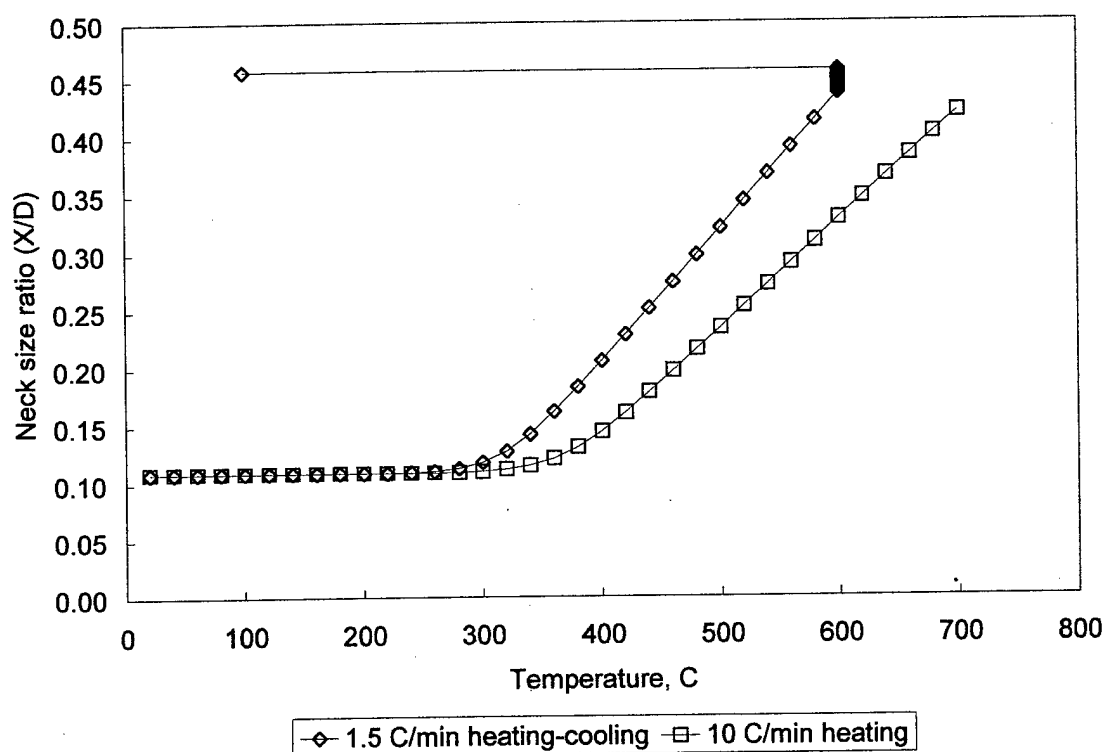


Figure 5.3: Computer simulation of neck size evolution versus temperature for quasi-PIM material. Initial neck size ratio of 0.11 was used.

### 5.3 Modeled Thermal Conductivity Evolution

Once input parameters for the sintering system have been refined, thermal conductivity may be modeled by combining the computer simulated neck size and the circuit model as described by Equation 5.12. The evolution of thermal conductivity may be predicted for different time-temperature profiles by altering the computer simulation inputs. A prediction of thermal conductivity versus temperature for quasi-PIM material in both

the *in situ* heating-cooling cycle and the 10°C/min constant heating rate is shown in Figure 5.4. Comparison of these modeled values with experimental results will be discussed in Chapter 6.

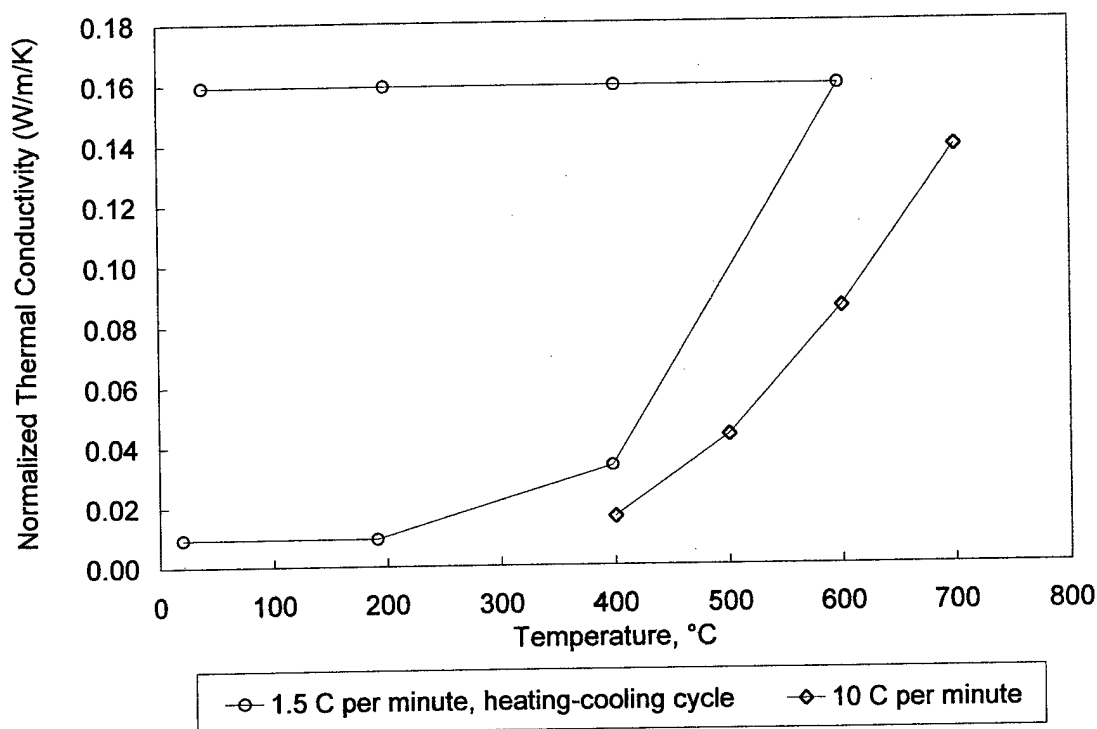


Figure 5.4: Computer simulation of thermal conductivity versus temperature for quasi-PIM material. Thermal conductivity is normalized with respect to wrought thermal conductivity at measurement temperature.

## **Chapter 6**

### **Discussion**

The objective of this chapter is to assess the results presented in Chapter 4, and determine whether the results support or disprove the hypothesis of the work. To that end, the first part of the chapter describes the relationship between transverse rupture strength and thermal conductivity as demonstrated by the results. Secondly, the capability to model this relationship is discussed, and lastly, the impact of the secondary results, and their relationship to the hypothesis is examined.

#### **6.1 Relationship between Strength and Thermal Conductivity**

Prior to discussing the relationship between strength and thermal conductivity, the basic assumptions made in the interpretation of experimental results are summarized as follows:

- Laser flash measurements do not adversely impact the condition of the sample material. Samples containing polymer showed evidence of decomposition of the polymer on the surface of the material, but no impact to the measurements. No changes to particle surface condition or sintering were observed.
- Transverse rupture strength is a function of normalized neck area  $(X/D)^2$ . Xu and German's model will be used as the primary method for predicting and describing

strength. In the form shown in Equation 2.51, it describes ultimate tensile strength.

$$\sigma = \sigma_o \frac{f_s N_c}{K\pi} \left( \frac{X}{D} \right)^2 \quad 2.51$$

- Transverse rupture strength is 1.6 to 2 times ultimate tensile strength<sup>80</sup>
- Thermal conductivity is a function of normalized neck area  $(X/D)^2$ , as described by Equation 5.14:

$$\kappa_{eff} = \frac{\kappa_i \kappa_n \pi \left( \frac{X}{D} \right)^2 D^2}{4\kappa_i (D - L_i) + 2\kappa_n L_i} + \frac{\kappa_s \kappa_g \left[ D^2 - \frac{\pi}{4} \left( \frac{X}{D} \right)^2 D^2 \right]}{D (\kappa_s + \kappa_g)} \quad 5.14$$

### 6.1.1 Experimental Observations

Room temperature transverse rupture strength measurements were compared to thermal conductivity measurements for three systems: quasi-PIM, PIM, and die-compacted nickel. The initial discussion will focus on the first two systems. The comparison of normalized strength to normalized thermal conductivity for the quasi-PIM system is shown in Figure 6.1. Based on the modeled dependence of both properties on  $(X/D)^2$ , a linear relationship was expected between the two properties. A linear regres-

sion was used to examine the results, with a strong correlation for the quasi-PIM comparison ( $R^2=0.99$ ), with 99% confidence in statistical significance.

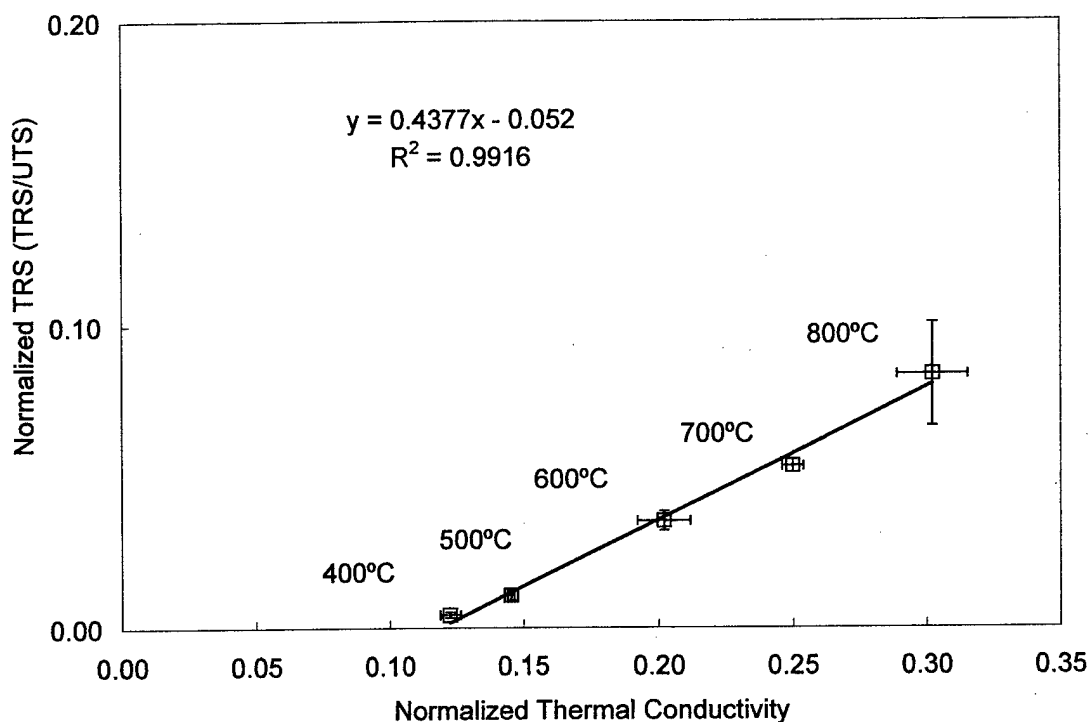


Figure 6.1: Room temperature transverse rupture strength versus thermal conductivity for quasi-PIM nickel. Samples heated at 10°C/min in hydrogen to the indicated peak temperature, water quenched. Linear trend line indicates a 0.99 correlation, with 99% confidence in statistical significance.

The same comparison is made for the injection-molded material in Figure 6.2. Data from 425°C after a two-hour hold, and increasing temperatures (500, 600, and 700°C) were used for the comparison.

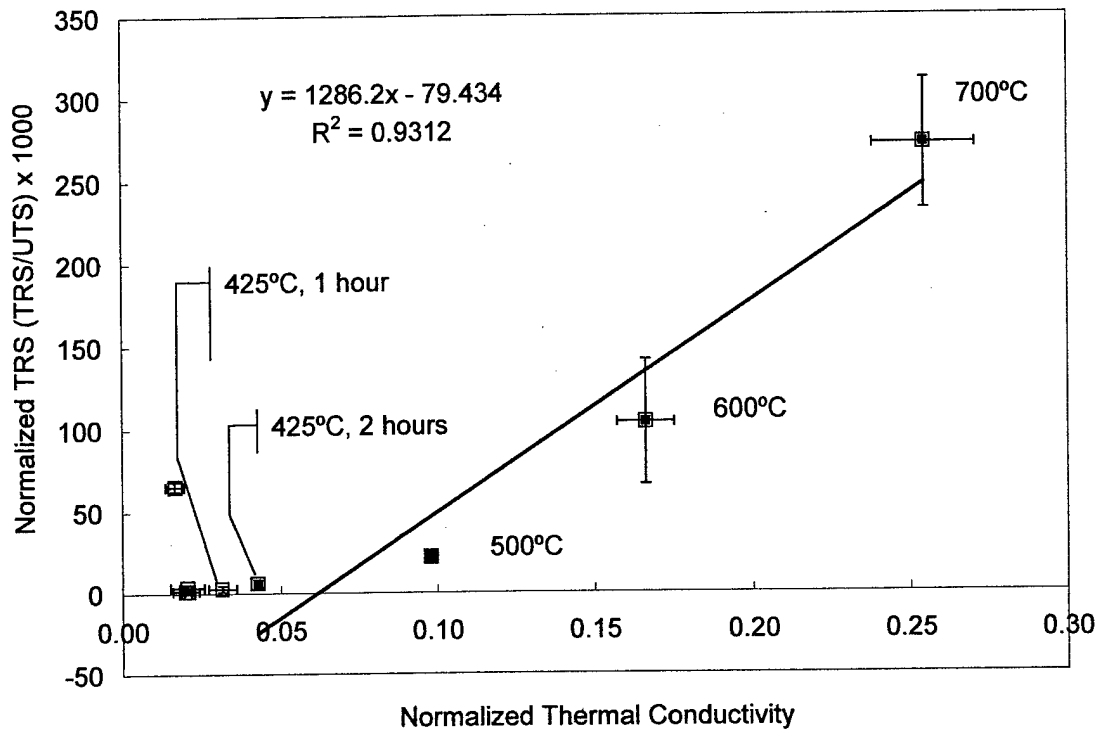


Figure 6.2: Room temperature transverse rupture strength versus thermal conductivity for injection molded nickel bars, heated at 3°C/min, with 2-hour hold at 425°C. Samples heated in hydrogen, removed from the furnace at the indicated temperatures, and cooled in air. Linear trend line shows a 0.93 correlation, with less than 95% confidence in statistical significance.

This comparison did not provide a strong correlation for a linear relationship between strength and thermal conductivity ( $R^2=0.93$ ), and there is less than 95% confidence that the results are statistically significant. Other possible relationships were explored, with the acknowledgement that a more complex relationship with a better correlation may not be as readily described by a physical model. A second order relationship was examined, with results shown in Figure 6.3 for the quasi-PIM material.

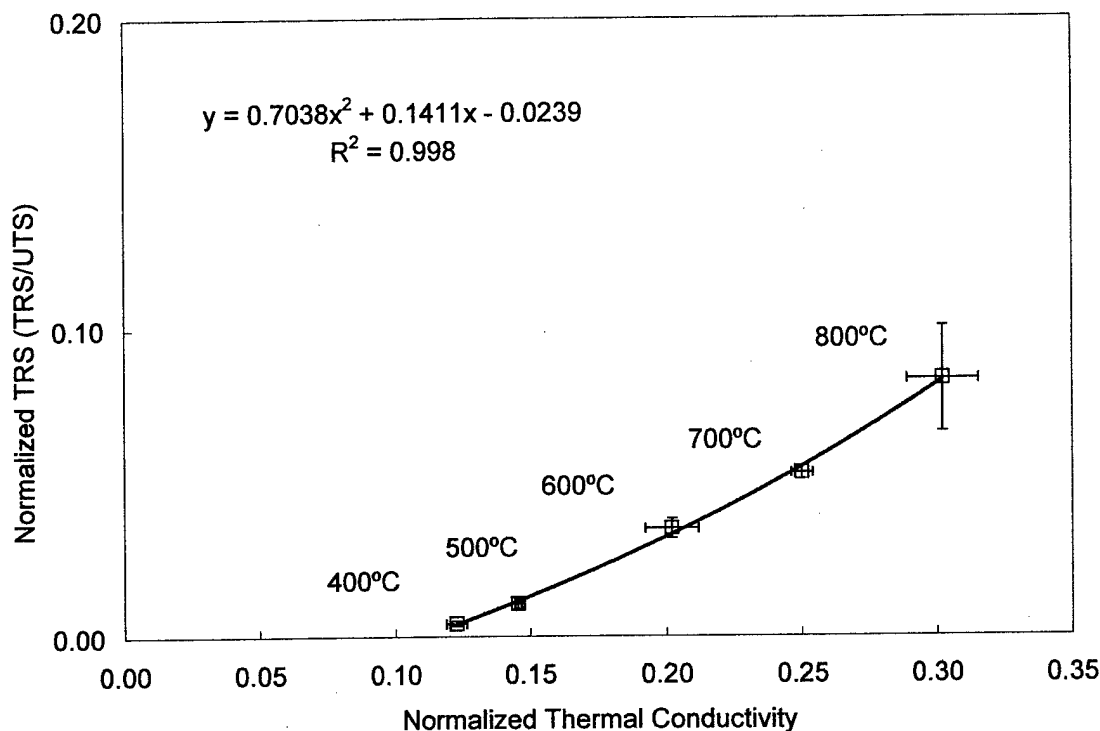


Figure 6.3: Room temperature transverse rupture strength versus thermal conductivity for quasi-PIM nickel. Samples heated at 10°C/min in hydrogen to the indicated peak temperature, water quenched. Second order polynomial trend line indicates 0.99 correlation, with 99% confidence in statistical significance.

For the quasi-PIM material, the second order relationship fits the experimental data approximately as well as the linear relationship did ( $R^2=0.99$ , with 99% confidence in statistical significance). A second order relationship between the two properties for the PIM material is shown in Figure 6.4.

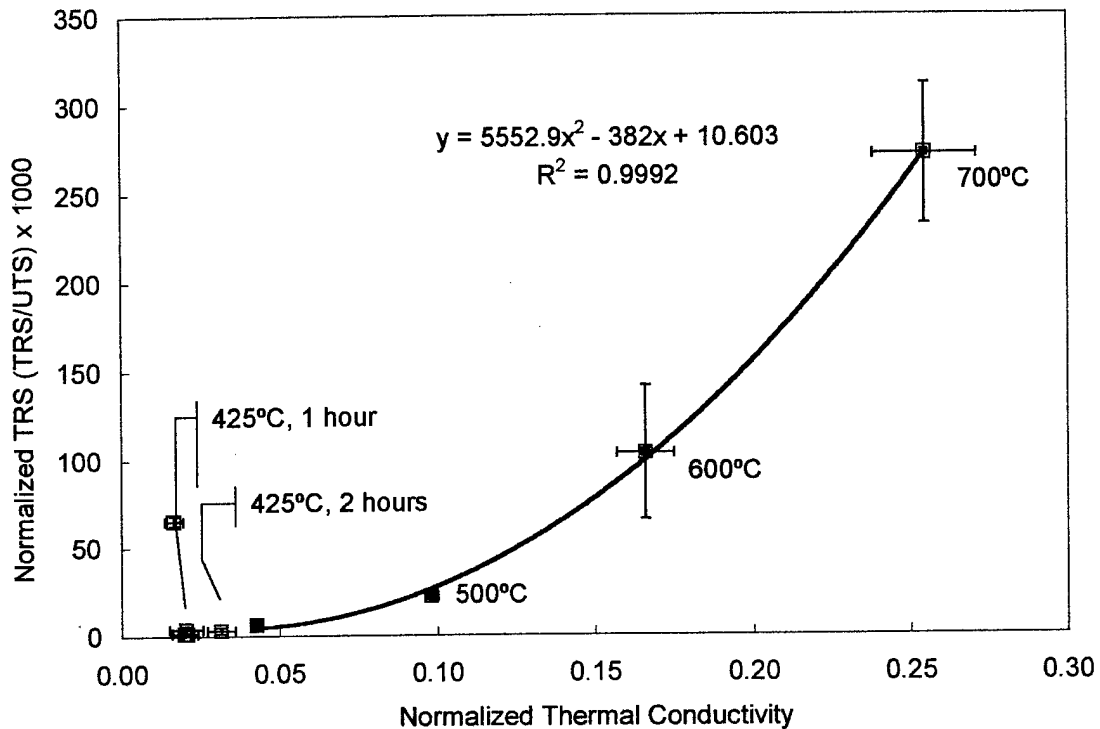


Figure 6.4: Room temperature transverse rupture strength versus thermal conductivity for injection molded nickel bars, heated at 3°C/min, with 2-hour hold at 425°C. Samples heated in hydrogen, removed from the furnace at the indicated temperatures, and cooled in air. 2<sup>nd</sup> order polynomial trend line shows a 0.99 correlation, with 99% confidence in statistical significance.

Results for the PIM system strongly support a second order relationship between strength and thermal conductivity during initial stage sintering, not the first order (linear) relationship initially expected. These data were re-examined for both systems using a linear plot of the logarithm of normalized TRS versus the logarithm of the normalized thermal conductivity. The slope of the linear plot, shown in Figure 6.5, was determined to describe the relationship between the two properties. With the data in this format,



there was an expectation that the extrapolated relationship should intercept the origin of the log-log axes. The fact that, in particular, the PIM data would not extend to the origin implies that the presumed relationship between the two properties alters at higher densities. This will be discussed in more detail later in this chapter.

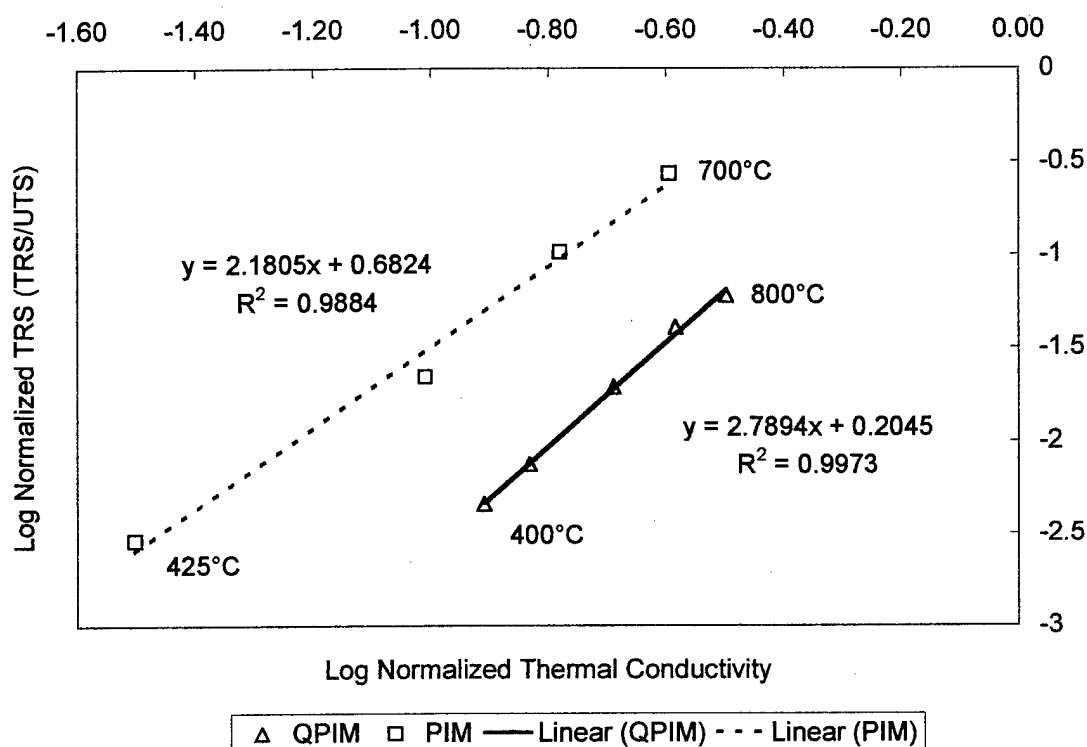


Figure 6.5: Logarithm of normalized room temperature TRS versus logarithm of normalized thermal conductivity for quasi-PIM and PIM nickel. Temperatures indicate lowest and highest peak temperatures for each set of samples.

The quasi-PIM material showed an approximate cubic relationship between thermal conductivity and strength ( $m=2.79$  with an  $R^2$  value of 0.998, 99% confidence in statistical significance). The PIM material showed more of a squared relationship between

thermal conductivity of strength ( $m=2.18$  with an  $R^2$  of 0.99, with over 95% confidence in statistical significance). In considering the difference between these values (2.79 versus 2.18), the PIM material is considered the more consistent, therefore more heavily weighted, source of data. The thermal conductivity disks were actually cut from transverse rupture bars, versus the quasi-PIM material, which was pressed in different dies. Additionally, PIM disks and bars were sintered together for each test temperature, ensuring the strongest possible correlation between the two specimen configurations. The slope of approximately 2 in Figure 6.5 agrees with the curve fitting shown in Figure 6.3 and Figure 6.4, indicating that thermal conductivity squared is proportional to strength. This leads to the re-examination of the assumption that both strength and thermal conductivity are directly proportional to the area of the interparticle neck  $(X/D)^2$ .

The assumption that strength is proportional to the square of the neck size ratio  $(X/D)^2$  was examined by plotting the logarithm of the strength versus the logarithm of the neck size ratio  $(X/D)$ , shown for the quasi-PIM material in Figure 6.6.

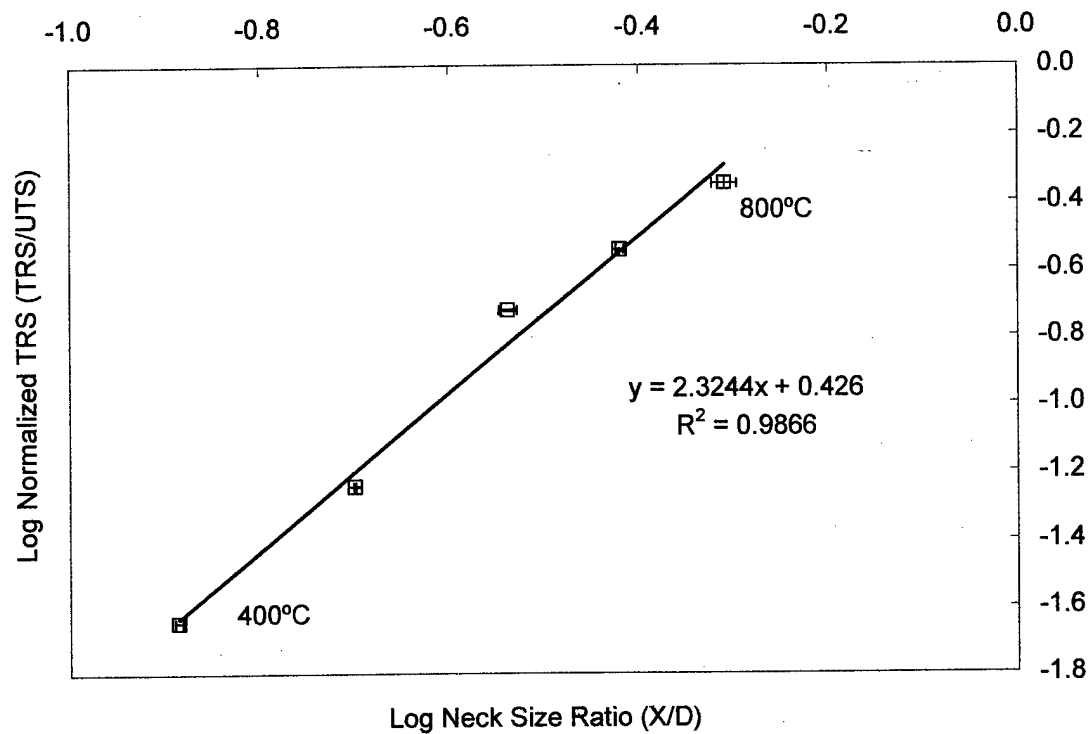


Figure 6.6: Logarithm of normalized strength versus logarithm of neck size ratio for quasi-PIM material. Neck size measurements made via SEM observation of ruptured bonds on fracture faces.

The slope of approximately 2 in this figure indicates a squared relationship between neck size ratio and strength, consistent with the model described in the assumptions. The statistical significance of the data is 0.99. The same comparison is shown for injection molded material in Figure 6.7.

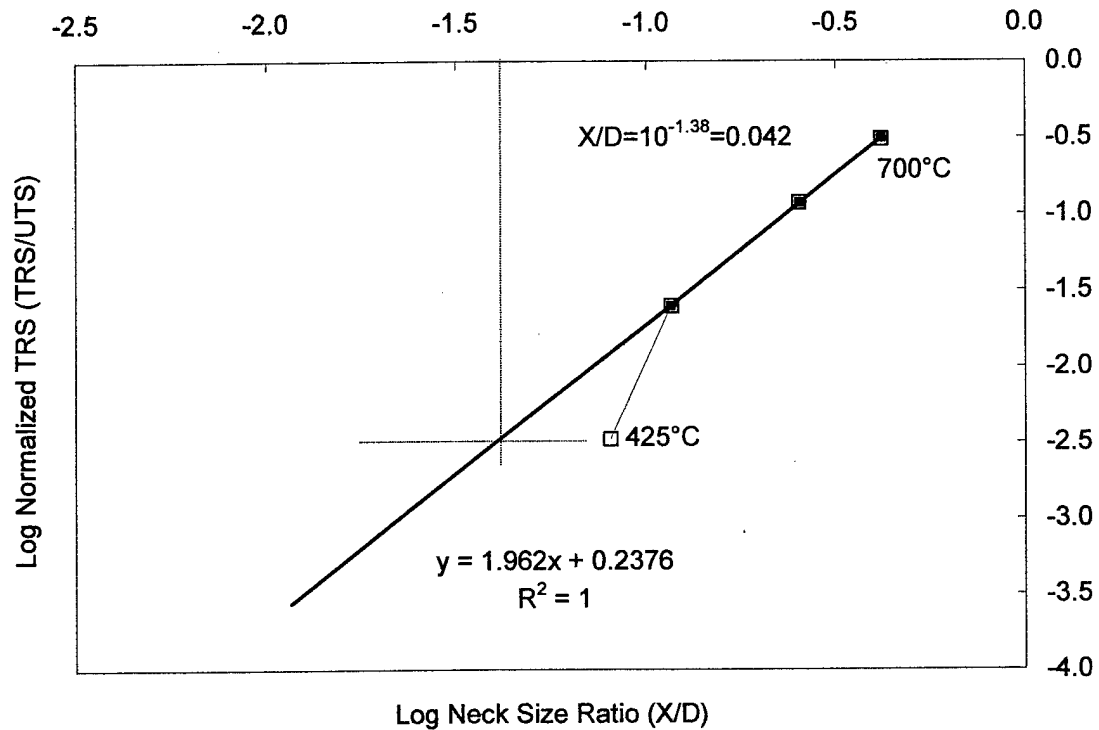


Figure 6.7: Room temperature transverse rupture strength versus neck size for PIM material. Trend line extended to determine a neck size that would match measured transverse rupture strength for 425°C sample.

Strength versus neck size ratio for the injection molded samples yielded similar results. However, the lowest temperature sample, sintered to 425°C, was out of family, indicating a lower thermal strength than the observed neck size would suggest. A trend line for the higher temperature points was extrapolated to assess what the neck size ratio should be for the lowest temperature sample to match the other data. A neck size ratio of 0.042 would match the trend established by the other measurements. Even with only three points, there is a 99% confidence in the statistical significance of the linear fit.

The same process was used to compare thermal conductivity versus neck size.

A comparison of thermal conductivity to neck size ratio for the quasi-PIM material is shown in Figure 6.8. Linear regression indicates that neck size is related to thermal conductivity through an exponent of 0.70. Confidence in the statistical significance is 99%.

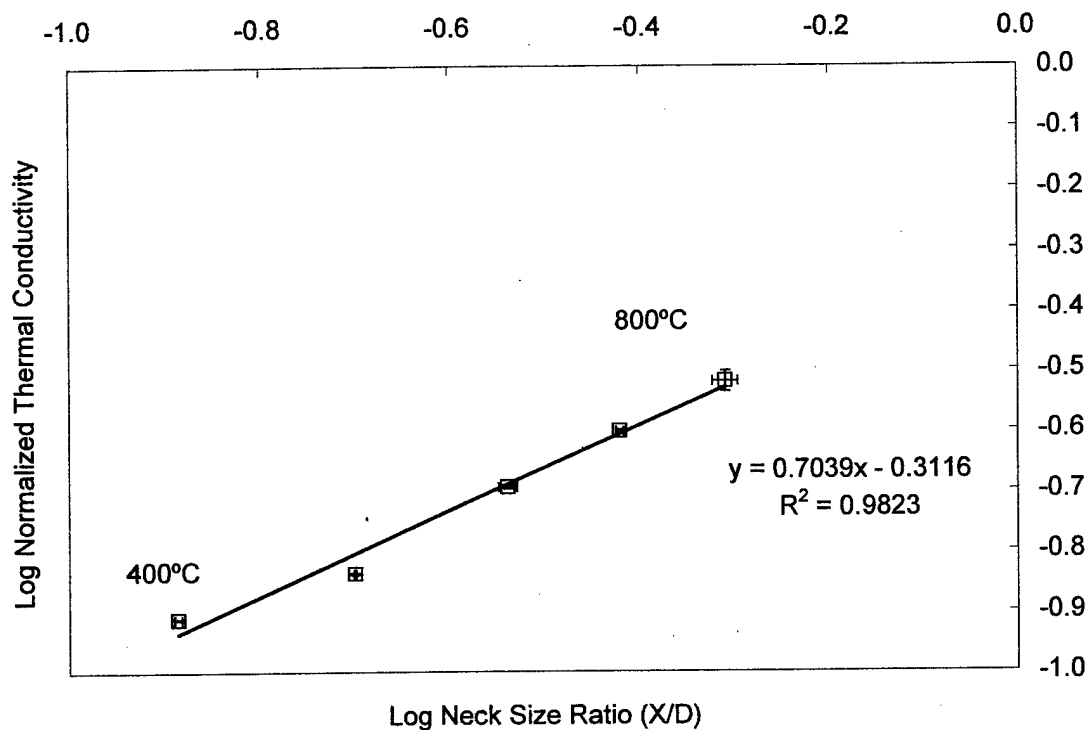


Figure 6.8: Logarithm of normalized thermal conductivity versus logarithm of neck size ratio for quasi-PIM material.

The same comparison is shown for injection-molded material in Figure 6.9

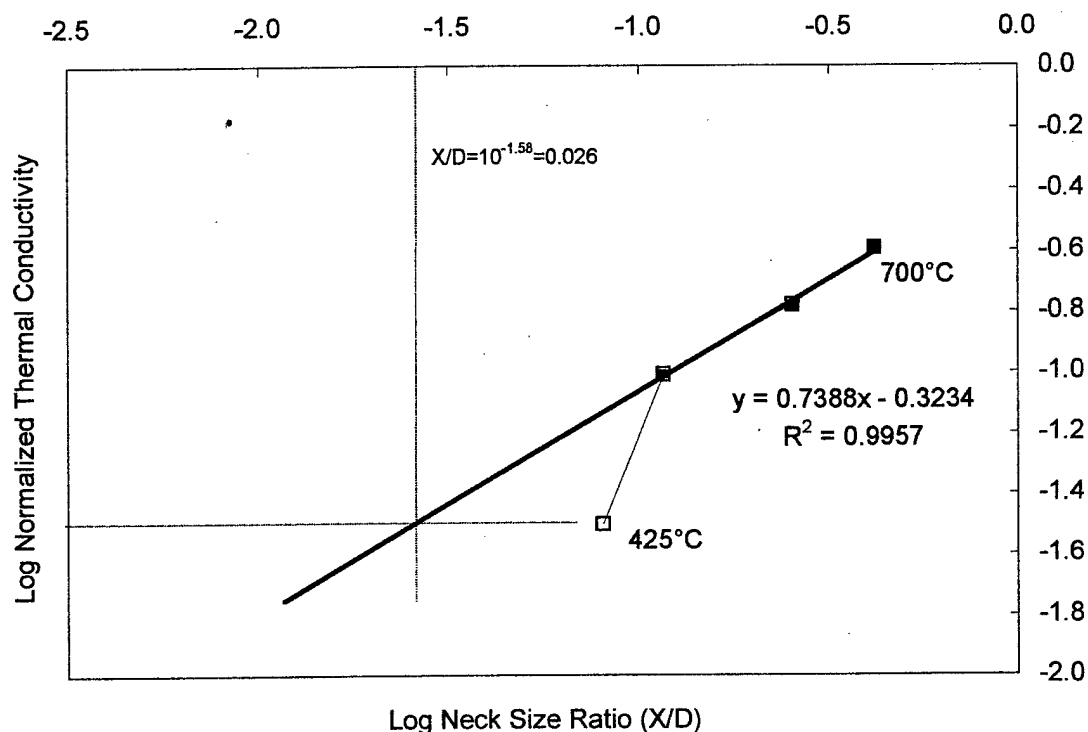


Figure 6.9: Thermal conductivity versus neck size for PIM material. Trend line extended to determine a neck size that would match measured thermal conductivity for 425°C sample.

Comparison of thermal conductivity versus neck size for the injection molded material also showed a strong correlation, with the exception of the datum from the sample that had been sintered to 425°C. This consistent departure for both mechanical strength and thermal conductivity indicates that measured values of both properties were lower than expected for the measured X/D. Again, the trend line for the three higher temperature points was extrapolated to determine the neck size that would correlate to the measured properties for the 425°C (2 hour hold) sample. A neck size of 0.026 would

correspond with the other measured values. Confidence in the statistical significance of the remaining three points is just less than 95%.

These results call into question the validity of the neck measurements made on the 425°C sample, although the same technique was used to measure each set of fracture surfaces, with consistent results made for the samples heated to 500°C and above. Several factors can explain the discrepancy. Firstly, the shape of the ruptured bond evolves with increasing temperature. Generally, the ruptured bonds at 425 and 500°C were long and narrow. As mentioned, the longest dimension was measured, which gave an indication of increasing bond size with temperature, but likely led to an overestimation of neck size for those temperatures. At 600°C and above, rupture sites were relatively equiaxed, so the largest dimension did not differ much from the smallest dimension of the ruptured bond. Secondly, the population of the bonds also increases with increasing temperature. A comparison of the fracture surfaces for the 425°C sample (Figure 6.10) and the 500°C sample (Figure 6.11) shows that although the observed ruptured bonds are similar in shape and size (measured values of 0.08 and 0.12 respectively), the population of ruptured bonds is much smaller in the lower temperature sample. To extend this observation, the fracture surface of the 425°C sample held for just one hour, versus two, showed zero, one, or two ruptured bond sites per image, but a measurement of these sites would not well represent the state of bonding. These physical observations suggest that the coordination number,  $N_c$ , is also evolving along with neck size. An increase in coordination number is expected with densification, and is often described in terms of density. Equation 6.1 describes the relationship:

$$N_c = 14 - 10.4(1 - V_s)^{0.38} \quad (6.1)$$

where  $V_s$  is the fractional density. During the thermal decomposition of the binder, as polymer at the interparticle contact point disappears, the effective coordination number likely drops until densification begins. Although the PIM material is generally isotropic in terms of density and binder distribution, any localized difference can cause a particle to shift preferentially toward one contact point, reducing the number of smaller contacts in favor of another, stronger bond. This process, described as “desintering”, can be likened to Oswald ripening, where a reduction in system energy occurs through the elimination of many smaller grains in favor of fewer larger grains.<sup>111</sup>

The combination of neck size and coordination number effects explains the behavior, but coordination number is difficult to evaluate experimentally. Fractal analysis of the material may provide additional insight for future study. For this work, an “effective neck size” was used for the 425°C sample, which reflected the observations made in the analysis of transverse rupture strength and thermal conductivity results. This assumption does not directly impact the construction of a relationship between strength and thermal conductivity, since the datum falls in line with other measured values on the comparison of the two properties as shown in Figure 6.4. The assumption only affects the discussion of X/D directly.



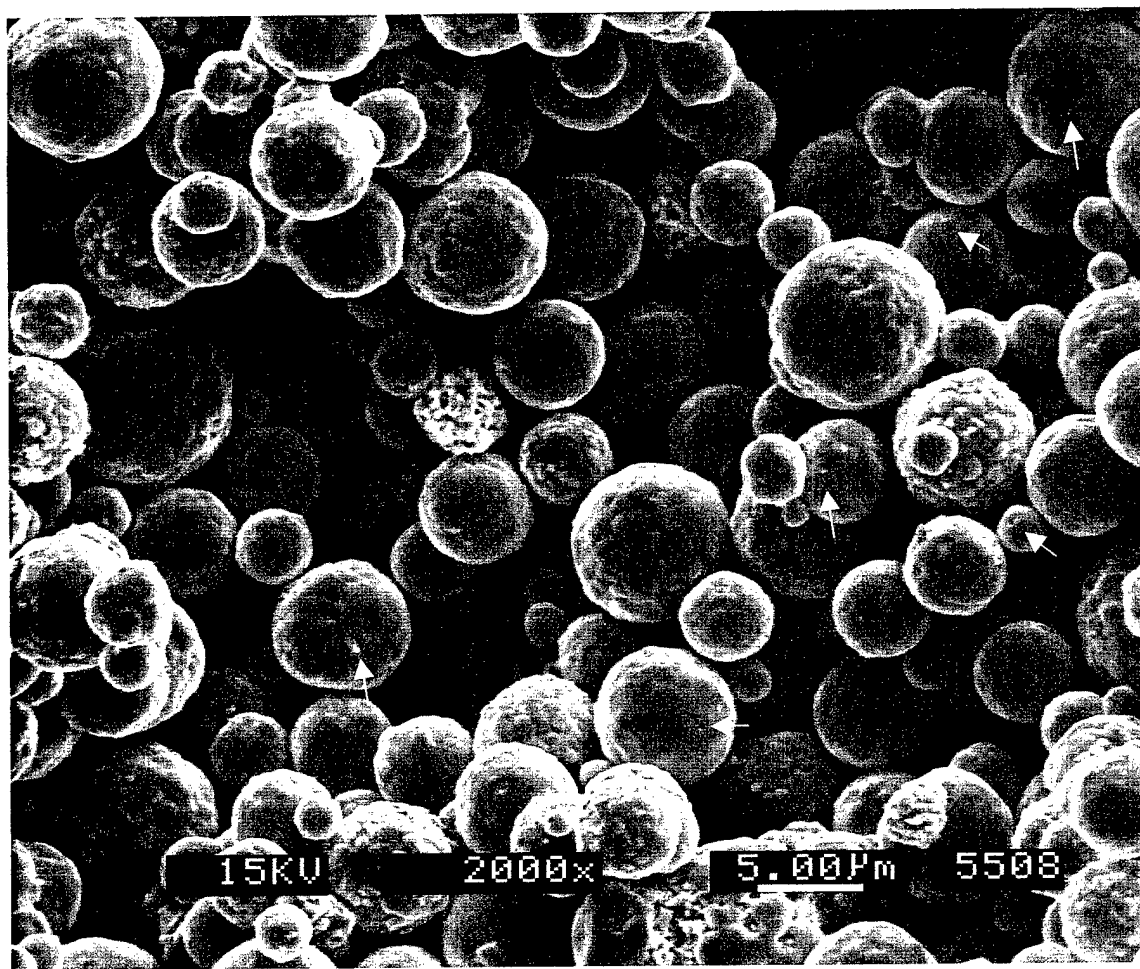


Figure 6.10: SEM image of fracture surface of PIM sample. Light spots on the particle surface indicate interparticle bonds that ruptured during fracture. Sample was heated to 425°C in flowing hydrogen, and cooled in air to room temperature for transverse rupture testing. Arrows indicate necks that were counted in the measurement.

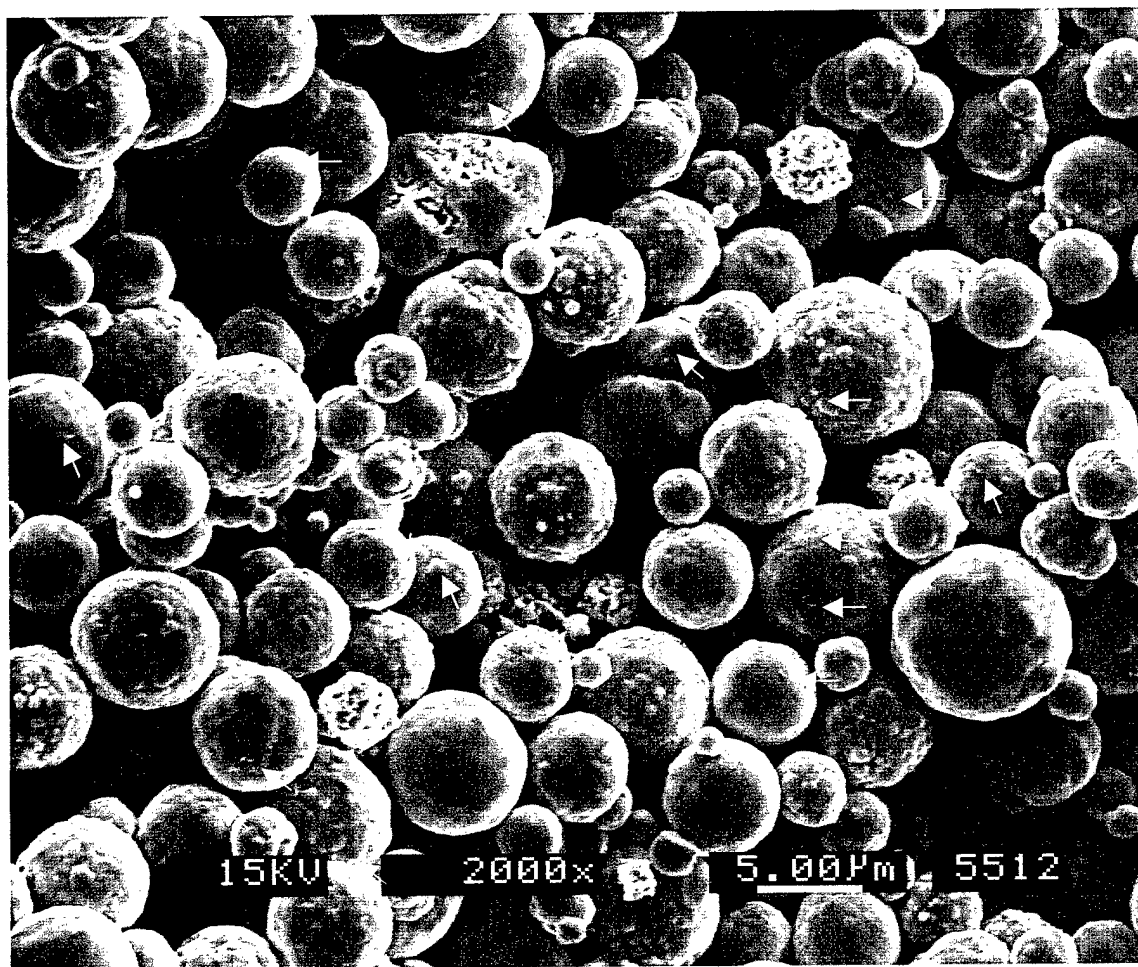


Figure 6.11: SEM image of fracture surface of PIM sample. Light spots on the particle surface indicate interparticle bonds that ruptured during fracture. Sample was heated to 500°C in flowing hydrogen, and cooled in air to room temperature for transverse rupture testing. Arrows indicate necks that were counted in the measurement.

Given that the data demonstrate a squared relation between strength and thermal conductivity, and a squared relation between strength and neck size ratio ( $X/D$ ), the conclusion to be investigated is that thermal conductivity is directly proportional to neck size ( $X/D$ ), versus a squared function as assumed. Linear regression shows that an exponent of 0.70 to 0.74 relates the two properties as shown in Figure 6.8 and Figure 6.9. If an effective neck size ratio of 0.034 (a compromise between the projections in Figure 6.7 and Figure 6.9) is used for the lowest temperature sample, the regression shows a shift toward an exponent of one, as expected. The revised plot is shown in Figure 6.12. Confidence in the statistical significance is 99%.

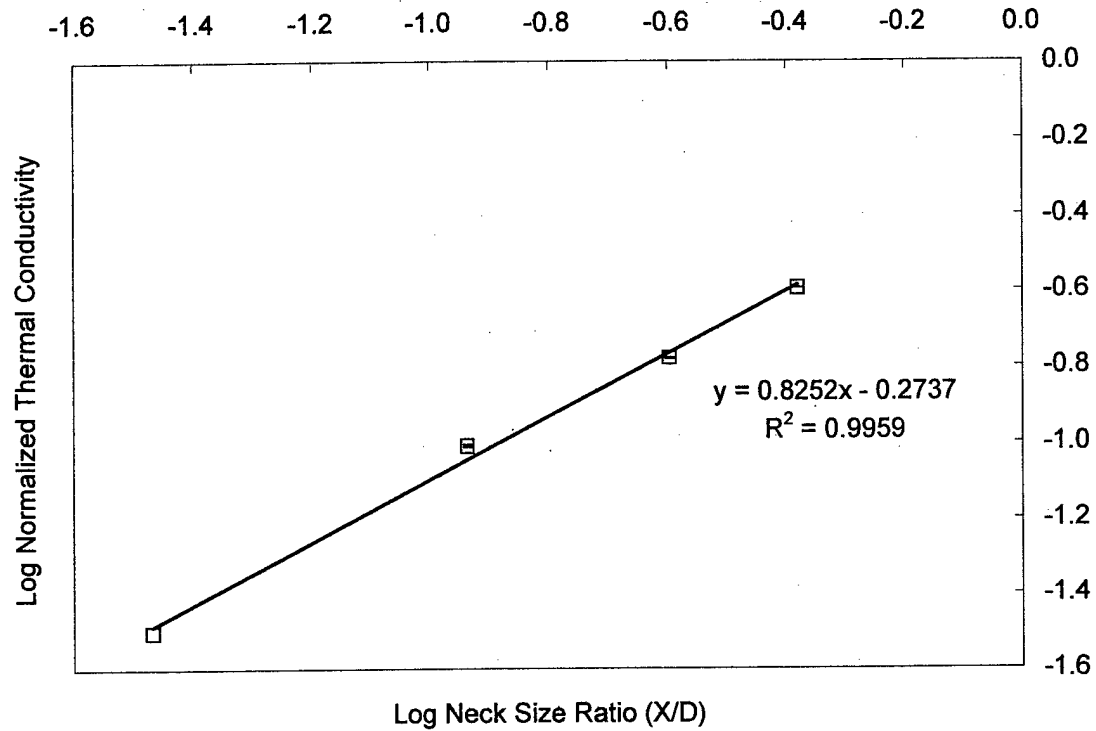


Figure 6.12: Thermal conductivity versus neck size ratio for PIM material, using revised neck size of 0.034 for 425°C sample

A final check of the relationship between strength and thermal conductivity is shown in Figure 6.13. The plot of the logarithm of the thermal conductivity divided by strength shows the difference between the two properties' dependence on neck size using Equation 6.2:

$$\log \left( \frac{\kappa}{\sigma_{ts}} \right) = \log \left( \frac{(X/D)^m}{(X/D)^n} \right) = \log \left( \frac{X}{D} \right)^{(m-n)} \quad ( 6.2 )$$

Examining only the dependence on neck size ratio, the two quantities can be divided by each other, and their exponents subtracted. When plotted, the slope of the curve indicates the difference between the two exponents. The slope of the PIM material data is negative one, indicating that the difference between the two exponential dependencies is one. The quasi-PIM data are less consistent, but also supports a difference of at least one between the exponents. Since strength has a demonstrated squared dependence on neck size ( $n=2$ ), thermal conductivity has dependence to the first power ( $m=1$ ). Confidence in the statistical significance of both sets of data is greater than 95%.

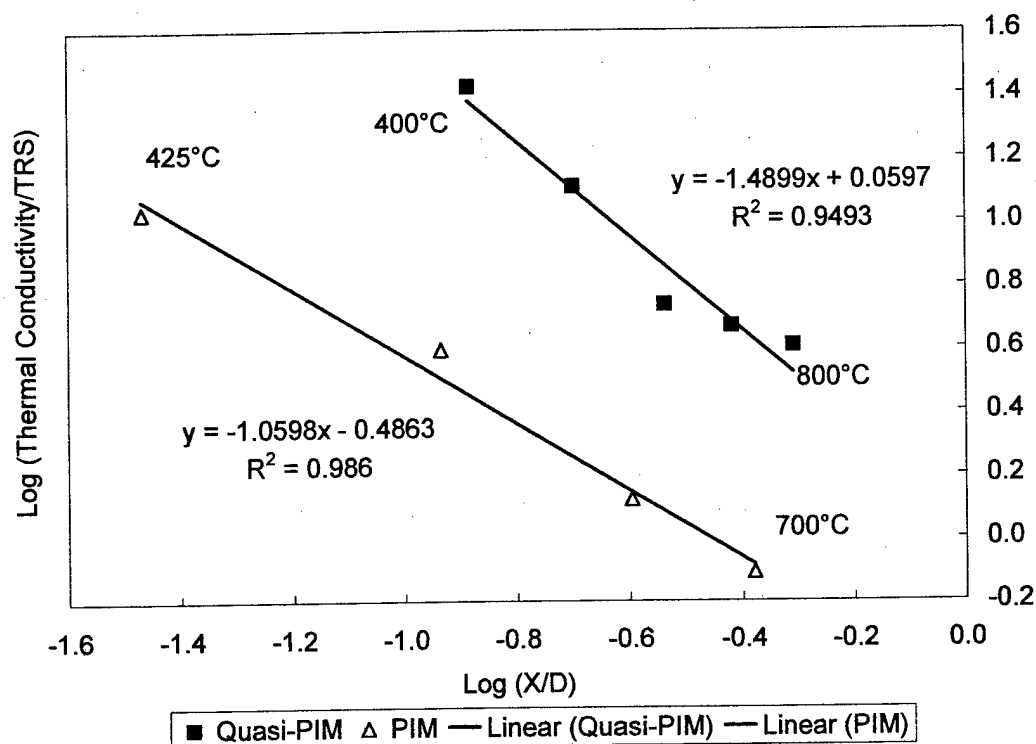


Figure 6.13: Logarithm of thermal conductivity divided by transverse rupture strength versus logarithm of the neck size for both quasi-PIM and PIM specimens. The slope shows the difference between the two properties' relation with neck size.

At this point, it is useful to re-examine the observation noted earlier in the chapter regarding the extrapolation of both thermal conductivity and strength measurements to full density. As previously stated, the relationship defined by data from initial stage sintering does not extend to the origin of a log-log scale, which represents normalized property values of one, or full density. Since the relationship defined between the two

properties in this work is dependant on neck size, the implication is that the relationship either changes in its dependence on neck size during later stages of sintering, or becomes dominated by another variable not considered in the initial stage model. To expand on this point, the relationship between neck size and density is of interest. Assuming mono-sized, spherical particles which sinter into tetrakaidecahedron-shaped grains at full density, the relationship between density and neck size is described by German as shown in Equation 6.3:<sup>80</sup>

$$\frac{X}{D} = \left( 4 \left( 1 - \left( \frac{V_g}{V_s} \right)^{1/3} \right) \right)^{1/2} \quad ( 6.3 )$$

where  $V_g$  is the green fractional density (when  $X$  is zero), and  $V_s$  is the sintered fractional density. This relationship is based upon models describing early stage sintering, and is not valid for  $X/D$  values greater than 0.5. However, experimentally measured  $X/D$  at full density is about 0.53,<sup>80,112</sup> therefore most of the neck growth occurs during initial stage sintering, where  $X/D$  grows from zero to approximately 0.3. This equation, plotted for several green fractional densities, along with the experimental data, is shown in Figure 6.14:

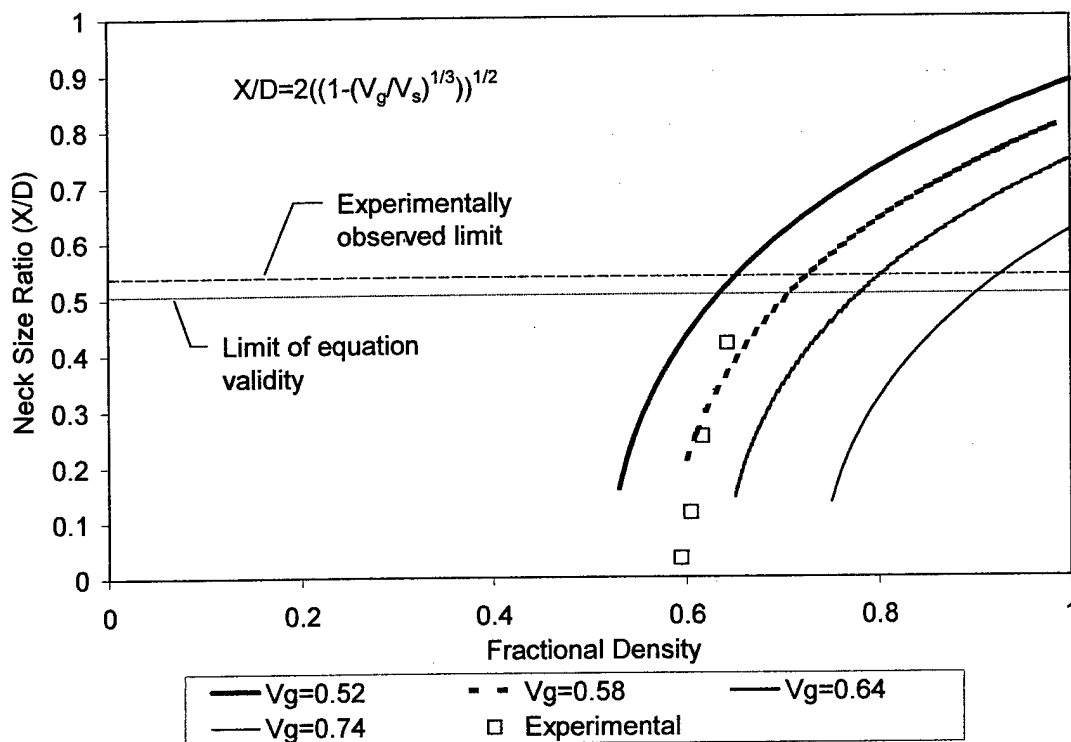


Figure 6.14: Fractional density versus neck size ratio for various green fractional densities. Both calculated and experimental values are shown, along with the limit of the model, and the experimentally observed limit of neck size ratio at full density.<sup>80,112</sup>

Although neck size changes rapidly during the early stages of sintering, most of the growth has already occurred prior to significant densification. The conclusion based on this observation is that another parameter, such as porosity, more effectively describes behavior past the early stages of sintering. This area is a topic of interest for future research.



To conclude the discussion on strength versus thermal conductivity experimental observations, the die-compacted test results must be addressed. Figure 6.15 shows the mean value of three strength measurements and two thermal conductivity measurements, with a 95% confidence level. Interpretation of the die-compacted results is somewhat difficult, given the high thermal conductivity of the 200°C samples, and the larger variability in both strength and conductivity measured values. Strength versus conductivity values are relatively consistent for the range of 250°C to 350°C. By 400°C,

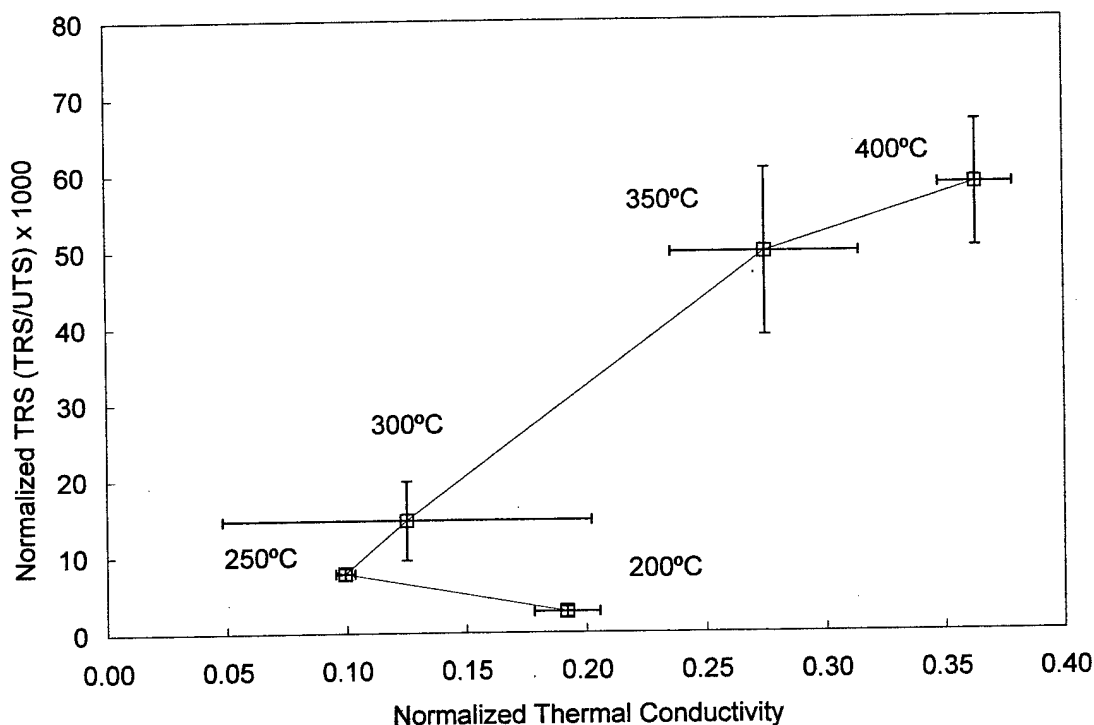


Figure 6.15: *In situ* transverse rupture strength versus thermal conductivity for die-compacted nickel, heated at 3°C/min. Samples heated in hydrogen, removed from the furnace at the indicated temperatures, and cooled in air.

thermal softening is already affecting the trend of increasing strength with temperature, which adds an additional factor into the relationship between the two properties.

Although no formal neck size assessment was done on the die-compacted materials, compaction and the resulting plastic deformation have created a pre-existing neck, as shown in the image of a fracture surface from a “green” sample in Figure 6.16. The neck size indicated from the SEM image is much larger than that observed with the other systems. The binder material, paraffin wax, is present in the die-compacted samples until approximately 280°C.

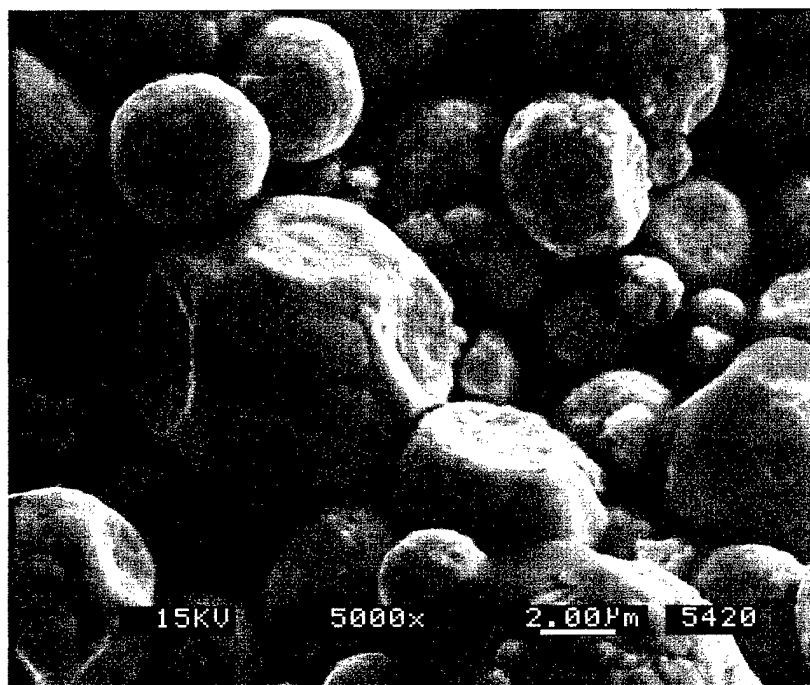


Figure 6.16: SEM image of flattened contact points on a fracture face of the die-compacted material. Samples were compacted to a fractional density of 0.75. This sample has been heated to 150°C to allow the paraffin wax binder to melt and flow to inter-particle contact points. Sample was fractured at room temperature.

The cause of the thermal conductivity spike in the 200°C sample is not known. There was an initial suspicion that binder melting and possible thermal decomposition at the measurement temperature of 200°C caused an errant reading. However, a repeated reading at room temperature yielded the same result. Since the die-compacted material exhibited so many additional variables, it was ultimately not pursued as a component of the model, or verified as part of the hypothesis. This conclusion is consistent with that of other researchers on die-compacted materials.<sup>73</sup>

## **6.2 Modeling Thermal Conductivity and Strength**

The application of models discussed in Chapters 2 and 5 gives further insight into the behavior of the system during initial stage sintering. Thermal conductivity models will be addressed first, then the model of transverse rupture strength.

### **6.2.1 Thermal Conductivity Models**

Experimental results were compared with several models to examine the revised premise that thermal conductivity is linearly related with neck size ratio. As previously mentioned, the injection-molded system was ultimately regarded as the more consistent material, therefore modeling observations were initially compared to the PIM material, then extended to the quasi-PIM material, which showed a less predictable behavior. Figure 6.17 illustrates the comparison of experimental data to the proposed circuit model, the Koh and Fortini model,<sup>46</sup> which is porosity-based, and models by Sui and Lee,<sup>109</sup> and

Jagota and Hui,<sup>114</sup> both based on granular bed analysis with a linear dependence on measurable particle contact radius ( $X/D$ ). Also included is the modified circuit model, which is the original circuit model divided by  $X/D$  to reduce to a linear dependence on neck size. The modified neck size of 0.034 is used for the 425°C datum for all models.

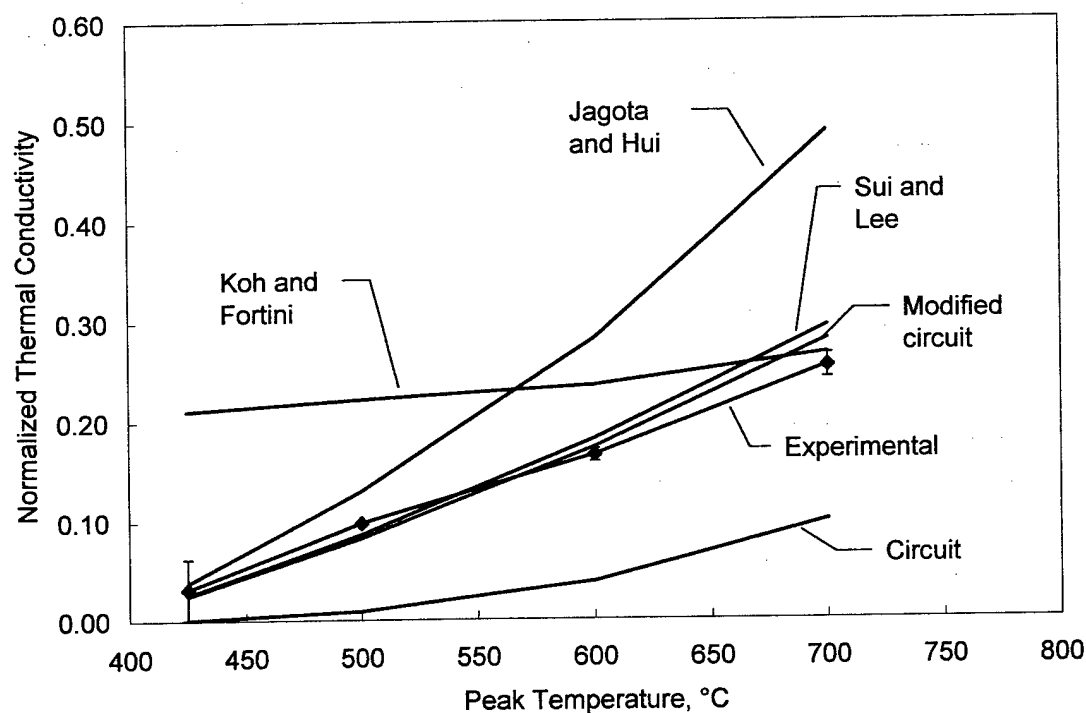


Figure 6.17: Experimental versus calculated thermal conductivity versus temperature for PIM material. Models use values of  $X/D$  as measured in SEM analysis.

Clearly the circuit model underestimates the conductivity, influenced in magnitude by the square of the neck size. The Jagota and Hui model, which incorporates an increasing coordination number and density as well as increasing neck size, shows too

large an increase in conductivity by incorporating these factors. The Sui and Lee model, which reduces to a strictly linear model based on a simple cubic structure for this range of porosity, also overestimates the magnitude. This departure is significant, since the system is more closely approaching that of body-centered cubic with increasing temperature. The porosity model does not capture the dramatic increase in conductivity associated with the initial onset of sinter bonding, although it does meet the experimental data by 700°C, when significant densification is beginning to take place. The modified circuit model, reduced to a linear dependence and based on simple cubic packing in a unit cell, becomes similar in magnitude and trend to the Sui and Lee model. These comparisons reinforce the conclusion that thermal conductivity is linearly dependent solely on neck size. Unfortunately, none of the cited models describing linear behavior appropriately describe this system.

A comparison of the same set of models to the quasi-PIM results is shown in Figure 6.18.

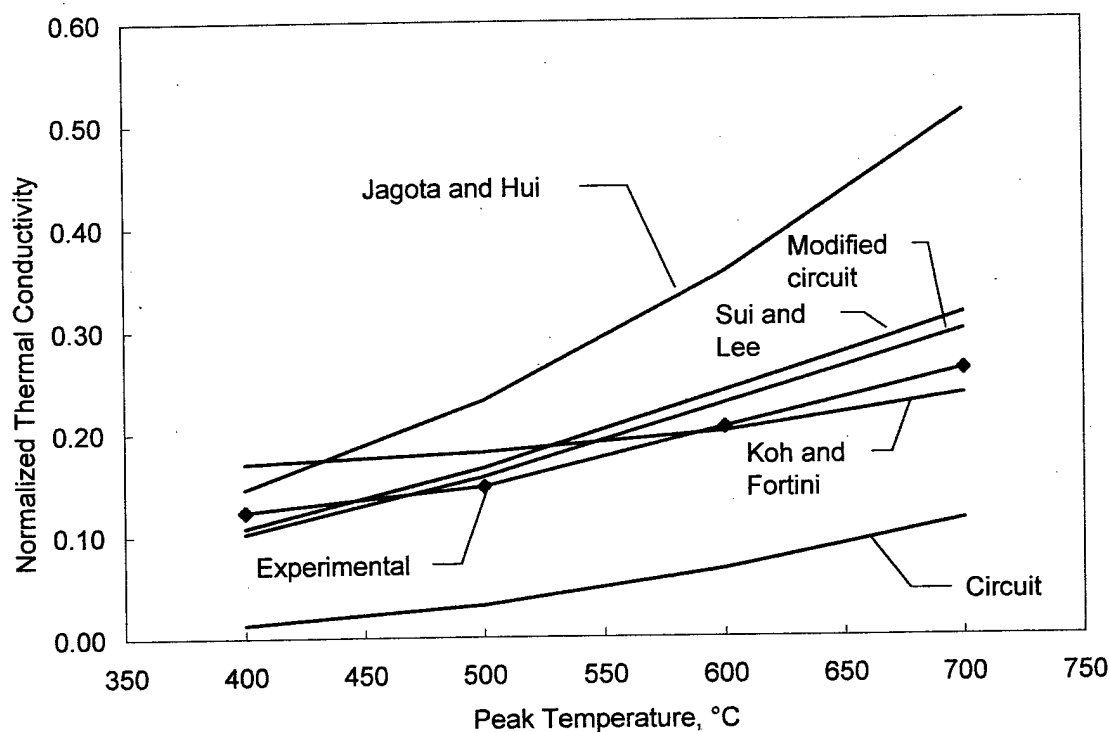


Figure 6.18: Experimental versus calculated thermal conductivity versus temperature for quasi-PIM material. Models use values of  $X/D$  as measured in SEM analysis.

Again, the circuit model significantly underestimates the conductivity, and the Jagota and Hui model overestimates values increasingly with higher temperatures. The porosity-based model is once more at a fairly constant value, but the magnitude is much more appropriate. Because the quasi-PIM material has an established neck from the pre-sintering process (initial  $X/D=0.13$ ), a less dramatic increase in thermal conductivity is expected through the series of measurements versus the PIM material. This makes the porosity model more appropriately applied here than with the PIM material; however, it

still misses the evolution that exists in the experimental data. Again, the modified circuit model and Sui and Lee model are similar, and both overestimate the thermal conductivity results.

Although the circuit model is attractive because it provides a physical sense of how neck growth affects the evolution of thermal conductivity during the initial stage of sintering, this work, and the work of other researchers has found that thermal conductivity is strictly a function of neck size in a linear relationship during the initial stage of sintering.<sup>45,113</sup> Repeated explorations of the incorporation of other parameters such as fractional density and coordination number result in conductivity that increases too rapidly with respect to measured values. A linear relationship provides the only satisfactory solution. Based on this assessment, a model was derived based on the PIM material system with a 0.992 root mean square correlation and 99% confidence in statistical significance. The relationship is described in Equation 6.4:

$$\frac{\kappa_{eff}}{\kappa_o} = 0.566 \left( \frac{X}{D} \right) + 0.021 \quad ( 6.4 )$$

where  $\kappa_{eff}$  and  $\kappa_o$  are the effective and wrought conductivity at test temperature. The comparison of this model with PIM data is shown in Figure 6.19.

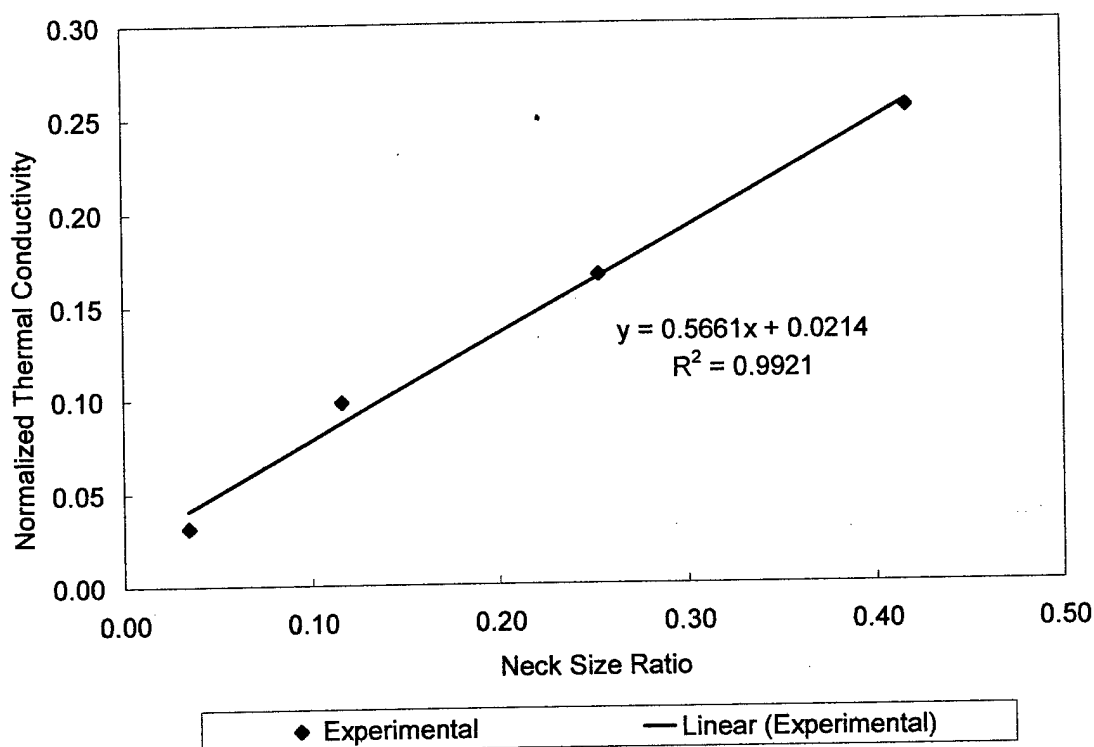


Figure 6.19: Calculated and experimental thermal conductivity versus peak sintering temperature. Conductivity values are normalized by conductivity for the wrought material at test temperature. Neck size ratio values experimentally determined from SEM images.

Returning to the experimental details for the injection molded material; it is of interest to examine the thermal behavior of the injection molded material prior to and during the thermal debinding hold. A comparison of these data with those of the raw powder is shown again in Figure 6.20.



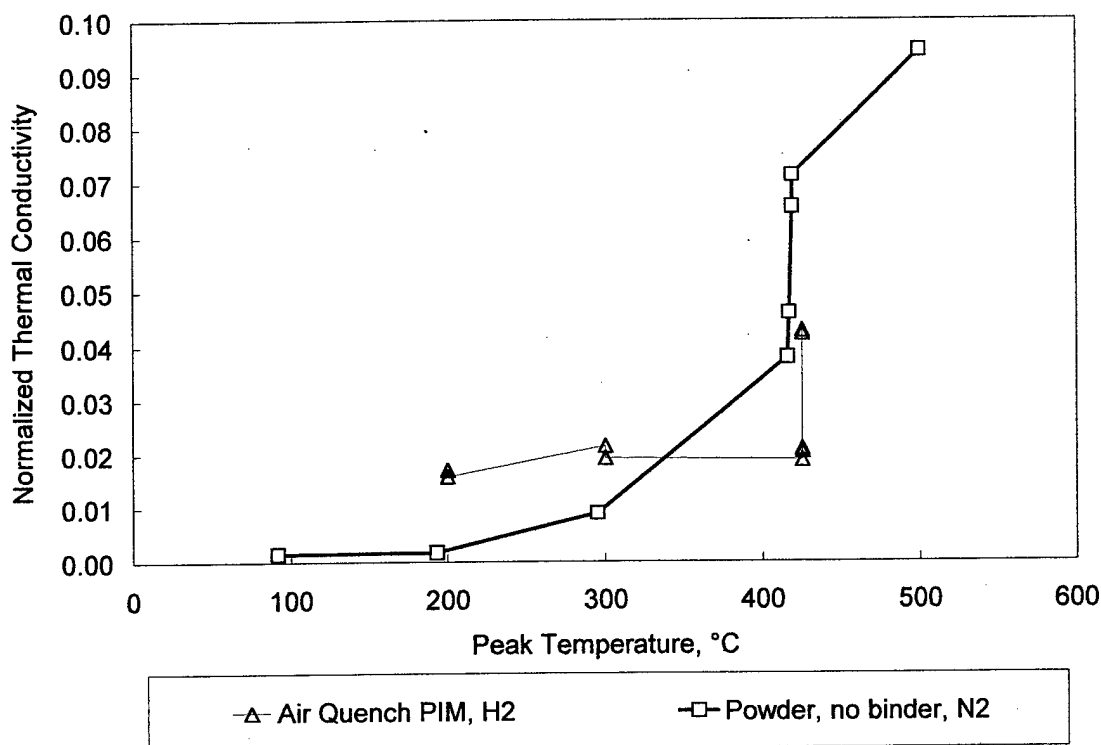


Figure 6.20: Measured thermal conductivity versus peak temperature for PIM material and raw powder. PIM material measured at 100°C, powder measured *in situ*. Both sets of measurements are normalized by wrought values at the measurement temperature.

Constant thermal conductivity is measured from the 200°C sample through a one-hour hold at 425°C, which corresponds with binder presence in the material. Although these measurements were taken at room temperature, the effect of binder melting and flowing during previous heating alters the subsequent behavior. Since the polymer melts by 140°C, the sample treated at 200°C has already experienced this phase change. The polymer has flowed to the interparticle contact points to create pendular bonds. Measured conductivity of the debinding material was significantly higher at this temperature

than that of the raw powder. This difference implies that the solid binder material still present at the interparticle contacts increases the overall effective conductivity versus the same metal powder with only gas in the pores. Although the polymer has a relatively low thermal conductivity compared to metal, it is still much more conductive than gas (approximately 0.3 W/m/K versus 0.02 W/m/K).<sup>104</sup> The implication is that even the smallest bit of remaining polymer strongly influences the overall conductivity of the debinding material. As early as 300°C, the powder begins to show increases in thermal diffusivity, indicating the initiation of sinter bonds, even in a non-reducing atmosphere. During the hold, the thermal diffusivity of the raw powder evolved more rapidly than that of the PIM material, implying that the presence of the binder impedes the initial growth of the neck below the thermal debind temperature. This is consistent with a reduced level of surface diffusion in the presence of the polymer layer.

These observations can be compared to models for granular material in point contact, specifically the Batchelor and O'Brien model described in Chapter 2. Figure 6.21 shows this comparison. The material with binder present at the contact is modeled by the superposition of the point contact model with the circuit model. The circuit model includes a 0.01D thickness layer of solid polymer at the interface, with a thermal conductivity of 0.3 W/m·K.<sup>104</sup> The thickness is based on SEM observations of surface roughness and appearance of interparticle contacts when polymer is no longer visible outside the contact.

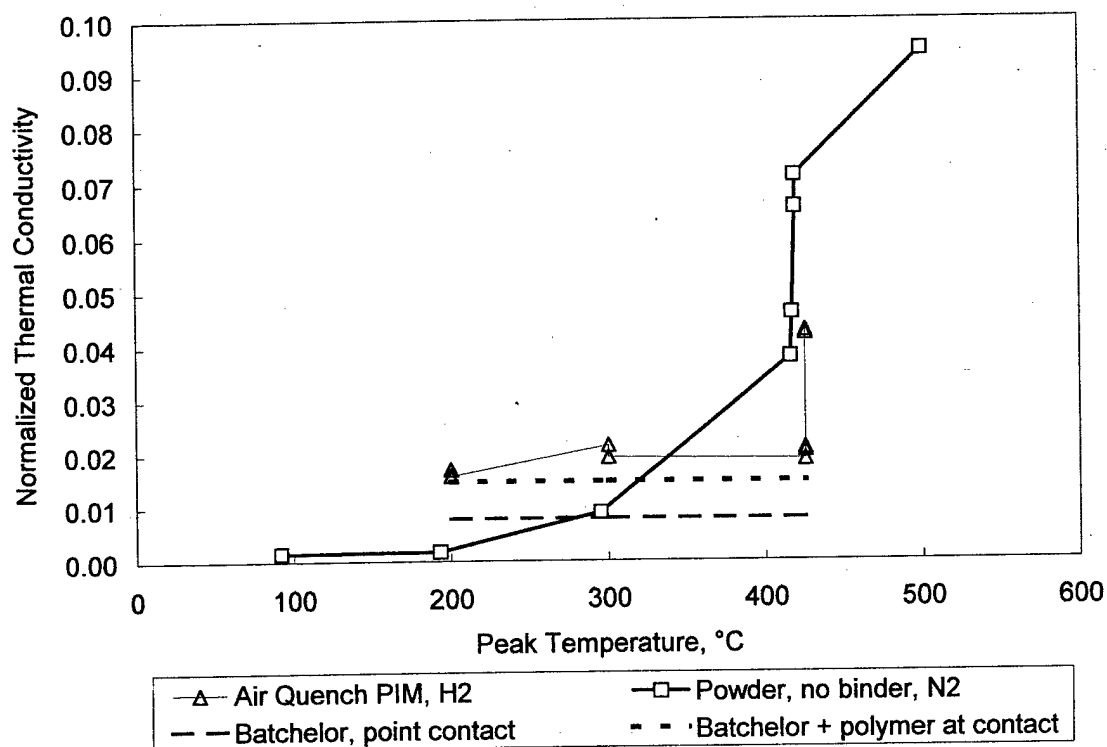


Figure 6.21: Experimental and modeled thermal conductivity versus peak temperature for PIM material and raw powder.

### 6.2.2 Transverse Rupture Strength Model

Transverse rupture strength results for the PIM material were compared with strength calculated by the Xu and German model described in Chapter 2, along with the Rice model and Bal'shin's exponential model, both functions of porosity (or density). This comparison is shown in Figure 6.22. Each of the models calculates ultimate tensile strength for the material. Since transverse rupture strength typically exceeds ultimate

tensile strength by a factor of 1.6 to 2, each model was scaled up by a factor of 1.6 for comparison with experimental results.<sup>80</sup>

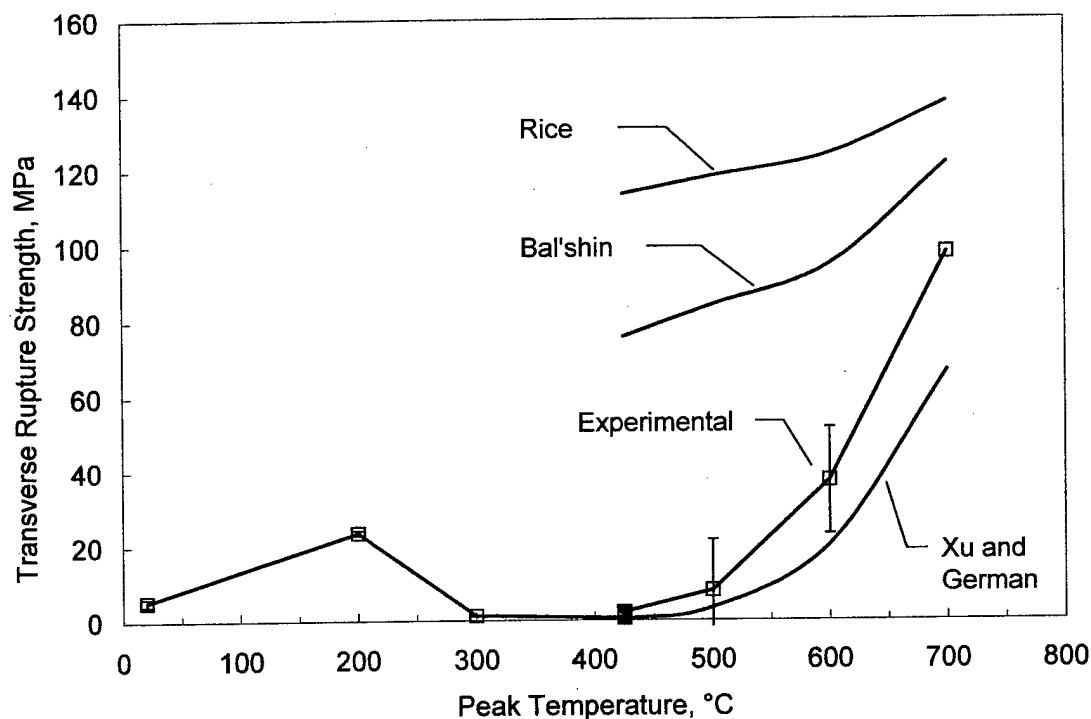


Figure 6.22: Experimental versus calculated transverse rupture strength for PIM material. Heating profile was 3°C/min, with 2-hour hold at 425°C. Samples heated in hydrogen, removed from the furnace and cooled in air

The calculated results show that, similar to the application of porosity-based models to the thermal conductivity prediction, porosity-based models do not capture the dramatic increase in strength observed experimentally, and both overestimate the strength realized during initial stage sintering. The Xu and German model correctly captured the behavior, but the magnitude of the model was lower than that of the measurements. In-

spection showed that even using a factor of 2 versus 1.6 would not account for the observed difference between modeled and observed values. This difference prompted an examination of the ultimate tensile strength values used in the calculation. The ductile nature of the wrought material led to the consideration of true stress, versus handbook ultimate tensile strength, as a more appropriate property.<sup>115</sup> True stress accounts for a reduction in cross-sectional area as a material undergoes plastic deformation. Since the interparticle bonds are showing some ductility on the fracture surface, particularly at 600°C and above, the true stress should better predict when a bond would fail. The conversion of engineering stress to true stress is described by Equation 6.5:

$$\sigma_{true} = \sigma_{eng} (1 + \epsilon_{eng}) \quad ( 6.5 )$$

where  $\sigma_{true}$  is the true stress,  $\sigma_{eng}$  is engineering stress, and  $\epsilon_{eng}$  is the engineering strain.<sup>116</sup> Based on handbook values and tensile test results for Novamet 4SP-10 nickel specimens from other work,<sup>117</sup> an ultimate tensile strength of 360 MPa was used as engineering stress, with an engineering strain of 0.50. The modified format of the Xu and German equation as applied for transverse rupture testing is shown in Equation 6.6.

$$\sigma_{trs} = 1.6 \sigma_{eng} (1 + \epsilon_{eng}) \frac{V_s N_c}{K \pi} \left( \frac{X}{D} \right)^2 \quad ( 6.6 )$$

where  $\sigma_{\text{trs}}$  is the predicted stress at the outer fibers at failure,  $\sigma_{\text{trs}}$  is the handbook ultimate tensile strength at test temperature, and  $\epsilon_{\text{eng}}$  is the percent elongation at failure. As previously described with the Xu and German model,  $V_s$  is the fractional density,  $N_c$  is the coordination number,  $K$  is a stress concentration factor (with a maximum value of 3 for ductile materials), and  $X/D$  is the neck size ratio. The model incorporating true stress and the experimental values are shown in Figure 6.23. The model matches the experimental data with a correlation coefficient of 0.99, and a confidence of 99% that the correlation is statistically significant.

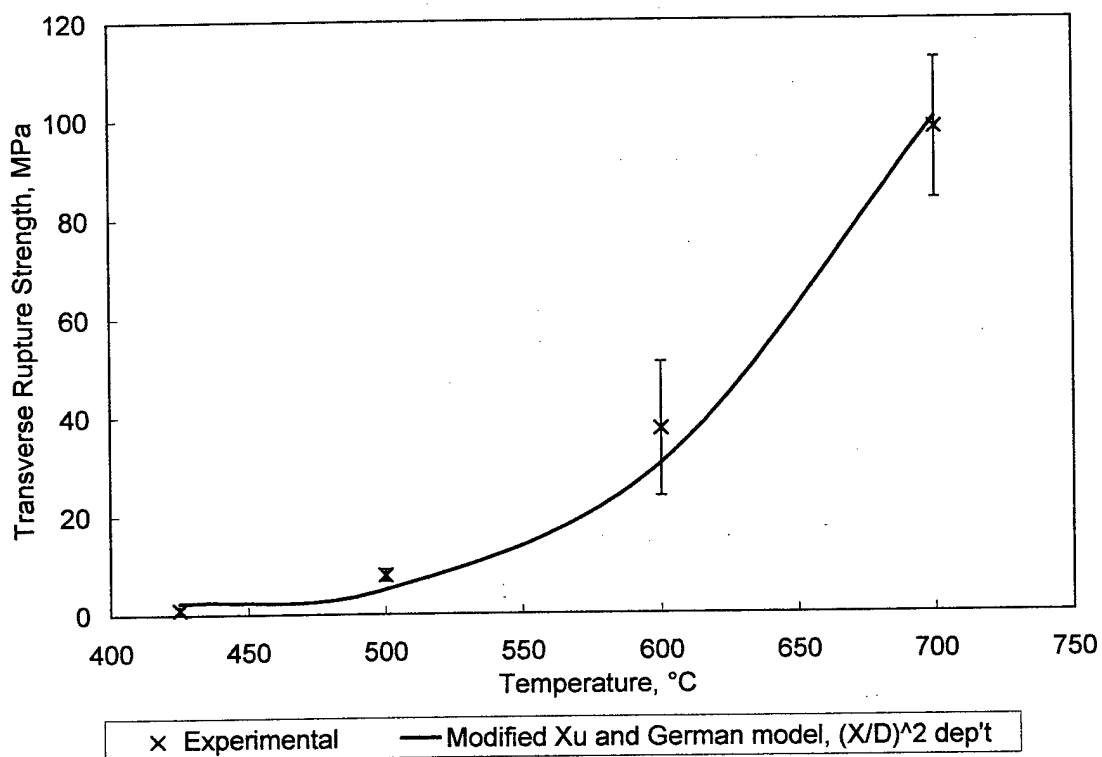


Figure 6.23: Experimental and calculated transverse rupture strength versus peak sintering temperature for PIM material. Samples were tested at room temperature. Error bars reflect a 90% confidence level.

The same modified model was applied to the quasi-PIM material, along with the porosity-based models for comparison. This result is shown in Figure 6.24.

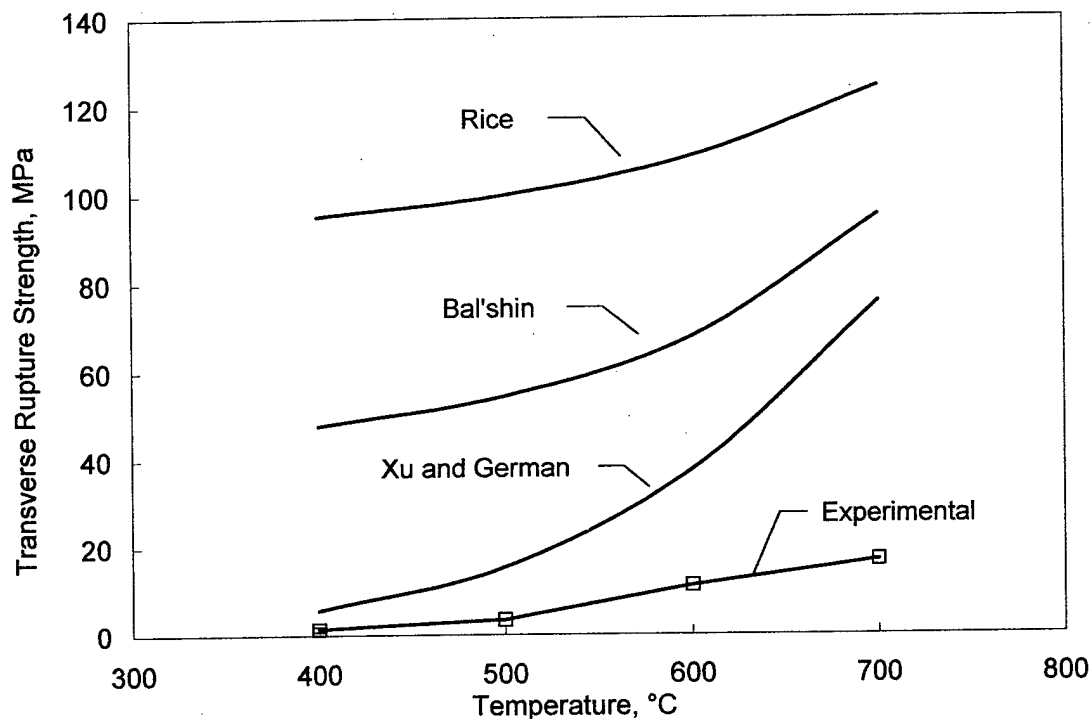


Figure 6.24: Experimental and calculated transverse rupture strength using multiple models for quasi-PIM material. Heating profile was 10°C/min to peak temperature, no hold. Samples heated in hydrogen, water quenched.

Clearly, the quasi-PIM material is failing in a manner not predicted by any of the models. Since neck size has the largest impact on strength, initial neck size observations were questioned and reconfirmed. The probability of a macroscopic manufacturing flaw would explain these results. The technique for making the quasi-PIM material included die-compaction at very light pressures. This process is made quite difficult by the spherical powder, which does not easily stick together. Delamination in the green specimens during ejection from the die was a problem initially, although it was thought that a suc-



cessful process had ultimately been found. It is likely that delamination flaws exist in the interior of the bars that were not noticed earlier. Although flaws were not evident during the sectioning and polishing of the samples, this possibility will be further explored. Additionally, although the quasi-PIM material was only lightly pressed, density gradients and polymer gradients are likely as a result of the pressing process. As described earlier in this discussion, a difference in density through the material can result in "desintering", accentuating gradients and voids as higher density regions pull particles away from low-density regions with fewer bonds. This process potentially drops the coordination number during predensification sintering, and magnifies flaws and voids as sintering progresses.

### 6.2.3 Relating Strength to Thermal Conductivity

Thermal conductivity can be related to strength through the common factor of neck size. Although this relationship is not as originally anticipated – neck size is linear with thermal conductivity, versus squared as predicted, the original hypothesis has been validated. Although currently system dependent, once the thermal conductivity relationship to neck size is profiled, strength can be predicted at any point, either *in situ* or at room temperature, if handbook values for wrought strength, percent elongation, and thermal conductivity are known. The key equations for thermal conductivity and strength as stated in Equations 6.4 and 6.6 can be tied together through  $(X/D)$  as shown in Equation 6.7:

$$\sigma_{ult} = \sigma_{eng} \left(1 + \varepsilon_{eng}\right) \frac{V_s N_c}{K\pi} \left[ \left( \frac{\kappa_{eff}}{\kappa_o} - \gamma \right) \frac{1}{\chi} \right]^2 \quad (6.7)$$

where  $\gamma$  and  $\chi$  are system dependent parameters equal to 0.566 and 0.021 respectively for this system. This relation can be used to predict transverse rupture strength by applying a factor of 1.6 to the ultimate tensile strength,  $\sigma_{ult}$ , predicted in Equation 6.7.

### 6.3 Modeling Capability

A combination of tools is required to implement a predictive capability based on Equation 6.7. Thermal diffusivity via laser flash and dimensional profiling via dilatometry are needed to create a profile of thermal diffusivity for a candidate system. Specific heat values from differential scanning calorimetry or handbook data are needed for a translation to thermal conductivity. A single cycle of each measurement can provide an entire profile of thermal conductivity evolution in a sintering material. Neck size must be either observed, or estimated, to complete the thermal model. Existing computer simulations, such as SintWin 2.3, can provide an estimate of neck size to help define the initial model. Once the two system-dependent parameters are defined, neck size can be validated through a thermal conductivity measurement, and mechanical strength can be predicted.

#### 6.4 Impact of Secondary Results

Although the secondary results are all related to the quasi-PIM material, which yielded questionable strength data, it is still worthwhile to consider other observed properties with respect to neck size. The consistent behavior of the quasi-PIM material during the secondary measurements indicates that other techniques are not as sensitive to internal flaws as a destructive strength test. If delamination flaws were in fact present, they would be more evident in ultrasonic and resonant frequency evaluation, where the transverse dimension (the thickness of the bar) is critical to the measurement. Such flaws may not affect electrical conductivity measurements, which measured parallel to a possible delamination flaw.

Young's modulus was evaluated via ultrasonic measurement and via resonant frequency testing. As in strength models, most Young's modulus models are based on porosity (or density). One model incorporating neck size has been proposed by Green in similar studies on ceramic materials.<sup>77,78</sup> In this case, bulk modulus is shown as a linear function of neck size ratio according to Equation 6.8:

$$\frac{B}{B_o} = \frac{3N_c}{8k} \left[ \frac{X}{D} \right] \left[ \frac{1-2\nu_o}{1-\nu_o^2} \right] \quad ( 6.8 )$$

where  $B$  and  $B_o$  are the bulk modulus of the porous and bulk material,  $k$  is a geometric constant ( $k=1$  for spherical particles), and  $\nu_o$  is Poisson's ratio of the bulk material. Since bulk modulus is related to Young's modulus by Equation 6.9:<sup>118</sup>

$$B = \frac{E}{3(1-2\nu)} \quad (6.9)$$

Young's modulus should also vary linearly with neck size ratio. Young's modulus as measured by both techniques is compared to neck size ratio in Figure 6.25.

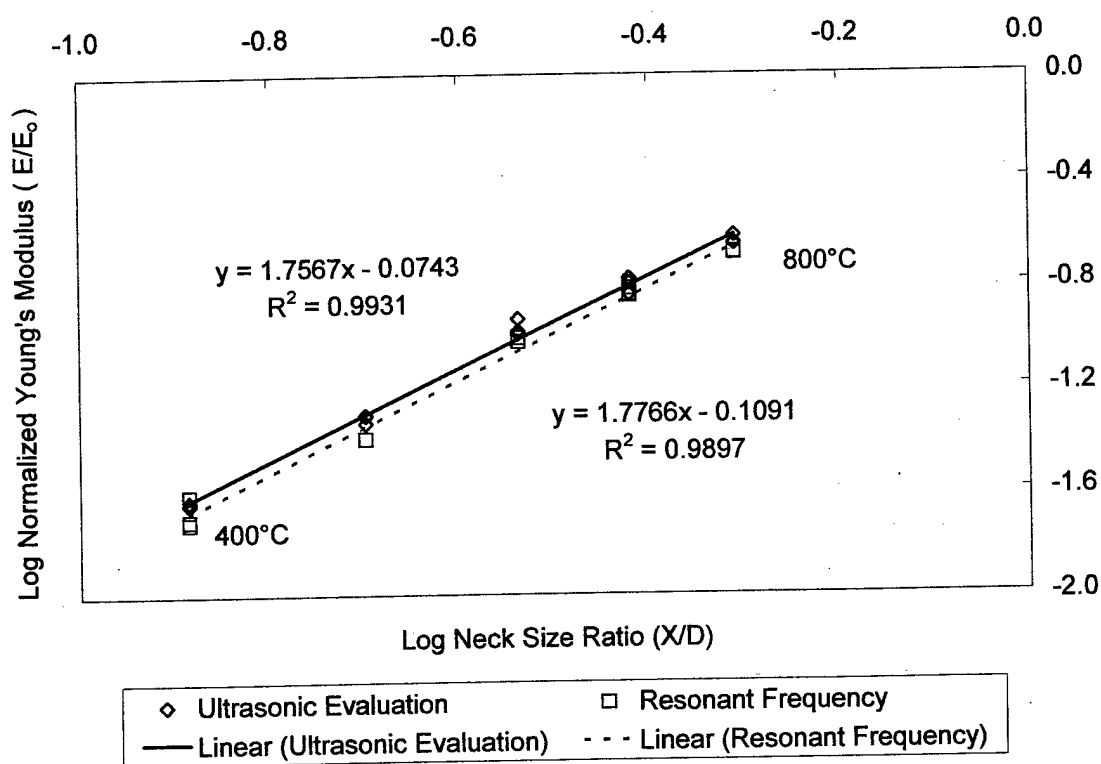


Figure 6.25: Elastic modulus versus neck size ratio for quasi-PIM material. Slope of linear regression indicates exponent of neck size in Young's modulus model. Confidence in statistical significance is 99% for both sets of data.

As noted in Chapter 4, results from the two techniques were very similar. Using the slope of the linear regression, both techniques yield dependence of Young's modulus on neck size closer to two, indicating a squared relationship. However, looking at the comparison of experimental results versus Green's predicted bulk modulus, shown in Figure 6.26, it is clear that the material's elastic properties were well below those predicted. Any assessment based on these values is speculative in nature. It should also be noted that the basis of Green's model is a small neck size with respect to particle size, so

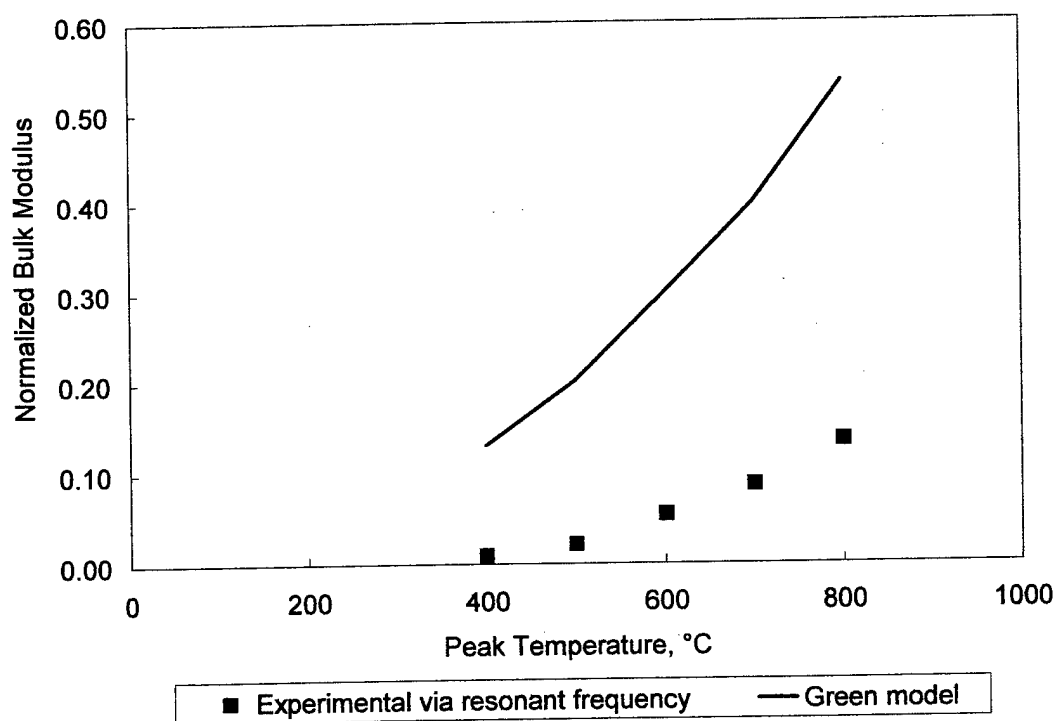


Figure 6.26: Calculated and measured bulk modulus of quasi-PIM material versus peak sintering temperature. Bulk modulus calculated from Young's modulus and Poisson's ratio values measured via resonant frequency evaluation.

values projected above 600°C overextend the intent of the model.

Electrical conductivity was compared to existing models presented by Ondracek, Koh and Fortini, and Havier, Panek, and Sajgalik, all described in Chapter 2. This comparison is shown in Figure 6.27. The first two models are porosity-based, while the third is a logarithmic function of neck size ratio. Although none of the models match the experimental data, the overlap between the lower limit Ondracek model, the Koh and Fortini model and the experimental data indicate that the measured values are at the lower limit of the expected magnitude. However, electrical conductivity varies more with increased sintering temperature than porosity-based models predict, with measured values overestimated at lower sintering temperatures, and underestimated at higher temperatures. The Havier model shows a sensitivity (slope) similar to the experimental data, although the model significantly overestimates the magnitude for this system.

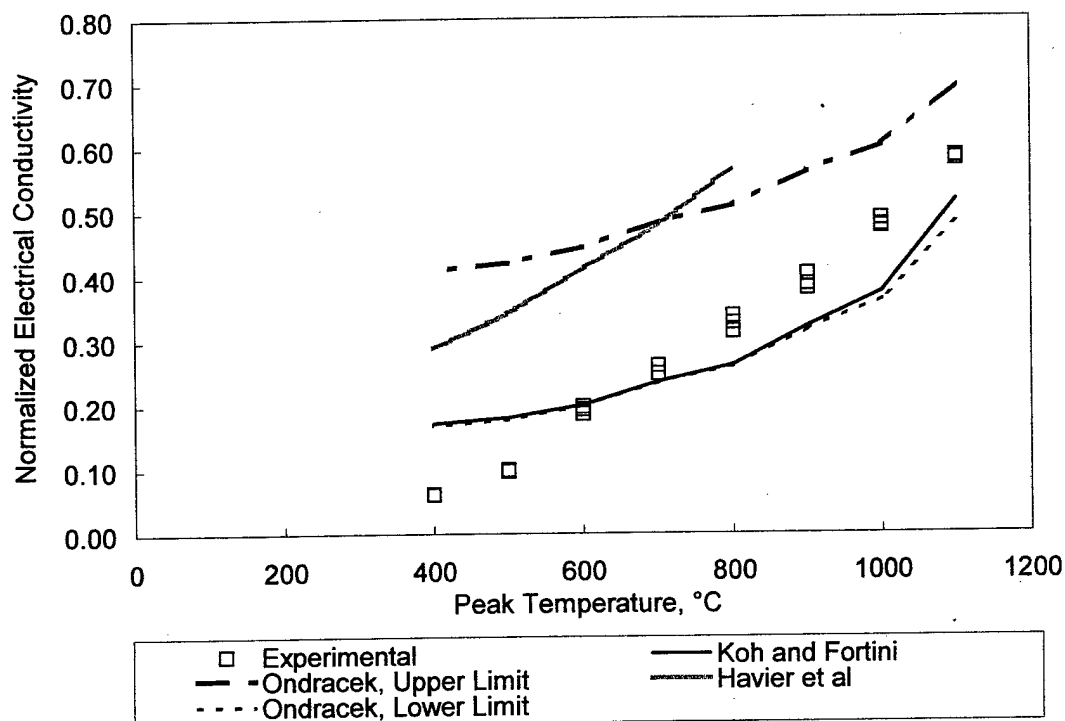


Figure 6.27: Calculated and experimental room temperature electrical conductivity versus peak sintering temperature for quasi-PIM material. Heating profile was 10°C/min to peak temperature, no hold. Samples were heated in hydrogen and water quenched.

Electrical conductivity results were also compared to neck size. Since electrical and thermal conductivity in a metal are influenced by the same mechanisms (free electron population and mobility), a linear dependence on neck size was expected. The comparison is shown in Figure 6.28. The Havier model was also included for comparison. Experimental results indicate an even greater sensitivity to neck size than the Havier model predicts. As noted in Figure 6.27, the magnitude predicted by the model is significantly higher than the measured values. However, as noted in Figure 4.29, the magnitude of

measured electrical conductivity does correspond to that predicted by the Wiedemann-Franz relationship based on measured thermal conductivity. This concurrence lends confidence that the measured values are representative of the system.

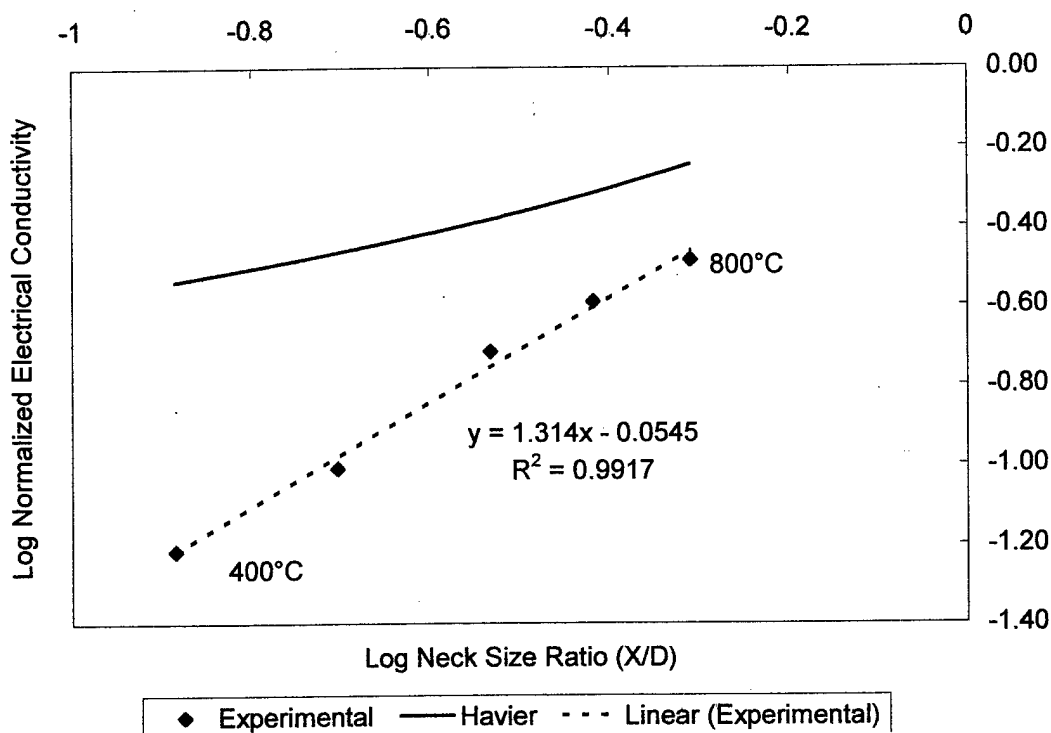


Figure 6.28: Electrical conductivity versus neck size for quasi-PIM material. Slope of linear regression indicates exponent of neck size in electrical conductivity model.

Linear regression analysis of the experimental data shows that the slope is slightly greater than one, indicating an approximately linear dependence of electrical conductivity on neck size. Confidence in the statistical significance of the data is greater than 99%.



In summary, the secondary test observations fall in line with those of the primary test observations – elastic properties and electrical conductivity appear to be strongly correlated to neck size. In particular, electrical conductivity results support conclusions reached in thermal conductivity evaluation – conductivity in early stage sintering varies linearly with neck size. As expected, porosity-based models (eg. Ondracek, Koh and Fortini) do not adequately describe the observed evolution during initial stage sintering. Comparison with a logarithmic model based on neck size showed a trend more similar to experimental data, but measured values were much lower in magnitude. Elastic properties (Young's modulus as measured by ultrasonic and resonant frequency evaluation) appear to vary with the square of neck size, or directly with the area of the neck, although this conclusion is more speculative with the given data. It is noted that this conclusion does not agree with Green's model, which describes elastic properties as a linear function of neck size. However, the secondary testing does demonstrate the correlation of each set of properties with the neck size for the given system. If the system profile is known, it is possible to infer one property from the other, in support of the hypothesis of this work.

## Chapter 7

### Conclusions

The goal of this work was to examine the hypothesis that thermal conductivity measurements could be used as a means to assess mechanical strength during the fragile initial stage of sintering. In pursuit of that goal, three areas were addressed. First, the viability of the laser flash technique as a sintering monitor for powder metallurgy materials was investigated. Second, a method was developed to assess and model thermal conductivity of powder metallurgy materials during initial stage sintering. Third, a relationship between thermal conductivity and mechanical strength was established. Research in each of these three areas yielded valuable conclusions, summarized below.

Laser flash analysis is indeed a viable means of monitoring initial stage sintering in both *in situ* and post-sintering applications. *In situ* observations show a clear evolution in thermal diffusivity and thermal conductivity with increasing temperature. Post measurement observations have demonstrated that the temperature transient associated with the laser flash does not impact sintering or structural integrity of powder metallurgy materials. Laser flash measurements do have a destructive effect on binder polymers present in the material. Ash on the surface of samples containing residual binder was evidence of thermal decomposition of the polymer as a result of the localized energy of the laser flash. However, the presence of the ash did not appear to affect the stability or accuracy of the measurement. An additional constraint related to the presence of binder is the con-

cern of fouling the optics train by conducting thermal debinding operations in the laser flash equipment. This concern leads to the conclusion that *in situ* testing of PIM materials during thermal debinding is not a recommended practice. However, room temperature evaluations on this segment of materials have been demonstrated as effective.

A technique to assess thermal conductivity of powder metallurgy materials has been developed and modeled. Knowledge of sample thickness during *in situ* measurements is critical, so it is essential to understand both thermal expansion and shrinkage behavior in the sintering system. Dilatometry conducted in conjunction with laser flash provides the necessary information. Thermal conductivity during early stage sintering has been shown to be a linear function of neck size, versus a squared function as originally suspected. Profiling a system for such a model must include an additional assessment of neck size, via SEM observation and computer simulation, as demonstrated in this work, or by some alternate method. Once an initial profile is established, neck size may be extracted from *in situ* laser flash measurements under any sintering conditions of interest.

Finally, a clear relationship between the evolution of thermal conductivity and mechanical strength has been demonstrated. Both properties are functions of neck size; therefore if neck size can be inferred from thermal conductivity evaluation, mechanical strength can be assessed. This correlation has been most clearly demonstrated in an injection-molded material, where thermal conductivity and strength are more sensitive to the onset of sinter bonding than die-compacted materials. Laser flash analysis, as a non-contact measurement, overcomes the difficulties of measuring strength mechanically in a

fragile material, providing the capability of a non-destructive means of assessing the onset of handling strength.

The views expressed in this publication are those of the author and do not reflect the official policy or position of the United States Air Force, Department of Defense, or the U. S. Government.

## References

- <sup>1</sup> R. M. German, *Powder Metallurgy Science*, 2d edition, Metal Powder Industries Federation, Princeton NJ, 1994.
- <sup>2</sup> R. M. German, *Sintering Theory and Practice*, John Wiley and Sons, Inc., New York, NY, 1996.
- <sup>3</sup> R. M. German, Lecture Notes from ESc 597A "*Sintering Theory and Practice*," The Pennsylvania State University, Fall 2000.
- <sup>4</sup> G. C. Kuczynski, "Self-Diffusion in Sintering of Metallic Particles," *Transactions AIME*, 1949, vol. 185, pp. 169-178.
- <sup>5</sup> R. L. Coble, "Initial Sintering of Alumina and Hematite," *Journal of the American Ceramic Society*, 1958, vol. 41, pp. 55-62.
- <sup>6</sup> W. D. Kingery and M. Berg, "Study of the Initial Stages of Sintering Solids by Viscous Flow, Evaporation-Condensation, and Self-Diffusion," *Journal of Applied Physics*, 1955, vol. 26, pp. 1205-1212.
- <sup>7</sup> P. Bross and H. E. Exner, "Computer Simulation of Sintering Processes," *Acta Metallurgica*, 1979, vol. 27, pp. 1013-1020.
- <sup>8</sup> M. F. Ashby, "A First Report on Sintering Diagrams," *Acta Metallurgica*, 1974, vol. 22, pp. 275-289.
- <sup>9</sup> F. B. Swinkels and M. F. Ashby, "A Second Report on Sintering Diagrams," *Acta Metallurgica*, 1981, vol. 29, pp. 259-281.
- <sup>10</sup> D. L. Johnson, "Recent Developments in the Theoretical Analysis of Solid State Sintering," *Sintering: Theory and Practice, Proceedings from the 5<sup>th</sup> International Round Table Conference on Sintering*, D. Kolar, L. Pejovnik, and M. M. Ristic (eds.), Elsevier Scientific, Amsterdam, 1982, pp. 17-26.
- <sup>11</sup> K. S. Hwang, R. M. German, and F. V. Lenel, "Analysis of Initial Stage Sintering Through Computer Simulation," *Powder Metallurgy International*, 1991, vol. 23, pp. 86-92.

- <sup>12</sup> S. G. Dubois, "Sintering of High Surface Area Tantalum Powder: Simulation and Experimental Verification," M. S. Thesis, The Pennsylvania State University, 1995.
- <sup>13</sup> B. L. Mordike, J. P. Jernot, and J. L. Chermant, "Sintering of Nickel Powders II. Influence of the Particle Size on the Physical Properties," *Zeitschrift fuer Metallkunde*, 1984, vol. 75, no. 12, pp. 918-922.
- <sup>14</sup> H. E. Exner, "Solid-State Sintering: Critical Assessment of Theoretical Concepts and Experimental Methods," *Powder Metallurgy*, 1980, vol. 23, no. 4, pp. 203-209.
- <sup>15</sup> S. H. Hillman and R. M. German, "Constant Heating Rate Analysis of Simultaneous Sintering Mechanisms in Alumina," *Journal of Materials Science*, 1992, vol. 27, pp. 2641-2648.
- <sup>16</sup> G. A. Shoales, *In Situ Strength Evolution in the Sintering of Bronze Powder Metal Compacts and Application to Thermal Cycle Design*, Ph. D. thesis, The Pennsylvania State University, 1998.
- <sup>17</sup> X. Xu, *Densification, Microstructure, and Strength Evolution in Sintering*, Ph. D. thesis, The Pennsylvania State University, 2000.
- <sup>18</sup> J. Ziman, "The Thermal Properties of Materials," *Materials*, W. H. Freeman and Company, San Francisco, CA, 1967, pp. 111-125.
- <sup>19</sup> R. J. Weiss, *Solid State Physics for Metallurgists*, Addison-Wesley Publishing Company, Inc., Reading, MA, 1963, pp. 286-290.
- <sup>20</sup> R. W. Powell, "Correlation of Metallic Thermal and Electrical Conductivities for Both Solid and Liquid Phases," *International Journal of Heat and Mass Transfer*, vol. 8, pp. 1033-1045.
- <sup>21</sup> Y. S. Touloukian, R. W. Powell, C. Y. Ho, and M. C. Nicolaou, *Thermophysical Properties of Matter, Volume 10: Thermal Diffusivity*, IFI/Plenum, New York, NY, 1973.
- <sup>22</sup> H. H. Hausner and J. H. Dedrick, "Electrical Properties as Indicators of the Degree of Sintering," *The Physics of Powder Metallurgy*, W. E. Kingston (ed.), McGraw-Hill, New York, NY, 1951, pp. 320-343.
- <sup>23</sup> R. Meyer, "The Measurement of Electrical Resistivity to Characterize a Sintered Product," *Powder Metallurgy International*, 1972, vol. 4, no. 2, pp. 63-66.
- <sup>24</sup> E. R. Leheup and J. R. Moon, "Electrical Conductivity and Strength Changes in Green Compacts of Iron Powder when Heated in Range 50-400°C in Air," *Powder Metallurgy*, 1980, vol. 4, pp. 217-220.

- <sup>25</sup> A. Lewis, "Nondestructive Inspection of Powder Metallurgy Parts through the Use of Resistivity Measurements," *Prevention and Detection of Cracks in Ferrous P/M Parts Seminar*, Metal Powder Industries Federation, Princeton, NJ, 1988, pp. 93-103.
- <sup>26</sup> A. Simchi and H. Danninger, "Electrical Conductivity and Microstructure of Sintered Ferrous Materials: Sintered Iron," *Powder Metallurgy*, 2000, vol. 43, no. 2, pp. 209-217.
- <sup>27</sup> A. Simchi, H. Danninger, and B. Weiss, "Microstructural Modeling of Electrical Conductivity and Mechanical Properties of Sintered Ferrous Materials," *Powder Metallurgy*, 2000, vol. 43, no. 3, pp. 219-227.
- <sup>28</sup> P. S. Kislyi, "Device for Measuring Shrinkage and Electrical Resistance," *Soviet Powder Metallurgy*, 1962, vol. 7, pp. 120-121.
- <sup>29</sup> J. M. Brettell, "Electrical Resistivity of Sintered Aluminum Powder Compacts," *Powder Metallurgy International*, 1981, vol. 13, no. 2, p 86-87.
- <sup>30</sup> J. P. Jernot and J. L. Chernat, "On the Importance of Contiguity and Electrical Conductivity for Sintered Materials," *Scripta Metallurgica*, 1982, vol. 16, no. 8, pp. 943-946.
- <sup>31</sup> R. W. Rice, "Evaluation and Extension of Physical Property-Porosity Models Based on Minimum Solid Area," *Journal of Materials Science*, 1996, vol. 31, no. 6, pp. 1509-1528.
- <sup>32</sup> J. S. Hirschhorn, *Introduction to Powder Metallurgy*, American Powder Metallurgy Institute, New York, NY, 1969, p. 267.
- <sup>33</sup> G. F. Bocchini, "The Influences of Porosity on the Characteristics of Sintered Materials," *Reviews of Powder Metallurgy and Physical Ceramics*, 1985, vol. 2, no. 4, pp. 313-360.
- <sup>34</sup> G. Ondracek and P. Nikolopoulos, "The Correlation between Properties and Porosity of Sintered Materials," *P/M-82 in Europe / International Powder Metallurgy Conference, Florence, Italy, June 20-25, 1982*, Associazione Italiana di Metallurgia, Milan, Italy, 1982, pp. 89-97.
- <sup>35</sup> D. R. Shonnard and S. Whitaker, "The Effective Thermal Conductivity for a Point-Contact Porous Medium: An Experimental Study," *International Journal of Heat and Mass Transfer*, 1989, vol. 34, no. 3, pp. 503-512.
- <sup>36</sup> A. A. Belyaev, A. Yu. Zubarev, E. W. Kats, and V. M. Kiseev, "Effective Thermal Conductivity of a Structured Powder," Translated from *Inzhenerno-Fizicheskii Zhurnal*, 1988, vol. 55, no. 1, pp. 122-130.

- <sup>37</sup> A. V. Luikov, A. G. Shashkov, L. L. Vasiliev and Y. E. Fraiman, "Thermal Conductivity of Porous Systems," *International Journal of Heat and Mass Transfer*, 1968, vol. 11, pp. 117-140.
- <sup>38</sup> G. K. Batchelor and R. W. O'Brien, "Thermal or Electrical Conduction Through a Granular Material," *Proceedings of the Royal Society of London, A. Mathematical and Physical Sciences*, 1977, vol. 355, no. 1680, pp. 313-335.
- <sup>39</sup> M. Haviar, Z. Panek, and P. Sajgalik, "The Use of Electrical Conductivity Measurements to Study Sintering Mechanisms," *Ceramics International*, 1985, vol. 11, no. 1, pp. 13-16.
- <sup>40</sup> H.S. Carslaw and J. C. Jaeger, *Conduction of Heat in Solids*, 2<sup>nd</sup> edition, Clarendon Press, Oxford, UK, 1959.
- <sup>41</sup> C. Argento and D. Bouvard, "Modeling the Effective Thermal Conductivity of Random Packing of Spheres Through Densification," *International Journal of Heat and Mass Transfer*, 1996, vol. 39, no. 7, pp. 1343-1350.
- <sup>42</sup> G. R. Hadley, "Thermal Conductivity of Packed Metal Powder," *International Journal of Heat and Mass Transfer*, 1986, vol. 29, no. 6, pp. 909-920.
- <sup>43</sup> J. C. Maxwell, *A Treatise on Electricity and Magnetism Vol. 2*, Dover Pub. Inc., New York, NY, 1954, pp. 435-441.
- <sup>44</sup> A. Birnboim, T. Olorunyolemi, and Y. Carmel, "Calculating the Thermal Conductivity of Heated Powder Compacts," *Journal of the American Ceramic Society*, 2001, vol. 84, no. 6, pp. 1315-1320.
- <sup>45</sup> T. Olorunyolemi, A. Birnboim, Y. Carmel, O. C. Wilson Jr., and I. K. Lloyd, "Thermal Conductivity of Zinc Oxide: From Green to Sintered State," *Journal of the American Ceramic Society*, 2002, vol. 85, no. 5, pp. 1249-53.
- <sup>46</sup> J. C. Y. Koh and A. Fortini, "Prediction of Thermal Conductivity and Electrical Resistivity of Porous Metallic Materials," *International Journal of Heat and Mass Transfer*, vol. 16, pp. 2013-2021.
- <sup>47</sup> P. Howard and M. J. Koczak, "How Porosity and Atmosphere Affect the Thermal Conductivity of P/M Parts," *International Journal of Powder Metallurgy and Powder Technology*, 1981, vol. 17, no. 1, pp. 25-35.
- <sup>48</sup> D. Kunii and J. M. Smith, "Heat Transfer Characteristics of Porous Rocks," *A.I.Ch.E. Journal*, 1960, vol. 6, no. 97, pp. 71-78.
- <sup>49</sup> A. V. Luikov, *Heat and Mass Transfer in Capillary-Porous Bodies*, Pergamon Press, New York, NY, 1966.



- <sup>50</sup> V. V. Murashov and M. A. White, "Thermal Conductivity of Crystalline Particulate Materials," *Journal of Materials Science*, 2000, vol. 35, pp. 649-653.
- <sup>51</sup> A. L. Loeb, "Thermal Conductivity: VIII, A Theory of Thermal Conductivity of Porous Materials", *Journal of the American Ceramic Society*, 1954, vol. 37, p. 96-99.
- <sup>52</sup> M. Golombok and L. C. Shirvill, "Laser Flash Thermal Conductivity Studies of Porous Metal Fiber Materials," *Journal of Applied Physics*, 1988, vol. 63, no. 6, pp. 1971-1976.
- <sup>53</sup> Y. Litovsky and M. Shapiro, "Gas Pressure and Temperature Dependences of Thermal Conductivity of Porous Ceramic Materials: Part 1, Refractories and Ceramics with Porosity below 30 %," *Journal of the American Ceramic Society*, vol. 75, 1992, p. 3425-3439.
- <sup>54</sup> H. Szelagowski, I. Arvanitidis, and S. Seetharaman, "Effective Thermal Conductivity of Porous Strontium Oxide and Strontium Carbonate Samples," *Journal of Applied Physics*, 1999, vol. 85, no. 1, pp. 193-198.
- <sup>55</sup> "ASTM B63-90 Standard Test Method for Resistivity of Metallically Conducting Resistance and Contact Materials," *Annual Book of ASTM Standards 2001*, vol. 02.04, American Society for Testing and Materials, West Conshohocken, PA, 2001, pp. 21-24.
- <sup>56</sup> D. C. Zenger, R. Ludwig, R. Zhang, and L. McCabe, "Detecting Cracks in Green P/M Components," *Advances in Powder Metallurgy and Particulate Materials*, Metal Powder Industries Federation, Princeton, NJ, 1995, pp. 9/3-9/16.
- <sup>57</sup> G. Bogdanov, R. Ludwig, and W. R. Michalson, "A New Apparatus for Non-Destructive Evaluation of Green-State Powder Metal Compacts using the Electrical Resistivity Method," *Measurement Science Technology*, 2000, vol. 11, pp. 157-166.
- <sup>58</sup> G. A. Weissler, "The Electrical Resistance of Metal Powder Compacts: Influence of Surface Layers," *Powder Metallurgy International*, 1979, vol. 11, no. 3, pp. 112-114.
- <sup>59</sup> R. F. Speyer, *Thermal Analysis of Materials*, Marcel Dekker, Inc., New York, NY, 1994, pp. 227-250.
- <sup>60</sup> L. M. Jiji, *Heat Transfer Essentials*, Begell House, Inc, New York, NY, 1998, p. 15.
- <sup>61</sup> W. J. Parker, R. J. Jenkins, C. P. Butler, and G. L. Abbott, "Flash Method of Determining Thermal Diffusivity, Heat Capacity, and Thermal Conductivity," *Journal of Applied Physics*, 1961, vol. 32, no. 9, pp. 1679-1684.
- <sup>62</sup> "ASTM E1461-92 Standard Test Method for Thermal Diffusivity of Solids by the Flash Method," *Annual Book of ASTM Standards 1999*, vol. 14.02, American Society for Testing and Materials, West Conshohocken, PA, 2001, pp. 575-582.

- <sup>63</sup> R. C. Campbell and S. E. Smith, "Flash Diffusivity Method: A Survey of Capabilities," *Electronics Cooling*, 2002, vol. A4, pp. 1-11.
- <sup>64</sup> R. D. Cowan, "Pulse Method of Measuring Thermal Diffusivity at High Temperatures," *Journal of Applied Physics*, 1963, vol. 34, no. 4, pp. 926-927.
- <sup>65</sup> J. A. Cape and G. W. Lehman, "Temperature and Finite Pulse-Time Effects in the Flash Method for Measuring Thermal Diffusivity," *Journal of Applied Physics*, 1963, vol. 34, no. 7, pp. 1909-1913.
- <sup>66</sup> R. E. Taylor and J. A. Cape, "Finite Pulse-Time Effects in the Flash Diffusivity Technique," *Applied Physics Letters*, 1964, vol. 5, no. 10, pp. 212-213.
- <sup>67</sup> L. M. Clark III and R. E. Taylor, "Radiation Loss in the Flash Method for Thermal Diffusivity," *Journal of Applied Physics*, 1975, vol. 46, no. 2, pp. 714-719.
- <sup>68</sup> J. A. Koski, "Improved Data Reduction Methods for Laser Pulse Diffusivity Determination with the Use of Minicomputers," *Proceedings of the Eighth Symposium on Thermophysical Properties*, <sup>vol. II</sup>, The American Society of Mechanical Engineers, New York, NY, 1981, pp. 94-103.
- <sup>69</sup> M-A. Thermitus, Anter Corporation, personal conversation, June 2002.
- <sup>70</sup> A. Cezairliyan, T. Baba, and R. Taylor, "A High-Temperature Laser-Pulse Thermal Diffusivity Apparatus," *International Journal of Thermophysics*, 1994, vol. 15, no. 2, pp. 317-341.
- <sup>71</sup> J. Gembarovic and R. E. Taylor, "A New Technique for Data Reduction in the Flash Method for the Measurement of Thermal Diffusivity," *High Temperatures - High Pressures*, 1994, vol. 26, pp. 59-65.
- <sup>72</sup> O. Hahn, F. Raether, M. C. Arduini-Schuster, and J. Fricke, "Transient Coupled Conductive/Radiative Heat Transfer in Absorbing, Emitting and Scattering Media: Application to Laser-flash Measurements on Ceramic Materials," *International Journal of Heat and Mass Transfer*, 1997, vol. 40, no. 3, pp. 689-698.
- <sup>73</sup> H. Danninger and G. Leitner, "In Situ Characterization of the Sintering Process in Ferrous Compacts through Thermal Diffusivity Measurement," *Advances in Powder Metallurgy and Particulate Materials -2002*, Metal Powder Industries Federation, Princeton, NJ, 2002, pp. 13-157 to 13-167.
- <sup>74</sup> M. Yu. Bal'shin, "Relation of Mechanical Properties of Powder Metals and their Porosity and the Ultimate Properties of Porous Metal-Ceramic Materials," *Doklady Akad. Science*, 1949, vol. 67, pp. 831-834.

- <sup>75</sup> V. A. Tracey, "A Critical Assessment of Strength Development in Porous Materials," *Modern Developments in Powder Metallurgy*, 1988, vol. 21, pp. 745-754.
- <sup>76</sup> V. A. Tracey, "Sintering of Porous Nickel," *Powder Metallurgy*, 1983, vol. 26, no. 2, pp. 89-92.
- <sup>77</sup> S. C. Nanjangud, R. Brezny, and D. J. Green, "Strength and Young's Modulus Behaviour of a Partially Sintered Porous Alumina," *Journal of the American Ceramic Society*, 1995, vol. 78, no. 1, pp. 266-268.
- <sup>78</sup> D. Hardy and D. J. Green, "Mechanical Properties of Partially Sintered Alumina," *Journal of the European Ceramic Society*, 1995, vol. 15, pp. 769-775.
- <sup>79</sup> J. F. Yang, T. Ohji, S. Kanzaki, A. Diaz, and S. Hampshire, "Microstructure and Mechanical Properties of Silicon Nitride Ceramics with Controlled Porosity," *Journal of the American Ceramic Society*, 2002, vol. 85, no. 6, pp. 1512-16.
- <sup>80</sup> R. M. German, "Manipulation of Strength During Sintering as a Basis for Obtaining Rapid Densification without Distortion," *Materials Transactions*, 2001, vol. 42, no. 7, pp. 1400-1410.
- <sup>81</sup> R. L. Coble and W. D. Kingery, "Effect of Porosity on Physical Properties of Sintered Alumina," *Journal of the American Ceramic Society*, 1956, vol. 39, no. 11, pp. 377-385.
- <sup>82</sup> R. W. Rice, "Comparison of Physical Property - Porosity Behavior with Minimum Solid Area Models," *Journal of Materials Science*, 1996, vol. 31, pp. 1509-1528.
- <sup>83</sup> P. Arato, E. Besenyeyi, A. Kele, and F. Weber, "Mechanical Properties in the Initial Stage of Sintering," *Journal of Materials Science*, 1995, vol. 30, no. 7, pp. 1863-1871.
- <sup>84</sup> G. A. Shoales, "In Situ Strength Evolution of P/M Compacts in Response to the Combined Effects of Time and Temperature during Sintering," *Advances in Powder Metallurgy and Particulate Materials - 1999*, Metal Powder Industries Federation, Princeton, NJ, 1999, pp. 3-249 to 3-261.
- <sup>85</sup> G. A. Shoales, "In Situ Strength Evolution During the Sintering of Bronze Powders," *Metallurgical and Materials Transactions A: Physical Metallurgy and Materials Science*, 1998, vol. 29A, no. 4, pp. 1257-1263.
- <sup>86</sup> X. Xu, "Densification and Strength Evolution in Solid-State Sintering. Part I Experimental Investigation," *Journal of Materials Science*, 2002, vol. 37, pp. 567-575.
- <sup>87</sup> X. Xu, "Densification and Strength Evolution in Solid-State Sintering. Part II Strength Model," *Journal of Materials Science*, 2002, vol. 37, pp. 117-126.
- <sup>88</sup> *Standard Test Methods for Metal Powders and Powder Metallurgy Products*, Metal Powder Industries Federation, Princeton, NJ, 1999.

- <sup>89</sup> N. E. Dowling, *Mechanical Behavior of Materials*, 2<sup>nd</sup> edition, Prentice-Hall, Inc., Upper Saddle River, NJ, 1999.
- <sup>90</sup> T. Allen, *Particle Size Measurement*, Vol. 1, 5th ed., Chapman and Hall, New York, NY, 1997, pp. 404-416.
- <sup>91</sup> *Standard Test Methods for Metal Powders and Powder Metallurgy Products*, Metal Powders Industry Federation, Princeton, NJ, 1999
- <sup>92</sup> Personal communication with Dr A. Thermitus, Anter Corporation, 23 May 2003.
- <sup>93</sup> G. Gaussorgues, *Infrared Thermography*, Chapman and Hall, London, UK, 1994.
- <sup>94</sup> Y. S. Touloukian and D. P. DeWitt, *Thermophysical Properties of Matter, Volume 8: Thermal Radiative Properties*, IFI/Plenum, New York, NY, 1972.
- <sup>95</sup> "ASTM E 494-95 Standard Practice for Measuring Ultrasonic Velocity in Materials", *Annual Book of ASTM Standards 2001*, Vol. 03.03, American Society for Testing and Materials, West Conshohocken, PA, 2001, pp. 192-204.
- <sup>96</sup> B. R. Tittmann, M. Abdel-Gawad, and K. Fertig, "Ultrasonic Characterization of Microstructure in Powder Metal Alloy", *Research in Nondestructive Evaluation*, vol. 2, pp. 119-133.
- <sup>97</sup> "ASTM E 1875-00 Standard Test Method for Dynamic Young's Modulus, Shear Modulus, and Poisson's Ratio by Sonic Resonance", *Annual Book of ASTM Standards 2001*, Vol. 03.01, American Society for Testing and Materials, West Conshohocken, PA, 2001, pp. 1091-1098.
- <sup>98</sup> P. A. Hoffman, *Thermoelastic Properties of Silicon Carbide-Titanium Diboride Particulate Composites*, M.S. thesis, The Pennsylvania State University, 1992, pp. 35-40.
- <sup>99</sup> M. J. Pan, *Microcracking Behavior of Particulate Titanium Diboride-Silicon Carbide Composites and Its Influence on Elastic Properties*, Ph.D. thesis, The Pennsylvania State University, 1994, pp. 88-94.
- <sup>100</sup> "ASTM B63-90 Standard Test Method for Resistivity of Metallically Conducting Resistance and Contact Materials", *Annual Book of ASTM Standards 2001*, Vol. 02.04, American Society for Testing and Materials, West Conshohocken, PA, 2001, pp. 21-24.
- <sup>101</sup> *ASM Metals Handbook*, 2nd edition, J.R. Davis (ed.), ASM International, Materials Park, OH, 1998.
- <sup>102</sup> L. Bjerregaard, *Metallog Guide*, 2d ed., Struers A/S, Denmark, 1996.
- <sup>103</sup> Personal communication with Mr. Lou Kohler, Novamet Inc., January 2002.

- <sup>104</sup> R. M. German and A. Bose, *Injection Molding of Metals and Ceramics*, Metal Powder Industries Federation, Princeton, NJ, 1997.
- <sup>105</sup> Y. S. Touloukian and E. H. Buyco, *Thermophysical Properties of Matter, Volume 4: Specific Heat*, IFI Plenum, New York, NY, 1970.
- <sup>106</sup> J. S. Agapiou and M. F. DeVries, "An Experimental Determination of the Thermal Conductivity of a 304L Stainless Steel Powder Metallurgy Material", *Journal of Heat Transfer*, May 1989, vol. 111, pp. 281-286.
- <sup>107</sup> Y. S. Touloukian, R. W. Powell, C. Y. Ho, and P. G. Klemens, *Thermophysical Properties of Matter, Volume 1: Thermal Conductivity Properties*, IFI/Plenum, New York, NY, 1972.
- <sup>108</sup> D. R. Clarke, "Materials Selection Guidelines for Low Thermal Conductivity Thermal Barrier Coatings,"  
<http://www.materials.ucsb.edu/MURI/papers/SanDiegoThermalSelection.pdf>
- <sup>109</sup> H. Szelagowski, I. Arvanitidis, and S. Seetharaman, "Effective Thermal Conductivity of Porous Strontium Oxide and Strontium Carbonate Samples", *Journal of Applied Physics*, 1999, vol. 85, no. 1, pp. 193-198.
- <sup>110</sup> T. S. Wei and R. M. German, "The Dilatometry Study of Sintering Mechanisms of Nickel in Constant Rate of Heating," *Modern Developments in Powder Metallurgy*, Proceedings of the 1984 International PM Conference, Toronto, Canada, vol. 15, Metal Powder Industries Federation, Princeton, NJ, 1985, pp. 307-326.
- <sup>111</sup> F. F. Lange, "De-Sintering, A Phenomenon Concurrent with Densification Within Powder Compacts: A Review", *Sintering Technology*, R. M. German, G. L. Messing, R. G. Cornwall (eds), 1996, pp. 1-12.
- <sup>112</sup> H. F. Fischmeister, E. Arzt, and L. R. Olsson, "Particle Deformation and Sliding during Compaction of Spherical Powders: A Study by Quantitative Metallography", *Powder Metallurgy*, 1978, no. 4, pp. 179-187.
- <sup>113</sup> W. W. M. Sui and S. H. K. Lee, "Effective Conductivity Computation of a Packed Bed using Constriction Resistance and Contact Angle Effects", *International Journal of Heat and Mass Transfer*, 2000, vol. 43, pp. 3917-3924.
- <sup>114</sup> A. Jagota and C. Y. Hui, "The Effective Thermal Conductivity of a Packing of Spheres," *Journal of Applied Mechanics*, 1990, vol. 57, pp. 789-791.
- <sup>115</sup> Personal communication with Dr P. Suri, 10 March 2003.
- <sup>116</sup> R. W. Hertzberg, *Deformation and Fracture Mechanics of Engineering Materials*, 3<sup>rd</sup> edition, John Wiley and Sons, New York, NY, 1989, p. 4.

<sup>117</sup> J. L. Johnson E. J. Westcot, "Metal Injection Molding of Commercially Pure Nickel for the Chemical Processing Industry", submitted to *International Journal of Powder Metallurgy*, March 2003.

<sup>118</sup> J. M. Gere and S. P. Timoshenko, *Mechanics of Materials*, PWS Engineering, Boston, MA, 2<sup>nd</sup> edition, p. 323.

## Appendix A

### Transverse Rupture Strength Raw Data

Table A.1: Room temperature transverse rupture strength raw data, quasi-PIM material. Samples sintered in vertical furnace at 10°C/min in hydrogen, no hold, water quenched.

Sample	Sinter Temp, °C	Fractional Density	TRS, MPa
24	400	0.55	1.5
23	400	0.54	1.4
22	400	0.55	1.2
21	500	0.56	3.6
19	500	0.55	3.2
18	600	0.58	11.7
17	600	0.57	10.7
16	600	0.57	11.1
15	700	0.59	17.0
14	700	0.60	17.2
13	700	0.58	16.6
12	800	0.62	23.7
11	800	0.62	29.2
10	800	0.63	26.6
9	900	0.65	31.8
8	900	0.65	34.0
7	900	0.66	35.0
6	1000	0.72	53.8
5	1000	0.72	55.1
4	1000	0.71	61.3
3	1100	0.76	79.7
2	1100	0.78	79.0
1	1100	0.76	74.1

Table A.2: Room temperature transverse rupture strength raw data, PIM material. Samples sintered in retort furnace at 2°C/min in hydrogen, 15 minute hold, air quenched.

Sample	Sinter Temp, °C	Fractional Density	TRS, MPa
G1	20	0.58	6.1
G2	20	0.58	5.9
G3	20	0.59	4.2
G4	20	0.58	4.9
200-1	200	0.59	23.8
200-2	200	0.59	23.0
200-3	200	0.59	23.9
300-4	300	0.59	0.9
300-5	300	0.59	1.6
300-6	300	0.59	1.4
425-7	425	0.59	0.5
425-8	425	0.59	0.5
425-9	425	0.58	0.6
425-1-22	425	0.59	0.5
425-1-24	425	0.58	0.5
425-2-19	425	0.60	0.8
425-2-20	425	0.60	1.4
425-2-21	425	0.59	0.9
500-10	500	0.61	7.4
500-11	500	0.60	8.6
500-12	500	0.60	7.9
600-25	600	0.61	29.6
600-26	600	0.62	42.6
600-27	600	0.62	39.7
700-13	700	0.64	100.3
700-14	700	0.64	89.9
700-15	700	0.64	103.5



Table A.3: *In situ* transverse rupture strength raw data, die-compacted material. Samples sintered at 3°C/min in hydrogen, no hold, fractured at indicated sinter temperature.

Sample	Sinter Temp, °C	Fractional Density	TRS, MPa
32	20	0.75	2.0
33	20	0.75	1.2
34	20	0.75	0.8
39	200	0.75	0.4
42	200	0.75	0.3
43	200	0.75	0.4
36	250	0.75	1.2
37	250	0.75	1.1
38	250	0.75	1.1
44	300	0.75	1.9
45	300	0.75	2.0
46	300	0.75	2.5
30	350	0.75	6.7
31	350	0.75	6.6
35	350	0.75	8.0
26	400	0.75	7.8
27	400	0.75	8.8
28	400	0.75	7.9
49	500	0.75	10.0
40	600	0.75	8.1

## Appendix B

### Raw Thermal Diffusivity Data

Table B.1: Post-sinter thermal diffusivity measurements, quasi-PIM material. Samples sintered in vertical furnace at 10°C/min in hydrogen, no hold, water quenched. Measurements were made at room temperature.

Sample	Sintering Temp, °C	Fractional density	Thermal diffusivity, cm <sup>2</sup> /s
q18	400	0.55	0.051
q12	500	0.56	0.060
q13	600	0.58	0.080
q14	600	0.62	0.081
q19	700	0.62	0.096
q20	700	0.62	0.102
q6	800	0.64	0.110
q5	800	0.64	0.110

Table B.2: Post-sinter thermal diffusivity measurements, PIM material. Samples sintered in retort furnace at 2°C/min in hydrogen, with a 2-hour hold at 425°C, air cooled. Measurements made at 100°C.

Sample	Sintering Temp, °C	Fractional density	Thermal diffusivity, cm <sup>2</sup> /s
200-1	200	0.59	0.006
200-2	200	0.59	0.005
300-1	300	0.59	0.007
300-2	300	0.59	0.007
425-1	425	0.59	0.006
425-2	425	0.59	0.007
425-1-1	425	0.59	0.007
425-2-1	425	0.59	0.014
425-2-2	425	0.59	0.015
500-1	500	0.60	0.032
500-2	500	0.60	0.032
600-1	600	0.62	0.053
600-2	600	0.62	0.054
700-1	700	0.64	0.078
700-2	700	0.64	0.081

Table B.3: Post-sinter thermal diffusivity measurements, die-compacted material. Samples sintered in Flaming Tensile Tester at 3°C/min in hydrogen, air-cooled. Measurements made at 200°C.

Sample	Sintering Temp, °C	Fractional density	Thermal diffusivity, cm <sup>2</sup> /s
s24	200	0.75	0.060
s35	200	0.75	0.057
s42	250	0.75	0.021
s43	250	0.75	0.022
s36	300	0.75	0.038
s37	300	0.75	0.039
s40	350	0.75	0.057
s41	350	0.75	0.064
s38	400	0.75	0.081
s39	400	0.75	0.078

## Appendix C

### Room Temperature Ultrasonic Evaluation Raw Data

Table C.1: Room temperature ultrasonic evaluation raw data for quasi-PIM material. Young's modulus calculated from time-of-flight data. Samples sintered in vertical furnace at 10°C/min in hydrogen, water-quenched at indicated sintering temperature.

Sample	Sintering Temperature, °C	Fractional Density	Young's Modulus, Pa
24	400	0.55	4.97E+09
23	400	0.54	4.98E+09
22	400	0.54	4.83E+09
21	500	0.55	1.05E+10
21	500	0.55	9.91E+09
20	500	0.56	9.84E+09
19	500	0.55	1.06E+10
18	600	0.58	2.20E+10
17	600	0.57	2.16E+10
16	600	0.57	2.46E+10
15	700	0.59	3.06E+10
15	700	0.59	3.14E+10
14	700	0.60	3.37E+10
13	700	0.58	3.51E+10
12	800	0.62	4.79E+10
11	800	0.62	4.76E+10
10	800	0.63	5.13E+10
9	900	0.65	6.12E+10
8	900	0.65	6.13E+10
7	900	0.66	5.47E+10
6	1000	0.72	8.12E+10
5	1000	0.72	7.53E+10
4	1000	0.71	8.10E+10
3	1100	0.76	1.03E+11
3	1100	0.76	1.10E+11
2	1100	0.78	9.38E+10
1	1100	0.76	1.39E+11

## Appendix D

### Room Temperature Resonant Frequency Evaluation Raw Data

Table D.1: Room temperature resonant frequency raw data for quasi-PIM material. Samples sintered in vertical furnace at 10°C/min in hydrogen, water-quenched at indicated sintering temperature.

Sample	Sintering Temp	Fractional Density	Young's Modulus	Shear Modulus	Poisson's Ratio	Bulk Modulus
	°C		GPa	GPa		GPa
24	400	0.55	4.1	1.9	0.11	1.8
23	400	0.54	5.1	1.8		1.7
22	400	0.54	4	1.8	0.11	1.7
21	500	0.55	8.4	3.7	0.14	3.9
20	500	0.56	8.4	3.6	0.15	4.0
18	600	0.58	20.4	8.7	0.17	10.3
17	600	0.58	19.7	8.4	0.17	10.0
16	600	0.57	19.7	8.5	0.16	9.7
15	700	0.59	29.9	12.7	0.18	15.5
14	700	0.60	31.5	13.2	0.20	17.2
13	700	0.58	29.6	12.7	0.17	14.9
12	800	0.62	43.3	18	0.20	24.4
11	800	0.62	42.9	17.8	0.21	24.4
10	800	0.63	43.4	17.8	0.22	25.9
9	900	0.65	56.6			
8	900	0.65	56.3			
7	900	0.66	58.5			
6	1000	0.72	79.9			
5	1000	0.72	80.4			

## Appendix E

### Room Temperature Electrical Conductivity Raw Data

Table E.1: Room temperature electrical conductivity raw data for quasi-PIM materials. Samples sintered in vertical furnace at 10°C/min in hydrogen, water-quenched at indicated sintering temperature.

Sample	Sintering Temperature	Fractional Density	Effective Resistivity	Effective Conductivity
	°C		$\Omega \cdot \text{m}$	$(\Omega \cdot \text{m})^{-1}$
24	400	0.55	1.13E-06	8.84E+05
23	400	0.54	1.13E-06	8.87E+05
22	400	0.54	1.11E-06	8.98E+05
21	500	0.55	6.90E-07	1.45E+06
20	500	0.56	7.06E-07	1.42E+06
18	600	0.58	3.47E-07	2.89E+06
17	600	0.58	3.55E-07	2.82E+06
16	600	0.57	3.68E-07	2.72E+06
15	700	0.59	2.76E-07	3.63E+06
14	700	0.60	2.63E-07	3.80E+06
13	700	0.58	2.62E-07	3.81E+06
12	800	0.62	2.02E-07	4.94E+06
11	800	0.62	2.10E-07	4.77E+06
10	800	0.63	2.18E-07	4.58E+06
9	900	0.65	1.80E-07	5.55E+06
8	900	0.65	1.70E-07	5.89E+06
7	900	0.66	1.77E-07	5.65E+06
6	1000	0.72	1.40E-07	7.14E+06
5	1000	0.72	1.43E-07	7.00E+06
4	1000	0.71	1.44E-07	6.96E+06
3	1100	0.76	1.17E-07	8.53E+06
2	1100	0.78	1.17E-07	8.54E+06
1	1100	0.76	1.18E-07	8.48E+06

**Appendix F**  
**Thermal Properties for Nickel**

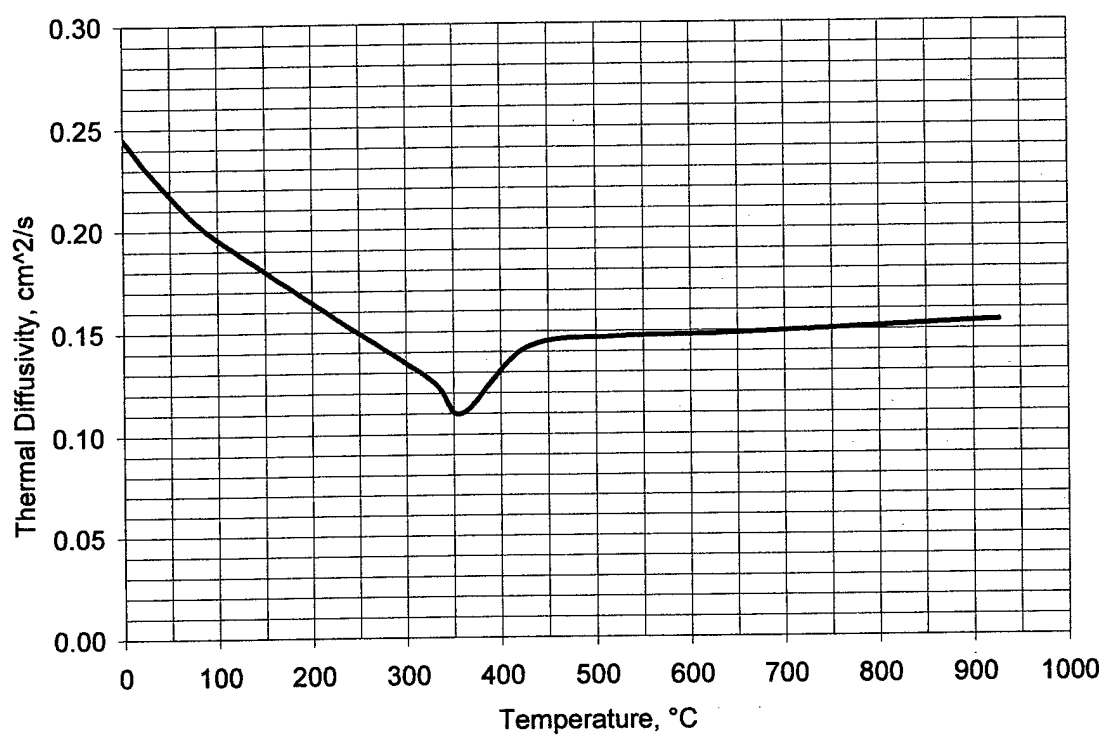


Figure F.1: Thermal diffusivity of nickel as a function of temperature, based on TPRC data<sup>21</sup>



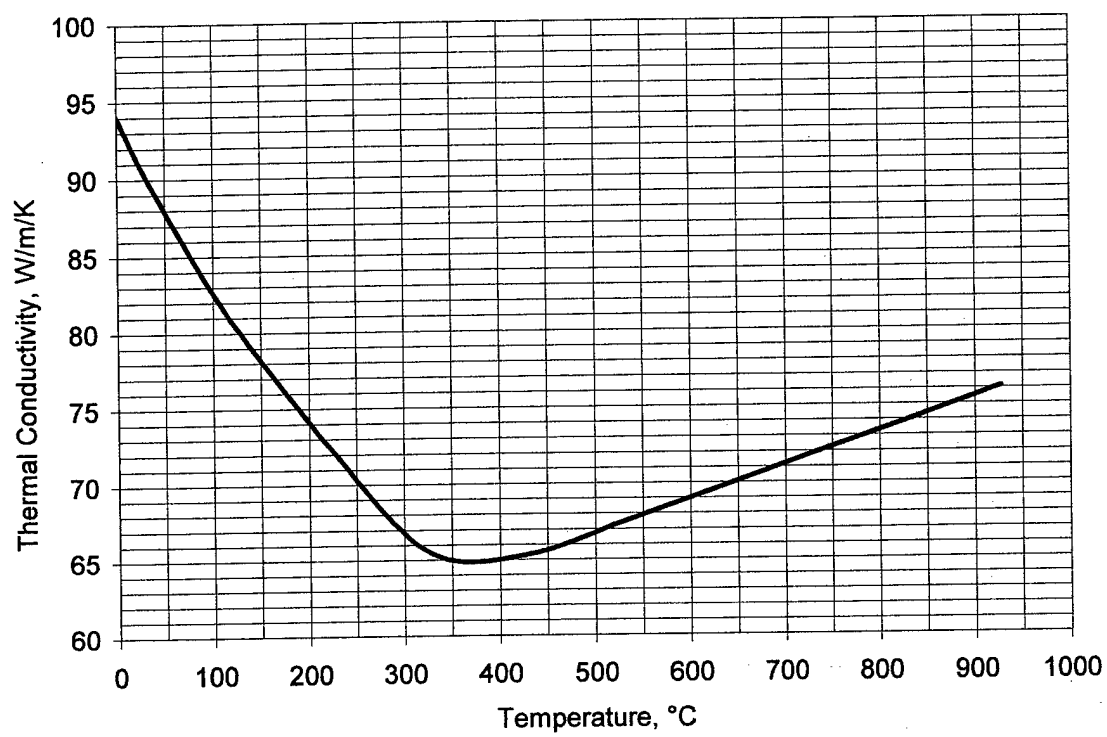


Figure F.2: Thermal conductivity of solid nickel as a function of temperature, based on TPRC data<sup>107</sup>

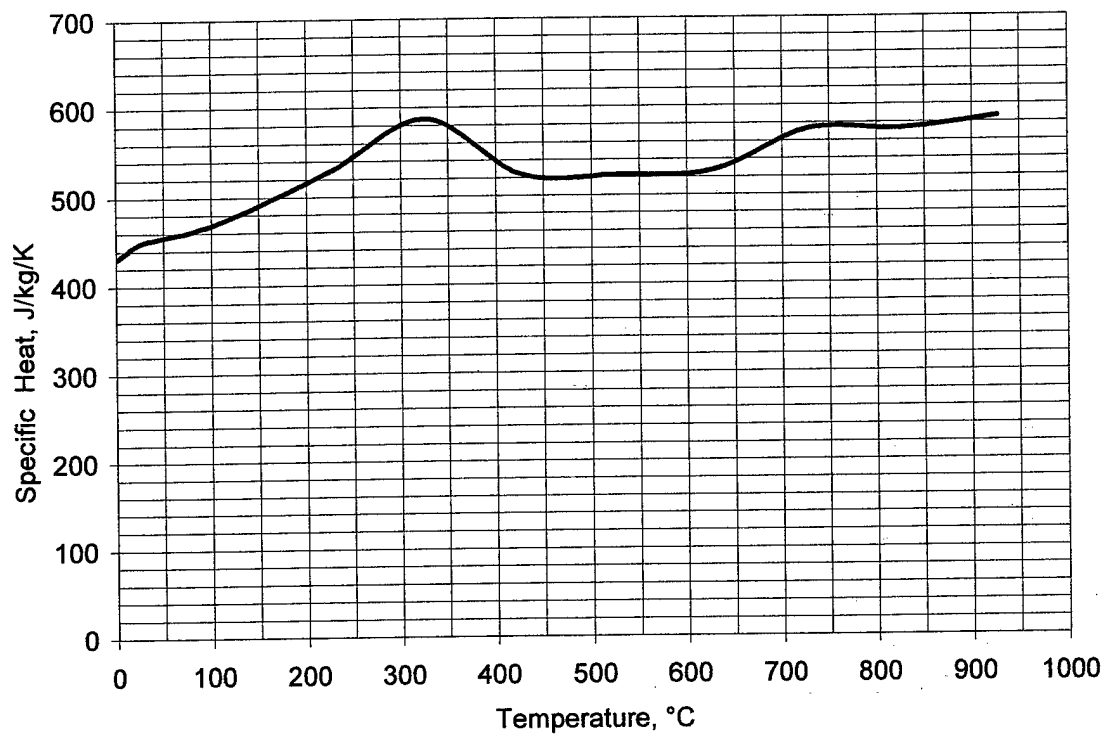


Figure F.3: Specific heat of solid nickel as a function of temperature, based on TPRC data<sup>105</sup>

Table F.1: Thermal properties of nickel as a function of temperature, based on TPRC data<sup>21, 107, 105</sup>

Temperature, K	Temperature, °C	Thermal Diffusivity, cm <sup>2</sup> /s	Thermal Conductivity, W/m·K	Specific Heat, J/kg·K
273	0	0.245	94	430
300	27	0.229	90.5	449
350	77	0.204	85	461
400	127	0.187	80.1	479
500	227	0.156	72.1	530
600	327	0.126	65.5	587
631	358	0.11		
700	427	0.142	65.3	524
800	527	0.147	67.4	523
900	627	0.148	69.6	527
1000	727	0.15	71.8	573
1100	827	0.152	73.9	573
1200	927	0.154	76.1	586



BOUNDARY THICKNESS AS MEASURED IN DIFFUSION PAPER,  $M^{**3}/SEC$   
 C DBT: GRAIN BOUNDARY DIFFUSION COEFFICIENT,  $M^{**3}/SEC$   
 C DL: A-THE DISTANCE BETWEEN TWO PARTICLES/2  
 C DSOT: FREQUENCY FACTOR FOR SURFACE DIFFUSION X ATOMIC DIAMETER  
 $M^{**3}/SEC$   
 C DST: SURFACE DIFFUSION COEFFICIENT,  $M^{**3}/SEC$   
 C DV: VOLUME DIFFUSION COEFFICIENT,  $M^{**2}/SEC$   
 C DVO: FREQUENCY FACTOR FOR VOLUME DIFFUSION,  $M^{**2}/SEC$   
 C FT: FINAL TEMPERATURE, K  
 C GS: SURFACE ENERGY,  $J/M^{**2}$   
 C H:  $=X$ , RADIUS OF THE CONTACT AREA, MICRON  
 C HR: HEATING RATE (K/MIN)  
 C HTP: HEATING TIME PERIOD, MINUTES, total time of sintering cycle  
 C ID: INITIAL DENSITY, (GREEN DENSITY)  $G/CM^{**3}$   
 C K: BOLTZMANN'S CONSTANT,  $1.38E-16 J/K$   
 C K1: CURVATURE DIFFERENCE BETWEEN CONVEX AND CONCAVE SURFACES,  $1/MICRON$   
 C K2: CURVATURE DIFFERENCES BETWEEN CONVEX SURFACE AND GRAIN  
 C BOUNDARY,  $1/MICRON$   
 C NC: COORDINATION NUMBER  
 C OM: ATOMIC VOLUME,  $M^{**3}$   
 C PO: PRE-EXPONENTIAL FOR VAPOR PRESSURE, MPA  
 C PV: VAPOR PRESSURE, MPA  
 C QB: ACTIVATION ENERGY FOR GRAIN BOUNDARY DIFFUSION,  $KJ/MOLE$   
 C QS: ACTIVATION ENERGY FOR SURFACE DIFFUSION,  $KJ/MOLE$   
 C QV: ACTIVATION ENERGY FOR VOLUME DIFFUSION,  $KJ/MOLE$   
 C QVA: ACTIVATION ENERGY FOR EVAPORATION,  $KJ/MOLE$   
 C R1: RADIUS OF CURVATURE AT STAGE 1, MICRON  
 C RX1: NET SINTERING RATE IN STAGE 1,  $MICRON/SEC$   
 C SH: SHRINKAGE, %  
 C SHR: SHRINKAGE RATE,  $\%/MIN$ .  
 C ST: STARTING TEMPERATURE, K  
 C T: TEMPERATURE, K  
 C TD: THEORETICAL DENSITY,  $G/CM^{**3}$   
 C TE: TEMPERATURE, K  
 C TF: FREQUENCY OF TAKING DATA, MIN  
 C TI: TIME INCREMENT, SEC  
 C TM: MELTING POINT, K  
 C TT: TIME, MIN  
 C X: NECK RADIUS, MICRON  
 C XI: INITIAL RADIUS OF THE CONTACT AREA, MICRON  
 C XSS: NECK GROWTH RATE DUE TO SURFACE DIFFUSION,  $MICRON/SEC$   
 C XSV: NECK GROWTH RATE DUE TO VOLUME DIFFUSION FROM SURFACE TO  
 C NECK,  $MICRON/SEC$   
 C XEV: NECK GROWTH RATE DUE TO EVAPORATION FROM SURFACE TO NECK  
 C  $MICRON/SEC$   
 C XGB: NECK GROWTH RATE DUE TO GRAIN BOUNDARY DIFFUSION  
 C XGV: NECK GROWTH RATE DUE TO VOLUME DIFFUSION FROM GRAIN BOUNDARY  
 C TO NECK,  $MICRON/SEC$   
 C XXI: CURVATURE OF NECK  
 C \*\*\*\*\*  
 SUBROUTINE SPHERE()  
 IMPLICIT DOUBLE PRECISION (A-H,O-Z)  
 DOUBLE PRECISION L,NC,ID,OM,K

```

INTEGER STAGE
COMMON/INITI/ID,TD,PIE,K,OM
COMMON/AAA/A
COMMON/MECH/F,DST,DV,DBT,PV
COMMON/ROUGS1/L,NC
COMMON /ROUGS2/X,AT,R1,DL
COMMON/ROUG1/TI,SHR
DIMENSION TT(3000),TE(3000),XA(3000),SH(3000),
+DD(3000),XN(3000),SRED(3000),ATT(3000),HR(4),FT(4),HTP(4)
CALL INPUTSPH(TD,OM,TM,DVO,QV,DS0T,QS,DB0T,QB,P0,QVA,GS,A
&ID,ST,HR,FT,HTP,H,NC,NHOLD)
iarea=0
NH=1
STAGE=1
IF (HR(NH).NE.0.0) THEN
  TF=20./HR(NH)
ELSE
  TF=1.0
ENDIF
K=1.38D-23
N=0
PIE=4.0*DATAN(1.0)
CALL SPHEREINIT(H,L,NC,X,AT,DL,S0,R1)
IF (X/A.GE..3) THEN
  WRITE(30,201)
201  FORMAT('XI IS GREATER THAN THE ASSUMPTION USED IN
  @DERIVING THE EQUATION')
  GOTO 181
ENDIF
IM=1
T=ST
IF (HRCNH).E0.0.0) T=FT(NH)
CON=A*1.0D-04
WRITE(30,873)
873 FORMAT('TEMP',4X,'TIME',7X,'NECK',6X,'AT 10X','RATIO',7X,'SHR',
  @9X,'SHRATE',5X,'XSS',5X,'XSV',5X,'XEV','XGB',5X,'XGV'5X,
  @'SLOPEN',7X,'SLOPES',7X,
  @'NECKRATE',4X,'AREARED',5X,'GAMMA')
C  CALCULATE DIFFUSION COEFFICIENTS
16 DST=DS0T*EXP(-QS*1E3/(8.31*T))
DBT=DB0T*EXP(-QB*1E3/(8.31*T))
DV=DV0*EXP(-QV*1E3/(8.31*T))
PV=P0*EXP(-QVA*1E3/(8.31*T))
C TOT IS ACCUMULATED SINTERING TIME WITHIN TF INTERVAL
TOT=0.
C STARTING TIME INCREMENT
T1=0.
F=1D06*GS*OM/(K*T)
c****Initialize for the case of initial neck:
c  ANG=DASIN((X+R1)/(R1+AT))
c  S0=4.*PIE*AT**2/NC-2.*PIE*AT*(AT-AT*DCOS(ANG))
c  iarea=0
C*****

```

```

15 CALL ADHESION(AT,X,R1,XSS,XSV,XEV,AREA,RX1S,T,TT)
CALL DENSIFICATION(AT,X,DL,R1,XGB,XGV,RX1G,TT)
RX1=RX1S+RX1G
TOT=TOT+TI
ANG=DASIN((X+R1)/(R1+AT))
ANGL=ANG/PIE*180.
C THIS SECTION CHECKS IF NECKS ARE IMPINCHING EACH OTHER.
IF(ANG.GE.DACOS(1.-2./NC)) THEN
  STAGE=2
  WRITE(50,311)TE(IM),TT(IM),SH(IM),SRED(IM),STAGE
  GOTO 18
ENDIF
IF (TF*60-TOT.GT. 1E-6) THEN
  TI=CON/RX1
  IF (TI+TOT-TF*60.LE.0.0) THEN
    N=N+1
    GO TO 15
  ELSE
    TI=TF*60.-TOT
    N=N+1
    GO TO 15
  ENDIF
ENDIF
200 XN(IM)=X
ATT(IM)=AT
SH(IM)=DL/L*100.
IF (IM.EQ.1) THEN
  SHR=SH(IM)/TF
ELSE
  SHR=(SH(IM)-SH(IM-1))/TF
ENDIF
C CALCULATE THE CONTRIBUTION OF EACH MECHANISM
XSSP=XSS/RX1*100.
XSVP=XSV/RX1*100.
X EVP=XEV/RX1*100.
XGBP=XGB/RX1*100.
XGVP=XGV/RX1*100.
C SRED: AREA REDUCTION DUE TO SINTERING
SAREA=4.*PIE*AT**2/NC-2.*PIE*AT*(AT-AT*DCOS(ANG))+AREA
if(iarea.eq.0) then
c  write(*,*)s0,area
  s0=sarea
  iarea=1
c  write(*,*)s0,iarea
c  read(*,*)temp
endif
c  SRED(IM)=100.*(SO
c  &-(4.*PIE*AT** 2/NC-2.*PIE*AT*(AT-AT*DCOS(ANG))+AREA))/SO
  sred(im)=100.*(s0-sarea)/s0
  IF (IM.EQ.1) THEN
    TT(1)=TF
  ELSE
    TT(IM)=TT(IM-1)+TF

```

```

ENDIF
IF(T.EQ.FT(NH)) TF=I.
TE(IM)=T-273
C THE NEXT THREE STATEMENTS ARE TO AVOID SMALL NEGATIVE
C DL WHICH OCCURS OCCATIONALLY BY VERY SMALL NUMERICAL ERRORS.
IF (DL.LE.O.DO) THEN
  DD(IM)=I.OD-I 5
  SLOPEN=O.O
  SLOPEA=O.O
  SLOPES=O.O
ELSE
  DD(IM)=DL
ENDIF
XA(IM)=X/A
IF (IM.NE.1) THEN
  IF (XA(IM)-XA(IM-1) ).GT.1 E-10) THEN
    SLOPEN=DLOG10(TT(IM)/TT(IM-1))/DLOG10(XA(IM)/XA(IM-1))
  ENDIF
  IF((SRED(IM).NE.0.).AND.(SRED(IM-1).NE.0.0).AND.
@ (SRED(IM)-SRED(IM-1) ).GT.1E-10)) THEN
    SLOPEA=DLOG 1 O(TT(IM)/TT(IM-1))/DLOG 1 O(DABS(SRED(IM)/SRED(IM-1)))
  ENDIF
  IF ((SH(IM).NE.O.) .AND. (SH(IM-1).NE.O.O) .AND.
@ (SH(IM)-SH(IM-1) ).GT. 1 E-06)) THEN
    SLOPES=DLOG 1 O(DABS(SH(IM)/SH(IM-1)))/DLOG 1 O(TT(IM)/TT(IM-1))
  ENDIF
ENDIF
WRITE(3,0,206)TE(IM),TT(IM),XN(IM),AT,XA(IM), SH(IM),SHR,
+XSSP,XSVP,XEVP,XGBP,XGVP,SLOPEN,
+SLOPES,RX1 ,SRED(IM),SLOPEA,sarea,s0,iarea
206 FORMAT(F5.0,3X,F8.1,3X,F7.4,3X,F9.6,3X,F
IF
@F6.3,3X,E10.3,3X,e10.3,3X,i5)
C OUTPUTS FOR THE GRAPHS
WRITE(50,311 )TE(IM),TT(IM), SH(IM),SRED(IM),STAGE
311 FORMAT(F5.0,3X,F8.1 ,3X,F9.3,3X,F1 5.5,3X,I2)
IF(TT(IM).GT.HTP(NH)) NH=NH+I
IF (NH.GT.NHOLD) GO TO 18
IF (T.EQ.FT(NH)) THEN
  TOT=O.
C STARTING TIME INCREMENT
  TI=O.
  IM=IM+1
  GO TO 15
ENDIF
IF (T+TF*HR(NH)-(FT(NH)- I.).GE.O.) THEN
  TF=(FT(NH)-T)/H R(NH)
  T=FT(NH)
  DST=DSOT*EXP(-QS*I D3/(8.31*T))
  DBT=DBOT*EXP(-QB*I E3/(8.31*T))
  DV=DVO*EXP(-QV*I E3/(8.31*T))

```



```

pV=PO*EXP(-QVA*I E3/(8.31*T))
F=1.OE06*GS*OM/(K*T)
IM=IM+1
TOT=O.
TI=O.
HR(NH)-O.
GO TO 15
ENDIF
T=T+HR(NH)*TF
IM=IM+1
GO TO 16
18 WRITE(30,873)
CLOSE(30)
CLOSE(SO)
181 RETURN
END
~*****

```

# INPUTSPH

```

C THIS SUBROUTINE READ THE INPUT VALUES FOR TANTALUM CONSTANTS IN
C TANTALUM.DAT THEN ASK FOR THE FILE NAME (ENTER WITHOUT THE EXTENTION)
C WHERE TO READ THE PROCESS VALUES SUCH AS THE PARTICLE SIZE, THE

C TEMPERATURE. IT ALSO CREATE THE OUTPUT FILE WITH THE SAME NAME THAN THE
C INPUT FILE BUT WITH THE EXTENTION .OUT.
SUBROUTINE INPUTSPH(TD,OM,TM,DVO,QV,DSOT,QS,DBOT,QB
&ID, ST,HR, FT,HTP,H,NC,NHOLD)
IMPLICIT DOUBLE PRECISION (A-H,O-Z)
DOUBLE PRECISION NC,ID,OM,PO
CHARACTER*12 FILE1, FILE2
DIMENSION HR(4),FT(4),HTP(4)
C READ IN THE DATA FILE NAMES
OPEN(UNIT=25,FILE='NAME S.DAT',STATUS='OLD')
READ (25,100) FILE 1, FILE2
100 FORMAT(A/,A)
CLOSE (25)
C READ MATERIAL CONSTANTS
C READ MATERIAL CONSTANTS
OPEN(20, FILE = FILE1, STATUS = 'OLD')
READ (20, *) TD,OM,TM,DVO,QV,DSOT,QS,DBOT,QB,PO,QVA,G
C 99 FORMAT(D9.1/,5(F9.3/,D9.1/),F9.3)
CLOSE (20)
C READ THE PROCESS CONSTANTS
OPEN(21,FILE=FILE2,STATUS='OLD')
READ(21, 96) A,ID,ST,H,NC,AHOLD
96 FORMAT(D10.5, 5(/,D10.5))
C 96 FORMAT(D9.2/,5(D9.1/),D9.4/,D9.1)
NHOLD=AHOLD
C Change Partical Diameter to partical Radius
A=A/2.0
ST=ST+273.
READ(21,*) HR(1),FT(1),HTP(1)
FT(1)=FT(1)+273.
IF (HR(1).NE.O.) HTP(1)=HTP(1)+(FT(1)-ST)/HR(1)

```

```

IF (NHOLD.GT.I) THEN
  DO 120 I=2,NHOLD
  READ(21,*) HR(I),FT(I),HTP(I)
  FT(I)=FT(I)+273 .
  IF (HR(I).NE.O.) THEN
    HTP(I)=HTP(I-1)+HTP(I)+(FT(I)-FT(I-1))/HR(I)
  ELSE
    HTP(I)=HTP(I-1)+HTP(I)
  ENDIF
120 CONTINUE
ENDIF
97 FORMAT(D10.5,/,D10.5,/,D10.5)
CLOSE(2 I)
C OPEN THE RESULT FILE
OPEN(30, FILE ='spheres.out', STATUS = 'UNKNOWN')
OPEN(UNIT=5 O,FILE='GRAPH.DAT', STATUS='UNKNOWN')
RETURN
END

```

```

C*****
C SPHEREINIT
C THIS SUBROUTINE CALCULATE THE INITIAL VALUES FOR THE PARTICLE SIZE,
C THENECK RADIUS...

```

```

SUBROUTINE SPHEREINIT(H,L,NC,X,AT,DL,SO,R1)
IMPLICIT DOUBLE PRECISION (A-H,O-Z)
COMMON/INITI/ID,TD,PIE,K,OM
COMMON/AAA/A
DOUBLE PRECISION L,NC,ID,K,OM
c TF (TD/TD.LE.0.605.0R.H.EQ.O.) THEN
  if(id/td.le.1.0.or.h.eq.O)then
C THIS FOR THE CASE OF LOOSE POWDER (H=O)
  ATI=A
  AT=A
c H=O.
  X=H
  L=A
C NC=I
  NC= 2*EXP(2.4*ID/TD)
  ELSE
  XI=O.DO
  DLI=O.DO
  AGLI=O.DO
C CALCULATION OF THE NECK RADIUS OF THE FLATTENED AREA
C AFTER POWDERS ARE PRESSED. THE EQUATION USED IS EMPERICAL
C AND IS BASED ON THE EXPERIMENTAL RESULTS OF KAKAR & CHAKLADER.
C XI=H=INITIAL NECK RADIUS
  CT=DSQRT((ID/TD-.605)/2.)
  ATI=(4./(4.-NC*(2.-(2.+CT*CT)*DSQRT(1.-CT*CT))))**.333333*A
  XI=CT*ATI
  AGLI=DASIN(CT)
  DLI=ATI-DSQRT(ATI*ATI-XI*XI)

```

```

X=XI
H=XI
DL=O
AT=ATI
L=ATI-DLI
ANG=AGLI
ENDIF
*****

SO=4.*PIE*AT** 2R\TC-2.*PTE*AT* (AT-L)
X=X+I.OD-04*A
c R1=0
rl=x**2/(2.*at)
CALL ROUS(R1,AT)
c***Now calculate the initial shrinkage
call roug(r l,dl)
L=L-dl
*****

IF (R1.LT.1E-10) THEN
  R1=X**2/2/AT
ENDIF
RETURN
END
C*****
C*****
C ADHESION
C THIS SUBROUTINE CALCULATES THE NEW NECK RADIUS FOR ADHESION

C MECHANISMS AND RECALCULATE AT AND R1.
SUBROUTINE ADHESION(AT,X,R1,XSS,XSV,XEV,AREA,RX1S,T,TI)
IMPLICIT DOUBLE PRECISION (A-H,O-Z)
COMMON/INITI/ID,TD,PIE,K,OM
COMMON/AAA/A
COMMON /MECH/F,DST,DV,DBT,PV
COMMON/ROUGS1/L,NC
DOUBLE PRECISION K1S,L,NC,ID,K,OM
K1S=1./R1-1./X+2./AT
K1G=1./R1-1./X
CALL FDVDXSPH(DVDXS,DV DXG)
XXI=R1*DSQRT((AT+R1+X+R1)*(AT-X))/(AT+R1)
AREA=6.2832*R1*((R1+X)*DASIN(XXI/R1)-XXI)
C CALCULATE THE NECK GROWTH RATE FOR DIFFERENT MECHANISMS
XSS=3.1416*2.D18*DST*X*K1S*F/DVDXS/R1
XSV=1.D12*DV*F*K1S/R1*AREA/DVDXS
XEV=31.6*ID03*PV*F*K1S*DSQRT(63.54/(6.2832*K*T))*AREA/DVDXS/TD
RX1S=XSS+XSV+XEV
X=X+RXIS*TI
CALL ROUS(R1,AT)
RETURN
END
C
*****

```

C DENSIFICATION  
 C THIS SUBROUTINE CALCULATES THE NEW NECK RADIUS FOR DENSIFICATION  
 C MECHANISMS AND RECALCULATE DL AND R1.

```

SUBROUTINE DENSIFICATION(AT,X,DL,R1,XGB,XGV,RX1G,TI)
IMPLICIT DOUBLE PRECISION (A-H,O-Z)
COMMON/INITI/ID,TD,PIE,K,OM
COMMON/AAA/A
COMMON/MECH/F,DST,DV,DBT,PV
COMMON/ROUGS1/L,NC
DOUBLE PRECISION L,ID,OM,K,NC
CALL FDVDXSPH(DVDXS,DVDXG)
XGB=8.D1 8*PIE*DBT*F*(X+R1)/R1/X/DVDXG
XXI=R1*DSQRT((AT+R1+X+R1)*(AT-X))/(AT+R1)
AREA=6.2832*R1*((R1+X)*DASIN(XXI/R1)-XXI)
XGV=4.D12*AREA*DV*F*(X+R1)/R1/X/X/DVDXG
RX1G=XGB+XGV
X=X+RX1G*TI
CALL ROUG(R1,DL)
RETURN
END

```

C  
 C \*\*\*\*\*

C ROUG  
 C THIS PROGRAM CALCULATE THE NECK RADIUS AND THE INTERPARTICLE  
 C DISTANCE IN THE DENSIFICATION CASE.  
 C DL AND R1(NECKRADIUS) ARE UNKNOWNNS.

```

SUBROUTINE ROUG(R1,DL)
IMPLICIT DOUBLE PRECISION (A-H,O-Z)
DOUBLE PRECISION Y(2),R1,DL
LOGICAL check
COMMON/ROUG1/TI,SHR
EXTERNAL FCN1
check=.false.
Y(1)=R1
Y(2)=DL
CALLnewtl(Y,check)
R1=Y(1)
DL=Y(2)
RETURN
END

```

C \*\*\*\*\*

C  
 C ROUS  
 C THIS PROGRAM CALCULATE THE NECK RADIUS AND TRUE RADIUS OF  
 C PARTICLES IN THE ADHESION CASE.  
 SUBROUTINE ROUS(R1,AT)  
 IMPLICIT DOUBLE PRECISION (A-H,O-Z)  
 DOUBLE PRECISION Y(2),R1,AT  
 LOGICAL check  
 EXTERNAL FCN2  
 check=.false.

```

Y(1)=R1
Y(2)=AT
CALL newt2(Y,check)
R1=Y(1)
AT=Y(2)
RETURN
END
C*****
C
      SUBROUTINE FDVDXSPH(DVDXS,DVDXG)
C THIS SUBROUTINE CALCULATES DV/DX FOR BOTH ADHESION AND
C DENSIFICATION MECHANISMS.
      IMPLICIT DOUBLE PRECISION (A-H,O-Z)
      COMMON/AAA/A
      COMMON/ROUGS1/L,NC
      COMMON/ROUGS2/X,AT,R1,DL
      DOUBLE PRECISION L,NC
      PIE=4.0D0*DATAN(1.0D0)
      YI=AT/(AT+R1)*(X+R1)
      AA=DSQRT((AT+R1+L-DL)*(R1+DL+(AT-L)))
      AB=(L-DL)/(AT+R1)
      AC=R1*AB+DL+(AT-L)
      AH=R1*AB/(AT+R1)
      AD=AT*(2.*AC-4./NC*AT)-2.*AC*AH*AT
      @+(X+R1)*(-2.*R1*R1*AB*AA/(AT+R1)**2+R1*AH*(AT+R1)/AA-R1*R1*AB
      @/AA)+R1*R1*AH*(R1*AB)**3/(AT+R1)+(X+R1)*(X+R1)*AH+AC*AC*AH
      AE=(AC*AC*AH-AC*AC*AB-(X+R1)*(X+R1)*AB-2.*(X+R1)*R1*AB+
      @(X+R1)*(X+R1)*AH+(R1*AH*AA+R1*R1*DATAN((L-DL)/(X+R1))))+
      @(X+R1)*(2.*AH*AA-2.*AA*R1*R1*AB/(AT+R1)**2
      @+R1*AH*(AT+R1)/AA+2.*R1'DATAN((L-DL)/(X+R1))-R1*R1*AB/AA)
      @-3.*R1*R1*AB+R1*R1*AH
      @+R1*R1*AB**3*AT/(AT+R1))+2.*AC*AT*(AB-AH)

      AF=(-2.*(X+R1)*AB*R1+R1*AH*AA+R1*R1*DATAN((L-DL)/(X+R1)))
      AG=-AC*AC*AT/(AT+R1)+2.*AC*AT*AT/(AT+R1)
      @+((X+R1)*(X+R1)*R1/(AT+R1)+(X+R1)*(-R1/(AT+R1))**2*AA
      @+R1*AH*(L-DL)/AA-R1*R1/AA)+R1**3/(AT+R1)-R1**3*AB*AB/(AT+R1))
      AGH=(-AF-AA*AG/(L-DL))/(AE+AA*AG/(L-DL)-(AT+R1)/(L-DL)*AG)
      ARH=(-AF-AA*AD/(AT+R1))/(AE-AD+AA*AD/(AT+R1))
      ATH=(1.+ARH)*AA/(AT+R1)-ARH
      ADH=AA/(L-DL)*(1.+AGH*((AA-AT-R1)/AA))
      AXXS=AB*ARH-R1*AB/(AT+R1)*(ATH+ARH)
      AXXG=AB*AGH-R1/(AT+R1)*ADH-R1*AB/(AT+R1)*AGH
      DVDXS=PIE*(-4./NC*AT*AT*ATH+1./3.*AC*AC*(2.*ATH-AB*ARH+AH*(ATH
      @+ARH))+2./3.*(AB*ARH-AH*(ATH+ARH)+ATH)*AC*(3.*AT-AC))-PIE*YI**2
      @2*AXXS
C DVDXS IS ONE SIDE ONLY
      DVDXG=PIE*(1./3.*AC*AC*(-ADH-AB*AGH+AH*AGH+R1/(AT+R1)*ADH)+2./
      73.*(AB*AGH-AH*AGH-R1/(AT+R1)*ADH+ADH)*AC*(3.*AT-AC))-PIE*YI**2
      @*AXXG
C DVDXG IS ONE SIDE ONLY
      RETURN
      END

```

```

C
C
C*****
C THE FOLLOWING PROGRAMS ARE A METHOD USING LINE SEARCHES AND
BACKTRAKING
C FOR ROOT FINDING FOR A NONLINEAR SYSTEM OF EQUATIONS.
C
SUBROUTINE Insrch(xold,fold,g,p,x,f,stpmax,check,func)
LOGICAL check
DOUBLE PRECISION f,fold,stpmax,g(*),p(*),x(*),xold(*),func,
*ALF,TOLX
PARAMETER (ALF=1.e-4,TOLX=1.E-9)
EXTERNAL func
INTEGER i
DOUBLE PRECISION a,alam,alam2,alamin,b,disc,f2,fold2,rhs1,rhs2,
*slope,sum,temp,test,tmpplan
check=.false.
sum=0
do 11 i=1,2
sum=sum+p(i)*p(i)
11 enddo
sum=sqrt(sum)
if(sum.gt.stpmax)then
do 12 i=1,2
p(i)=p(i)*stpmax/sum
12 enddo
endif
slope=0
do 13 i=1,2
slope=slope+g(i)*p(i)
13 enddo
test=0
do 14 i=1,2
temp=abs(p(i))/max(abs(xold(i)),1)

if(temp.gt.test)test=temp
14 enddo
alamin=TOLX/test
alam=1
1 continue
do 15 i=1,2
x(i)=xold(i)+alam*p(i)
15 enddo
f=func(x)
if(alam.lt.alamin)then
do 16 i=1,2
x(i)=xold(i)
16 enddo
check=.true.
return
else if(f.le.fold+ALF*alam*slope)then
return
else

```

```

if(alam.eq.1)then
  tmplan=-slope/(2*(f-fold-slope))
else
  rhs1=f-fold-alam*slope
  rhs2=f2-fold2-alam2*slope
  a=(rhs1/alam**2-rhs2/alam2**2)/(alam-alam2)
  b=(-alam2*rhs1/alam**2+alam*rhs2/alam2**2)/(alam-alam2)
  if(a.eq.0)then
    tmplan=-slope/(2.*b)
  else
    disc=b*b-3.*a*slope
    tmplan=(-b+sqrt(disc))/(3.*a)
  endif
  if(tmplan.gt..5*alam)tmplan=.5*alam
endif
alam2=alam
f2=f
fold2=fold
alam=max(tmplan,.1*alam)
goto 1
END
C
C
SUBROUTINEnewtl(x,check)
  INTEGER MAXITS
  LOGICAL check
  DOUBLE PRECISIONx0(2),x(2),fvec(2) ,TOLF,TOLMIN,TOLX,STPMX
  PARAMETER (MAXITS=500,TOLF=1.D-06,TOLMIN=1.D-8,
    *TOLX=1.D-09,STPMX=50)
  COMMON /newtv/ fvec
  INTEGER i,its,j
  DOUBLE PRECISION det,den,f,fold,stpmax,sum,temp,test,
    *fjac(2,2),g(2),p(2),xold(2),fmin1
  EXTERNAL fmin1
  f=fmin1(x)

  xO(1)=x(1)
  x0(2)=x(2)
  test=0
  do 11 i=1,2
    if(abs(fvec(i)).gt.test)test=abs(fvec(i))
  11 enddo
  if(test.lt..01*TOLF)return
  sum=0
  do 12 i=1,2
    sum=sum+x(i)**2
  12 enddo
  stpmax=STPMX*max(sqrt(sum),float(2))
  do 21 its=1,MAXITS
    call fdjac1(x,fvec,fjac)
    do 14 i=1,2
      sum=0

```

```

      do 13 j=1,2
        sum=sum+fjac(j,i)*fvec(j)
13   enddo
      g(i)=sum
14   enddo
      do 15 l=1,2
        xold(i)=x(i)
15   enddo
      fold=f
      det=fjac(1,1)*fjac(2,2)-fjac(1,2)*fjac(2,1)
      p(1)=-(fjac(2,2)*fvec(1)-fjac(1,2)*fvec(2))/det
      p(2)=-(fjac(1,1)*fvec(2)-fjac(2,1)*fvec(1))/det
      call lnsrch(xold,fold,g,p,x,f,stpmax,check,fmin1)
      test=0
      do 17 i=1,2
        if(abs(fvec(i)).gt.test)test=abs(fvec(i))
17   enddo
      if (test.lt.TOLF)then
        check=.false.
        return
      endif
      if(check)then
        test=0
        den=max(f,.5*2)
        do 18 i=1,2
          temp=abs(g(i))*max(abs(x(i)),1.)/den
          if (temp.gt.test)test=temp
18   enddo
        if(test.lt.TOLMIN)then
          check=.true.
        else
          check=.false.
        endif
        return
      endif
      test=0
      do 19 i=1,2
        temp=(abs(x(i)-xold(i)))/max(abs(x(i)),1.)
        if (temp.gt.test)test=temp
19   enddo
      if (test.lt.TOLX)return
21   enddo
      write(*,*)'MAXITS exceeded in newt'
      x(1)=x0(1)
      x(2)=x0(2)
      END
      C
      C
      SUBROUTINE fdjac1(x,fvec,df)
      INTEGER NMAX
      DOUBLE PRECISION df(2,2),fvec(2),x(2),EPS
      PARAMETER(NMAX=40,EPS=1.E-4)

```



```

INTEGER i,j
DOUBLE PRECISION h,temp,f(NMAX)
do 12 j=1,2
  temp=x(j)
  h=EPS*abs(temp)
  if(h.eq.0)h=EPS
  x(j)=temp+h
  h=x(j)-temp
  call fnc1(x,f)
  x(j)=temp
do 11 i=1,2
  df(i,j)=(f(i)-fvec(i))/h
11 enddo
12 enddo
return
END
C
C
C
FUNCTION fmin1(x)
DOUBLE PRECISION fmin1,x(2),fvec(2)
COMMON/newtv/fvec
INTEGER i
DOUBLE PRECISION sum
call fnc1(x,fvec)
sum=0
do 11 i=1,2
  sum=sum+fvec(i)**2
11 enddo
fmin1=0.5*sum
return
END
C
C
SUBROUTINE newt2(x,check)
INTEGER MAXITS
LOGICAL check
DOUBLE PRECISION x0(2),x(2),fvec(2),TOLF,TOLMIN,TOLX,STPMX
PARAMETER (MAXITS=500,TOLF=1.D-06,TOLMIN=1.D-08,
*TOLX=1.D-09,STPMX=50)

COMMON /newtv/ fvec
INTEGER i,its,j
DOUBLE PRECISION det,den,f,fold,stpmax,sum,temp,test,
*fjac(2,2),g(2),p(2),xold(2),fmin2
EXTERNAL fmin2
f=fmin2(x)
x0(1)=x(1)
x0(2)=x(2)
test=0
do 11 i=1,2
  if(abs(fvec(i)).gt.test)test=abs(fvec(i))
11 enddo

```

```

if(test.lt..01*TOLF)return
sum=0
do 12 i=1,2
sum=sum+x(i)**2
12 enddo
stpmax=STPMX*max(sqrt(sum),float(2))
do 21 its=1,MAXITS
call fdjac2(x,fvec,fjac)
do 14 i=1,2
sum=0
do 13 j=1,2
sum=sum+fjac(j,i)*fvec(j)
13 enddo
g(i)=sum
14 enddo
do 15 i=1,2
xold(i)=x(i)
15 enddo
fold=f
det=fjac(1,1)*fjac(2,2)-fjac(1,2)*fjac(2,1)
P(1)=-(fjac(2,2)*fvec(1)-fjac(1,2)*fvec(2))/det
p(2)=-(fjac(1,1)*fvec(2)-fjac(2,1)*fvec(1))/det
call lnsrch(xold,fold,g,p,x,f,stpmax,check,fmin2)
test=0
do 17 i=1,2
if (abs(fvec(i)).gt.test)test=abs(fvec(i))
17 enddo
if (test.lt.TOLF)then
check=.false.
return
endif
if(check)then
test=0
den=max(f,.5*2)
do 18 i=1,2
temp=abs(g(i))*max(abs(x(i)),1.)/den
if(temp.gt.test)test=temp
18 enddo
if (test.lt.TOLMIN)then
check=.true.
else
check=.false.

endif
return
endif
test=0
do 19 i=1,2
temp=(abs(x(i)-xold(i)))/max(abs(x(i)),1.)
if (temp.gt.test)test=temp
19 enddo
if(test.lt.TOLX)return
21 enddo

```

```

write(*,*)'MAXITS exceeded in newt'
x(1)=x0(1)
x(2)=x0(2)
END
C
C
SUBROUTINE fdjac2(x,fvec,df)
INTEGER NMAX
DOUBLE PRECISION df(2,2),fvec(2),x(2),EPS
PARAMETER(NMAX=40,EPS=1.E-4)
INTEGER i,j
DOUBLE PRECISION h,temp,f(NMAX)
do 12 j=1,2
  temp=x(j)
  h=EPS*abs(temp)
  if(h.eq.0)h=EPS
  x(j)=temp+h
  h=(j)-temp
  call fnc2(x,f)
  x(j)=temp
  do 11 i=1,2
    df(i,j)=(f(i)-fvec(i))/h
  11 enddo
12 enddo
return
END
C
C
C
FUNCTION fmin2(x)
DOUBLE PRECISION fmin2,x(2),fvec(2)
COMMON /newtv/ fvec
INTEGER i
DOUBLE PRECISION sum
call fnc2(x,fvec)
sum=0
do 11 i=1,2
  sum=sum+fvec(i)**2
11 enddo
fmin2=0.5*sum
return
END
C
C*****

C*****

SUBROUTINE FNC1(Y,fvec)
C IMPLICIT DOUBLE PRECISION (A-H,O-Z)
DOUBLE PRECISION fvec(*),Y(*),AT,A,R1,DL,X,L,NC
COMMON /ROUGS1/L,NC
COMMON/ROUGS2/X,AT,R1,DL
COMMON/AAA/A

```

```

fvec(1)=(AT+Y(1))**2-(L-Y(2))**2-(X+Y(1))**2
fvec(2)=4./3.*(A**3-AT**3)/NC-Y(1)*(L-Y(2))**2+(X+Y(1))
@**2/(Y(1)+AT)+1./3.*(Y(1)*(L-Y(2))/(AT+Y(1)))**3+(X+
@Y(1))*Y(1)**2*(L-Y(2))/(Y(1)+AT)**2*(DSQRT(DABS(
@ (AT+Y(1)+L-Y(2))*((AT-L)+Y(1)+Y(2))))))
@+(X+Y(1))*Y(1)*Y(1)*DATAN((L-Y(2))/(X+Y(1)))
@+1./3.*(Y(1)*(L-Y(2))/(AT+Y(1))+Y(2)+(AT-L)**2*(2.*AT-Y(1)
@*(L-Y(2))/(AT+Y(1))-Y(2)+L)
RETURN
END

```

```

C*****
SUBROUTINE FNC2(Y,fvec)
C IMPLICIT DOUBLE PRECISION (A-H,O-Z)
DOUBLE PRECISION Y(*),fvec(*),DL,A,X,AT,L,NC,R1
COMMON /ROUGS1/L,NC
COMMON/ROUGS2/X,AT,R1,DL
COMMON/AAA/A
fvec(1)=(Y(2)+Y(1))**2-(L-DL)**2-(X+Y(1))**2
fvec(2)=4./3.*(A**3-Y(2)**3)/NC-Y(1)*(L-DL)*Y(1)**2+(X+Y(1))
@**2/(Y(2)+Y(1))+1./3.*(Y(1)*(L-DL)/(Y(2)+Y(1)))**3+(X+
@Y(1))*Y(1)**2*(L-DL)/(Y(2)+Y(1))**2*(DSQRT(DABS((
@Y(2)+Y(1)+L-DL)*((Y(2)-L)+Y(1)+DL))))
@+(X+Y(1))*Y(1)*Y(1)*DATAN((L-DL)/(X+Y(1)))
@+1./3.*(Y(1)*(L-DL)/(Y(2)+Y(1))+DL+(Y(2)-L))**2*(2.*Y(2)-Y(1)
@*(L-DL)/(Y(2)+Y(1))-DL+L)
C WRITE(30,69)X,Y(2),Y(1)
C 69 FORMAT('X=',D12.5,'AT=',D12.5,'R1=',D12.5)
RETURN
END

```

```

C*****
C      RACINE
C THIS SUBROUTINE FINDS THE ROOT OF A EQUATION.
SUBROUTINE aRACINE(X0)
IMPLICIT DOUBLE PRECISION (A-H,O-Z)
EXTERNAL AFNC
TOL=1.E-9
ITERS=0
ITS=100
XN=X0-.1
XN1=X0+.1
XOLD=XN
XNEW=XN1
1 IF (ABS(XNEW-XOLD)/ABS(XNEW).GT.TOL.AND.ITERS.LT.ITS.AND.
@ (AFNC(XN1)-AFNC(XN)).GT.0.0) THEN
XOLD=XNEW
XNEW=XN-AFNC(XN)*(XN1-XN)/(AFNC(XN1)-AFNC(XN))

```

```

PROD = AFNC(XN)*AFNC(XN1)

```

```
IF (PROD.LT..0) THEN
  XN1=XNEW
ELSE
  XN=XNEW
ENDIF
ITERS=ITERS+1
GOTO 1
ENDIF
X0=XNEW
RETURN
END
```

## **Vita**

Constance E. Schlaefer

### **Degrees:**

B.S. Engineering Mechanics, June 1988  
United States Air Force Academy, Colorado Springs, CO

M.S. Mechanical Engineering, December 1993  
University of California, Santa Barbara, CA

Ph.D. Engineering Science and Mechanics  
Pennsylvania State University, University Park, PA

### **Employment Record:**

Officer, United States Air Force  
June 1988 through present  
    Satellite Launch Controller, Vandenberg AFB, CA  
    Assistant Professor of Engineering Mechanics, USAF Academy, CO  
    Chief, Space Launch Range Op. Test and Eval., Kirtland AFB, NM  
    Wing Executive Officer, Kirtland AFB, NM

### **Recent Publications:**

C.E. Schlaefer and R.M. German, "Thermal Conductivity Evaluation of PIM Powders to Evaluate Pre-densification Sintering Phenomena," 2002 World Congress on Powder Metallurgy & Particulate Materials, Orlando, FL. Metal Powder Industries Federation, Princeton, NJ, 2002